A COUPLED FINITE-DISCRETE ELEMENT FRAMEWORK FOR SOIL-STRUCTURE INTERACTION ANALYSIS

By

Viet Duc Hoang Tran

Department of Civil Engineering and Applied Mechanics

McGill University
Montréal, Québec, Canada

August 2013

A thesis submitted to McGill University in partial fulfillment of the requirements for the degree of Doctor of Philosophy

ABSTRACT

Modeling soil-structure interaction problems involving granular material and large deformation is a challenging task particularly for geotechnical engineering. Using standard finite element methods has been found to be inefficient to model soil-structure interaction at the soil particle scale. Soil-structure interactions such as erosion void around tunnel lining and geogrid reinforcement may not be properly captured using the finite element method. The discrete element method, on the other hand, has proven its efficiency in modeling the behavior of granular soil domains at the microscopic scale. It is however not suitable to model structural elements using this numerical method due to the continuum behavior of the structure. The coupling of the finite and discrete element methods, which takes advantages of the two methods, is a promising approach to model such geotechnical engineering problems. This thesis is devoted to develop a coupled Finite-Discrete element framework for soil-structure interaction analysis and validate the developed algorithm by comparing numerical simulations with experimental data.

The research results have been published in refereed journals and conference proceedings amounting to 3 journal papers and 5 conference papers. These papers are compiled to produce 7 chapters and 1 appendix in this manuscript-based thesis. Experimental and discrete element investigations of earth pressure acting on cylindrical shaft are first presented along with a new gravitational packing technique that has been used to replicate the real sample packing process. Results from the numerical simulation and experimental work are then compared. The efficiency of the discrete element method in solving problems involving granular material and large deformation is demonstrated.

The rest of the thesis is devoted to describe the development of a three-dimensional coupled Finite-Discrete element method and its implementations. To analyze a given soil-structure interaction problem using the developed coupled

Finite-Discrete element framework, the structure is modeled using finite elements while the soil is modeled using discrete elements. Interface elements are used to ensure the force transmission between the finite and discrete element domains. Explicit time integration is used in both the finite and discrete element calculations. Different damping schemes are applied to each domain to relax the system. A multiple-time-step scheme is applied to optimize the computational cost. The developed coupled Finite-Discrete element framework is used to investigate selected soil-geogrid interaction problems including pullout test of biaxial geogrid embedded in granular material, strip footing over geogrid reinforced sand and geogrid-reinforced fill over strong formation containing void. The results of the numerical analysis are compared with experimental data. Micro-mechanical behavior of the soil domain is analyzed and displacements, stresses and strains developing in the geogrid are investigated. Conclusions and recommendations are made regarding the three-dimensional soil-structure interaction using the discrete element and coupled Finite-Discrete element methods.

RÉSUMÉ

La modélisation de l'interaction sol-structure présent plusieurs défis, particulièrement dans les sols granulaires et pour des grandes déformations. L'analyse par éléments finis est souvent utilisée mais celle-ci ne permet pas une modélisation à l'échelle des particules de sol. Ce dernier type d'analyse est requis pour la modélisation de problèmes d'interaction complexe tels que ceux de l'érosion des sols autour de l'enveloppe d'un tunnel ou du comportement d'une membrane géotextile. La méthode de modélisation par éléments discrets est un moyen efficace et reconnu pour modéliser le comportement granulaire des sols au niveau microscopique. Par contre, cette méthode n'est pas appropriée pour modéliser les structures solides et continues. Le couplage entre les éléments finis et les éléments discrets est une technique prometteuse qui combine les avantages des deux méthodes. Cette thèse est consacrée au développement de l'analyse couplée Éléments finis-Éléments discrets pour l'interaction sol-structure et à la validation des algorithmes par une comparaison des simulations numériques avec des résultats expérimentaux.

Les résultats de la recherche ont été publiés dans les journaux avec comité de lecture (3 articles) m et dans des comptes-rendus de conférence (5 articles). La thèse est soumise sous la forme d'une thèse avec manuscrits et comporte 7 chapitres principaux et une annexe. Le premier cas étudié est celui de la pression des sols sur un cylindre. Un nouvel algorithme de placement des particules par gravité et de compaction est proposé afin de mieux représenter le processus de préparation des échantillons en laboratoire. Les résultats de simulation sont comparés et validés par rapport aux résultats expérimentaux et démontrent l'applicabilité de la procédure pour l'analyse du comportement des matériaux granulaires pour des grandes déformations.

Les chapitres suivants sont dédiés au développement d'analyses ridimensionnelles couplées et à leur validation. Les éléments structuraux sont modélisés par

éléments finis tandis que le sol est modélisé par des éléments discrets. Des éléments spéciaux sont développés pour effectuer le couplage entre les deux domaines. Une intégration numérique du type explicite est utilisée pour tous les calculs dans le domaine temporel. Différents types d'amortissement sont utilisés pour chacun des domaines (finis ou discrets) afin de stabiliser le système. Une approche avec intervalles de temps multiple est utilisée afin d'optimiser le temps de calcul. La procédure est utilisée afin d'analyser la résistance à l'arrachement d'une membrane géotextile incorporée dans un milieu granulaire, et le comportement d'une semelle de fondation reposant sur un dépôt de sable renforcé avec des géotextiles au-dessus d'une cavité profonde. Les résultats des simulations numériques sont comparés aux données expérimentales. Les déplacements, les contraintes et les déformations dans le géotextile et le sol sont analysés. Des conclusions et des recommandations sont formulées pour l'analyse tridimensionnelle couplée de l'interaction sol-structure.

ACKNOWLEDGMENTS

First of all, I wish to express my great gratitude to my supervisors Prof. Mohamed Meguid and Prof. Luc Chouinard for their guidance, support and understanding throughout the years. I am truly indebted to both for their motivating enthusiasm and leading me to a stimulating research program.

Special thanks to Dr. Kien Dang for his kind help and advice during this research.

Many thanks to my colleagues in the geotechnical group at McGill University who directly or indirectly have contributed to the accomplishment of this thesis.

A special thanks is due to the Technical Staff of the Department of Civil Engineering and Applied Mechanics at McGill University, notably Dr. Bill Cook and Mr. Jorge Sayat.

I would like to acknowledge the financial support of the McGill Engineering Doctoral Award.

Above all, I owe deep appreciation and thanks to my parents, Mr. Dong Tran and Mrs. Xo Hoang, and my brother, Mr. Nam Tran their prolonged understanding, support and encouragement.

And, thank you Kim, for your support, your patience, and your love.

PUBLICATIONS TO DATE

Journal papers

[J1] **Tran, V. D. H**., Meguid, M. A., and Chouinard, L. E. "Discrete Element and Experimental Investigations of the Earth Pressure Distribution on Cylindrical Shafts." *ASCE International Journal of Geomechanics (In Press)*, 2012.

[J2] **Tran, V. D. H.**, Meguid, M. A., and Chouinard, L. E. "A Finite–Discrete Element Framework for the 3D Modeling of Geogrid–Soil Interaction Under Pullout Loading Conditions." *Geotextiles and Geomembranes*, 37 (1-9), 2013.

[J3] **Tran, V. D. H.**, Meguid, M. A., and Chouinard, L. E. "Three Dimensional Analysis of Geogrid Reinforced Soil Using Finite-Discrete Element Framework." *ASCE International Journal of Geomechanics* (submitted), April 2013.

Conference papers

[C1] **Tran, V. D. H.**, Meguid, M. A., and Chouinard, L. E. "Coupling of Random Field Theory and the Discrete Element Method in the Reliability Analysis of Geotechnical Problems." *Canadian Society for Civil Engineering (CSCE) Annual Conference*, Edmonton, Canada. Paper No. GEN-1022, May 2012.

[C2] **Tran, V. D. H.**, Meguid, M. A., and Chouinard, L. E. "A Discrete Element Study of the Earth Pressure Distribution on Cylindrical Shafts." *Tunneling Association of Canada (TAC) Conference*, Montreal, Canada. Paper No. 112, October 2012.

[C3] **Tran, V. D. H.**, Yacoub, T. E., and Meguid, M. A. "On the analysis of vertical shafts in soft ground: Evaluating Soil-Structure Interaction Using

Two Different Numerical Modeling Techniques." Submitted to *The 66th Canadian Geotechnical Conference*, Montreal, Canada, October 2013.

[C4] **Tran, V. D. H.**, Meguid, M. A., and Chouinard, L. E. "Soil-Geogrid Interaction Analysis Using a Coupled Finite-Discrete Element Method." Submitted to *The 66th Canadian Geotechnical Conference*, Montreal, Canada, October 2013.

[C5] **Tran, V. D. H.**, Meguid, M. A., and Chouinard, L. E. "The Application of Coupled Finite-Discrete Element Method in Analyzing Soil-Structure Interaction Problems." Submitted to *III International Conference on Particle-based Methods– Fundamentals and Application*, Stuttgart, Germany, September 2013.

Other

[P1] **Tran, V. D. H.**, Meguid, M. A., and Chouinard, L. E. "An Algorithm for the Propagation of Uncertainty in Soils using the Discrete Element Method." *The Electronic Journal of Geotechnical Engineering*, 17(V), 3053-3074, 2012.

[P2] **Tran, V. D. H.**, Meguid, M. A., and Chouinard, L. E. "Numerical Simulation of Shear Tests Using the Discrete Element Method." *McGill CEGSS Conference*, Montreal, Canada. Paper No. GEO-04, April 2012.

TABLE OF CONTENTS

LIST OF FIGURES

LIST OF TABLES

LIST OF SYMBOLS

Roman Symbols

a	Radius of the model shaft
B	Width of the strip foundation
c	Damping coefficient for the mass proportional damping
C_u	Soil coefficient of uniformity
C_c	Soil coefficient of curvature
D	Model shaft diameter
d_0	Distance between two particle centers
D_5	Particle diameter corresponding to 5 % passing
D_{50}	Particle diameter corresponding to 50 % passing
D_r	Relative density
E	Particle material modulus
F_{bt}	Bearing resistance of geogrid transverse members
$f^{c,j}$	Contact force vector at contact point c
$\vec{\mathbf{F}}_{contact}$	Total contact force
F_f	Geogrid frictional resistance
$\vec{\mathbf{F}}_N$	Normal force of a contact
F_p	Total geogrid pullout resistance
$\vec{\mathbf{F}}_T$	Tangential force of a contact
h	Depth of a earth pressure measurement point
H	Height of a soil domain
i, j	Cartesian coordinates
K	Sum of normal stiffnesses of all particles interacting with a wall
K	Stiffness matrix

K_i	Per-particle stiffness of contacts in which particle *i* participates
K_o	Lateral earth pressure coefficient at-rest
K_N	Normal stiffness at a contact
K_r	Rolling stiffness of an interaction
K_T	Tangential stiffness at a contact
$k_n^{(A)}$	Normal stiffness of particle A
$k_n^{(B)}$	Normal stiffness of particle B
$\mathbf{M}$	Mass matrix
m_i	Mass of particle *i*
$\vec{\mathbf{M}}_r$	Resistant moment
N	Coordination number, number of geogrid layers
N_c	Number of contacts within a measurement box
n_i	Unit branch vector component in the *i* direction
N_i	Shape functions
N_p	Number of particles
p	Active earth pressure acting on a vertical shaft
$\mathbf{P}$	External force vector
P_0	Initial earth pressure acting on a vertical shaft
P_{xx}	Average tensile force
q	Foundation pressure
r_A, r_B	Radii of particles A and B
s	Shaft radius reduction
S_{xx}	Stress in the x-direction within the geogrid
U_x	Geogrid frontal displacement
V	Volume of a measurement rectangular box
$\mathbf{x}$	Displacement vector
$x^{c,i}$	Branch vector connecting two contact particles

$x^{(i)}$	Coordinate of node i of a quadrilateral
$x^{(O)}$	Temporary center node

Greek Symbols

α	The angle that the failure surface makes with the horizontal
β_r	Rolling resistance coefficient
γ	Soil unit weight
$\delta\vec{\mathbf{\Delta}}_T$	Incremental tangential displacement
$\delta\vec{\mathbf{F}}_T$	Incremental tangential force
$\mathbf{\Delta}$	Contact penetration depth
Δt_{cr}	Critical time-step
Δt_{FE}	Time-step in the finite element domain
Δt_{DE}	Time-step in the discrete element domain
$\vec{\mathbf{\Delta}}_N$	Normal penetration between two particles
η_r	A dimensionless coefficient
λ	Earth pressure coefficient on the radial plane
λ_m	Maximum eigenvalue
$\vec{\boldsymbol{\theta}}_r$	Rolling angular vector
ν	Poisson's ratio
σ , σ_v	Current normal stress acting on a wall
σ_{ij}	Average stresses within a box
σ_0	Desired normal stress acting on a wall

σ_θ	Circumferential stress in soil
σ_r	Radial stress in soil
σ_z	Vertical stress in soil
φ_{micro}	Microscopic friction angle
ϕ	Internal friction angle (deg)
$\mathbf{\Phi}_{ij}$	Fabric tensor

CHAPTER 1

Introduction

1.1. Introduction

The interaction between soil and geotechnical structures has been attracting enormous research attention in the last few decades. Beside experimental studies, numerical methods have proven to be efficient in modeling the soil-structure interaction at the macroscopic scale level. The finite element method (FEM) has been widely used to model soil-structure interaction in many geotechnical engineering problems including tunneling process (Mroueh and Shahrour, 2002), deep excavation (Zdravkovic et al., 2005) and pile foundation (Karthigeyan et al., 2007). However, it is challenging for standard finite element methods to properly model the soil-structure interaction at the particle scale level. For geotechnical engineering problems that involve particle movement such as void erosion around tunnel lining (Meguid and Dang, 2009), earth pressure on cylindrical shaft (Tobar and Meguid, 2011) and geogrid reinforcement (Michalowski, 2004), the soil-structure interaction nature may not be properly captured using FEM.

The discrete element method (DEM) has proven to be promising for modeling geotechnical engineering problems which involve granular material and large deformation (Herten and Pulsfort, 1999; Cui and O'Sullivan, 2006; Guerrero et al., 2006). Although DEM is considered efficient in modeling soil particles, it is challenging to properly model the behavior of structural elements using discrete particles due to the continuum behavior of the structure. The coupling of the finite and discrete element methods, which takes advantages of the two methods, is a promising approach for modeling soil-structure interaction.

1.2. Research Motivation

Although the coupling of FEM and DEM was initially used by researchers to solve dynamic impact problems (Han et al., 2002; Xiao and Belytschko, 2004; Dhia and Rateau, 2005; Bhuvaraghan et al., 2010), little work has been done to develop a coupling approach in geotechnical engineering. A two-dimensional coupled FE-DE framework was proposed by Onate and Rojek (2004) to solve dynamic geotechnical engineering problems. Fakhimi (2009) proposed a combined method to simulate triaxial tests by using finite elements to model the membrane and discrete elements to model the soil sample. The simulation required a very fine FE mesh with a large number of elements to maintain numerical stability. Coupled FE-DE simulations reported by Villard et al. (2009), Elmekati and Shamy (2010) and Dang and Meguid (2013) were not validated with experimental data.

Thus, the goal of the thesis is to develop a coupled FE-DE framework suitable for soil-structure interaction analysis validated using experimental data. This involves developing a new DEM packing method, simulating DE problems, and conducting soil-structure interaction analysis using the developed FE-DE framework.

1.3. Objective and Scope

The research presented in this thesis has two major objectives. The first objective is to validate the use of the discrete element method in investigating geotechnical engineering problems involving large deformation. This objective is achieved by addressing the following:

1) Develop a gravitational packing method to simulate the soil deposition.
2) Investigate the earth pressure distribution on cylindrical shaft in soft ground using the discrete element method. The numerical simulation is validated by comparing the numerical results with experimental data.

The second objective is to develop a coupled Finite-Discrete element framework and use the framework to investigate geotechnical engineering problems involving soil-structure interaction and granular material. This is achieved by addressing the following:

3) Develop a coupled Finite-Discrete element framework and implement the developed framework into an open source code.

4) Analyze pullout test of biaxial geogrid embedded in granular material.

5) Analyze strip footing over geogrid-reinforced sand.

6) Analyze geogrid-reinforced fill over strong formation containing void.

1.4. Contributions of authors

Papers J1, J2, J3, C1, C2, C3, C4 and C5 listed in the publication list are included in the thesis. All papers are the candidate's original work.

The coupled Finite-Discrete element framework developed in the thesis is a continuation of the original work of Dang and Meguid (2010, 2013). Dang developed the initial framework and used it to simulate a tunnelling process. The author has moved the original finite element engines into a new version of the open source discrete element code YADE. Original C++ codes were modified by the author in order to make them compatible with the new version of YADE. Bugs detected from the original framework have been fixed. New C++ engines for discrete and finite element as well as coupled Finite-Discrete element analyses used in the thesis are written by the author. The author has wrapped all developed C++ engines in Python, a scripting language in YADE. This assures rapid and flexible simulation process. A manual for the developed coupled Finite-Discrete element framework written by the author is presented in the appendix of the thesis.

All the formulation, program coding, and the preparation of the manuscripts were completed by the candidate, under the supervision of Prof. Mohamed Meguid and Prof. Luc Chouinard, his thesis supervisors.

1.5. Thesis Organization

This thesis consists of seven chapters. The chapters essentially reflect the order in which the research was carried out. Chapter 2 presents recent developments in modeling soil-structure interaction problems involving granular material and large deformation. Chapters 3 and 4 are modified versions of journal papers J1 and J2 while chapter 5 and 6 are parts of journal paper J3 in the publication list.

Chapter 3 illustrates the advantages of the discrete element method in modeling geotechnical engineering problems involving granular material and large deformation. In this chapter, numerical studies that have been conducted to investigate the earth pressure distribution on cylindrical shaft in soft ground are presented. Previous experimental work conducted by the research group is summarized first. The experiment consists of a mechanically adjustable lining installed in granular material under axisymmetric condition. The shaft radius is gradually reduced and the earth pressure acting on the shaft is measured for different induced wall movements. A discrete element analysis is then performed to simulate the experiment using a new gravitational packing. Input parameters for the simulation are determined using experimental results of direct shear tests. The microscopic behavior of the soil domain is obtained from the discrete element simulation. The chapter is a modified version of paper J1 in the publication list.

Chapter 4 presents the coupled Finite-Discrete element framework developed to simulate soil-structure interaction. Force transmission between the finite and discrete element domains is assured using interface elements. Explicit time integration is used in both the finite and discrete element calculations. Different damping schemes are applied to each domain to relax the system. A multiple-time-step scheme is applied to optimize the computational cost. The developed coupled Finite-Discrete element framework is used to investigate a pullout test of a biaxial geogrid embedded in granular material. The geogrid is modeled using finite elements while the soil is modeled using discrete elements. The results of the analysis are compared with experimental data. The displacements and stresses developing in the geogrid as well as the micro-mechanical behavior of the soil domain are investigated. The proposed coupled Finite-Discrete element method has proven its efficiency in modeling pullout test in three-dimensional space and capturing the response of both the geogrid and the surrounding material. The chapter presents the work carried out in paper J2 in the publication list.

Chapter 5 investigates the behavior of a strip foundation over geogrid reinforced sand using the developed coupled Finite-Discrete element framework. The numerical simulation is validated by comparing the numerical results with the experimental data and the soil-geogrid interlocking effect is demonstrated. The deformation and stress distribution within the geogrid as well as the behavior of the soil domain relative to soil displacements, contact orientations, contact forces are also analyzed. The proposed coupled Finite-Discrete element method has demonstrated its efficiency in investigating the three-dimensional soil-geogrid interaction at the microscopic scale. The chapter is part of paper J3 in the publication list.

Chapter 6 presents a numerical simulation of geogrid-reinforced fill over strong formation containing void using the proposed coupled Finite-Discrete element framework. The backfill soil is modeled using discrete elements while the geogrid is modeled using finite elements. The use of geogrid to reinforce a fill over a void is proven to be effective in preventing soil from moving toward the void. The developed coupled Finite-Discrete element framework efficiently captures the deformations and stresses of the geogrid as well as the soil displacements, contact orientations, stresses and porosity changes. The chapter is part of paper J3 in the publication list.

Conclusions drawn from this research and recommendations for future research are outlined in chapter 7.

CHAPTER 2

Literature Review

Literature related to the modeling of soil-structure interaction in geotechnical engineering as well as the available techniques to couple the finite and discrete element methods are summarized below.

2.1. Soil-Structure Interaction Modeling using the Finite Element Method

The finite element method has been widely used to model soil-structure interaction in many geotechnical engineering problems such as tunneling, deep excavation and pile foundation. Modeling the tunneling process using FEM has been performed by researchers including Mroueh and Shahrour (2002), Galli et al. (2004), Kasper and Meschke (2004), Meguid and Rowe (2006) and Yoo (2013). Soil-wall interaction during excavation process has been studied by Faheem et al. (2004), Zdravkovic et al. (2005) and Finno et al. (2007). Similarily, FEM has been used to model soil-pile interaction (Pan et al., 2002; Khodair et al., 2005; Maheshwari et al., 2005; Karthigeyan et al., 2007). Soil-structure interaction is often assured using interface elements (Bfer, 1985; Van Langen and Vermeer, 1991; Karabatakis and Hatzigogos, 2002). In the above studiess, the soil-structure interactions using interface elements were often considered at the macroscopic scale.

In geotechnical engineering problems such as those involving erosion voids next to tunnel lining (Zienkiewicz and Huang, 1990; Meguid and Dang, 2009), earth pressure on cylindrical shaft (Berezantzev, 1958; Tobar and Meguid, 2011) and geogrid reinforced soil (Agaiby et al., 1995; Palmeira, 2004; Michalowski, 2004), it is necessary to model the soil-structure interaction at the particle scale level to properly capture the soil particle-structure interaction. Voids due to erosion around tunnel linings often have irregular shapes and sizes and it is challenging to model the void development using FEM especially when the void size increases (Meguid and Dang, 2009). The active earth pressure on a cylindrical shaft is generally reached with sufficient shaft wall movement. For the case of a shaft surrounded by granular soil, the required shaft movement to reach the full active condition was found to range from 2.5% to 4% of the shaft radius (Tran et al., 2012). The problem involves granular material and large deformation which makes it challenging to properly capture the earth pressure acting on the shaft wall using traditional FEM. In reinforced soil problems such as geogrid pullout test (Palmeira, 2004), geogrid reinforced foundation (Michalowski, 2004) and geogrid reinforced fill over void (Agaiby et al., 1995), soil-geogrid interlocking effect is considered an important feature. However, it is challenging to model the interlocking effect using FEM due to its particle based interaction. Moreover, the geogrid geometry is often simplified either as a truss structure (in 2D analysis) or a continuous sheet (in 3D analysis) which ignores the interlocking effect.

Although the above soil-structure interaction problems may be modeled using an adaptive remeshing approach (Zienkiewicz and Huang, 1990; Zienkiewicz et al., 1995) or a multiscale approach (Hughes, 1995; Garikipati and Hughes, 1998), numerical simulations involving large soil deformation and unpredictable discontinuities using these approaches did not receive much research attention in the literature.

2.2. Granular Modeling using the Discrete Element Method

The discrete element method has proven to be a promising approach to capture the response of granular material experiencing large deformation. The method was first proposed by Cundall and Strack (1979) and has been widely used to analyze geotechnical problems. In this method, a soil domain is modeled using a set of discrete particles interacting at their contact points. Particles can have different shapes such as discs, spheres, ellipsoids and clumps. The real grain size distribution can be modeled using particles with variable sizes. The interaction between particles is regarded as a dynamic process that reaches static equilibrium when the internal and external forces are balanced. The dynamic behavior is represented by a time-step algorithm using an explicit time-difference scheme. Newton's and Euler's equations are used to determine particle displacement and rotation.

In a typical simulation step, forces and torques acting on each discrete particle are accumulated from the contacts in which the particle participates. These generalized forces are the used to update its position (Equation 2-1) and orientation (Equation 2-2).

For position update:

$$\ddot{\mathbf{u}}_{\mathbf{i}} = \mathbf{F}_{\mathbf{i}} / m_i \tag{2-1}$$

where, m_i, $\ddot{\mathbf{u}}_{\mathbf{i}}$ and $\mathbf{F}_{\mathbf{i}}$ are the mass, the current acceleration and the total force acting on particle *i*, respectively.

For orientation update (spherical particles):

$$\dot{\boldsymbol{\omega}}_{\mathbf{i}} = \mathbf{T}_{\mathbf{i}} / I_i \tag{2-2}$$

where, $\dot{\boldsymbol{\omega}}_{\mathbf{i}}$, I_i and $\mathbf{T}_{\mathbf{i}}$ are the current angular acceleration, the moment of inertia and the total torque acting on particle *i*, respectively.

The discrete element method has been used to study different geotechnical problems involving granular materials. Laboratory tests have been modeled using DEM to investigate the microscopic behavior of soil samples. The force distribution and shear band developing during a direct shear test using DEM were reported by Thornton et al. (2003). Cui and O'Sullivan (2006) employed DEM to investigate macroscopic and microscopic responses of granular soil samples under direct shear condition. Park et al. (2009) modeled rock joints under direct shear using bonded-particles. Triaxial tests of granular soil samples were modeled by Ng (2004), Cui et al. (2007) and Belheine et al. (2009). Similarily, simple shear test simulation using DEM was reported by Jiang et al. (2003) and Duriez et al. (2011). Numerical results of the above studies show a good agreement with experimental data which demonstrates the efficiency of DEM in simulating laboratory tests.

Large scale geotechnical problems have been also modeled using DEM. Lobo-Guerrero et al. (2006) investigated the behavior of railtrack ballast degradation during cyclic loading. The particle breakage process was visualized and the effect of crushing on the behavior of track ballast material was investigated. Bearing capacity of driven piles in crushable granular materials was studied by Lobo-Guerrero and Vallejo (2005) using breakable DE particles. Deluzarche and Cambou (2006) employed the same approach to study rockfill dam behavior. Those simulations were capable of simulating particle breakage process which is difficult to observe using experimental tests.

Earth pressure acting on vertical shafts was studied by Herten and Pulsfort (1999). Spherical particles were used to model the soil domain. The circular shaft was assumed to behave as segments made from small flat walls. The shaft wall was gradually moved inward and lateral pressures acting on the shaft wall were recorded. Results of the numerical simulation were then compared with experimental data.

A simplified DEM model was developed by Maynar et al. (2005) to study the underground tunneling process. Input parameters for the numerical simulation were determined using triaxial test calibration. The excavation process was modeled and the tunnel face stability was analyzed. The thrust and torque evolution with respect to the movement of earth pressure balance machine were investigated.

Gabrieli et al. (2009) studied the behaviour of a shallow foundation on a model slope. A particle upscale approach was proposed to reduce the number of DE particles required for the simulation. Displacement fields and contact force networks of the model were obtained at the microscopic level.

Jenck et al. (2009) employed DEM to model granular fill supported by piles. A simplified two-dimensional DE model was developed to investigate soil improvement using vertical rigid piles. Macro scale responses of the platform over piles such as soil arching, loads transfer to the piles and platform settlement were analyzed. The DE simulation was compared with experimental data. Parametric studies were performed to investigate the influence of microscopic parameters on the macroscopic response of the model.

It can be seen that although DE simulations have been reported in the literature, the number of DE validations is still limited and needs to be expanded. Moreover, the studied DE models were often simplified in 2D space (Lobo-Guerrero and Vallejo, 2005; Deluzarche and Cambou, 2006; Lobo-Guerrero et al., 2006; Jenck et al., 2009) which limits the capability of DEM to capture the 3D soil behavior at the microscopic level.

The modeling of soil-structure interaction using DEM has been reported by Villard and Chareyre (2004), McDowell et al. (2006), Han et al. (2011) and Chen et al. (2012). Villard and Chareyre (2004) used two-dimensional DEM to model the failure of geosynthetic sheets anchored in trenches. The geosynthetic sheets were modeled using "dynamic spar elements" while backfill soil was modeled using disk elements. Contact laws between dynamic spar elements and disks were introduced to assure their interaction. Pullout strengths of different anchorage shapes as well as deformation and failure mechanism of the system were investigated.

McDowell et al. (2006) and Chen et al. (2012) used DEM to model both the geogrid and the backfill soil. The geogrid was modeled using a set of spherical particles bonded together to form the geogrid shape. The interaction between the geogrid and the surrounding soil was obtained through the contact between discrete particles. The geogrid was then pulled out to investigate the peak mobilised resistance and associated displacement (McDowell et al., 2006). In Chen et al. (2012), the behavior of the geogrid-reinforced ballast under cyclic loading was investigated and the effectiveness of the geogrid reinforcement was examined.

Han et al. (2011) used DEM to model geogrid-reinforced embankment over piles. The 2D embankment was modeled using disk elements and the 2D geogrid was modeled using bonded particles. The changes of stresses, porosities and displacements within the embankment fill as well as the behavior of the geogrid were investigated.

In the above soil-structure interaction simulations, the structural elements were modeled using dynamic spar elements or bonded particles which do not represent the continuous nature of the structure. Moreover, due to the inflexibility of the bonded particles and dynamic spar elements, the real deformation as well as strains and stresses within the structure may not be accurately captured.

2.3. Coupling the Finite and Discrete Element Methods

To take advantage of both FEM and DEM, the coupling of the two numerical methods has been proposed. In this approach, the analyzed problem is divided into FE and DE domains. Several algorithms have been developed to assure the load transfer from the FE domain to DE domain and vice versa.

A procedure for combining finite and discrete elements to simulate the shot peening process was proposed by Han et al. (2002). Spherical shot was modeled using rigid discrete elements while the target material was modeled using deformable finite elements. The developed algorithm could capture the dynamic nature of the shot peening. However, the element size in the impact area should be no larger than d/10 where d is the diameter of the shot. This requires a large number of finite elements which results in high computational cost. A simulation of the shot peening process using a combined finite-discrete element approach was also reported by Bhuvaraghan et al. (2010).

An algorithm for coupling the finite and discrete element methods was reported by Fakhimi (2009). The algorithm was capable of modeling deformable membrane in a laboratory triaxial test. The membrane was modeled using FE while the soil was modeled using DE. The membrane-soil interaction was based on the contact between DE and external face of the FE membrane. Both FE and DE computations were integrated explicitly using a central difference scheme.

Xiao and Belytschko (2004) proposed a bridging domain method for coupling continuum models with molecular models. In this approach, the continuum and molecular domains were overlapped in a bridging sub-domain. Using the linearization of Halmitonian dynamics for both molecular and continuum models, this multi-scale method can avoid spurious wave reflections at the molecular/continuum interface. A multiple-time-step algorithm was also proposed within this framework. Similar techniques to combine the finite and discrete element domains were reported by Dhia (1998) and Dhia and Rateau (2005).

Although the above coupling approaches have shown their efficiency in analyzing certain engineering problems, their applications in geotechnical engineering are still very limited. Villard et al. (2009) proposed a coupled FE-DE approach to model earth structures reinforced by geosynthetic. Interface elements were proposed to assure the interaction between the FE and DE domains. The framework was used to model the interaction between a geosynthetic sheet and surrounding soil. The geosynthetic sheet was modeled using FE while the soil was modeled using DE. Elmekati and Shamy (2010) used a similar approach to model a rigid pile in contact with granular soil. The near-field zone surrounding the pile was modeled using DE whereas FE was used to model far-field zones. The interaction between the FE and DE domains was assured using a wall set of polygons having the same geometry of finite element surfaces at the interface.

Dang and Meguid (2013) proposed a coupled FE-DE approach to model soil-structure interaction problems involving large deformation. The domain involving the large deformation was modeled using DE while FE was used to model the rest of the domain. Interface elements at the boundary of the two domains were introduced to transmit interacting forces between the DE and FE domains. Explicit time integration with different damping schemes were applied to each domain in order to relax the system and to reach the convergence condition. Since a relatively coarse FE mesh is required, the algorithm reduces the computational time. The framework was then used to simulate a soft ground tunneling problem involving soil loss near an existing lining.

2.4. Conclusion for the Literature Review

Based on the previous literature review and in addition to the review presented in the coming chapters, it can be seen that little work has been done to date to validate discrete element simulations of problems particularly those involving granular material and large deformation. Although the coupled finite-discrete element approach has been used in geotechnical engineering to model certain soil-structure interaction problems, the available validation of the coupling approach is still very limited. Therefore, there is a need to model and validate complicated soil-structure interaction problems such as those of three-dimensional soil-geogrid interaction. It is also necessary to develop an efficient coupled finite-discrete element framework that reduces computational cost and modeling effort. Such development will be presented in this thesis along with experiments and numerical simulations of geotechnical engineering problems.

CHAPTER 3

Discrete Element Simulation and Experimental Study of the Earth Pressure Distribution on Cylindrical Shafts *

Abstract

Experimental and numerical studies have been conducted to investigate the earth pressure distribution on cylindrical shafts in soft ground. A small scale laboratory setup that involves a mechanically adjustable lining diameter installed in granular material under axisymmetric condition is first described. The earth pressure acting on the shaft and the surface displacements are measured for different induced wall movements. A numerical modeling is then performed using the discrete element method to allow for the simulation of the large soil displacement and particle rearrangement near the wall. The experimental and numerical results are summarized and compared against previously published theoretical solutions. Conclusions regarding the soil failure and the pressure distributions in both the radial and circumferential directions are presented.

Keywords: discrete element method, cylindrical shaft, earth pressure, retaining structures.

---

* A version of this chapter has been published in *International Journal of Geomechanics ASCE*, 2012 (in press).

3.1. Introduction

The discrete element method (DEM) has been more and more widely used to simulate geotechnical problems. Since it was first proposed by Cundall and Strack (1979), the method has proven to be a promising approach to capture the response of granular materials. A great number of papers on the DEM have been published such as Jiang et al. (2003); Cui and O'Sullivan (2006); Yan and Ji (2010) and Chen et.al. (2012). One approach to implement the DEM in geotechnical engineering is to investigate the microscopic soil behavior by fitting the macro-scale response of actual geotechnical problems with the macro-scale response of the DE simulations. Although extensive studies have been performed on the quantitative validation of standardized laboratory tests including the direct shear test and the triaxial test (Liu et al., 2005; Cui and O'Sullivan, 2006; Belheine et al., 2009; O'Sullivan and Cui, 2009), the number of DE validations of larger scale problems (Jenck et al., 2009; Chen et al.2012) is still limited and needs to be expanded. The quantitative validation of such geotechnical problems is therefore necessary.

This study aims at conducting a quantitative validation of a practical geotechnical problem and providing an insight into the behavior of the structure and surrounding soil. The earth pressure distribution on cylindrical shafts is selected since cylindrical structures such as vertical shafts and caissons are widely used in practice and the determining the earth pressure on these structures has received extensive research attention in the past three decades. Experimental and theoretical studies have been conducted to understand the mechanics behind the observed lateral pressure distribution along a vertical shaft and calculate the stress changes within the soil surrounding the shaft structure. Among the reported experimental studies are those of Walz (1973); Lade et al. (1981); Konig et al. (1991); Chun and Shin (2006) and Tobar and Meguid (2011) which made significant progress in measuring the lateral earth pressure due to the movement of a shaft wall. Many theoretical studies on the same topic have been recently reported such as Cheng and Hu (2005); Cheng et al. (2007); Salgado and Prezzi (2007); Andresen et al. (2011) and Osman and Randolph (2012).

An attempt has been made by Herten and Pulsfort (1999) to apply the DEM to simulate a laboratory size shaft construction. Although the study provided useful results, the circular shaft was assumed to behave as a small flat wall which has lead to an inadequate simulation of the arching effect and the stress distribution around the shaft. Furthermore, a quite small segment of the shaft geometry was modeled resulting in the presence of rigid boundaries close to the investigated area. Therefore, there is a need for an improved DE simulation of the problem considering the problem geometry as well as realistic soil properties.

In this paper, an experimental study of a model shaft installed in granular material is first presented. The recorded lateral earth pressures acting on the shaft with different wall movements is measured. A DE model that has been developed to simulate the shaft model is then introduced. A suitable packing method to generate the soil domain is proposed and a calibration test is conducted to determine the input parameters needed for the simulation. The results of the experimental and numerical studies are then analyzed and conclusions are made regarding the distribution of the radial and circumferential stresses around the shaft as well as the extent of soil shear failure.

3.2. Experimental Study

An experimental study was performed to investigate the active earth pressure on circular shafts in dry sand. During the experiment, the shaft diameter was uniformly reduced while recording the radial earth pressures at different depths. The experimental setup consisted of an instrumented shaft installed in soil contained within a cylindrical concrete container. Details of the test setup and procedure have been reported elsewhere (Tobar and Meguid, 2011) and are briefly summarized below.

3.2.1. Model shaft

The model shaft consisted of six curved lining segments cut from a steel tube with 101.6 mm in outer diameter and 6.35 mm in thickness. The lining segments were fixed in segment holders which in turn, were attached to hexagonal nuts using steel hinges (see Figure 3-1). The nuts could move vertically along an axial rod which could be rotated using a pre-calibrated handle. The shaft was placed on a plexiglass plate attached firmly to the base of the container. The initial diameter of the shaft is 150 mm and the length of the shaft is 1025 mm with a surrounding soil height of 1000 mm. Shims bent from gauge steel strips were used to cover the spaces between the lining segments. They were placed on the outer surface of the lining and overlapped the steel segments such that one edge of each shim was fixed to one lining segment, whereas the other edge was free to slide over the lining segment. This mechanism keeps the shaft segments from colliding to one another during the inward movement and the decrease in circumference during the inward movement is assured without generating gap between the segments (Figure 3-1c).

In order to reduce the shaft diameter, the axial rod is rotated forcing the hexagonal nuts to move vertically; the segment holders and the lining segments are then pulled radially inward. These movements force the shaft diameter to decrease uniformly. Two additional segment guide disks were also installed to protect the shaft linings from rotational movement or sliding out of the segment holders (Figure 3-1b).

3.2.2. Concrete container

A cylindrical concrete tank with inner diameter of 1220 mm provided the axisymmetric condition for the experiment. The tank diameter was chosen to minimize the boundary effects on the behavior of the soil-shaft interaction during the experiment. Previous experimental results of Chun and Shin (2006) and Prater (1977) suggest that soil failure zone extends laterally from 1 to 3 times the shaft radius. Therefore, negligible soil movement is expected in the present investigation at a radial distance of 240 mm from the outer perimeter of the shaft. The depth of the container is 1070 mm to support the full length of the shaft. The interior side of the container was smoothed and lined with plastic sheets to reduce the soil-wall friction. In addition, a sand auger system was used to remove sand after each test through a circular hole in 150 mm diameter located sideways at the base of the container. An overview of the experimental setup and the model shaft is shown in Figure 3-1a.

3.2.3. Data recording

Load cells and displacement transducers were used to measure the earth pressure and wall movement during the test. Three load cells were installed behind the lining segments at three locations along the shaft: 840 mm, 490 mm and 240 mm below the sand surface, respectively. The load cells were equipped with sensitive circular areas of one inch diameter in contact with the soil. Two displacement transducers were located near the top and bottom of the shaft lining. All load cells and displacement transducers were connected to a data acquisition system and controlled though a personal computer.

3.2.4. Testing procedure

Before each test, all instruments were examined and the shaft was adjusted to have an initial diameter of 150 mm. The concrete container was then filled with coarse sand (Granusil silica 2075, Unimin Corp.) through raining process with a target depth of one meter from the shaft base. A summary of the sand properties is given in Table 3-1. A hopper positioned 1500 mm above the tank was used to spread the sand uniformly over the container. Sand was placed in three layers and as soon as the sand height reached slightly over 1m, the raining process was stopped and extra sand was removed. The sand height was checked using laser sensors to ensure consistent initial conditions for each test. The shaft diameter was then reduced slowly and readings were taken for each movement increment. The test was stopped when the reduction in the shaft radius reached 5 mm.

Table 3-1 Soil properties used in the experimental study

Parameter	Value
Specific gravity	2.65
Coefficient of uniformity - C_u	3.6
Coefficient of curvature - C_c	0.82
Void ratio	0.78
Unit weight γ (kN/m^3)	14.7
Internal friction angle ϕ (deg)	41
Cohesion (kN/m^2)	0

3.3. Discrete Element Simulation

The discrete element method considers the interaction between distinct particles at their contact points. Different types of particles have been developed including discs, spheres, ellipsoids and clumps. Particles in a sample may have variable sizes to represent the grain size distribution of the real soil. The interaction between particles is regarded as a dynamic process that reaches static equilibrium when the internal and external forces are balanced. The dynamic behavior is represented by a time-step algorithm using an explicit time-difference scheme. Newton's equations and Euler's equations are used to determine particle displacement and rotation. A flowchart illustrating DE simulation is shown in Figure 3-2.

The DE simulations in this study are conducted using the open source discrete element code YADE (Kozicki and Donze, 2009; Šmilauer et al., 2010). Spherical particles of different sizes are used for this study. The contact law between particles is briefly described below (Figure 3-3).

If two particles A and B with radii r_A and r_B are in contact, the contact penetration depth is defined as:

$$\mathbf{\Delta} = r_A + r_B - d_0 \tag{3-1}$$

where, d_0 is the distance between the two centers of particle A and B.

The force vector $\vec{\mathbf{F}}$ which represents the interaction between the two particles is decomposed into normal and tangential forces:

$$\vec{\mathbf{F}}_N = K_N . \vec{\mathbf{\Delta}}_N \tag{3-2a}$$

$$\delta\vec{\mathbf{F}}_T = -K_T . \delta\vec{\mathbf{\Delta}}_T \tag{3-2b}$$

where, $\vec{\mathbf{F}}_N$ and $\vec{\mathbf{F}}_T$ are the normal and tangential forces; K_N and K_T are the normal and tangential stiffnesses at the contact; $\delta\vec{\mathbf{\Delta}}_T$ is the incremental tangential displacement, $\delta\vec{\mathbf{F}}_T$ is the incremental tangential force and $\vec{\mathbf{\Delta}}_N$ is the normal penetration between the two particles. K_N and K_T are defined by:

$$K_N = \frac{k_n^{(A)} k_n^{(B)}}{k_n^{(A)} + k_n^{(B)}} \tag{3-3}$$

where, $k_n^{(A)}$ and $k_n^{(B)}$ are the particle normal stiffnesses.

The particle normal stiffness is related to the particle material modulus *E* and particle diameter *2r* such that:

$$k_n^{(A)} = 2E_A r_A \tag{3-4a}$$

$$k_n^{(B)} = 2E_B r_B \tag{3-4b}$$

K_N can be rewritten as:

$$K_N = \frac{2E_A r_A E_B r_B}{E_A r_A + E_B r_B} \tag{3-5}$$

The interaction tangential stiffness K_T is determined as a given fraction of the computed K_N. The macroscopic Poisson's ratio is determined by the K_T/K_N ratio while the macroscopic Young's modulus is proportional to K_N and affected by K_T/K_N. The tangential force $\vec{\mathbf{F}}_T$ is limited by a threshold value such that:

$$\vec{\mathbf{F}}_T = \frac{\vec{\mathbf{F}}_T}{\left\|\vec{\mathbf{F}}_T\right\|}\left\|\vec{\mathbf{F}}_N\right\|\tan(\varphi_{micro}) \text{ if } \left\|\vec{\mathbf{F}}_T\right\| \geq \left\|\vec{\mathbf{F}}_N\right\|\tan(\varphi_{micro}) \tag{3-6}$$

where, φ_{micro} is the microscopic friction angle.

A rolling angular vector $\vec{\boldsymbol{\theta}}_r$ is implemented to represent the rolling behavior between two particles A and B. This vector describes the relative orientation change between the two particles and can be defined by summing the angular vector of the incremental rolling (Belheine et al., 2009, Šmilauer et al., 2010):

$$\vec{\boldsymbol{\theta}}_r = \sum d\vec{\boldsymbol{\theta}}_r \tag{3-7}$$

A resistant moment $\vec{\mathbf{M}}_r$ is computed by:

$$\vec{\mathbf{M}}_\mathrm{r} = \begin{cases} \mathrm{K_r}\vec{\boldsymbol{\theta}}_\mathrm{r} \text{ if } \mathrm{K_r}\left\|\vec{\boldsymbol{\theta}}_\mathrm{r}\right\| < \left\|\vec{\mathbf{M}}_\mathrm{r}\right\|_\mathrm{lim} \\ \left\|\vec{\mathbf{M}}_\mathrm{r}\right\|_\mathrm{lim} \dfrac{\vec{\boldsymbol{\theta}}_\mathrm{r}}{\left\|\vec{\boldsymbol{\theta}}_\mathrm{r}\right\|} \text{ if } \mathrm{K_r}\left\|\vec{\boldsymbol{\theta}}_\mathrm{r}\right\| \geq \left\|\vec{\mathbf{M}}_\mathrm{r}\right\|_\mathrm{lim} \end{cases} \tag{3-8}$$

where,

$$\left\|\vec{\mathbf{M}}_\mathrm{r}\right\|_\mathrm{lim} = \eta_r \left\|\vec{\mathbf{F}}_N\right\| \frac{r_A + r_B}{2} \tag{3-9}$$

K_r is the rolling stiffness of the interaction computed by:

$$K_r = \beta_r \left(\frac{r_A + r_B}{2}\right)^2 K_T \tag{3-10}$$

where, β_r is the rolling resistance coefficient and η_r is a dimensionless coefficient.

To record macroscopic stress components, a measurement rectangular box with volume V is used. The average stresses within the box are given by:

$$\sigma_{ij} = \frac{1}{V}\sum_{c=1}^{N_c} x^{c,i} f^{c,j} \tag{3-11}$$

where, N_c is the number of contacts within the measurement box, $f^{c,j}$ is the contact force vector at contact c, $x^{c,i}$ is the branch vector connecting two contact particles A and B, and indices i and j indicate the Cartesian coordinates.

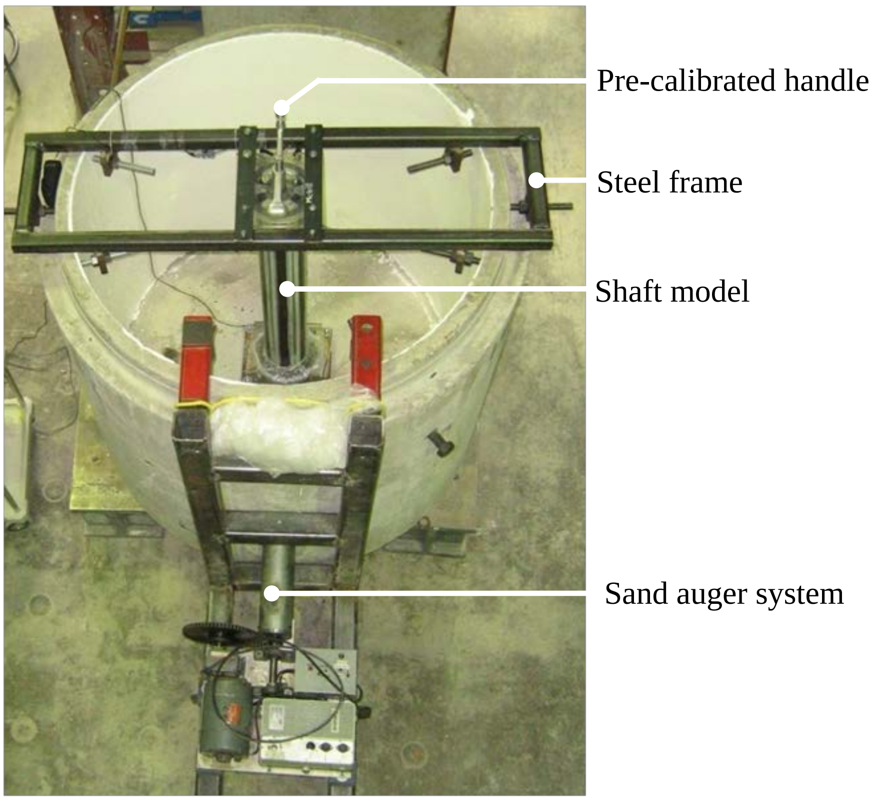

a)

Figure 3-1 a) An overview of the experimental setup; b) Model shaft during assemblage and c) Lower-end section during assemblage (Adapted from Tobar, 2009)

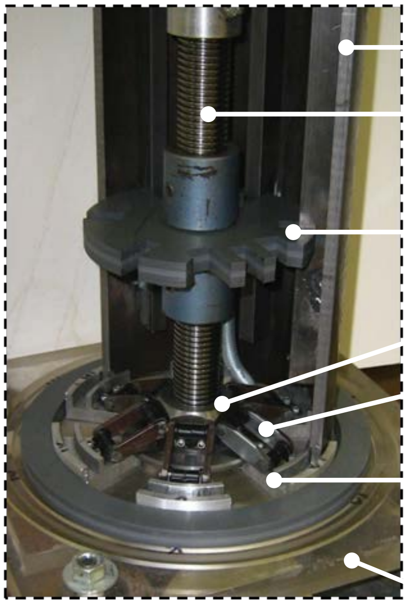

b)

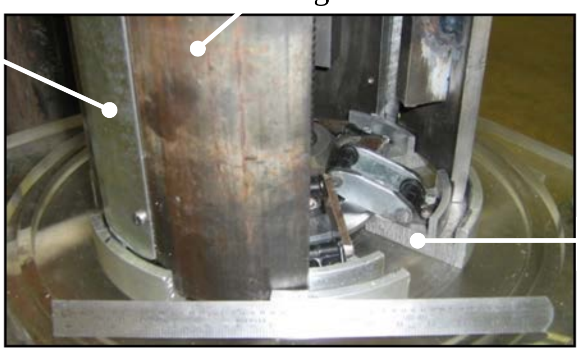

c)

Figure 3-1 (continued)

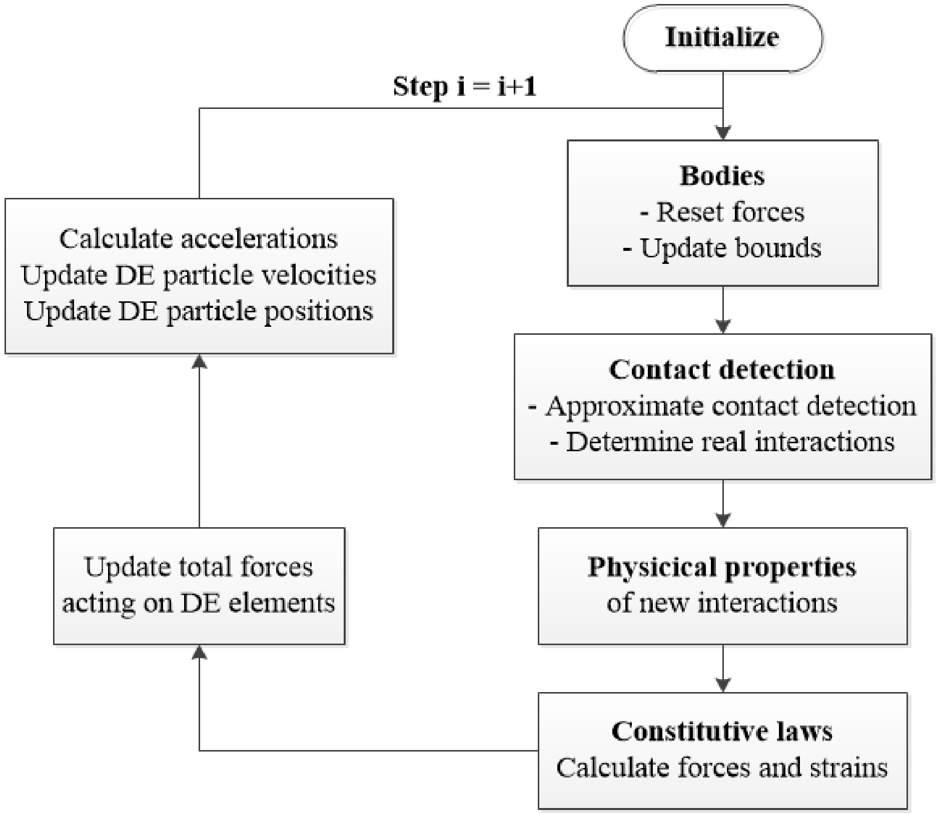

Figure 3-2 Flowchart of DE simulation

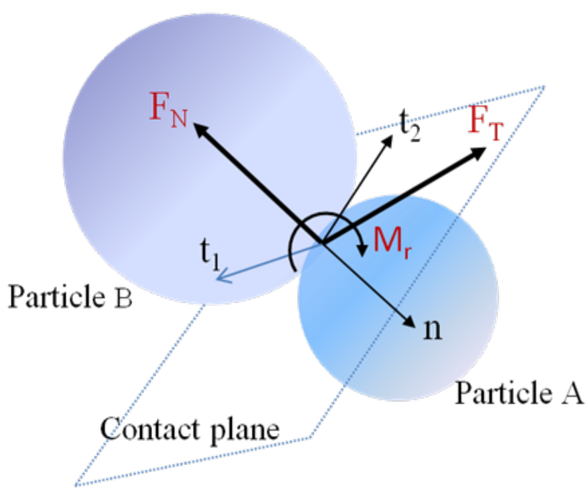

Figure 3-3 Interaction between two DE particles

3.4. DE Sample Generation

In this study, an appropriate sample generation technique is proposed in order to generate DE samples for both the calibration test and shaft simulation. Although there are several available methods that can be used to construct DE specimens, no agreement has been reached regarding the most suitable approach to generate soil specimens. Users have to adopt methods that provide best replication of the real packing process while keeping the computational cost acceptable. Since the sand used in the physical test was generated in layers under gravity, the gravitational approach appears to be a suitable choice in the present study. Although other techniques such as the compression method (Cundall and Strack, 1979), the triangulation-based approach (Labra and Oñate, 2009) and the radius expansion method (Itasca, 2004) can minimize the time required to generate specimens, they have certain features that are not suitable for this study. For example, the compression method uses pressurized boundaries to maintain the equilibrium condition which violates the initial condition in real sand deposit, whereas the triangulation-based approach lacks the control of the particle size distribution which is necessary to replicate real soil behavior. The radius expansion approach tends to generate a specimen with an isotropic stress state (O'Sullivan, 2011).

The gravitational packing technique used in this study is a multi-layer packing method. This packing technique originated from the one proposed by Ladd (1978) for real specimen preparation and is similar to the Multi-layer with Under-compaction Method proposed by Jiang et al. (2003). Modifications are made to simulate the real packing of the sand around the vertical shaft. The packing procedure is described as follow:

The number of layers is first chosen and the volume of particles for each layer is calculated based on the target void ratio of the final soil specimen. The packing procedure is illustrated in Figure 3-4. To generate the first layer, a set of non-contacting particles is first generated inside a box following a pre-determined particle size distribution until the target volume is reached. The height of the box is chosen to be larger than the target height of the layer to insure that all particles can be generated without overlapping. Gravity is then applied to all particles allowing them to move downward and come in contact with each other. The interparticle friction angle is set to zero. It is noticed that even when the friction angle is zero, the DE generated samples are generally looser than the real ones. The same observation is made by Cui and O'Sullivan (2006). To increase the density of the packing, lateral shaking movement is applied to the box to help small particles move into voids between larger particles. The first layer generation is completed when the system reaches equilibrium. For the second layer, the height of the box is increased and the second "cloud" of non-contacting particles is generated in the area above the existing particles. Gravity and shaking are then applied and the system is allowed to come into equilibrium. The procedure is repeated until the final specimen is formed. The proposed multi-layer approach helps increase the density of the packing while keeping the packing pattern realistic. A packing process of about 200,000 particles using 10 packing layers requires nearly 48 running hours on a personal computer to reach equilibrium which is considered acceptable with respect to DE simulations.

The behavior of a DE specimen depends not only on the packing structure but also on the particle size distribution. It is essential that particle generation follows the predefined particle size distribution which has a great influence on the behavior of the discrete element system. However, the true replication of grain size is usually restricted by the high computational cost caused by the large number of particles. Since the volume of a particle with radius r is proportional to r^3, a large number of small particles are needed to generate a very small volume. This leads to an extremely high number of particles required to fill up the soil domain which in turn dramatically increases the simulation cost. In addition, the high computational cost is also caused by the decrease in critical time step needed for stable analysis which is proportional to the mass of the particles. For these reasons, particles smaller than D_5 (particle diameter corresponding to 5% passing) are neglected in this study to reduce the computational cost. This is appropriate as these particles are assumed to have minor effect on the force chains that transmit stresses within the sample (Cheung, 2010; Calvetti, 2008).

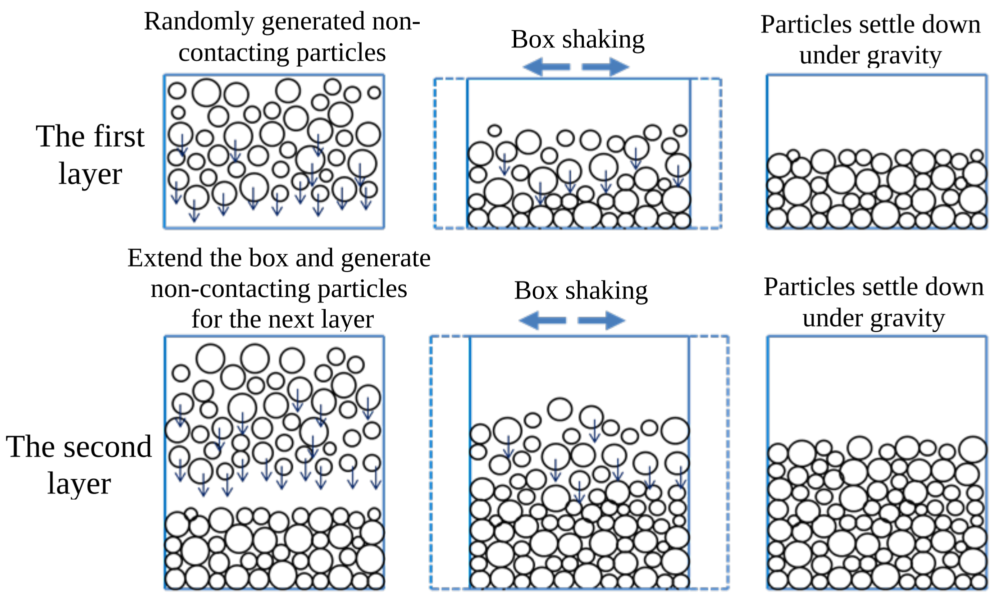

Figure 3-4 The multi-layer gravitational packing procedure

For the simulation of geotechnical engineering problems, particle up-scaling is often used to reduce the number of modeled particles. Careful consideration of particle sizes is usually made to keep balance between the computational cost and the scaling effects on the sample responses. In this study, the scale factors (ratio of a numerical particle size to its real particle size) are chosen as 4 and 25 for the direct shear test and the shaft simulation respectively and will be discussed in following sections. The particle size distributions used in the DE analysis are shown in Figure 3-5.

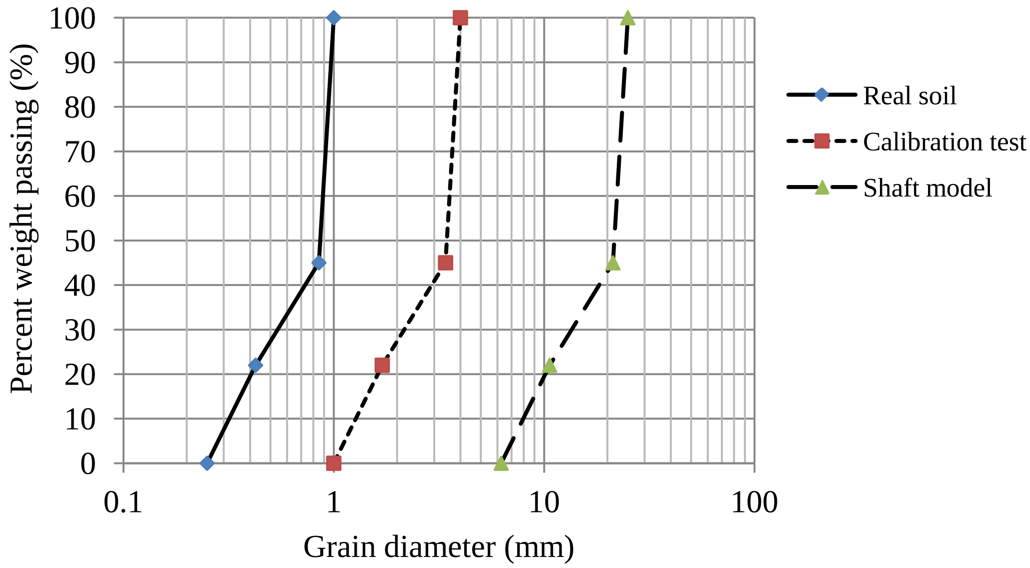

Figure 3-5 Grain size distributions

3.5. Model Calibration Using Direct Shear Test

In order to determine the input parameters for the numerical model, calibration is first conducted using the results of direct shear tests. Numerical simulations of direct shear tests are performed and microscopic parameters for the DE simulation are identified by comparing the numerical results with the experimental data.

The apparatus used for the physical tests consists of a shear box (60 mm x 60 mm) split horizontally into two halves. To apply direct shear to the sample, one part of the box was moved with a constant velocity of 0.021 mm/s while the other part was kept stationary. Three different normal stresses, 13.6 kPa, 27.3 kPa and 40.9 kPa were used in this study using vertical loads applied on top of the shear box. The initial sample height was about 25 mm with the height to width ratio of 1: 2.4.

The numerically simulated shear box consists of two parts and each part comprises 5 rigid boundaries: one horizontal boundary and four vertical boundaries (Figure 3-6a). The numerical shear box has the same dimensions as the actual one to replicate the testing conditions. A specimen is generated using the gravitational method illustrated in the previous section. Since the size of the box is relatively small, only one packing layer is necessary and all particles are generated and settled at the same time. Using a scale factor of 4, the generated specimen consists of over 14,000 particles with diameters ranging from 1.0 mm to 4.0 mm. This number of particles is sufficient to represent the test and consistent with the previous studies (Cui and O'Sullivan, 2006; Yan and Ji, 2010).

After the sample generation is completed, the specimen is subjected to three different vertical stresses of 13.6 kPa, 27.3 kPa and 40.9 kPa. During shearing, one part of the shear box is moved with the same velocity used in the actual test allowing the upper boundary to move vertically. When the current normal stress σ does not match the desired value σ_0, the upper plate is adjusted by moving it in the vertical direction a distance of $dy = (\sigma - \sigma_0)/K$ where the stiffness K is determined by adding the normal stiffnesses of all active particle-upper plate interactions. This method allows for the normal stress to be maintained with an error of less than 1%.

The model calibration is generally a challenging task as the behavior of discrete element samples depends not only on the microscopic parameters but also on particle shapes, particle size distribution, contact models and packing technique. While the adopted packing method and particle size distribution are considered realistic, spherical particle shapes and the contact model are somewhat artificial. These assumptions are usually overcome by choosing appropriate input parameters for the simulation. This calibration approach has been successfully used by other researchers (Belheine et al., 2009).

The most important microscopic parameters that would affect the behavior of the direct shear test are the friction angle, the rolling resistance and the contact stiffnesses. These parameters are varied to match the results obtained from the real test data. Other parameters are identified as follow: particle density is 2650 kg/m^3 following the specific gravity of the sand, particle cohesion is set to zero and the K_T/K_N ratio is fixed to be 0.25 as suggested by Calvetti (2008). It is noted that the friction angle between particles and the upper and lower walls of the box is given a value of 45^o to reduce the slippage at these boundaries. Frictionless contacts at all vertical plates are assumed.

To perform the calibration, the shear displacement-shear stress curves are plotted for the three applied normal stresses. The shear stress is calculated as the sum of forces in the x-direction acting on the upper boundary divided by the cross-sectional area and the normal stress is calculated as the total force acting on the upper plate divided by the cross-sectional area. The rolling resistance coefficient β_R together with the normal and tangential stiffnesses are varied first to match the slope of the curve, the friction angle is then modified to match the peak shear stress. It is observed that the most appropriate combination is a friction angle of 34^o, β_R of 0.05, and a particle material modulus of 38 MPa. A summary of the selected parameters is given in Table 3-2. The shear displacement-shear stress curves and normal stress-shear stress relationship are given in Figure 3-7. The figure shows a good agreement between the numerical and physical direct shear tests. The contact force network at shear displacement of 2 mm is illustrated in Figure 3-6b. The centers of contacting particles are connected using lines with thickness representing the magnitude of the normal contact force. It is apparent that contact forces are transmitted diagonally from the lower left to upper right of the box. This anisotropic force distribution has been observed by other authors (Yan and Ji, 2010, Thornton and Zhang, 2003).

Table 3-2 Particles' properties for DE simulations

Parameter	Value
Particle density (kg/m^3)	2650
Particle material modulus E (MPa)	38
Ratio K_T/K_N	0.25
Friction angle φ (degrees)	34
β_R	0.05
η_R	1
Damping coefficient	0.2

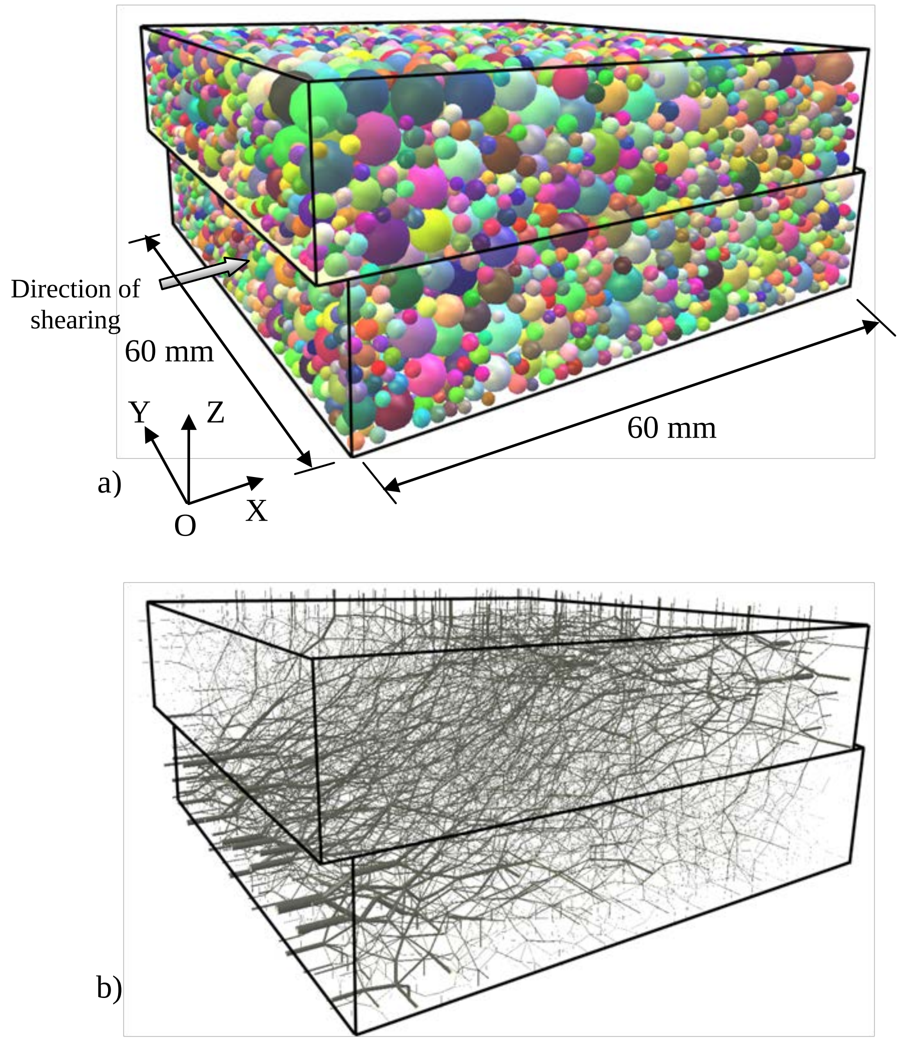

Figure 3-6 a) Three-dimensional direct shear sample and b) Three-dimensional contact force network (at shear displacement of 2 m)

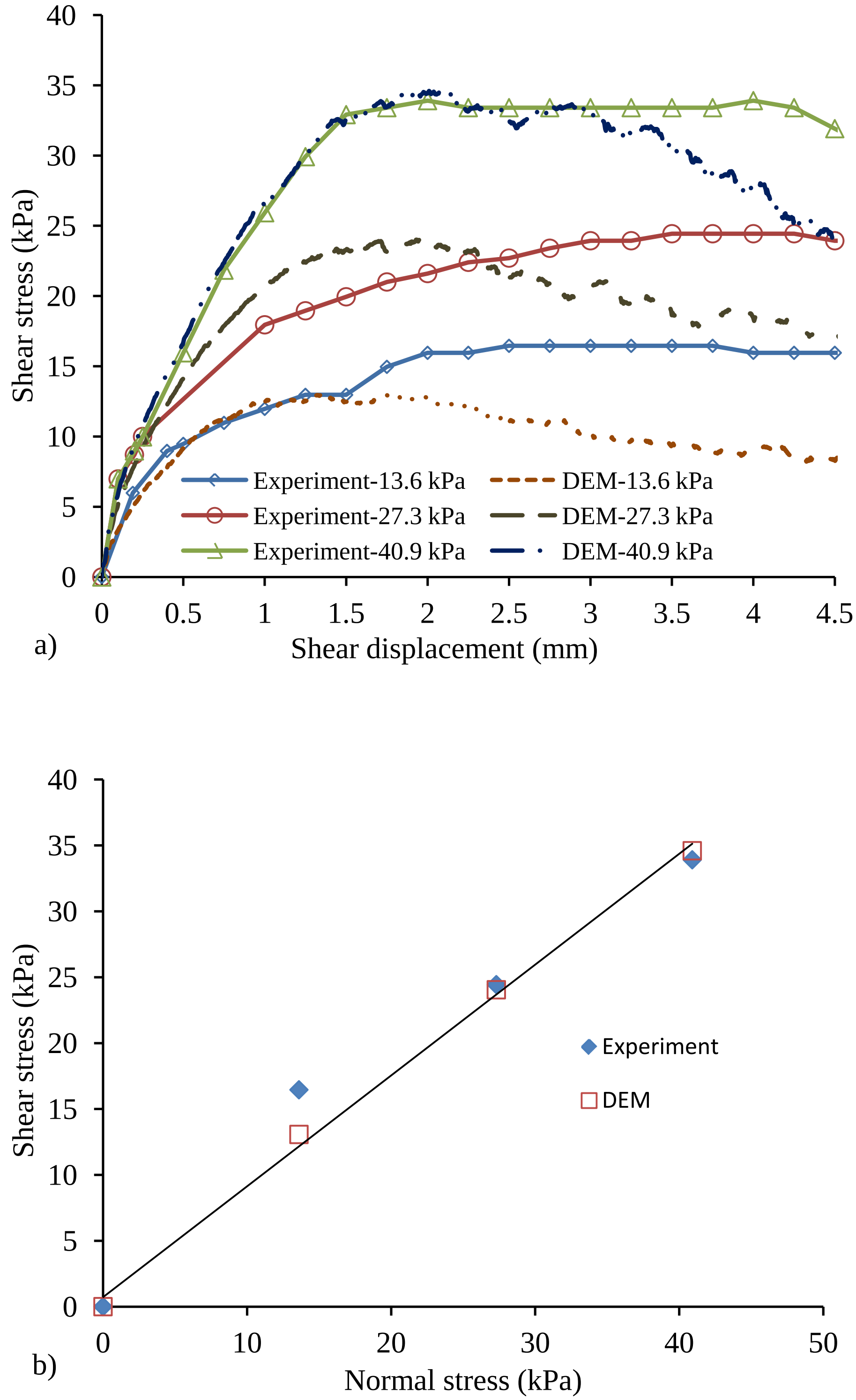

Figure 3-7 Direct shear test results

3.6. Shaft-Soil Interaction Simulation

The vertical shaft is modeled using a cylinder 1.0 m in height and initial diameter of 150 mm that comprises 12 equally distributed segments. Since the modeled problem is axisymmetric, only part of the domain is modeled to reduce the computational cost. In addition, better representation of the experiment can be achieved by simulating one "slice" of the soil domain with a large number of particles while keeping the simulation time acceptable. To capture the problem geometry, a quarter of the problem is modeled in this study. The model consists of a quarter of the shaft and four boundaries including three vertical and one horizontal at the bottom of the container (Figure 3-8). Each quarter of the shaft is divided into three segments to capture the curved shaft geometry. The friction angles between particles and the wall boundaries are set to zero and pressures acting on the shaft are recorded at the middle segment to reduce the boundary effects. Similar technique has been used by Weatherley et al. (2011) to model slope collapse and hopper flow problems.

The soil domain is generated using the proposed multi-layer packing technique with 10 layers. In order to replicate the actual soil generation process, the friction coefficient between the particles and the shaft is assumed to have a value of 0.2 to account for the frictional contact between the shaft and the soil and is maintained during the entire simulation. Using a scale factor of 25 and a total of over 245,000 particles are generated with diameters ranging from 6.25 mm to 25 mm. The average void ratio of the generated soil sample is about 0.85 which is slightly greater than the void ratio of the real sand (0.78). This is attributed to the removal of excess sand to reach the target sample height.

The generated soil sample is checked to assure its equivalence (have the same characteristics) to the soil specimen used in the direct shear test calibration. The fabric tensor and coordination number are determined for the two samples at their initial states. The fabric tensor is given by:

$$\mathbf{\Phi}_{ij} = \frac{1}{N_c}\sum_{N_c} n_i n_j \tag{3-12}$$

where, N_c is the number of contacts and n_i is the unit branch vector component in the i direction.

The coordination number N is defined as:

$$N = \frac{2N_c}{N_p} \tag{3-13}$$

where, N_p is the number of particles.

It is shown that both specimens have almost the same coordination number of about 6.3 and the fabric tensor components are also nearly identical ($\mathbf{\Phi}_{xx}$ and $\mathbf{\Phi}_{yy}$ of about 0.33, $\mathbf{\Phi}_{zz}$ of about 0.34 where z is the gravitational direction) which prove the equivalence of the two soil samples.

The input parameters for the simulation are then assigned to the particles based on the results of the calibration test. The scale factors in the calibration and in the shaft simulation were examined to make sure that the microscopic parameters obtained from the calibration can be used for the simulation. The calibration of the direct shear test provides two important microscopic parameters which are the particle stiffnesses and friction angle. Since preliminary studies of the shaft simulation have shown that the stiffnesses have a very small influence on the overall response, only the particle friction angle was considered when determining the scale factors. In the direct shear calibration, different scale factors were tested to investigate the variability of the macro friction angle with the change of particle sizes. It is observed that for scale factors of 2, 3, 4 and 5, the macroscopic friction angle varies in a narrow range between 38 and 41.5 degrees. The randomness of the generation process at these scale factors has a minor influence on the macro response since the number of particles of the specimen has become large enough to represent the sample. Larger scale factors lead to a wide scattering of the macro friction angle due to the decrease of the number of particles (less than 8,000 particles). The microscopic parameters obtained from the direct shear calibration with a scale factor of 4, therefore, can represent the actual soil. According to Potyondy and Cundall (2004), when the number of particles is large enough (in the shaft simulation is over 245,000 particles with a scale factor of 25), the macroscopic response becomes independent of the particle sizes. Therefore, the microscopic parameters of the calibration can be used for the shaft simulation.

The diameter of the shaft is incrementally reduced to model the active condition. Lateral earth pressures on the shaft and stresses in the soil domain are recorded at different wall movements using Equation 3-11. Stresses are obtained using measurement boxes with dimensions of 0.08 m x 0.08 m x 0.08 m. The simulation process finishes when the reduction in the shaft radius reaches 5 mm.

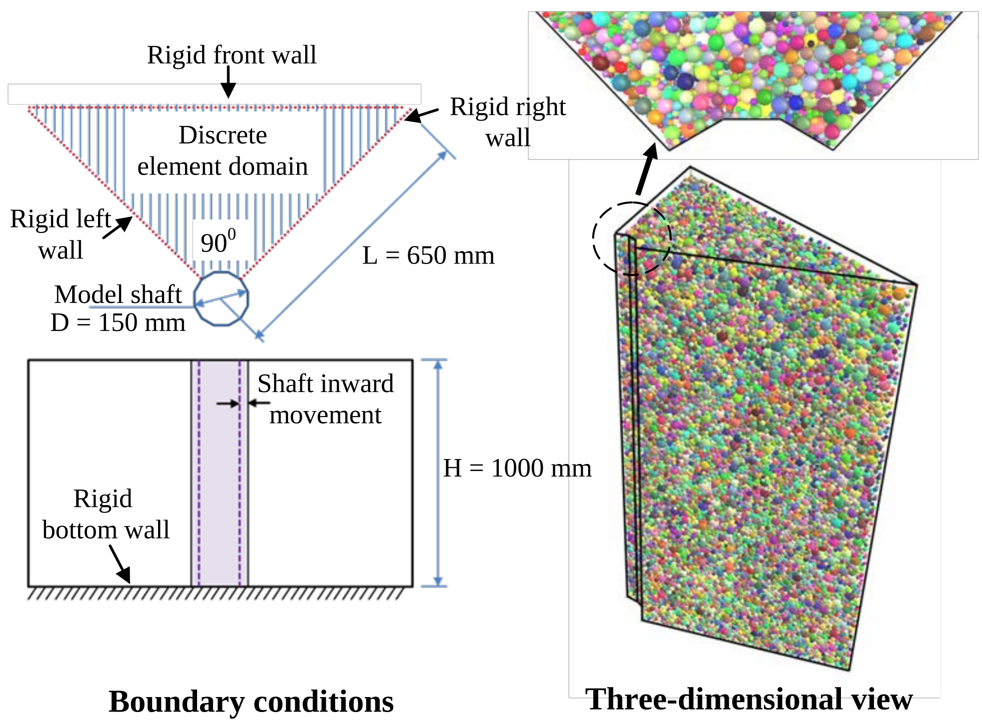

Figure 3-8 Boundary conditions and 3D views of the model shaft

3.7. Results and Discussions

Selected experimental results (tests T5, T6 and T7) are reported in this section at three different locations. The measured earth pressure is then compared with the DE simulation results.

3.7.1. Initial earth pressures

The calculated and measured initial earth pressures on the shaft wall are shown in Figure 3-9 along with the conventional at-rest condition (K_o-line where, $K_o = 1 - \sin\phi$). The DE results were found to be consistent with the measured earth pressure.

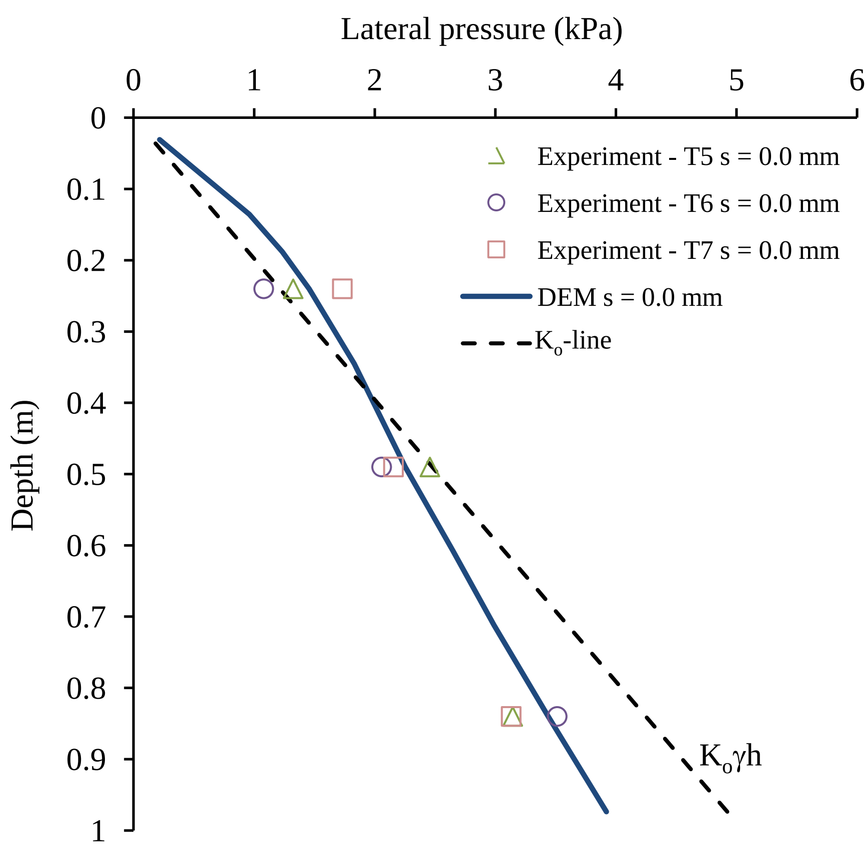

Figure 3-9 Initial earth pressures on the shaft

3.7.2. Earth pressure reduction with wall movement

Lateral pressures at different locations along the shaft are shown in Figure 3-10 to 3-13. The pressures are plotted versus the wall movement. Both the DE simulation and the experimental results showed a consistent reduction in lateral pressures as the wall movement increases. The earth pressure became independent of the wall movement when the displacement reached about 3 mm. To study the effects of the wall movement on the active earth pressure, the pressure, p, at a certain depth is normalized with respect to the initial pressure, p_0.

Normalized earth pressures at the three examined levels (0.24H, 0.49H and 0.84H) for different shaft wall movements are illustrated in Figure 3-14, 3-15 and 3-16, respectively. It can be seen that the DE results are in good agreement with the experimental data. For a very small wall movement, a large reduction in lateral earth pressure is observed. At a wall movement of 0.5 mm, the calculated earth pressures decreased from 100% at the initial state to 55% at 0.24H and 0.49H and to 45% at 0.84H. For the same wall movement, the measured earth pressures reached about 65% at 0.24H and 0.49H and about 50% at 0.84H. With further increase in wall movement, the DE results were found to be identical to the measured values. For movements between 1 mm and 2 mm, the earth pressure decreased to 25% of the initial value at 0.24H and 0.49H and to 18% at 0.84H. Additional movements larger than 3 mm did not cause significant pressure reduction and the lateral pressures became constant when reached approximately 20% of the initial pressure at 0.24H and 0.49H and approximately 10% at 0.84H. It can be concluded that the axisymmetric active earth pressure fully develops when the shaft wall moves about 2 to 3 mm or about 2.5% to 4% of the shaft radius. Furthermore, the most rapid reduction in the earth pressure is observed near the bottom of the shaft.

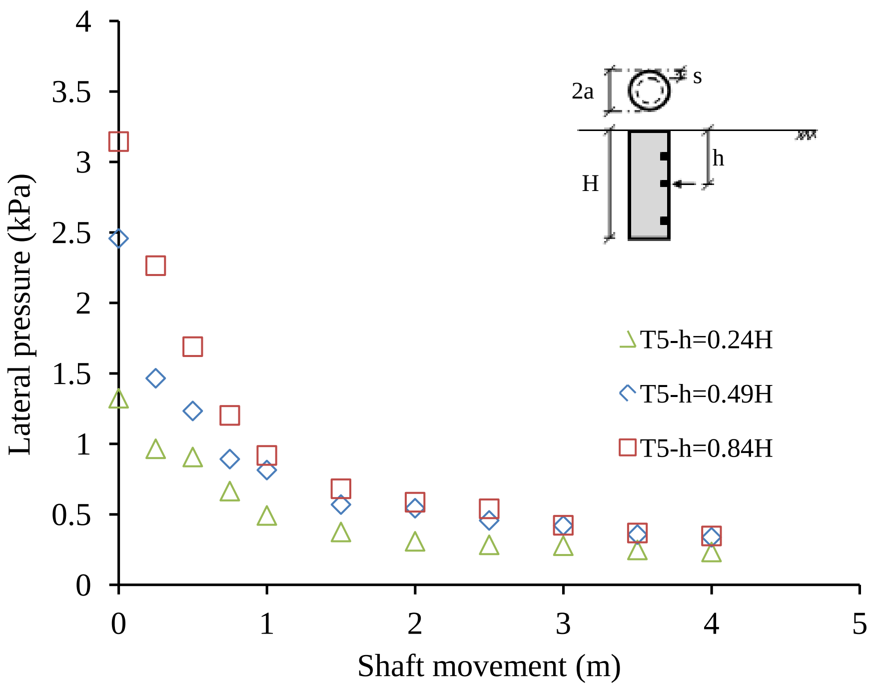

Figure 3-10 Earth pressures on the shaft at different depths (test T5)

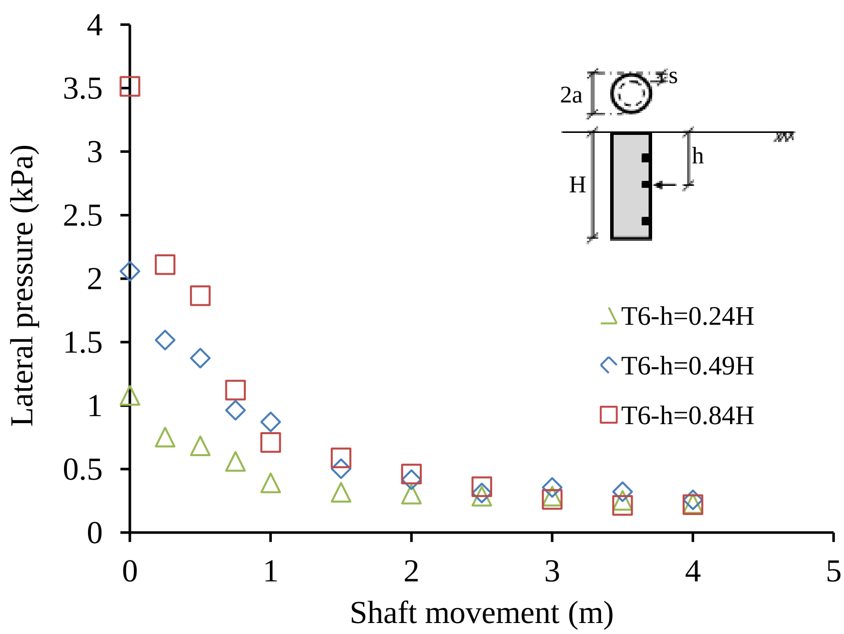

Figure 3-11 Earth pressures on the shaft at different depths (test T6)

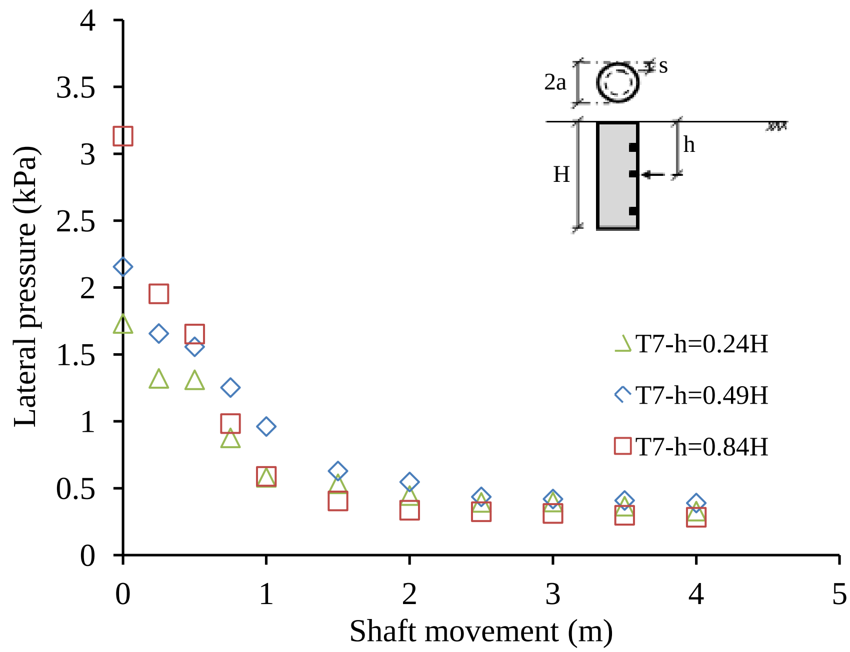

Figure 3-12 Earth pressures on the shaft at different depths (test T7)

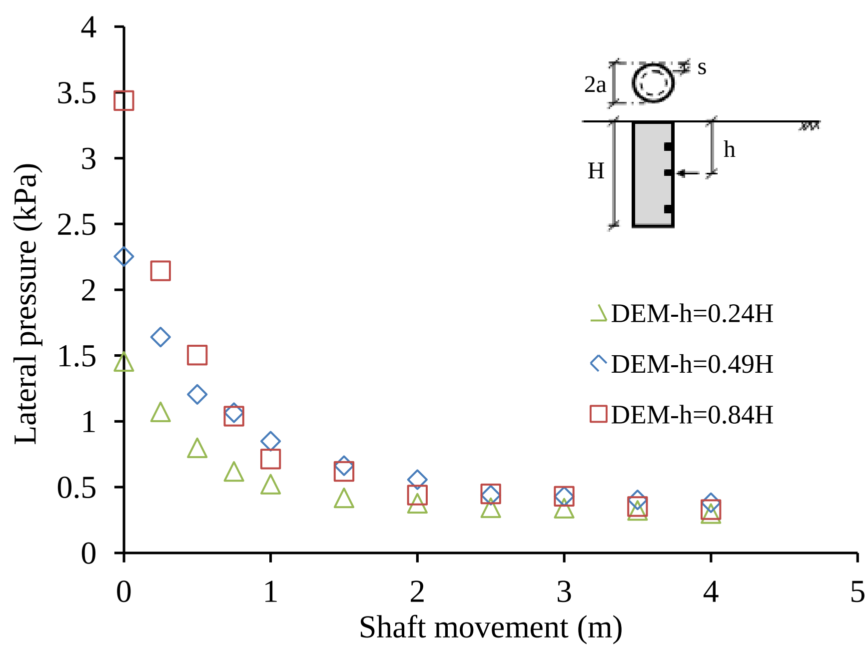

Figure 3-13 Earth pressures on the shaft at different depths (DEM simulation)

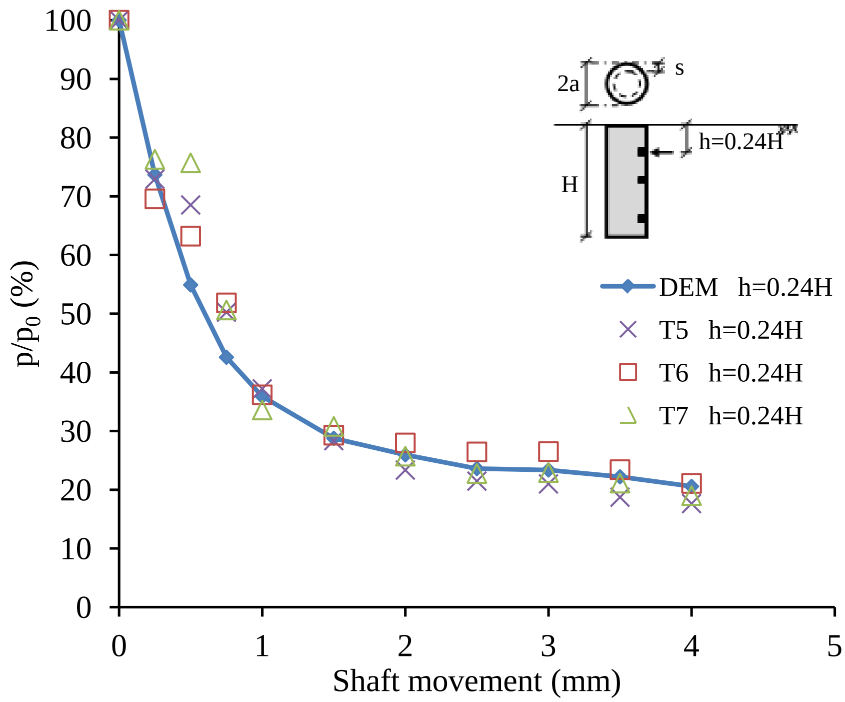

Figure 3-14 Normalized pressures on the shaft at the depth 0.24H

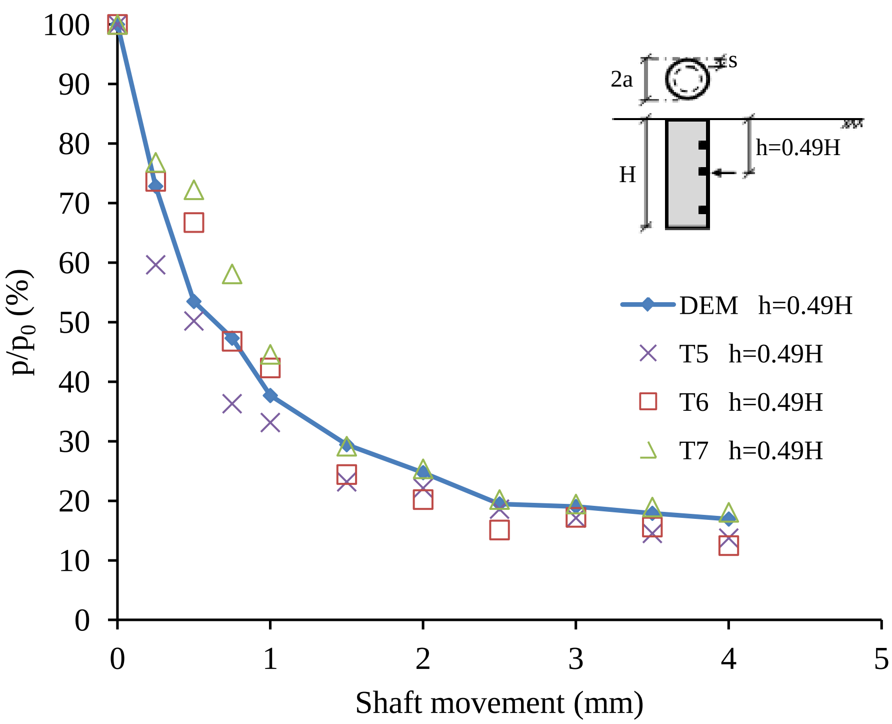

Figure 3-15 Normalized pressures on the shaft at the depth 0.49H

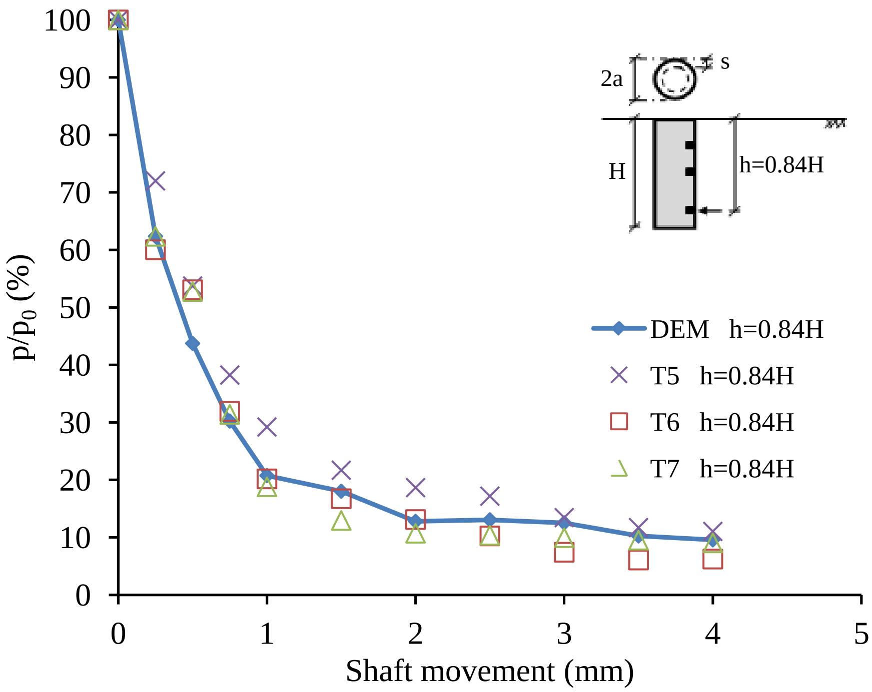

Figure 3-16 Normalized pressures on the shaft at the depth 0.84H

3.7.3. Earth pressure distribution with depth

The calculated and measured earth pressure distributions with depth are plotted in Figure 3-17. The earth pressures are normalized with respect to the shaft radius and the unit weight of the soil while the depth is normalized with respect to the shaft radius. For a wall movement of 1 mm or 0.1% of the shaft height, both the calculated and measured earth pressures showed an increase from the sand surface to the middle of the shaft and then a decrease within the lower half of the shaft. The earth pressure continued to decrease with the increase in wall movement up to 4 mm or 0.4% of the shaft height. It can be seen that at this wall movement, the pressure distribution became more uniform with depth. The above results are compared with different analytical solutions. Four solutions are chosen to evaluate in this study including the methods of Terzaghi (1943); Berezantzev (1958); Prater (1977) and Cheng & Hu (2005).

It is realized that the pressure distributions following the solutions of Terzaghi and Berezantzev with λ (the earth pressure coefficient on radial planes) equals 1 are in good agreement with the numerical and experimental results provided that enough wall movement is allowed. These two solutions suggest a quite uniform pressure distribution with depth. Prater's solution, which is based on Coulomb's wedge analysis with the value $\lambda = K_o$, leads to zero earth pressure at h/a of about 9. This is inconsistent with the numerical and experimental results. However, the solution suggested that the maximum earth pressure can be used for design purposes. In the case of small wall movement, the upper bound solution with $\lambda = K_o$ as proposed by Cheng & Hu provides a good agreement with the calculated and measured values for the upper half of the shaft. However, the method indicates a continuing increase in the lateral pressure with depth which is not consistent with the experimental results. The above comparisons suggest that there is a strong relationship between lateral earth pressure and soil movement around the shaft.

3.7.4. Extent of shear failure

Figure 3-18 shows the displacement field around the shaft for a wall movement of 3 mm. It can be seen that a non-uniform failure zone of conical shape has developed along the shaft as illustrated in Figure 3-18b. The zone increased in size from the bottom of the shaft up to a region of 0.2 m in radius at the surface (about 2.5 times the shaft radius). The angle α that the failure surface made with the horizontal was found to be about 75^{o}. This observed failure region is consistent with the stress distributions discussed in the previous sections.

Figure 3-19 shows a cross-sectional view of the contact force network within the DEM domain for the cases of no wall movement (initial state) and a wall movement of 3 mm. Each contact force is illustrated by a line connecting the centers of two contacting particles while the width of the line is proportional to the magnitude of the normal contact force. It can be observed that when the shaft radius is reduced, the contact forces within the shear failure zone decrease in the radial direction and increase in the circumferential direction. This visualization represents the arching effect generated around the cylindrical shaft.

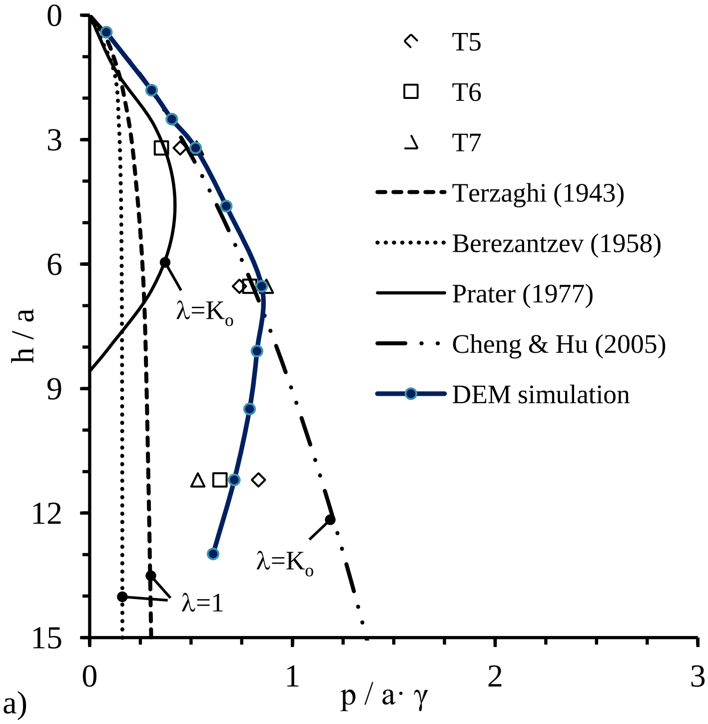

a)

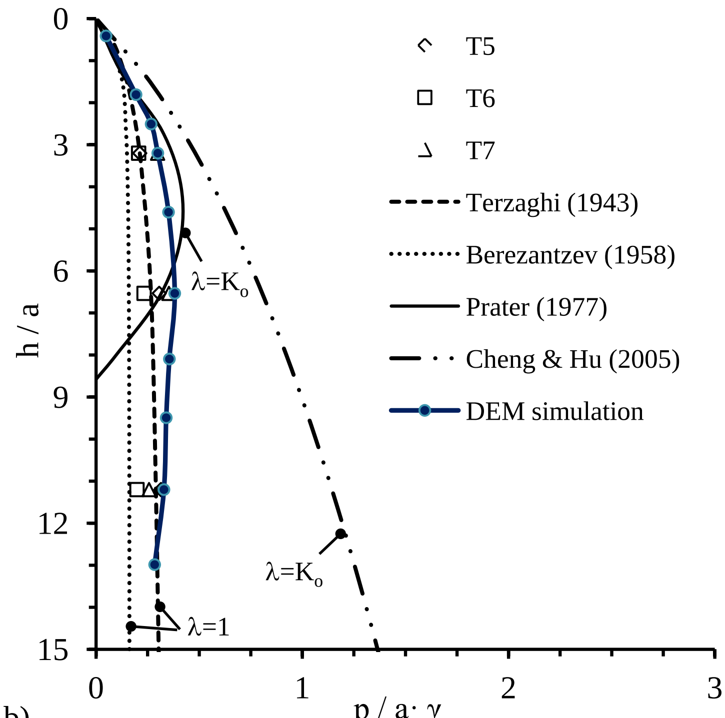

b)

Figure 3-17 Comparison between modeled results and theoretical earth pressures along the shaft. a) Shaft movement = 1 mm and b) Shaft movement = 4 mm

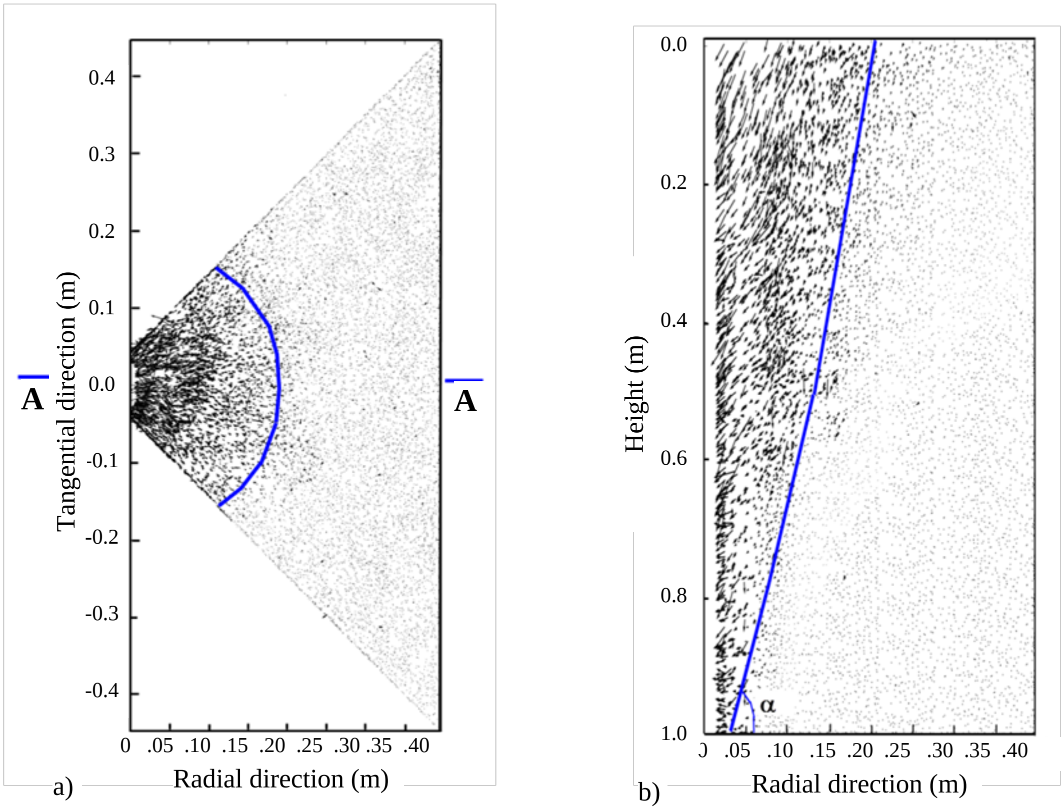

Figure 3-18 Displacement field at shaft movement of 3 mm.

a) Plan view and b) Cross sectional A-A view

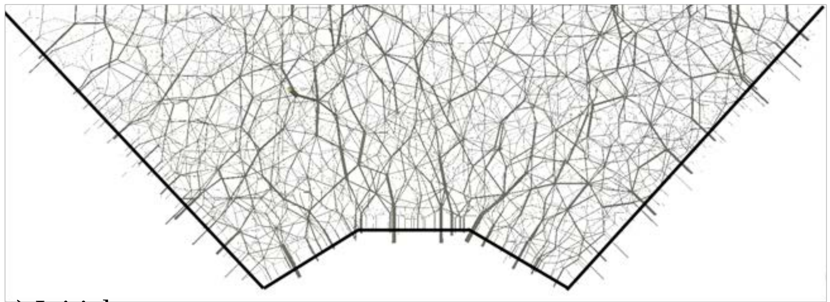

a) Initial state

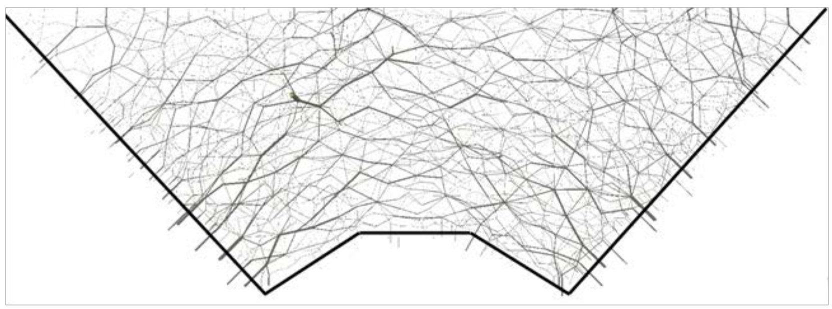

b) s = 3 mm

Figure 3-19 Contact force networks

3.7.5. Stress distribution within the soil

Stresses within the soil mass including the radial, circumferential and vertical components (see Figure 3-20) are analyzed at a chosen depth of 0.49H using the DEM. The radial stress versus radial distance from the shaft centre is shown in Figure 3-21. It can be seen in Figure 3-21a that radial stresses near the shaft wall dropped rapidly even for a small wall movement of 1 mm. Increase in wall movements from 2 mm to 3 mm caused the radial stress to further decrease. However, no significant change in radial stress was observed for movements larger than 3 mm. The radial stress in the vicinity of the shaft remained at about 60% of the initial value for wall movement of 1 mm and about 40% for wall movement of 3 mm. The distribution of the radial stress in a cross section is shown in Figure 3-21b. It was found that the changes in radial stress mostly occurred within 0.3 m from the center of the shaft. The stresses outside this region remained close to its initial state despite the wall movement.

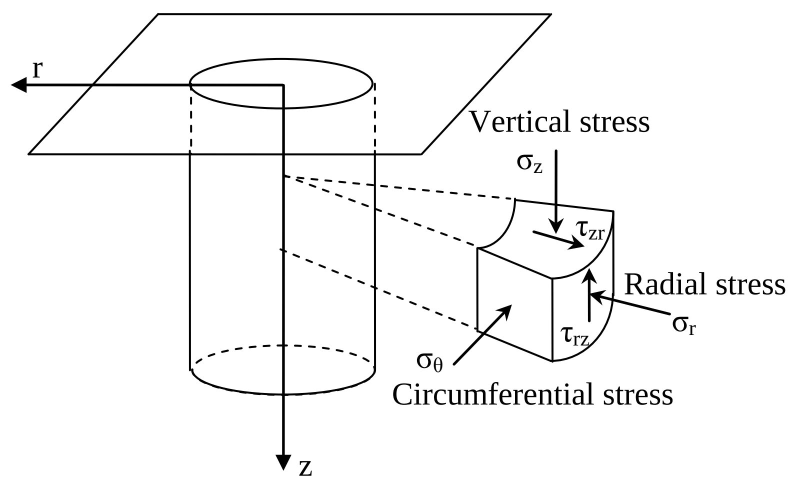

Figure 3-20 Stresses acting on a soil element

The relief of radial stresses due to soil movement causes vertical (along the shaft height) and horizontal (in the circumferential direction) arching, and results in stress redistribution in the vicinity of the shaft. The circumferential stresses versus radial distance are shown in Figure 3-22. From Figure 3-22a, it can be seen that the circumferential stresses near the shaft were smaller than the initial value for all wall movements. The circumferential stresses increased with distance from the shaft due to horizontal arching. At a distance of about 0.2 m from the shaft center, the circumferential stress reached a maximum value that is larger than the initial value. A decreasing trend was observed with further increase in distance and the circumferential stresses returned to its initial state far away from the shaft. It can also be seen from Figure 3-22a that larger wall movements lead to slightly larger circumferential stresses. The largest circumferential stress was obtained at a wall displacement of 4 mm and was found to be about 10% higher than the initial circumferential stress. Figure 3-22b illustrates a contour plot of the circumferential stress distribution. It can be seen from the figure that shaft movements larger than 3 mm did not cause significant changes to the stress distribution. This is attributed to the vertical arching resulting from the established failure surface after a certain wall movement (about 2 to 3 mm). At that stage, gravity effect dominates leading to the development of a stable arch resulting in nearly constant circumferential and radial stresses.

Figure 3-23 shows the calculated stress components near the middle of the wall when the wall movement reached 2 mm. The circumferential stress was found to be slightly larger than the radial stress in the close vicinity of the shaft. However, at a distance of 0.3 m from the shaft, the circumferential and radial components converged and became equal to the lateral stress at rest. The vertical stress dropped from the in-situ condition near the shaft to about half of its value.

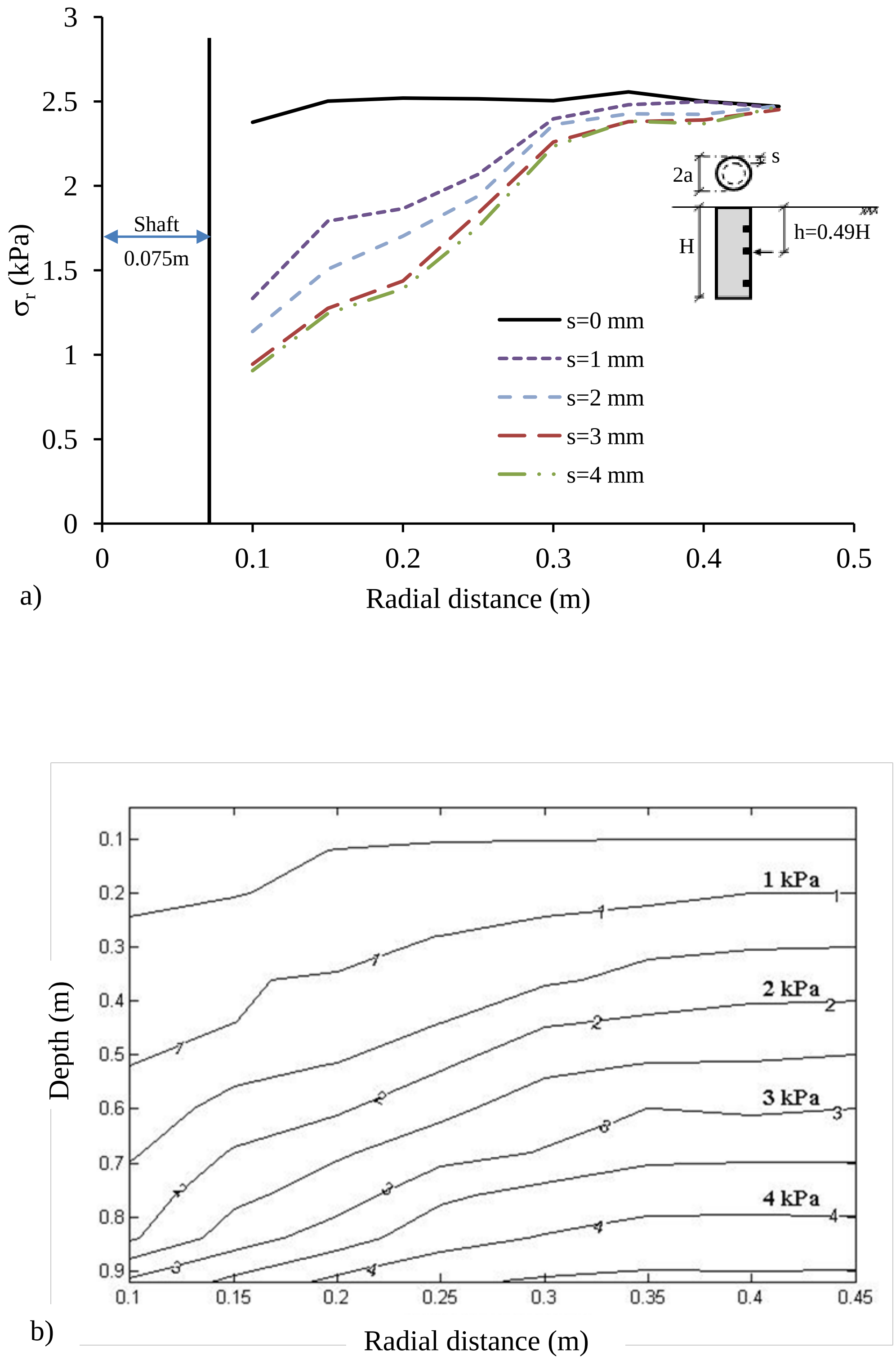

Figure 3-21 a) Radial stress distribution at the depth 0.49H and b) Radial stress distribution in the cross section A-A (s = 3 mm)

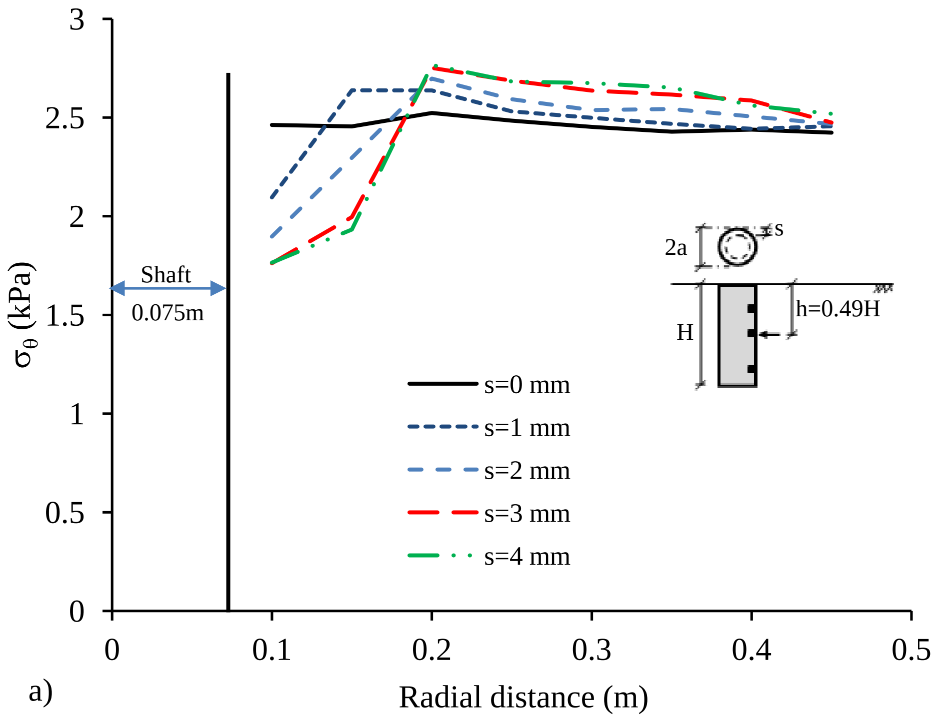

a)

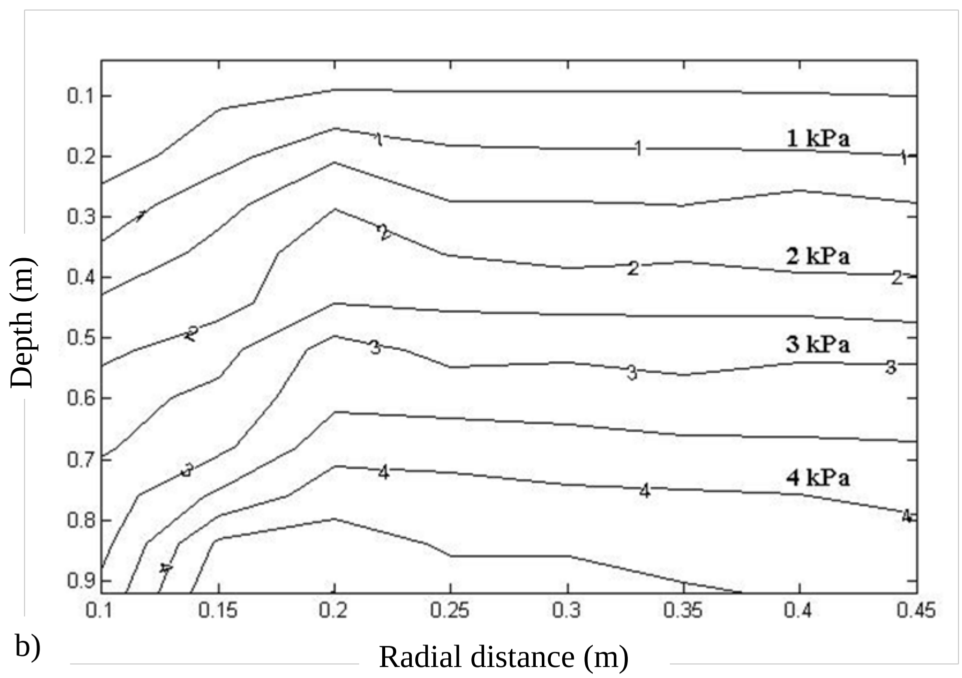

b)

Figure 3-22 a) Circumferential stress distribution at the depth 0.49H and b) Circumferential stress distribution in the cross section A-A (s = 3 mm)

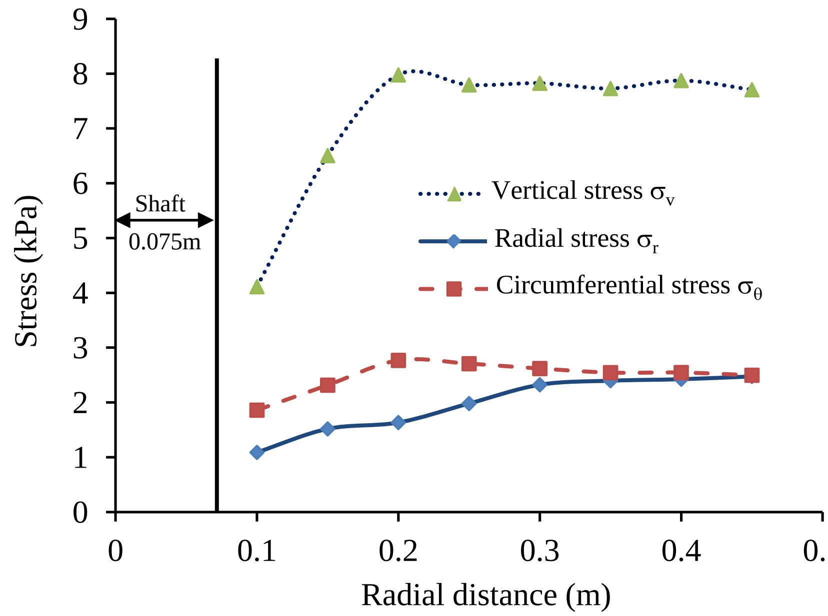

Figure 3-23 Stresses at the depth 0.49H and shaft movement 2 mm

3.8. Summary and Conclusions

In this paper, an experimental study was performed to investigate the lateral earth pressure acting on a cylindrical shaft. The axisymmetric geometry of the test setup allowed for a proper measurement of the lateral earth pressure. A numerical investigation was then performed using a specifically designed DE model. A modified multi-layer gravitational packing method that is able to capture some of the important properties was proposed to generate the soil domain. The particle size distribution of the real sand was considered and a calibration was conducted using direct shear test to determine the input parameters needed for the discrete element analysis. A quarter of the shaft geometry was numerically modeled and the lateral pressures acting on the shaft wall were recorded. Stresses within the soil domain were calculated and the arching effect was discussed. The results of the experimental and numerical studies were compared against some of the available analytical solutions.

The DE simulation of the vertical shaft agreed well with the experimental data. Based on the physical and numerical studies, a small shaft movement can lead to a rapid decrease in the earth pressure acting on the shaft wall. The required shaft movement to reach the full active condition was found to range from 2.5% to 4% of the shaft radius or 0.2% to 0.3% of the shaft height. At this wall movement, the earth pressure can significantly decrease to a value of 10% of the initial pressure and the lateral pressure becomes uniform with depth. The analytical solutions of Terzaghi and Berezantzev were found to be in good agreement with the observed pressure distribution.

The movement of the shaft wall resulted in stress redistribution within the soil medium. The arching effect has lead to a decrease in radial stresses and increase in circumferential stresses within a region of radius 0.3 m from the shaft center. The stresses in the soil domain became quite stable when the wall movement reached 3 mm. The agreement between the numerical and measured results demonstrated the efficiency of the DEM in validating geotechnical problems involving granular material and large deformation.

Preface to Chapter 4

The results presented in the previous chapter demonstrate the efficiency of the discrete element method in investigating the behavior of granular material. In these analyses, the soil particles were modeled using spherical particles whereas the wall was modeled as a rigid boundary. Therefore, the response of the wall was not investigated. In problems involving soil-structure interaction, it is challenging to simultaneously model both the 3D discontinuous nature of the soil and the continuous nature of the structural elements using traditional discrete or finite element method. The coupling of the finite and discrete element methods allows for the simulation of such problems. In this chapter, a coupled Finite-Discrete framework is presented and then used to investigate the behavior of a biaxial geogrid sheet embedded in sand material subjected to pullout loading.

CHAPTER 4

Three-Dimensional Modeling of Geogrid-Soil Interaction under Pullout Loading Conditions *

Abstract

The behavior of a geogrid-soil system is dependent on the properties of the geogrid material, the backfill soil and the interface condition. Modeling the geogrid-soil interaction taking into account the true geogrid geometry is a challenging numerical problem that requires the consideration of the discontinuous nature of the soil and the different modes of resistance that contribute to the pullout capacity of the geogrid layer. In this study, a coupled Finite-Discrete framework has been developed to investigate the behavior of a biaxial geogrid sheet embedded in granular material and subjected to pullout loading. Validation is performed by comparing experimental data and numerically calculated results using the proposed model. The detailed behavior of the geogrid and the surrounding soil is then investigated. The numerical results indicated the suitability of the coupled model to solve this class of problems.

Keywords: soil reinforcement, biaxial geogrid, pullout loading, finite-discrete element.

---

* A version of this chapter has been published in *Geotextiles and Geomembranes, 2013*, 37: 1-9.

4.1. Introduction

Geosynthetics are extensively used in civil engineering practice to facilitate cost effective building, environmental, transportation and other construction projects. A geogrid is geosynthetic material used to reinforce soils and improve the overall performance of foundations, roadways, walls and slopes. In the past two decades, both theoretical and experimental studies have been used to investigate the mechanics of reinforced soil systems under pullout loading condition (Farrag et al., 1993; Bergado and Chai, 1994; Ochiai et al., 1996; Sugimoto et. al., 2001; Palmeira, 2004; Moraci and Recalcati, 2006; Sieira et al., 2009). While it possible to track the load-displacement response of geogrid in pullout experiments, the behavior of the backfill soil as it interacts with the geogrid material is hard to evaluate experimentally and numerical methods are considered more suitable for that purpose.

Finite element method (FEM) is widely used as a numerical tool to model the soil reinforcement pullout procedure (Sugimoto and Alagiyawanna, 2003; Khedkar and Mandal, 2009). The geogrid geometry is often simplified either as a truss structure (in 2D analysis) or a continuous sheet (in 3D analysis). Using this approach makes it difficult to separate the contributions of the frictional and bearing resistances with respect to the overall pullout capacity of a reinforced system. In addition, it makes it also challenging to determine the stress and strain distributions in the geogrid members as well as in the surrounding soil material.

As an alternative to the continuum approach, the discrete element method (DEM) has been used by several researchers to model the soil-geogrid interaction. McDowell et al. (2006) and Chen et al. (2012) used DE method to model both the geogrid and the backfill soil. In this approach, the geogrid is modeled using a set of spherical particles bonded together to form the geogrid shape. The interaction between the geogrid and the surrounding soil is obtained through the contact between discrete particles. Although microscopic parameters of the geogrid bonded particles are determined using some index load tests, the complex geogrid deformation during the actual test may not be accurately captured due to the inflexibility of the bonded particles. Moreover, since a set of bonded discrete particles can roughly capture the geogrid continuous nature, the accuracy of the strains and stresses within the geogrid layer may not be obtained.

To take advantage of both the FE and DE methods, the reinforcement layer can be modeled using FE whereas the backfill soil can be modeled using DE method. The coupling of the two methods can efficiently model the behavior of the geogrid as well as the backfill soil material. This approach has been used by several researchers to solve certain problems such as: geosynthetic-reinforced earth structures (Villard et al., 2009), pile installation (Elmekati and Shamy, 2010) and earth pressure on tunnel linings (Dang and Meguid, 2011). In this paper, a coupled Finite-Discrete element (FE-DE) framework is presented. Geogrid pullout tests based on laboratory experiments are modeled using the developed framework. The results of the numerical simulation including the detailed response of the geogrid and the surrounding soil are presented and compared with experimental data. Although emphasis is placed in this study on the frictional and bearing components of the pullout resistance, displacements, stresses, and strain fields in the vicinity of the geogrid layer are also highlighted.

4.2. Coupled Finite-Discrete Element Framework

The coupled FE-DE framework used in this study is a continuation of the original work of Dang and Meguid (2010, 2013). The developed algorithm is implemented into an open source discrete element code YADE (Kozicki and Donze, 2009; Šmilauer et al., 2010) and is briefly described in the following sections.

4.2.1. Discrete Elements

The contact law between particles used in the framework is briefly described below:

If two particles A and B with radii r_A and r_B are in contact, the contact penetration depth is defined as:

$$\mathbf{\Delta} = r_A + r_B - d_0 \tag{4-1}$$

where, d_0 is the distance between the two particle centers.

The force vector $\vec{\mathbf{F}}$ that represents the interaction between the two particles is decomposed into normal and tangential forces:

$$\vec{\mathbf{F}}_N = K_N . \vec{\mathbf{\Delta}}_N \tag{4-2a}$$

$$\delta\vec{\mathbf{F}}_T = -K_T . \delta\vec{\mathbf{\Delta}}_T \tag{4-2b}$$

where, $\vec{\mathbf{F}}_N$ and $\vec{\mathbf{F}}_T$ are the normal and tangential forces; K_N and K_T are the normal and tangential stiffnesses at the contact; $\delta\vec{\mathbf{\Delta}}_T$ is the incremental tangential displacement, $\delta\vec{\mathbf{F}}_T$ is the incremental tangential force and $\vec{\mathbf{\Delta}}_N$ is the normal penetration between the two particles.

The normal stiffness at the contact is defined by:

$$K_N = \frac{k_n^{(A)} k_n^{(B)}}{k_n^{(A)} + k_n^{(B)}} \tag{4-3}$$

where, $k_n^{(A)}$ and $k_n^{(B)}$ are the particle normal stiffnesses.

The particle normal stiffness is related to the particle material modulus *E* and particle diameter *2r* such that:

$$k_n^{(A)} = 2E_A r_A, k_n^{(B)} = 2E_B r_B \tag{4-4}$$

K_N can be rewritten as:

$$K_N = \frac{2E_A r_A E_B r_B}{E_A r_A + E_B r_B} \tag{4-5}$$

The tangential stiffness K_T is defined relative to K_N as $K_T = \alpha K_N$. The tangential force $\vec{\mathbf{F}}_T$ is limited by a threshold value such that:

$$\vec{\mathbf{F}}_T = \frac{\vec{\mathbf{F}}_T}{\left\|\vec{\mathbf{F}}_T\right\|}\left\|\vec{\mathbf{F}}_N\right\|\tan(\varphi_{micro}) \text{ if } \left\|\vec{\mathbf{F}}_T\right\| \geq \left\|\vec{\mathbf{F}}_N\right\|\tan(\varphi_{micro}) \tag{4-6}$$

where, φ_{micro} is the microscopic friction angle between particles.

The rolling resistance between two particles A and B is characterized by the rolling angular vector $\vec{\boldsymbol{\theta}}_r$. This vector describes the relative orientation change between the two particles and can be defined by summing the angular vector of the incremental rolling (Šmilauer et al., 2010):

$$\vec{\boldsymbol{\theta}}_r = \sum d\vec{\boldsymbol{\theta}}_r \tag{4-7}$$

The rolling resistance moment $\vec{\mathbf{M}}_r$ is computed as:

$$\vec{\mathbf{M}}_\mathrm{r} = \begin{cases} \mathrm{K_r}\vec{\boldsymbol{\theta}}_\mathrm{r} & \text{if } \mathrm{K_r}\left\|\vec{\boldsymbol{\theta}}_\mathrm{r}\right\| < \left\|\vec{\mathbf{M}}_\mathrm{r}\right\|_\mathrm{lim} \\ \left\|\vec{\mathbf{M}}_\mathrm{r}\right\|_\mathrm{lim}\dfrac{\vec{\boldsymbol{\theta}}_\mathrm{r}}{\left\|\vec{\boldsymbol{\theta}}_\mathrm{r}\right\|} & \text{if } \mathrm{K_r}\left\|\vec{\boldsymbol{\theta}}_\mathrm{r}\right\| \geq \left\|\vec{\mathbf{M}}_\mathrm{r}\right\|_\mathrm{lim} \end{cases} \tag{4-8}$$

where,

$$\left\|\vec{\mathbf{M}}_\mathrm{r}\right\|_\mathrm{lim} = \eta_r \left\|\vec{\mathbf{F}}_N\right\|\frac{r_A + r_B}{2} \tag{4-9}$$

where, η_r is a dimensionless coefficient.

The rolling stiffness K_r of the interaction is defined as:

$$K_r = \beta_r \left(\frac{r_A + r_B}{2}\right)^2 K_T \tag{4-10}$$

where, β_r is the rolling resistance coefficient.

In order to assure the stability of DE simulation, a critical time-step Δt_{cr} is determined:

$$\Delta t_{cr} = \min_i \sqrt{2} \sqrt{\frac{m_i}{K_i}} \tag{4-11}$$

where, m_i is the mass of particle *i*, K_i is per-particle stiffness of contacts in which particle *i* participates.

4.2.2. Finite Elements

In the coupled FE-DE framework, a dynamic relaxation method is used for the finite element analysis in which the numerical model is damped until a steady state condition is reached (Dang and Meguid, 2010). As the dynamic explicit approach is also used in the discrete element analysis, it is possible to couple the two compatible approaches.

For a given structural system, the general equation that needs to be solved using the dynamic relaxation approach is:

$$\mathbf{Kx} + c\mathbf{M}\dot{\mathbf{x}} + \mathbf{M}\ddot{\mathbf{x}} = \mathbf{P} \tag{4-12}$$

where, $\mathbf{K}$ is the stiffness matrix, c is the damping coefficient for the mass proportional damping, $\mathbf{M}$ is the mass matrix, $\mathbf{P}$ is the external force vector and $\mathbf{x}$ represents the displacement vector.

The time-step Δt_{FE} is calculated based on the element consistent tangent stiffness:

$$\Delta t_{FE} \le \left[\Delta t_{FE} \right] = \frac{2}{\sqrt{\lambda_m}} \tag{4-13}$$

where, λ_m is the maximum eigenvalue,

$$\lambda_m \le \max_i \sum_{j=1}^{n} \frac{\left| K_{ij} \right|}{M_{ii}} \tag{4-14}$$

In Equation 4-14, K_{ij} is an element of the global tangent stiffness matrix and M_{ii} is an element of the diagonal mass matrix.

The flowchart of the dynamic explicit FE simulation is shown in Figure 4-1.

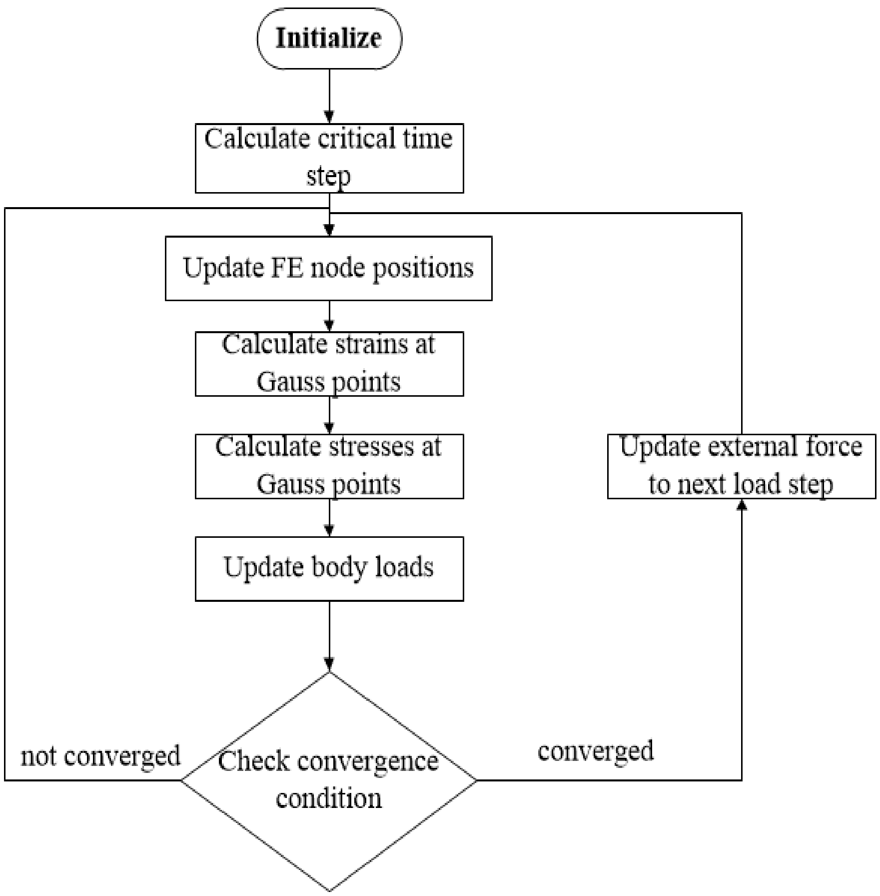

Figure 4-1 Flowchart of dynamic explicit FE simulation

4.2.3. Interface Elements

In this study, interface elements are used to transmit contact forces between the FE and DE domains. Triangular facets are used as interface elements since they have the flexibility to represent complex surfaces and can be generated directly from coordinates of the finite elements. If an element has a triangular or a tetrahedron shape, the triangular facet is directly defined by the three nodes of the element located on the interface. In the case of quadrilateral or hexahedral elements, the contact interface is divided into four triangular facets by creating a temporary center node defined by:

$$x^{(O)} = \frac{1}{4}\sum_{i=1}^{4} x^{(i)} \tag{4-15}$$

where, $x^{(i)}$ is the coordinate of node i of the quadrilateral. A description of a DE particle in contact with a FE domain is shown in Figure 4-2.

The contact algorithm between a discrete element and an interface element is similar to those between discrete particles. By determining the contact between discrete particles and interface elements, interaction forces transmitted to the FE nodes including the normal force $\vec{\mathbf{F}}_N$ and tangential force $\vec{\mathbf{F}}_T$ at contact can be achieved (Figure 4-3):

$$\vec{\mathbf{F}}_i = \vec{\mathbf{F}}_{contact}.N_i \tag{4-16}$$

where, $\vec{\mathbf{F}}_{contact} = \vec{\mathbf{F}}_N + \vec{\mathbf{F}}_T$ is the total contact force, N_i is the shape functions obtained using the natural coordinates of the contact point.

As the time-step Δt_{FE} required for FE is much larger than that for DE (Δt_{DE}), using a single time-step for both FE and DE based on the smallest time-step was found to be uneconomic. Therefore, the coupling framework used in this study allows for different time-steps for each domain. The time-step in the FE domain is selected as $\Delta t_{FE} = n\Delta t_{DE}$ where n is an integer such that $n \le \frac{[\Delta t_{FE}]}{\Delta t_{DE}}$. This algorithm has been implemented by executing the FE solver for every *n* DE computations (Figure 4-4). A similar multiple-time-step algorithm is also described in Xiao and Belytschko (2004) and Elmekati and Shamy (2010).

The procedure of the FE-DE coupling is described in Figure 4-5. A typical calculation cycle consists of the following main steps: i) Collision detection between DE particles and interface elements. ii) Calculation of interaction parameters of each contact. iii) Calculation of interaction forces between soil particles and between soil particles and interface elements. iv) DE particle velocities are calculated and new particle positions are updated. For every *n* time steps, the FE solver is executed and forces acting on FE nodes are updated to determine node displacements. v) Repeat the steps (i) - (iv) until convergence is reached. For every cycle, the convergence condition based on unbalanced forces of the DE and FE domains is checked.

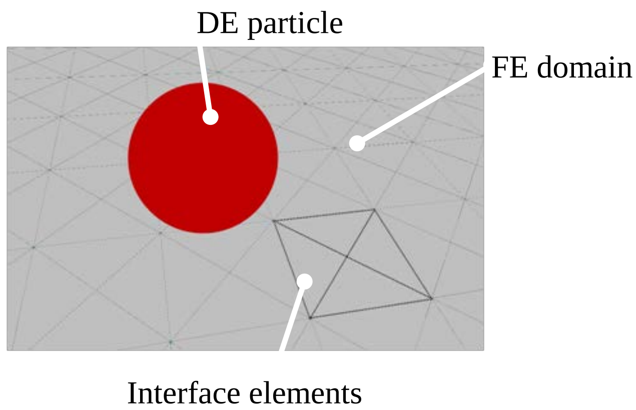

Figure 4-2 Coupling FEM and DEM using interface elements

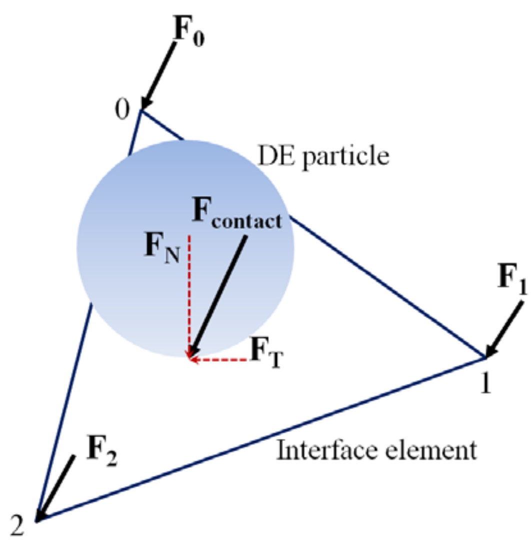

Figure 4-3 Forces transmitting to FE nodes through DE particle - interface element interaction

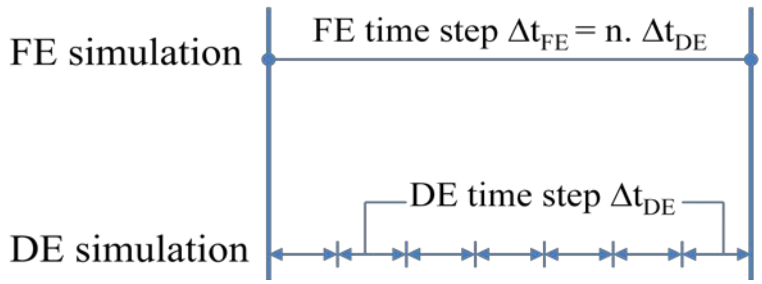

Figure 4-4 Multi-time step algorithm

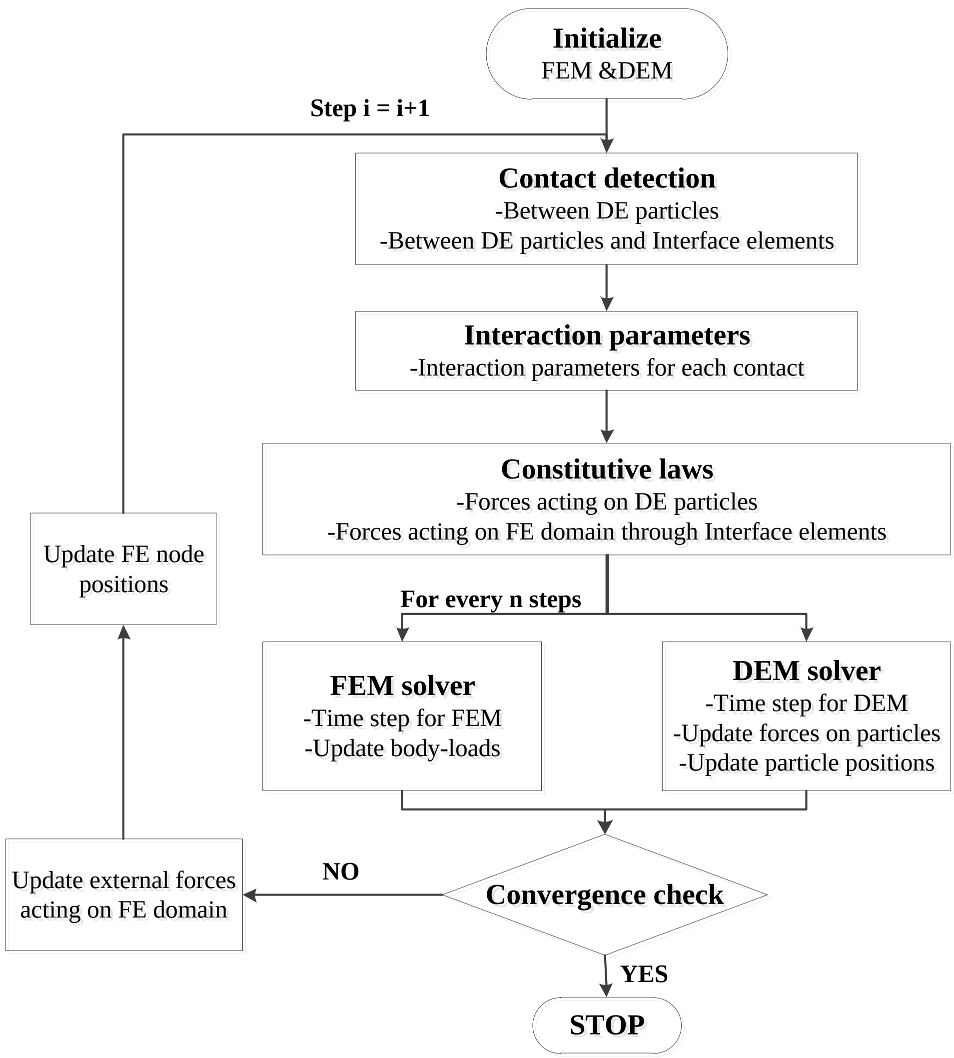

Figure 4-5 Flow chart of the coupled Finite-Discrete element method

4.3. Model Generation

In this study, an experimental pullout test performed on a geogrid type SS-1 (Alagiyawanna et al., 2001; Sugimoto and Alagiyawanna, 2003) is adopted and numerically modeled using the proposed coupled FE-DE model. Details of the laboratory test are summarized as follows:

The soil container was reported to be 0.68 m in length, 0.3 m in width and 0.625 m in height. The front wall composed of six acrylic plates each of 0.3 m width and 0.1 m height to reduce the friction between soil and the wall. The soil used in the experiment was Silica Sand No. 5 with D_{50} = 0.34 mm and a peak friction angle of 29.9^o (D_r = 70%) as obtained from laboratory triaxial tests. A geogrid specimen (Tensar SS-1 with polypropylene material and stiffness 285.6 kN/m at a strain of 3%) of 500 mm in length and 300 mm in width was used throughout the experiments. The sand was placed in layers using raining technique and the pullout load was applied using a clamp attached to the front end of the geogrid sheet. Vertical stresses 49 kPa and 93 kPa were applied on the top and bottom of the box using air bags to prevent vertical movement of the geogrid during the test. The geogrid was pulled out at a constant rate of 1.0 mm/min and both the load and lateral movement were measured using load cells and displacement gauges, respectively.

The numerical model has been developed such that it follows the geometry and test procedure used in the actual experiment. The geogrid is modeled using FE while the soil is modeled using DE, as discussed in section 4.2. Interface elements are used to simulate the interaction between the two domains. All components are generated inside YADE using two corresponding FE and DE packages.

The biaxial SS-1 geogrid, which comprises 8 longitudinal elements and 19 transverse elements, is modeled using 8-noded brick elements with 8 integration points (Figure 4-6). A non-deformable clamp is introduced at one end of the geogrid. The initial distance between the front wall and the 1st transverse member is 30 mm assuring all transverse members are still in the soil domain during the test (the maximum pullout displacement is 25 mm). A linear elastic material model is used for the geogrid sheet and its properties are determined by matching the experimental load-displacement curve obtained from the conducted index tests at a medium strain of 2% (as shown in Table 4-1). It is noted that the local increase in joint thickness is not considered in the geogrid model in order to simplify the analysis. The full geometry of the geogrid which comprises over 1300 finite elements and 20,000 interface elements is shown in Figure 4-6.

The sand used in the experiment is modeled using spherical particles. Since it is numerically prohibitive to simulate millions of particles with true sizes, particle up-scaling is necessary to reduce the number of modeled particles. Consideration of particle sizes is usually made to keep the balance between the computational cost and the scaling effects on the sample response. In this study, the sand is modeled using discrete particles with a mean diameter of 5.1 mm (15 times the real D_{50}) and a standard deviation of 1.0 mm. Particle properties are determined by matching the results of the numerical and experimental triaxial test. The packing process of the numerical triaxial test specimen is similar to the one used for the soil sample in the pullout test which is described in the following part. The matching procedure was as following: the rolling resistance coefficient β_r together with the normal and tangential stiffnesses were varied first to match the slope of the numerical deviator stress – axial strain curve with the experimental curve; the friction angle was then modified to match the peak deviator stress. It is found that the most appropriate combination corresponds to a friction angle with a tangent ($\tan\varphi$) of 0.54 and a particle material modulus (E) of 100 MPa. A summary of the selected parameters is given in Table 4-1.

Table 4-1 Input parameters for the simulation

Type of elements	Parameter	Value
Discrete particles	Density (kg/m^3)	2640
	Material modulus E (MPa)	100
	Ratio K_T/K_N	0.1
	Coefficient of friction ($\tan\varphi$)	0.54
	β_r	0.05
	η_r	1.0
	Damping coefficient	0.2
Finite elements	Young modulus E (MPa)	2.8E+3
	Poisson's ratio ν	0.3
Interface elements	Material modulus E (MPa)	100
	Ratio K_T/K_N	0.1
	Coefficient of friction ($\tan\varphi$)	0.95

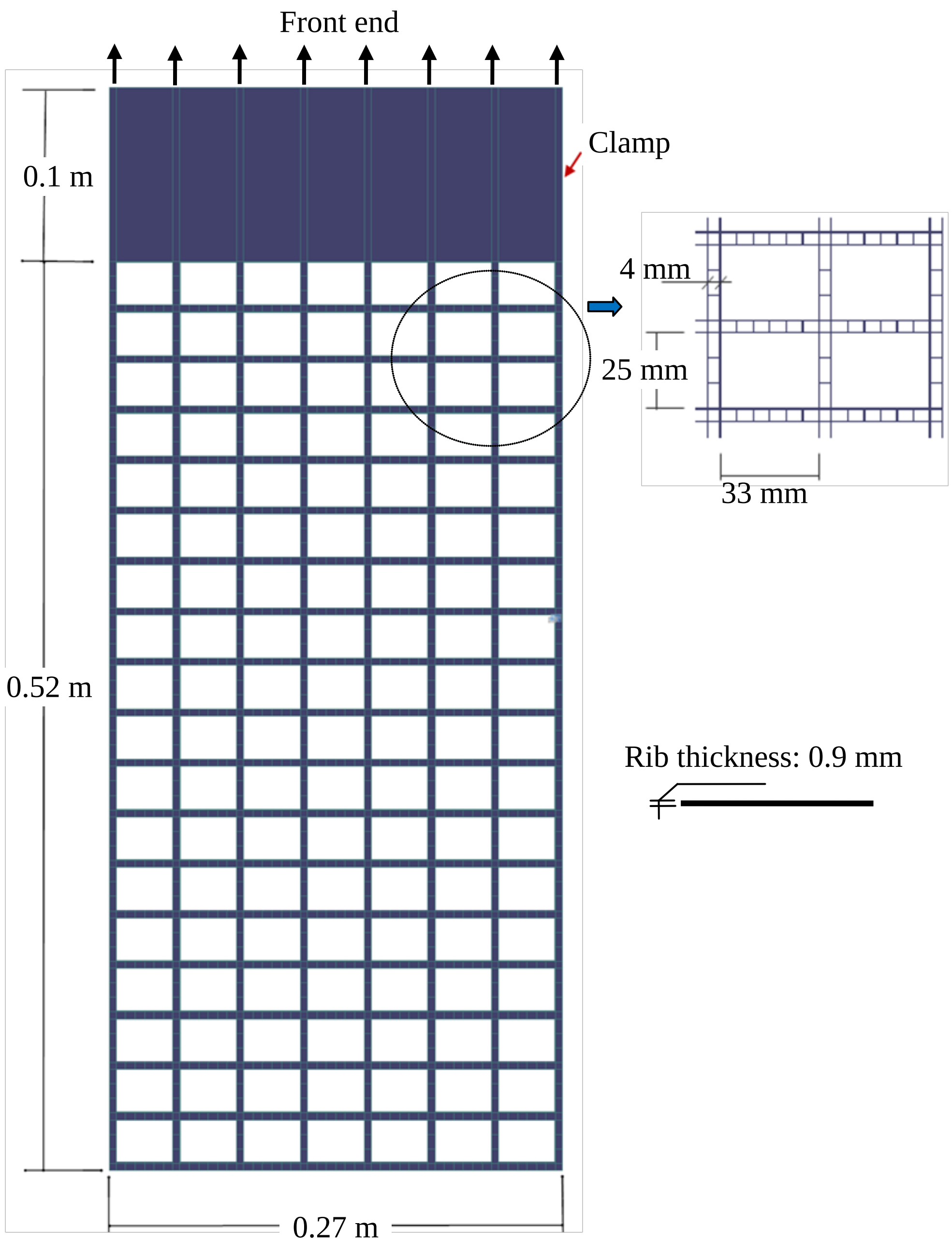

Figure 4-6 Geometry of the geogrid

Several packing algorithms have been developed to generate discrete element specimens (Cundall and Strack, 1979; Jiang et al., 2003; Labra and Oñate, 2009; Dang and Meguid, 2010). Appropriate methods are selected to provide the best replication of the actual packing process. In this study, soil sample is generated using the gravitational approach to represent the actual soil placement in layers under gravity. This packing technique originated from the one proposed by Ladd (1978) for real specimen preparation and is similar to the Multi-layer Under-compaction Method proposed by Jiang et al. (2003). Some modifications are made in the present study to match the actual soil properties as described below:

Four layers of particles with thicknesses of about 0.15 m each are generated to form the soil sample. To build the first layer, a set of non-contacting particles is generated until the target volume is reached. This target volume is calculated based on the porosity of the real sand, which is 0.39. The initial height of the box is chosen to be larger than the target height of the layer to insure that all particles can be generated without overlapping. Gravity is then applied to all particles allowing them to move downward and come in contact with each other. The interparticle friction angle is initially set to zero. It is noticed that even when the friction angle is zero, the generated sample is looser than the actual one. To increase the density of the packing, lateral shaking is applied to the box to help small particles move into the voids located between larger particles. The generation of the first layer is considered complete when the system reaches equilibrium. For the second layer, the height of the box is increased and the second "cloud" of non-contacting particles is generated in the area above the existing particles. Gravity and shaking are then applied and the system is allowed to come into equilibrium.

When the second layer is completed, particles above the geogrid level (if any) are removed and the finite element used to model the geogrid as well as the interface elements are generated. At this stage, the geogrid is assumed to be non-deformable in order to maintain its initial geometry during the sample generation process. The third and fourth layers are then generated using the same procedure.

The homogeneous distribution of the contact force after the packing process is checked using the fabric tensor. It can be seen that in the vicinity of the geogrid, the fabric tensor components are nearly identical ($\mathbf{\Phi}_{xx}$ and $\mathbf{\Phi}_{yy}$ of about 0.33, $\mathbf{\Phi}_{zz}$ of about 0.34 where z is the gravitational direction). The 3D geometry of the final sample is partially shown in Figure 4-7.

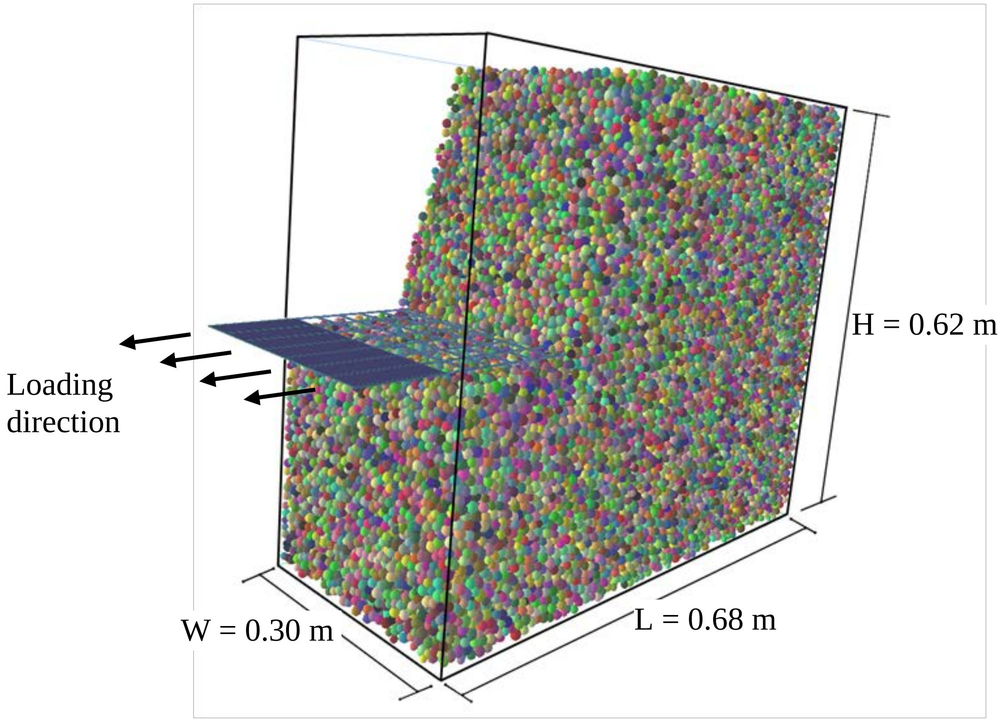

Figure 4-7 Initial DE specimen (partial view for illustration purpose)

4.4. Pullout Test Model

After the final specimen is formed, the input parameters (Table 4-1) are then assigned to the discrete particles and the finite elements. No friction is used for the interaction between the particles and the box (smooth rigid) to reduce the boundary effects. A parametric study was conducted to examine the effect of the contact parameters between the discrete particles and interface elements on the calculated response of the pullout model. Results indicated that the stiffnesses at the interface do not have a significant effect on the pullout test results. Therefore, the stiffnesses of the interface have been assigned the same values as that of the discrete particles. These findings are consistent with those reported by Villard et al. (2009) for similar geosynthetic-soil interaction problems. On the other hand, the coefficient of friction between the discrete particles and interfaces was found to affect the overall response of the soil-geogrid system. In this study, the particle-interface coefficient of friction is determined to be 0.95 based on matching the numerical results with experimental data. This has resulted in a slightly high coefficient of friction reflecting the fact that spherical particles usually mobilize less frictional contact with structural surfaces as opposed to real sand particles. In addition, and since the local increase in geogrid thickness at the joints is not explicitly modeled, the contribution of the joints to the overall pullout resistance is also considered as part of the geogrid frictional resistance.

Following the above step, the geogrid is allowed to freely deform and the two vertical stresses (σ_v) 49kPa and 93kPa are applied above and below the soil sample. The vertical stress is kept constant during the test using a stress control mechanism: when the current normal stress σ is different from the target value σ_v, the upper (or lower) plate is moved vertically a distance of $dz = (\sigma - \sigma_v)/K$ where the stiffness K is determined by adding the normal stiffnesses of all active particle- plate interactions. This mechanism allows for a constant vertical stress to be maintained.

The pullout procedure is numerically performed using a displacement control approach: lateral displacements were applied to the clamp in 12 steps. In each step, the clamp was forced to move with a same rate of the experiment (in simulation time scheme) until an increase of displacement of 2.5mm was reached. The clamp movement was then stopped until convergence conditions are satisfied in both the DE and FE domains. Additional frontal displacements were applied in subsequent steps and the procedure continued until the frontal displacement U_x reached 25 mm.

4.5. Results and Discussions

4.5.1. Validation of the numerical model

It is noted that both the experiment and the numerical simulation aimed at investigating the behavior of the geogrid and surrounding soil prior to failure. The relationship between the pullout force and the frontal displacement is shown in Figure 4-8 as obtained from both the experimental and numerical models. The numerical results generally agreed with the experimental data except for smaller pullout forces that are calculated for frontal displacements less than 7 mm. This is expected given the limited number of discrete particles used to represent the backfill soil resulting in underestimating the interaction between particles and interfaces particularly at the early stages of the test. The pullout force at a given frontal displacement slightly increased as the vertical stress (σ_v) changes from 49 kPa to 93 kPa. Sugimoto and Alagiyawanna (2003) observed a small slippage of the geogrid at both stress levels leading to marginal difference in pullout resistance. Figure 4-9 shows the displacement distributions along the geogrid. It can be seen that geogrid displacements decrease with distance from the face. For all examined frontal displacements the geogrid displacement (U_x) occurs within a limited region from the front side to about the middle of the geogrid. Very small displacements were calculated outside this region. Figure 4-9 also confirms the agreement between the measured and calculated displacement using the proposed framework.

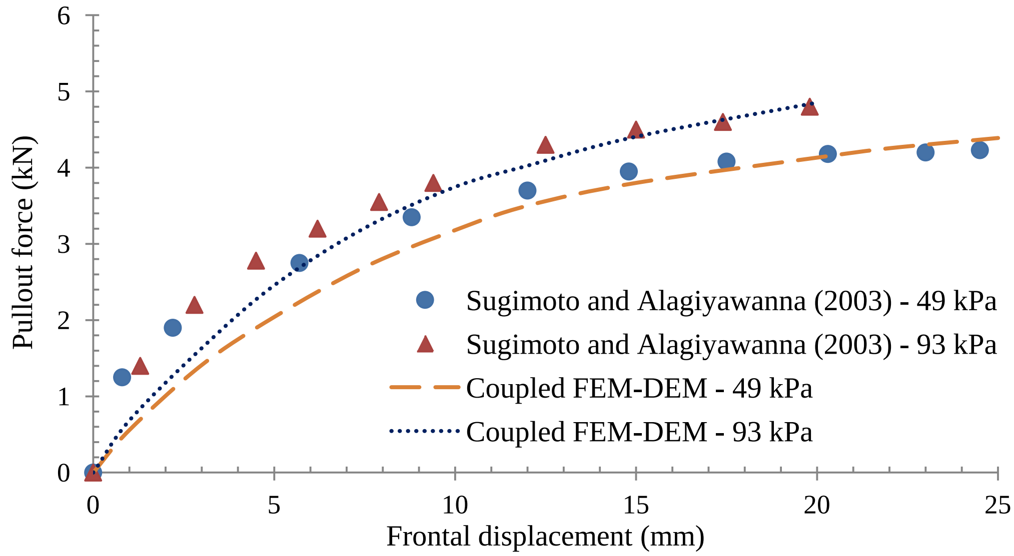

Figure 4-8 Pullout response of the geogrid

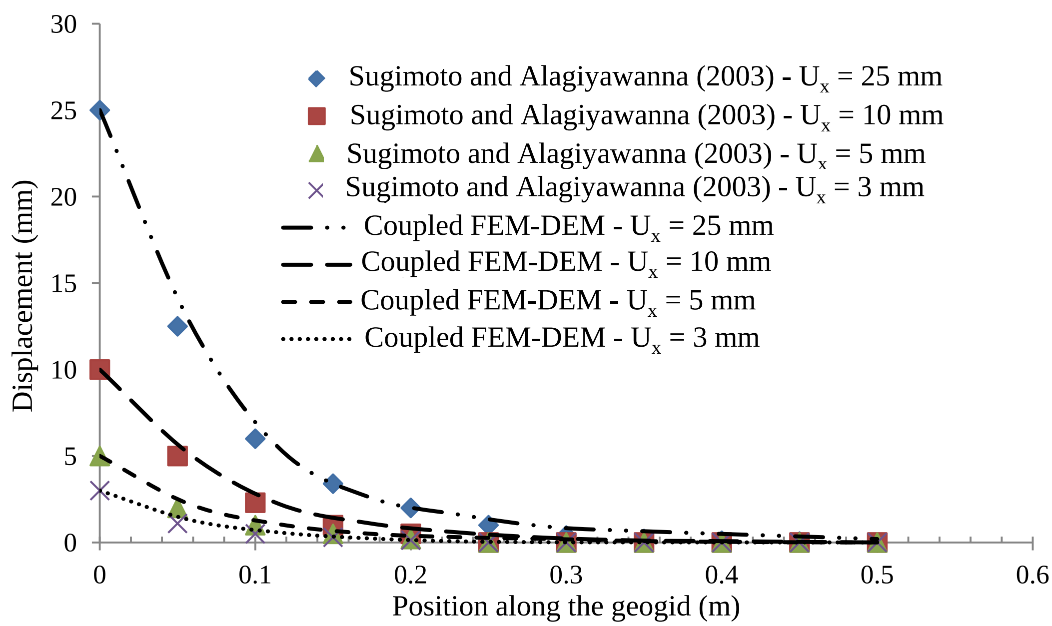

Figure 4-9 Horizontal Displacement along the geogrid (σ_v = 49 kPa)

4.5.2. Response of the Geogrid

The deformed shape of the geogrid for a frontal displacement (U_x) of 10 mm and a vertical pressure (σ_v) of 49 kPa is shown in Figure 4-10. The largest deformation of the geogrid is found to occur in the vicinity of the applied load and rapidly decreases with distance towards the rear side of the box. The longitudinal elements of the geogrid experienced deformation in its axial direction with the largest elongation occurring near the loading side. It is also noted that part of the geogrid that is connected to the loading clamp has to be in air during the test which results in softer behavior and larger elongation in that region. Transverse members, on the other hand, showed a dominant bending deformation particularly near the loaded side. This bending behavior originates from the frictional forces acting at the upper and lower geogrid surfaces as well as the bearing forces acting as the geogrid pushed against the soil.

The stress distribution within the geogrid is shown in Figure 4-11. In consistency with the displacement pattern, the stresses S_{xx} were highest near the front side and rapidly decreased to a negligible value at a distance of about 50% of the geogrid length. It can be also realized that stresses in the longitudinal members are much larger compared to the transverse ones.

The tensile force distributions in the longitudinal members for different frontal displacements are illustrated in Figure 4-12. At a given location along the geogrid, the average tensile force (P_{xx}) in all longitudinal members was found to increase with the increase in frontal displacements. For the investigated range of frontal displacements, the force P_{xx} was large near the front end and rapidly decreased towards the middle of the geogrid. Beyond the middle zone, P_{xx} became negligible due to the insignificant displacement of the geogrid experienced by the rest of the geogrid.

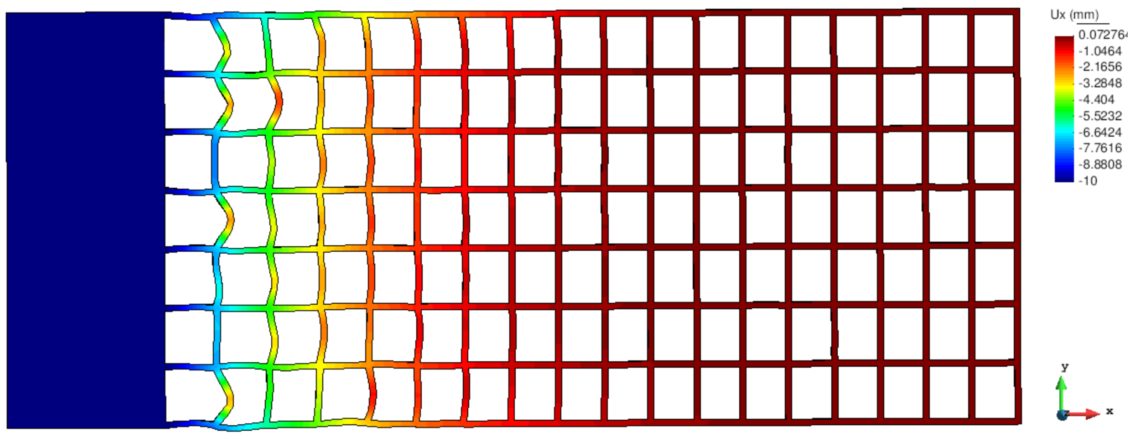

Figure 4-10 Geogrid deformation and displacement at

U_x = 10 mm and σ_v = 49 kPa

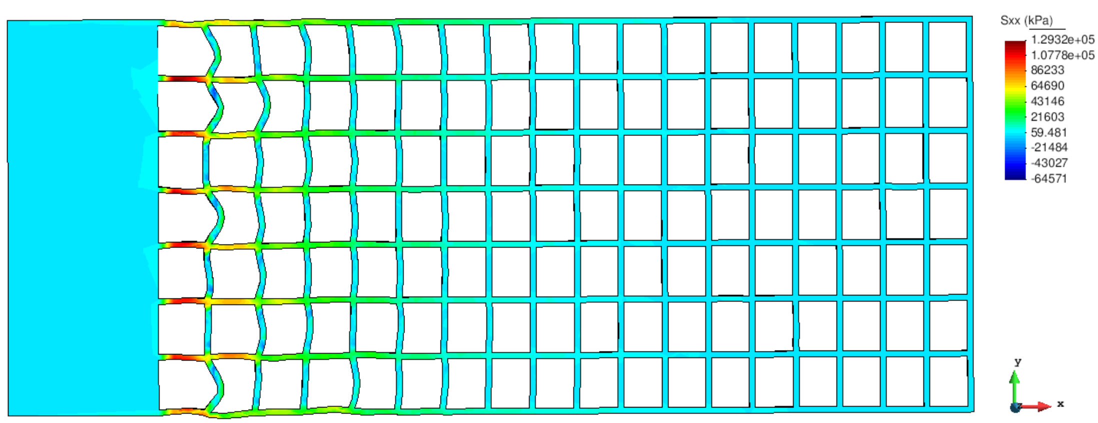

Figure 4-11 Geogrid stress S_{xx} at U_x = 10 mm and σ_v = 49 kPa

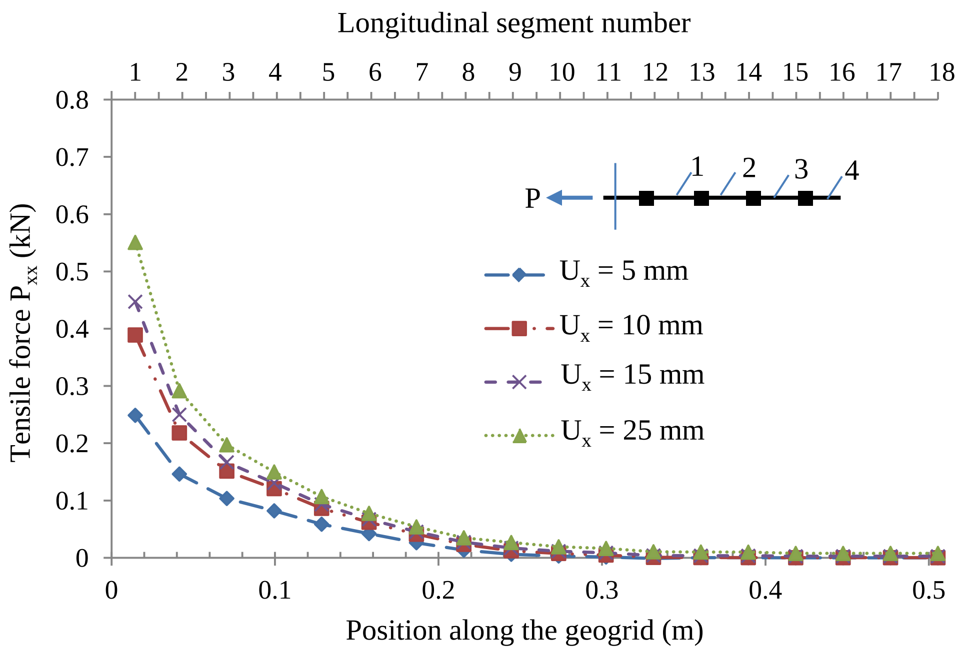

Figure 4-12 Average tensile force P_{xx} in the longitudinal members (σ_v = 49 kPa)

4.5.3. Pullout Resistance

The used geogrid comprises longitudinal and transverse members as well as joints connecting these members. Each of these components contributes to the total pullout force. Since the resistance of the joints in this study is numerically included in the frictional resistance of the geogrid, the total pullout resistance F_p can be written as:

$$F_p = F_f + F_{bt} \tag{4-17}$$

where, F_f is the frictional resistance on the geogrid surface and F_{bt} is the bearing resistance of the transverse members.

The frictional and bearing resistances are determined numerically based on the contact forces between the discrete particles and the corresponding interface elements. Contribution of each component to the total pullout resistance is shown in Figure 4-13. It can be seen that the contribution of the bearing resistance is less than that of the frictional resistance for all considered frontal displacements leading to the frictional component (F_f) dominating the pullout resistance F_p. However, the rate of increase in F_f became very small when the frontal displacements (U_x) reached about 18 mm as slippage of the geogrid started to develop and most of the shear forces between the particles and interfaces reached their maximum values (see Equation 4-6). The bearing resistance of the transverse elements, on the other hand, shows an increase in value for all examined frontal displacements.

The accumulated contribution of the different transverse members to the total bearing resistance is shown in Figure 4-14. Transverse members located within the first 0.18 m measured from the front side contributed to about 90% of the total bearing resistance. It is also noted that more than 50% of the total bearing is resisted by transverse members in the first 0.06 m measured from the front side of the box. The large bearing contribution from the geogrid transverse members close to the front side has also been mentioned by other authors such as

Costalonga (1988 and 1990), Milligan et al. (1990) and Palmeira (1987, 2004 and 2009).

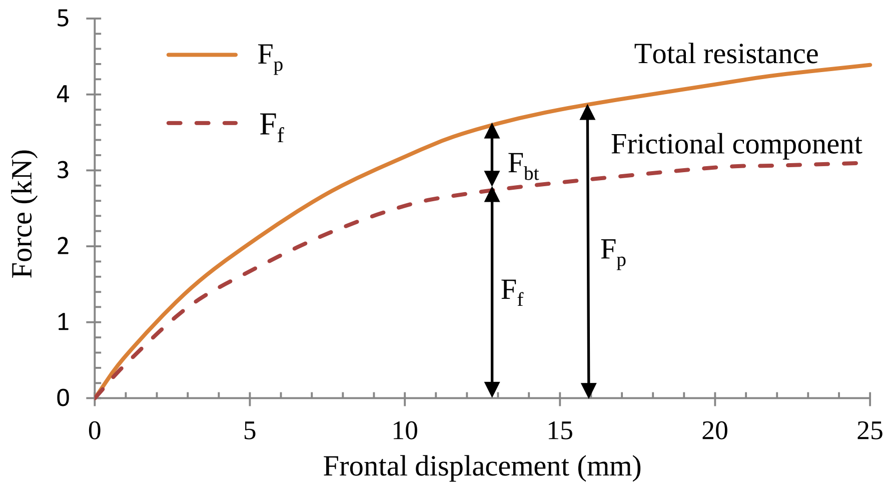

Figure 4-13 Components of the pullout resistance (σ_v = 49 kPa)

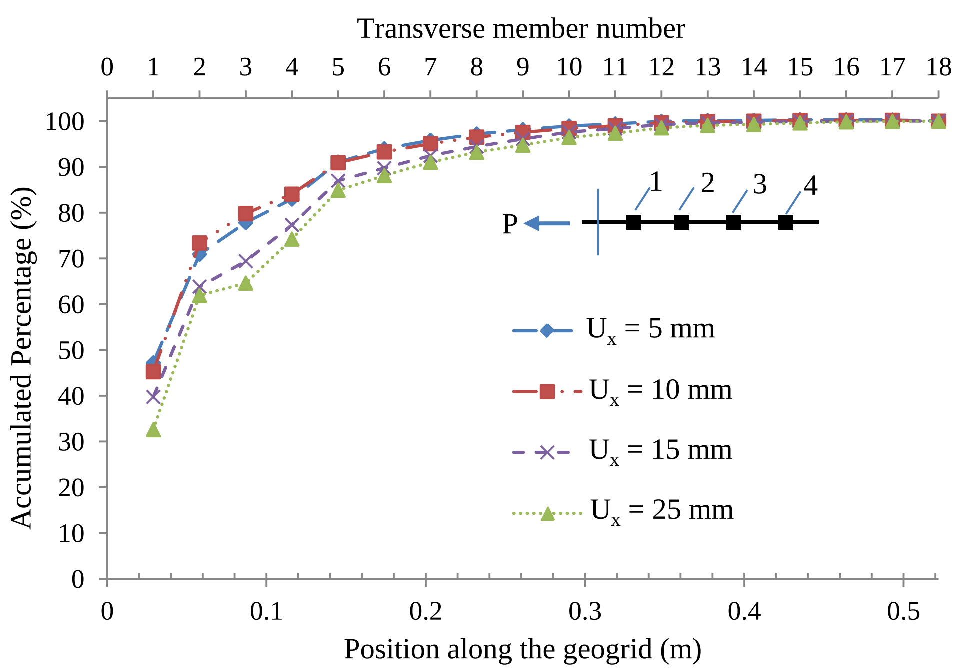

Figure 4-14 Accumulated contribution of the transverse members to the total bearing resistance at different locations along the geogrid (σ_v = 49 kPa)

4.5.4. Response of the Backfill Soil

Figure 4-15 shows the displacement field across the soil domain at a frontal displacement of 10 mm. It can be seen that most of the soil movement developed near the front face of the box leading to soil densification in that area. Soil movement gradually decreased and became negligible around the middle of the geogrid as there is no significant geogrid displacement in this area. Soil in the vicinity of the geogrid tends to move horizontally towards the front face whereas near the front face soil tends to move vertically away from the geogrid. These observations agree well with the results of the X-ray radiographs reported by Alagiyawanna et al. (2001). The pattern of soil movement in pullout tests has also been reported by Jewell (1980) and Dyer (1985). The movement of the soil particles results in a change in the direction of contacts between particles. The contact force networks within the soil domain for both a) initial condition; and b) for frontal displacement of 10 mm are shown in Figure 4-16. Each contact force is illustrated by a line connecting the centers of two contacting elements while the width of the line is proportional to the magnitude of the normal contact force. For the initial condition, most of the contact forces are oriented vertically in response to the applied pressure above and below the soil sample. As the geogrid is pulled out, soil particles started to move resulting in an increase in contact forces in the horizontal direction while the magnitudes of the contact forces in the vertical direction are maintained. This newly introduced horizontal component resulted in the development of diagonal contact forces as shown in Figure 4-16b. Contact forces that originate from the geogrid have larger values as they transmit forces from the geogrid to the surrounding soil. Large contact forces are observed in the vicinity of the front face in consistency with the soil densification near the vertical boundary. The contact force distribution is in agreement with the distributions observed by Dyer (1985) using the photo-elasticity approach (Figure 4-16).

The strain field of the soil domain is achieved using a tessellation approach (Bagi, 2006; Šmilauer et al. 2010) and the results are shown in Figure 4-17. It can be seen that most strains generally occurred in the vicinity of the geogrid while the largest strain tends to develop near the front face.

The stress distributions within in the soil around the geogrid are shown in Figure 4-18. The stresses within a representative volume V are calculated by:

$$\sigma_{ij} = \frac{1}{V}\sum_{c=1}^{N_c} x^{c,i} f^{c,j} \tag{4-18}$$

where, N_c is the number of contacts within the volume V, $f^{c,j}$ is the contact force vector at contact c, $x^{c,i}$ is the branch vector connecting two contact particles A and B, and indices i and j indicate the Cartesian coordinates.

It should be noted that the vertical and horizontal stresses presented in Figure 4-18 are recorded at a distance of 100 mm above the geogrid. For all examined frontal displacements, there is an increase in both the vertical and horizontal stresses with a maximum increase in the close vicinity of the front face of the box. This increase may be due to the use of horizontal plates to control the vertical pressure. Beyond approximately half the geogrid length measured from the front face, stresses remain close to their initial values. It can be seen that for this pullout test, the extent of the affected area of the geogrid and backfill material under pullout load is generally limited to no more than 50% of the geogrid length.

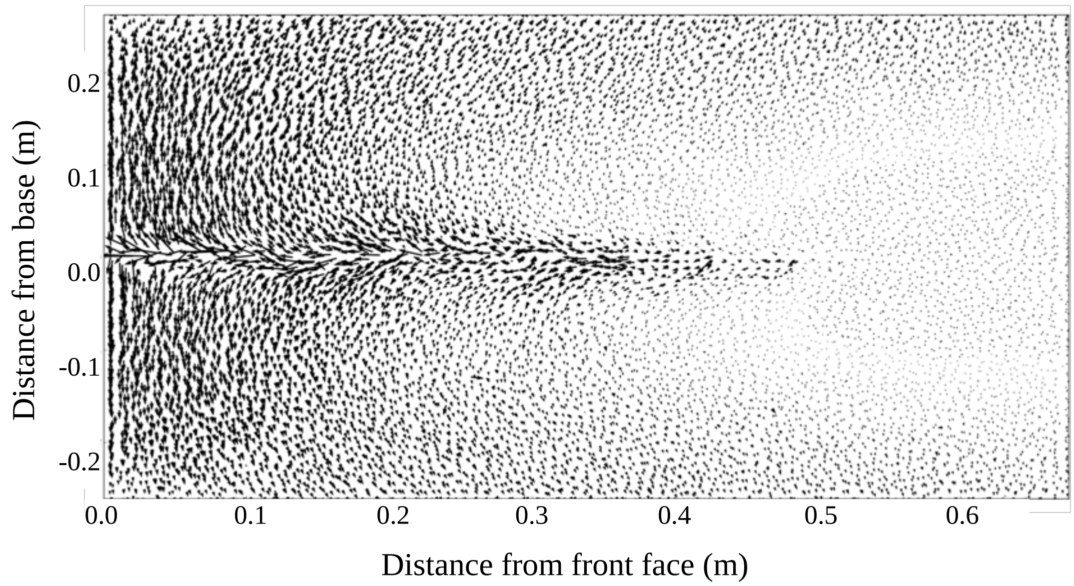

Figure 4-15 Displacement field of the soil domain at U_x = 10 mm and σ_v = 49 kPa

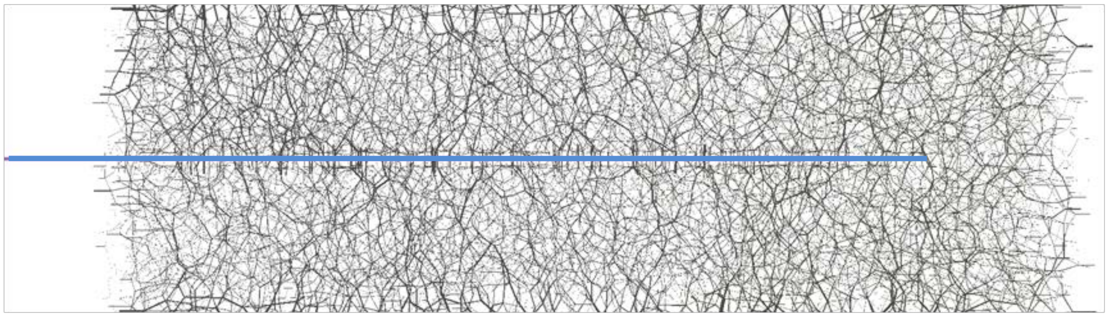

a) Contact-force network at the initial condition ($\sigma_v = 49kPa$)

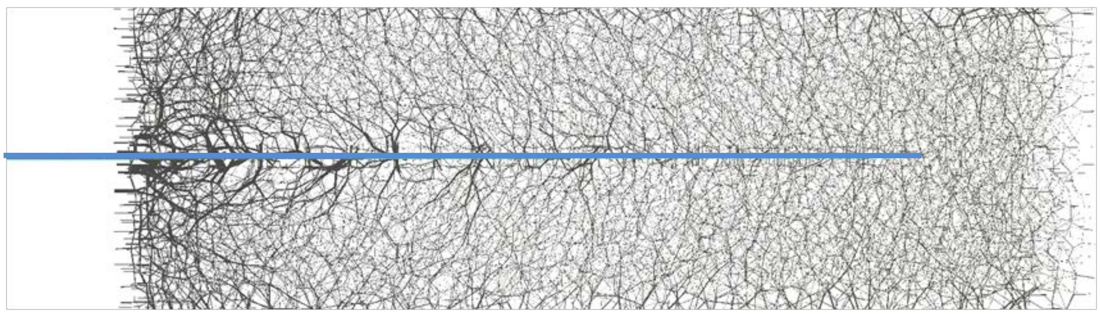

b) Contact-force network at U_x = 10 mm ($\sigma_v = 49kPa$)

Figure 4-16 Contact force networks within the soil around the geogrid

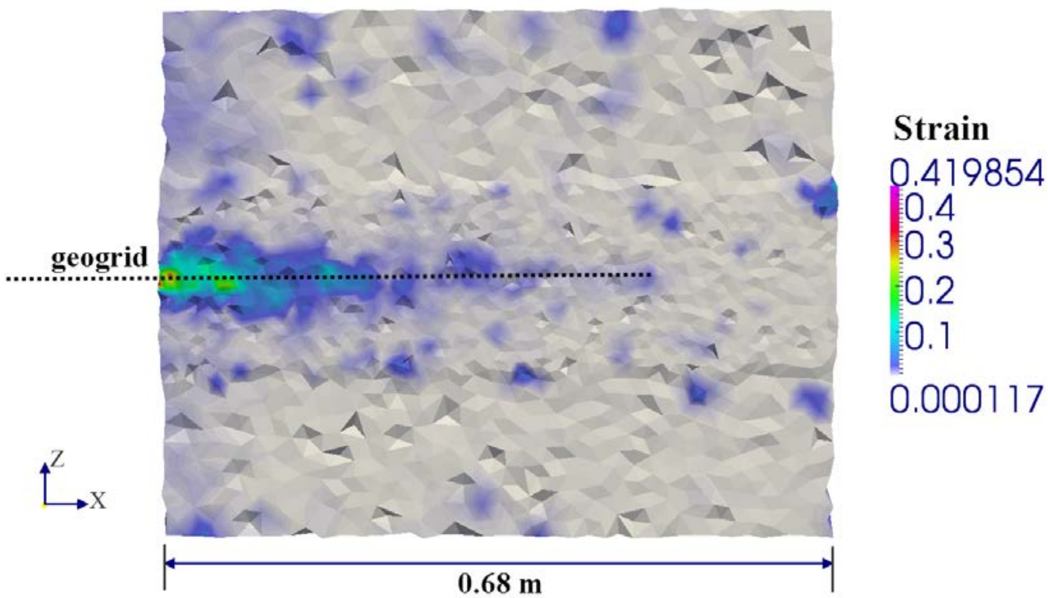

Figure 4-17 Strain field within the soil domain at U_x = 10 mm and σ_v = 49 kPa

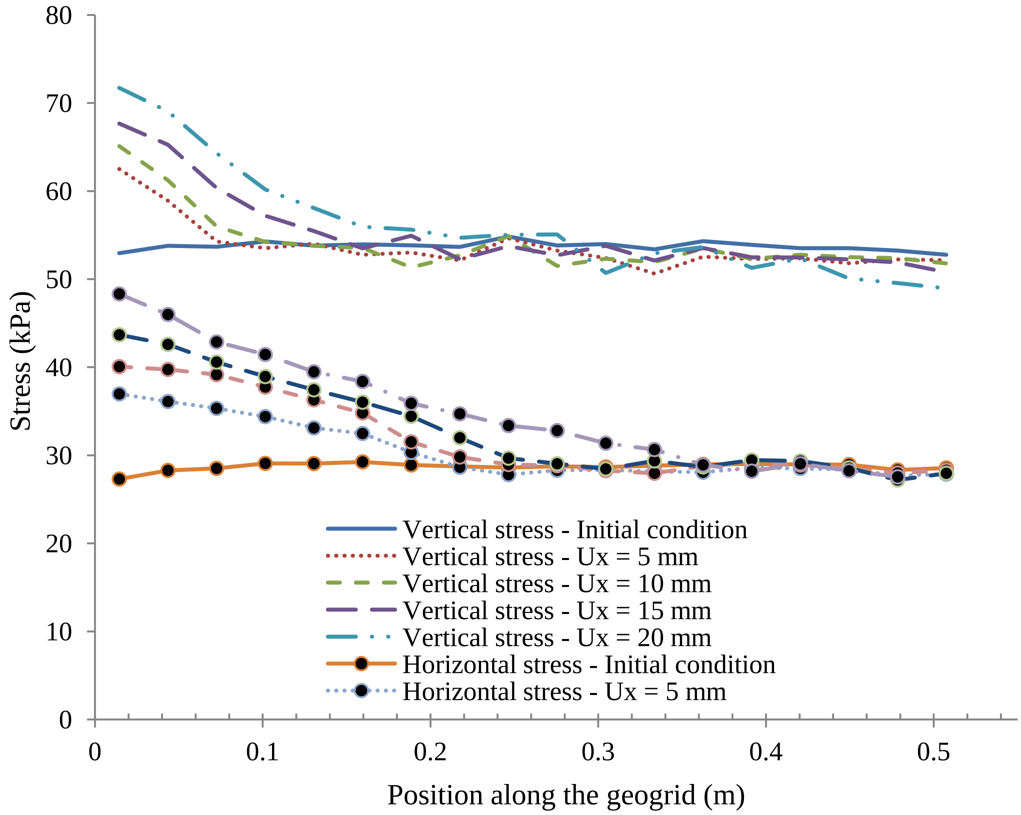

Figure 4-18 Distribution of vertical and horizontal stresses in soil (σ_v = 49 kPa)

4.6. Summary and Conclusions

In this paper, a framework for coupling finite and discrete element methods was developed. Interface elements were introduced to ensure the transmission of forces between the DE and FE domains. A multiple-time-step scheme was applied to optimize the computational cost. Using the developed framework, a three-dimensional numerical study was performed to investigate the behavior of a biaxial geogrid embedded in granular material under pullout loading condition. The geogrid was modeled using finite elements while the backfill material was modeled using discrete elements. The results of the analysis were compared with experimental data. The displacements and stresses developing in the geogrid were analyzed and the micro-mechanical behavior of the soil domain was investigated.

Most of the geogrid stresses and displacements occurred near the front side of the box with rapid decrease with distance and reached very small values around the middle of the geogrid. For the investigated geogrid and soil conditions, the contribution of the frictional resistance to the total pullout resistance was found to be larger than the bearing resistance. The contribution of the bearing resistance to the overall capacity increased as the geogrid displacement increased. The soil movement and the contact force distribution within the soil domain agreed with experimental observations. An increase in soil stresses and strains was observed near the front face.

Finally, the proposed coupled FE-DE method has proven to be efficient to model the pullout experiment in three-dimensional space and capture the response of both the geogrid and the surrounding backfill material.

Preface to Chapter 5

The developed coupled Finite-Discrete element framework has demonstrated its efficiency in investigating the 3D response of soil-geogrid interaction under geogrid pullout testing condition. To continually demonstrate the robustness of the coupled Finite-Discrete element algorithm, the framework is now used to analyze a strip footing over geogrid-reinforced sand. Both unreinforced and geogrid reinforced foundations are studied from which the efficiency of geogrid reinforcement is investigated. The capability of the framework to model the soil-geogrid interaction at the microscopic scale is demonstrated.

CHAPTER 5

Three-Dimensional Analysis of Geogrid Reinforced Foundation Using Finite-Discrete Element Framework *

Abstract

Three-dimensional analysis of soil-structure interaction problems considering the detailed response at the particle scale level is a challenging numerical modeling problem. An efficient numerical framework that takes advantage of both the finite and discrete element approaches to investigate soil-geogrid interaction is described in this paper. The method uses finite elements to model the structural components and discrete particles to model the surrounding soil to reflect the discontinuous nature of the granular material. The coupled framework is used to investigate the behavior of strip footing over geogrid-reinforced sand. The numerical results are validated using experimental data. New insight into the three-dimensional interaction between the soil and the geogrid is presented.

Keywords: geogrid reinforcement, finite-discrete element, strip foundation, numerical simulation.

* A version of this chapter has been submitted to *International Journal of Geomechanics ASCE*, 2013.

5.1. Introduction

Continuum approaches (e.g., Finite Element and Finite Difference) are generally used for the numerical analysis of soil-structure interaction problems. The finite element method (FE) has proven to be a powerful tool to model both structural elements and the surrounding soil. Although FE can be used efficiently to model the soil behavior at the macroscopic scale, the discontinuous nature of the soil particles is not easy to represent. This discontinuous nature has an important role in the behavior of different soil-structure interaction systems such as soil-geogrid interlocking (McDowell et al., 2006), soil arching in embankments (Han et al., 2011) and particle erosion in the vicinity of subsurface structures (Meguid and Dang, 2009). The discrete element method (DE) proposed by Cundall and Strack (1979) is an alternative approach for the modeling of these systems. While the DE method can efficiently model soil discontinuous behavior (Maynar and Rodríguez, 2005; Lobo-Guerrero and Vallejo; 2006; Tran et al., 2012), using the DE method to model structural elements can lead to inaccurate responses. Researches including McDowell et al. (2006), Han et al. (2011) and Chen et al. (2012), used sets of discrete particles bonded together to model structural components. However, since micro voids generally develop in a structure generated by bonded particles, the continuous nature of the structure may not be fully captured.

To take advantage of both FE and DE methods, the structure can be modeled using FE whereas the soil can be modeled using the DE method. The coupling of the two methods can efficiently model the behavior of both the soil and the structure. This approach has been used by several researchers to analyze certain geotechnical problems. Elmekati and Shamy (2010) used this approach to model pile installation in which the pile was modeled using FE while the surrounding soil was modeled using DE. Dang and Meguid (2013) studied the earth pressure distribution on tunnel linings by modeling the tunnel lining using FE and surrounding soil using DE. Geotextile-reinforced embankment analysis using a coupled framework was reported by Villard et al. (2009). Soil-geogrid interaction during the geogrid pullout process was studied by Tran et al. (2013). The geogrid was modeled using FE representing the 3D geometry of the geogrid whereas the backfill soil was modeled using DE. The soil-geogrid interaction was ensured using interface elements. In this paper, a coupled Finite-Discrete element (FE-DE) framework that is capable of modeling soil-structure interaction problems at the microscopic scale level is used to investigate the behavior of foundation over reinforced soil. Literature review of the investigated problem is presented below.

Over the past three decades, the use of geosynthetics to increase bearing capacity of shallow foundations has received extensive research attention. The bearing capacity of reinforced soil has been studied experimentally by many researches across the world, including Guido et al. (1986), Huang and Tatsuoka (1990), Khing et al. (1993), Shin et al. (1993), Das et al.(1994), Yetimoglu et al. (1994), Adams and Collin (1997), Dash et al. (2001), DeMerchant et al. (2002), Patra et al. (2006), Basudhar et al. (2007), Chen et al. (2007), Chen et al. (2009), Abu-Farsakh et al. (2008), Ghazavi and Lavasan (2008), Ghosh and Dey (2009), Latha and Somwanshi (2009a, b), Sadoglu et al. (2009), Choudhary et al. (2010), Mohamed (2010) and Tafreshi and Dawson (2010). Results from these experimental studies show that the bearing capacity of a given foundation generally increases with the placement of geosynthetic material within the supporting ground. The effects of different variables such as geosynthetic length, vertical spacing between multiple reinforcing layers, depth to the top layer, number of layers and types of geosynthetics that contribute to the bearing capacity were also examined. Analytical solutions were also developed by Binquet and Lee (1975a,b), Michalowski (2004), Wayne et al. (1998), Kumar and Saran (2003), Abu-Farsakh et al. (2008), Huang and Menq (1997) and Sharma et al. (2009). Numerical simulation is an alternative way to study the stresses and strains within soil and in the geosynthetic layers. Finite element modeling of reinforced foundations has been reported by Yetimoglu et al. (1994), Kurian et al. (1997), Siddiquee and Huang (2001), Yamamoto and Otani (2002), Basudhar et al. (2007), Chung and Cascante (2007), Ghazavi and Lavasan (2008), Latha and

Somwanshi (2009a, b) and Li et al. (2012). In these studies, the reinforcement was often simplified either as a truss structure (in 2D analysis) or a continuous sheet (in 3D analysis). This simplification does not represent the true geometry of the geosynthetics particularly for geogrids. The interaction between geogrid and the surrounding soil was often modeled using interface elements in which contact properties were considered while the interlocking effect is not generally represented. It is known that the soil-geogrid interlocking in reinforced soils plays an important role in the bearing capacity of the foundation (Guido et al., 1986). The interlocking of the soil particles through the apertures of the grid mobilizes tensile strength in the reinforcing layer and generate anchoring effect in the soil-geogrid system. This leads to better geotechnical performance compared to geotextile-reinforced soil foundations. The coupled FE-DE approach presented in this study allows for the interlocking effect to be explicitly simulated considering the soils as DE particles while the 3D geometry of the geogrid is represented using FE elements. The interaction between the two domains is ensured using interface elements.

5.2. Model Generation

In this study, the experimental results reported by Das et al. (1994) and Khing et al. (1993) of a strip foundation supported by geogrid-reinforced sand is used to validate the proposed coupled FE-DE model. The soil container was reported to be 1.1m in length, 0.3m in width and 0.9m in height. The walls were polished to reduce the friction between the soil and the wall. The strip foundation had a width of 76 mm (noted as B) and a length of 300 mm. A rough condition at the base of the foundation was generated by cementing a thin layer of sand at the contact surface. The soil used in the experiment was medium-grained silica sand with D_{50} = 0.51 mm, average dry unit weight of 17.14 kN/m^3 and a peak friction angle of 41^o (at D_r = 70%) obtained from laboratory direct shear tests. Biaxial geogrids (Tensar SS-0 with PP/HDPE copolymer material and tensile modulus of 182 kN/m at 2% strain) of 760 mm in length and 300mm in width were used in the experiment. The top geogrid layer was installed at a depth 25 mm (0.33B) below the foundation base. The number of geogrid layers installed in soil was varied and the distance between two adjacent layers was 25 mm (0.33B). The sand was placed in layers of 25mm using raining technique. The geogrid layers were placed at predetermined locations. The model foundation was then placed on the soil surface and vertical loading was applied using a hydraulic jack. The load and the corresponding foundation settlement were measured during the tests using a proving ring and two dial gauges.

The numerical model has been developed such that it follows the geometry and test procedure used in the actual experiment. It is noted that due to the high computational time required for the coupled FE-DE analysis, up to two geogrid layers are considered in this study. The geogrid is modeled using FE while the soil is modeled using DE as discussed in the previous sections. Interface elements are used to simulate the interaction between the two domains. All components are generated inside YADE using two corresponding FE and DE packages.

The biaxial SS-0 geogrid, which comprises 11 longitudinal elements and 21 transverse elements, is modeled using 8-node brick elements with 8 integration points (Figure 5-1). A linear elastic material model is used for the geogrid sheet and its properties are determined by matching the experimental load-displacement relationship obtained from the conducted index tests at a strain of 2% (as shown in Table 5-1). It is noted that the local increase in joint thickness is not considered in the geogrid model in order to simplify the analysis. The full geometry of the geogrid which comprises over 1900 finite elements and 29,000 interface elements is shown in Figure 5-1.

The sand used in the experiment is modeled using spherical particles. Since it is numerically prohibitive to simulate millions of particles with true sizes, particle up-scaling is necessary to reduce the number of modeled particles. Consideration of particle sizes is usually made to keep the balance between the computational cost and the scaling effects on the sample response. In this study, the sand is modeled using discrete particles with a mean diameter of 10.2 mm (20 times the real D_{50}) and a standard deviation of 2.0 mm.

To generate DE samples, appropriate packing methods are considered to provide the best replication of the actual packing process. Several packing algorithms have been developed to generate discrete element specimens (Cundall and Strack, 1979; Jiang et al., 2003; Labra and Oñate, 2009; Dang and Meguid, 2010a; Tran et al. 2012). In this study, soil samples are generated using the gravitational approach proposed by Tran et al. (2012) to represent the actual soil placement in layers under gravity as described below:

Layers of particles with thicknesses of about 0.05 m each are generated to form the soil sample. To build the first layer, a set of non-contacting particles is generated until the target volume is reached. This target volume is calculated based on the porosity of the sand, which is 0.36. The initial height of the box is chosen to be larger than the target height of the layer to insure that all particles can be generated without overlapping. Gravity is then applied to all particles allowing them to move downward and contact with each other. The interparticle friction angle is initially set to zero. It is noticed that the generated sample is looser than the actual one even when the friction angle is zero. To increase the density of the packing, lateral shaking is applied to the box to help small particles move into the voids located between larger particles. The generation of the first layer is considered to be completed when the system reaches equilibrium. For the second layer, the height of the box is increased and the second "cloud" of non-contacting particles is generated in the area above the existing particles. Gravity and shaking are then applied and the system is allowed to come into equilibrium. The geogrids are generated during the packing process to ensure the proper interaction with the DE particles. Particles above the geogrid level are removed and the geogrid and interface elements are generated. At this stage, the geogrid is assumed to be non-deformable in order to maintain its initial geometry during the sample generation process. A next cloud of particles is generated and the procedure is repeated until the final specimen is formed. The generated assembly is then checked using the fabric tensor and contact orientation as shown in following parts. The 3D geometry of the final sample with over 245,000 particles is shown in Figure 5-2. A partial view of the particle-geogrid interaction is shown in Figure 5-3. It can be seen that the interlocking of the soil through the apertures of the grid is properly simulated by allowing the particles to penetrate into the geogrid apertures. Furthermore, the particles from one side of the geogrid can interact with other particles from the other side which represents closely the real behavior of the soil-geogrid interaction.

Microscopic parameters used for the simulation are identified as follow: particle density is 2650 kg/m^3 following the specific gravity of the sand, K_T/K_N ratio is fixed to be 0.25, β_R is 0.01 and particle material modulus of 38 MPa as suggested by Tran et al. (2012). The friction angles of DE particles are determined by matching the results of the numerical and experimental direct shear tests. The numerically simulated shear box has dimensions of 60 mm x 60 mm. The generated direct shear test sample consists of over 100,000 particles with a mean diameter of 1.0 mm (double the real D_{50}). The packing process mentioned above is used to generate the specimen to ensure its equivalence (same characteristics) to the soil sample used in the analysis (Tran et al. 2012). The microscopic friction angle is varied to match the peak friction angle of the experiment. A friction angle tangent ($\tan\varphi$) of 0.68 is found to provide the best agreement with the experiment. It is noted that although the particle size used in the numerical direct shear test differs from that used in the simulation, the parameters obtained from the direct shear test were found to represent the real soil and can be used in the numerical model. The randomness of the generation process at these scale factors was found to have a minor influence on the macro response since the number of particles in the specimens is large enough to represent the sample (Tran et al. 2012).

Table 5-1 Input parameters for the simulation

Type of elements	Parameter	Value
Discrete particles	Density (kg/m^3)	2650
	Material modulus E (MPa)	38
	Ratio K_T/K_N	0.25
	Coefficient of friction ($\tan\varphi$)	0.68
	β_r	0.01
	η_r	1.0
	Damping coefficient	0.2
Finite elements	Young modulus E (MPa)	1.4E+3
	Poisson's ratio ν	0.3
Interface elements	Material modulus E (MPa)	38
	Ratio K_T/K_N	0.25
	Coefficient of friction ($\tan\varphi$)	0.42

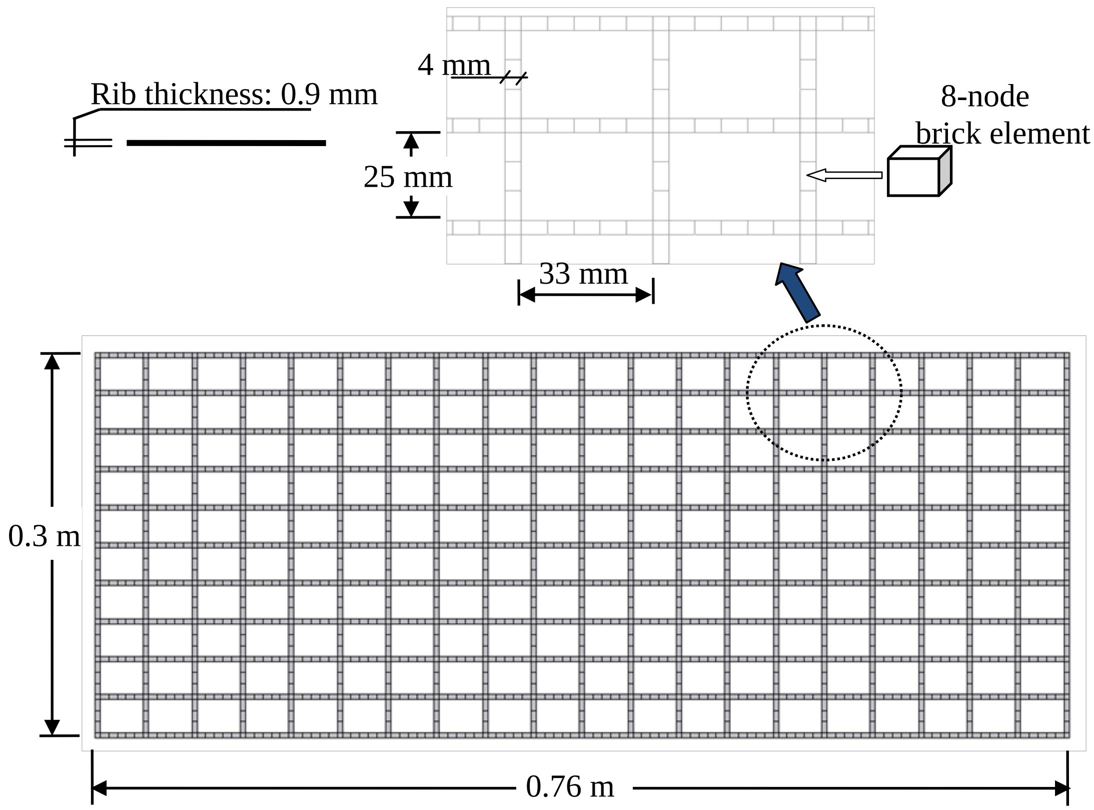

Figure 5-1 Plan view of the geogrid

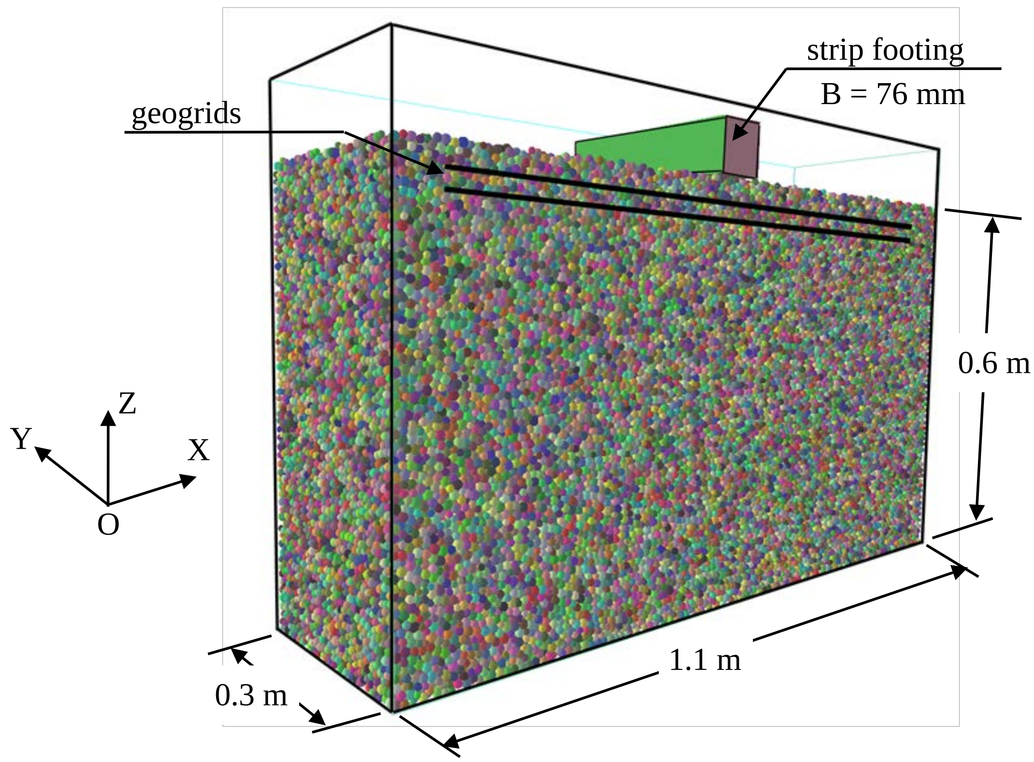

Figure 5-2 Initial geometry of the geogrid reinforced foundation

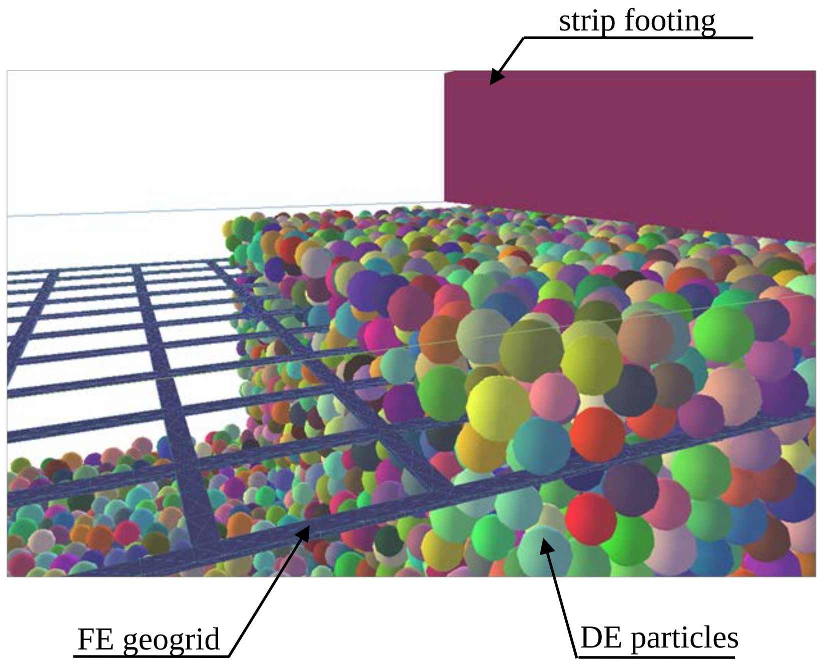

Figure 5-3 Partial view of the DE particle-geogrid interaction

5.3. Numerical Simulation

After the final specimen is formed, the strip footing (76 mm x 300 mm, Figure 5-2) is numerically generated and initially placed at the surface of the soil layer. The input parameters (Table 5-1) are then assigned to the discrete particles and the finite elements. No friction is used for the interface between the particles and the box walls whereas a high friction angle with tangent of 1.0 is applied for the interaction between the foundation base and DE particles to simulate the rough foundation base used in the experiment. A parametric study was conducted to examine the effect of the DE particle-interface interaction on the response of the strip footing model. Results indicated that the stiffnesses of the interface elements do not have a significant effect on the simulation results. Therefore, the stiffnesses of the interface elements are assigned the same values as the DE particles. These findings are consistent with those reported by Villard et al. (2009) for similar geosynthetic-soil interaction problems. On the other hand, the coefficient of friction between the discrete particles and interface elements was found to affect the overall response of the soil-geogrid system. In this study, the particle-interface coefficient of friction has to be determined in order to reach a good agreement between the numerical and experimental results. It is due to the fact that spherical particles usually mobilize less frictional contact with structural surfaces as opposed to real sand particles. A parametric study was conducted to investigate the influence of the particle-interface friction coefficient on the overall behavior, from which a particle-interface coefficient of friction of 0.42 is determined for the simulation (Table 5-1).

Before applying loads to the foundation, the fabric tensor and contact orientation are investigated. The fabric tensor is determined by:

$$\mathbf{\Phi}_{ij} = \frac{1}{N_c}\sum_{N_c} n_i n_j \tag{5-1}$$

where, N_c is the number of contacts and n_i is the unit branch vector component in the i direction. The calculated fabric tensor components are nearly identical ($\mathbf{\Phi}_{xx}$

and $\mathbf{\Phi}_{yy}$ of about 0.33, $\mathbf{\Phi}_{zz}$ of about 0.34 where, z is the gravitational direction). The distribution of contact orientation is shown in Figure 5-4. It can be seen that the contacts are homogeneously distributed in all directions.

Following the above steps, the geogrids are then allowed to freely deform and pressure at the foundation base is applied in small increments using a stress control mechanism: for each loading stage, when the current pressure σ is different from the target value σ_v, the foundation moves vertically a distance of $dz = (\sigma - \sigma_v)/K$ where, the stiffness K is determined by adding the normal stiffnesses of all active particle-foundation base interactions. This mechanism allows for a constant pressure to be maintained. Each load increment is kept constant until convergence conditions are satisfied in both the DE and FE domains. The foundation pressure is then increased for the next stage.

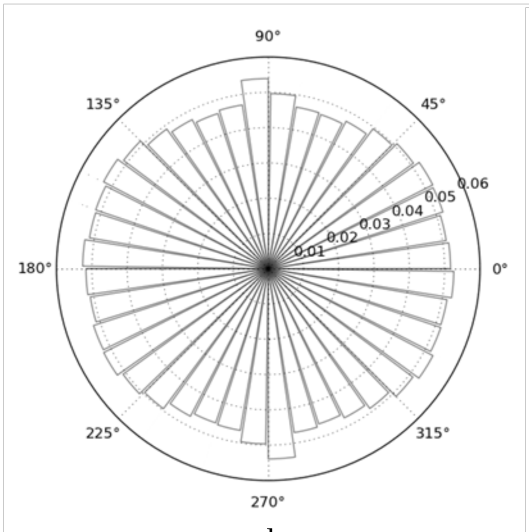

xz plane

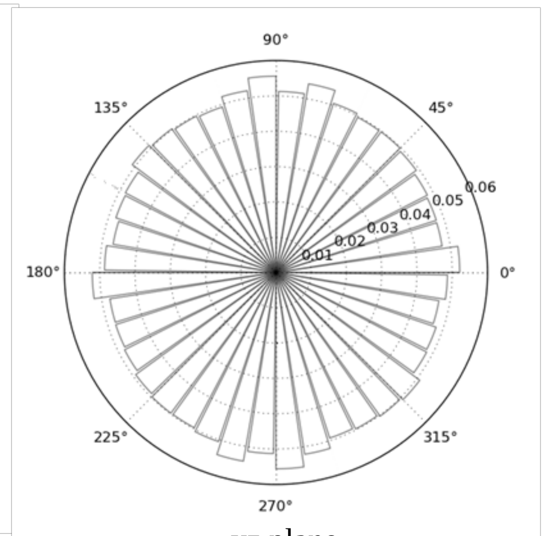

yz plane

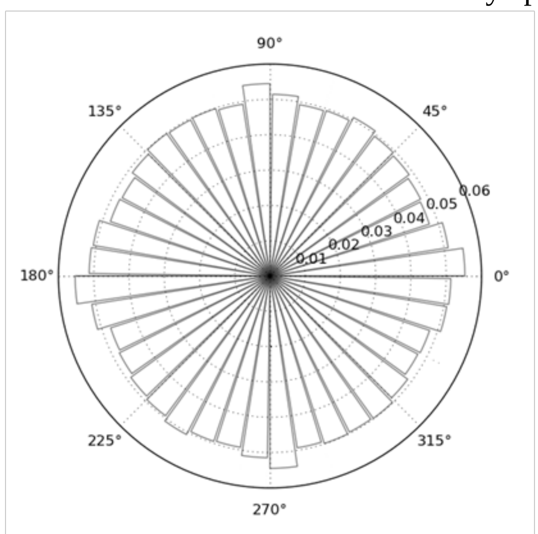

xy plane

Figure 5-4 Distributions of the contact orientation at initial condition

5.4. Results and Discussions

5.4.1. Validation of the Numerical Model

In this section, the use of one or two geogrid sheets to reinforce the soil is analyzed and compared to the case of no reinforcement. To validate the model, the coupled FE-DE simulation results are first compared with the experimental data. Figure 5-5 shows the relationship between the foundation pressure and settlement for three cases: no reinforcement (N = 0), one geogrid layer (N = 1) and two geogrid layers (N = 2). It can be seen that the numerical results agreed well with the experimental data for all cases. For a given settlement, the load the foundation can carry increased with the use of geogrid reinforcement. The ultimate bearing capacity also increased with the number of geogrid layers (N). It is also observed that the increase in the ultimate bearing capacity occurred with an increase in the foundation settlement. The ultimate bearing capacity calculated by Das et al. (1994) is consistent with the numerical results. This confirms the agreement between the experiment and numerical simulations using the proposed numerical framework.

5.4.2. Response of the Geogrids

The deformed shapes of the geogrid layers for a foundation pressure q = 125 kPa are shown in Figure 5-6. The vertical displacement of the geogrid for one reinforcement layer (N = 1) is shown in Figure 5-6a whereas the case of two geogrid layers (N = 2) is shown in Figure 5-6b. It can be seen that the vertical displacement of the geogrid for N = 1 is generally larger than that for N = 2. In addition, the vertical displacement of the upper geogrid sheet is larger than that of the lower one. Consistent with the displacement pattern, the tensile stresses in the geogrid for N = 1 were found to be larger than that for N = 2 (Figure 5-7). It is also noted that the upper geogrid layer experienced higher tensile stresses than the lower layer. In both cases, the deformations of the geogrids occurred mainly in a region below the foundation and very small deformations were observed outside that region. The stresses S_{xx} were highest below the foundation and decreased with distance from the loading area. The vertical displacement and tensile stress distributions of the geogrid for N = 1 are shown in Figure 5-8. It can be seen that the vertical displacements and tensile stresses of the geogrid occurred within a distance of 1.5B from the foundation center and became negligible outside this region. The maximum calculated vertical displacements and tensile stresses in the geogrid for different footing pressures are shown in Figure 5-9. It is observed that for a given pressure, the vertical displacements and tensile stresses in the geogrid were larger for N = 1 than for N = 2. It is also noted from Figure 5-9a and 5-9b that the deformation and tensile stresses of the upper geogrid layer were generally larger than the lower one for N = 2.

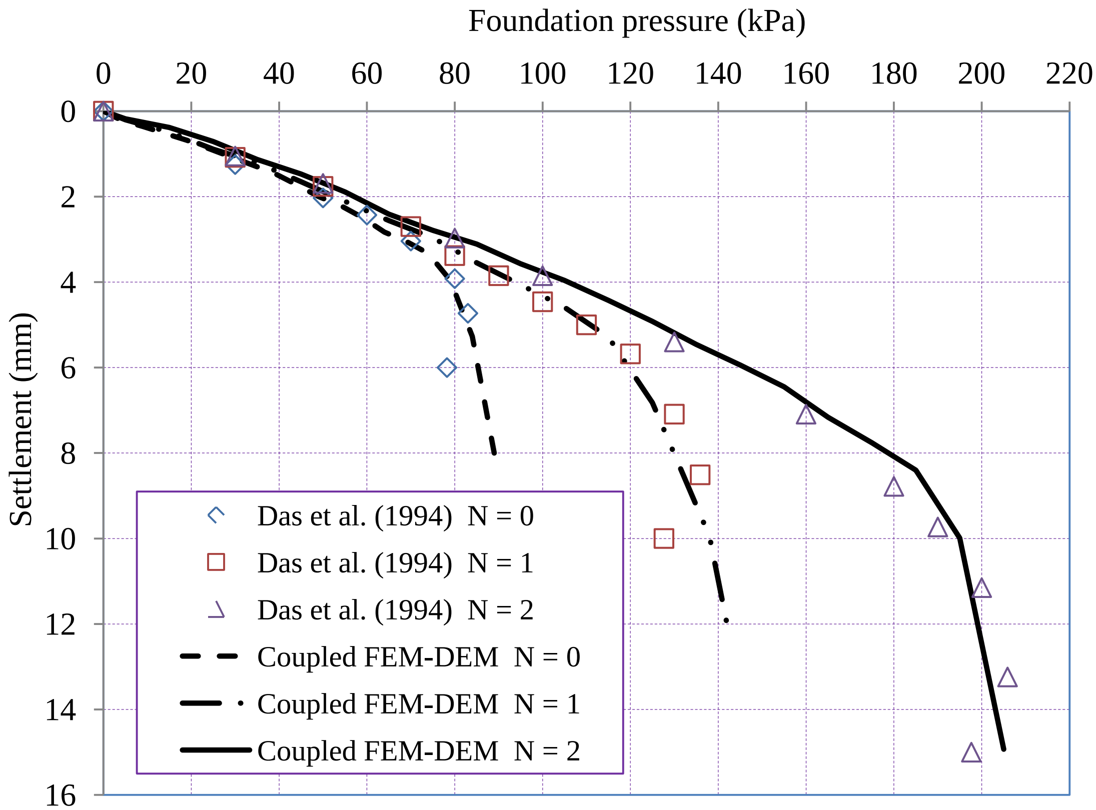

Figure 5-5 Load-settlement curves of the geogrid reinforced foundation

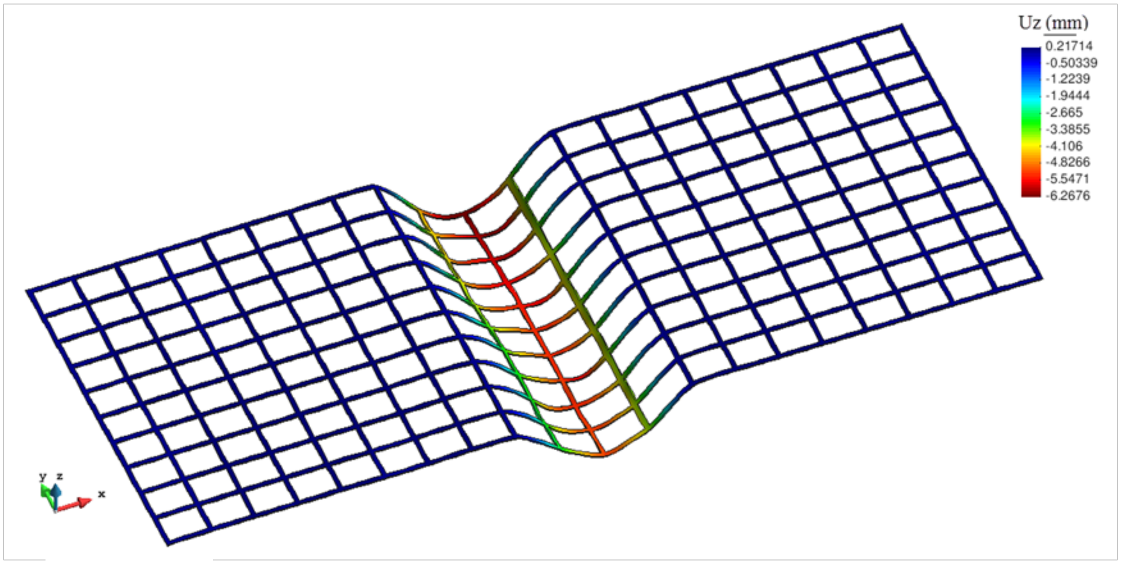

a) N = 1

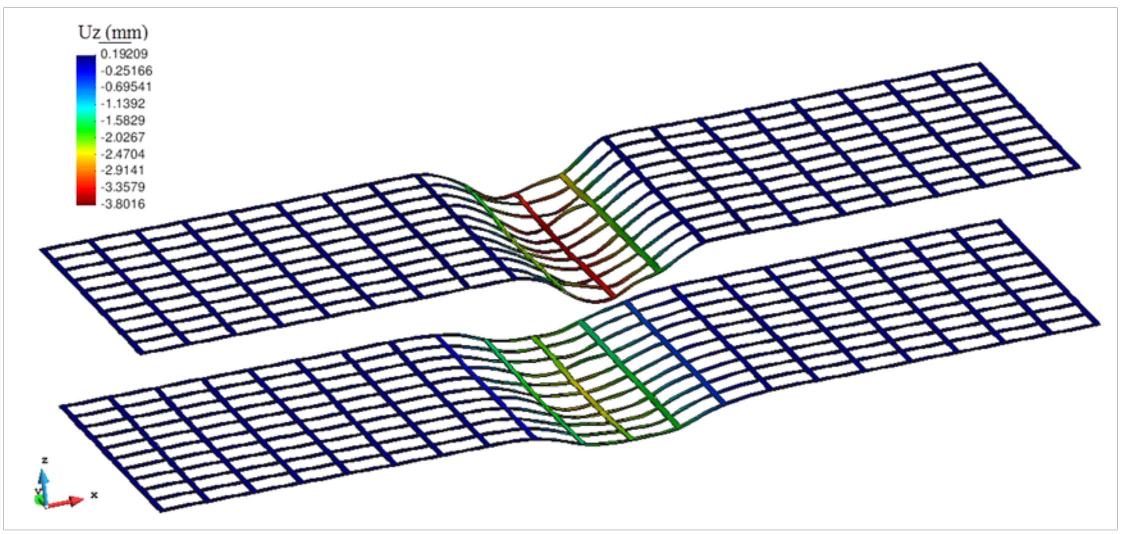

b) N = 2

Figure 5-6 Geogrid vertical displacement at foundation pressure q = 125 kPa

a) one geogrid layer and b) two geogrid layers

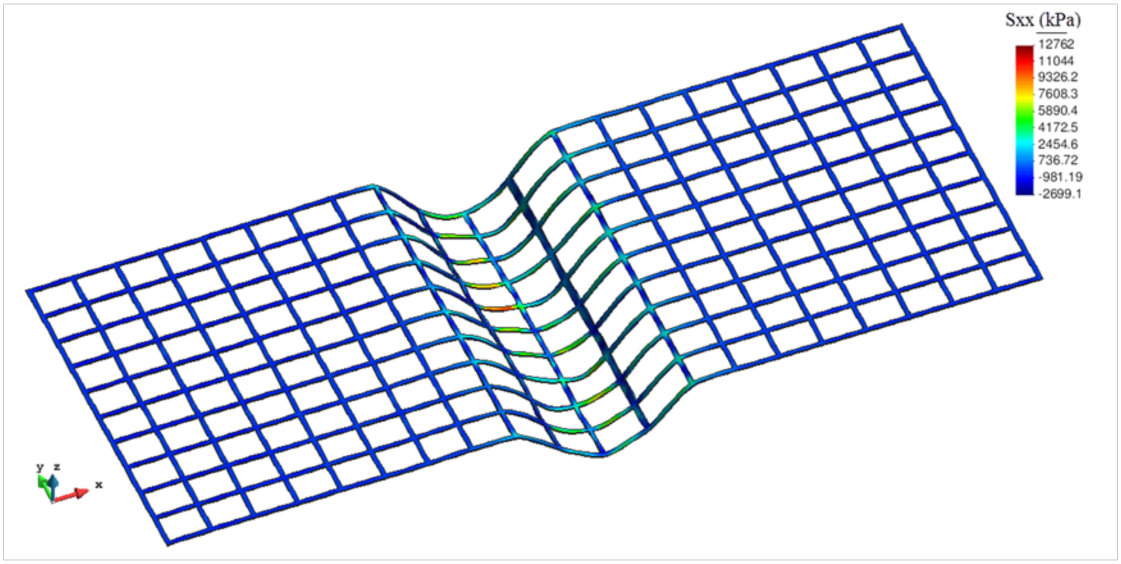

a) N = 1

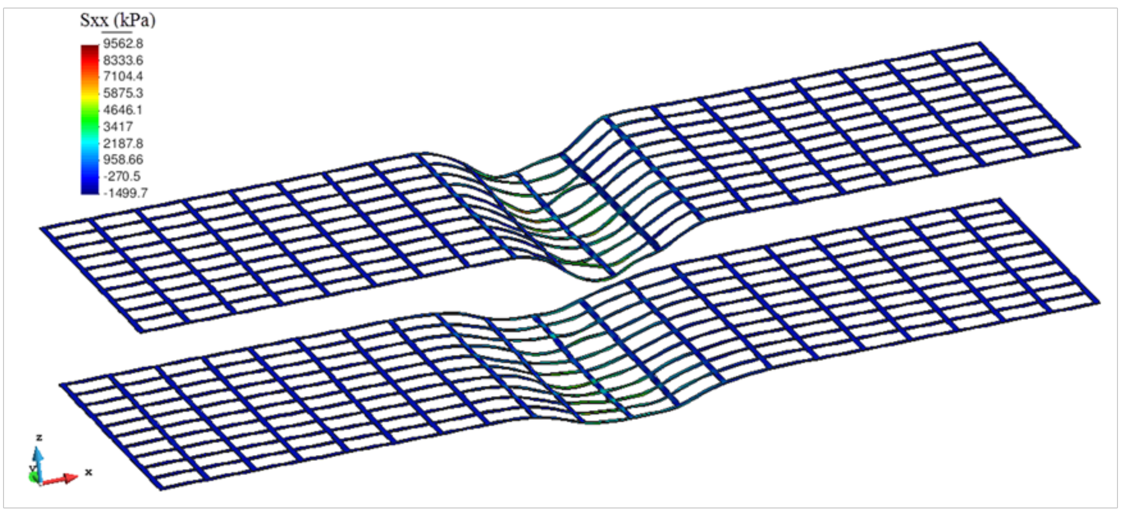

b) N = 2

Figure 5-7 Geogrid stress S_{xx} at foundation pressure q = 125 kPa

a) one geogrid layer and b) two geogrid layers

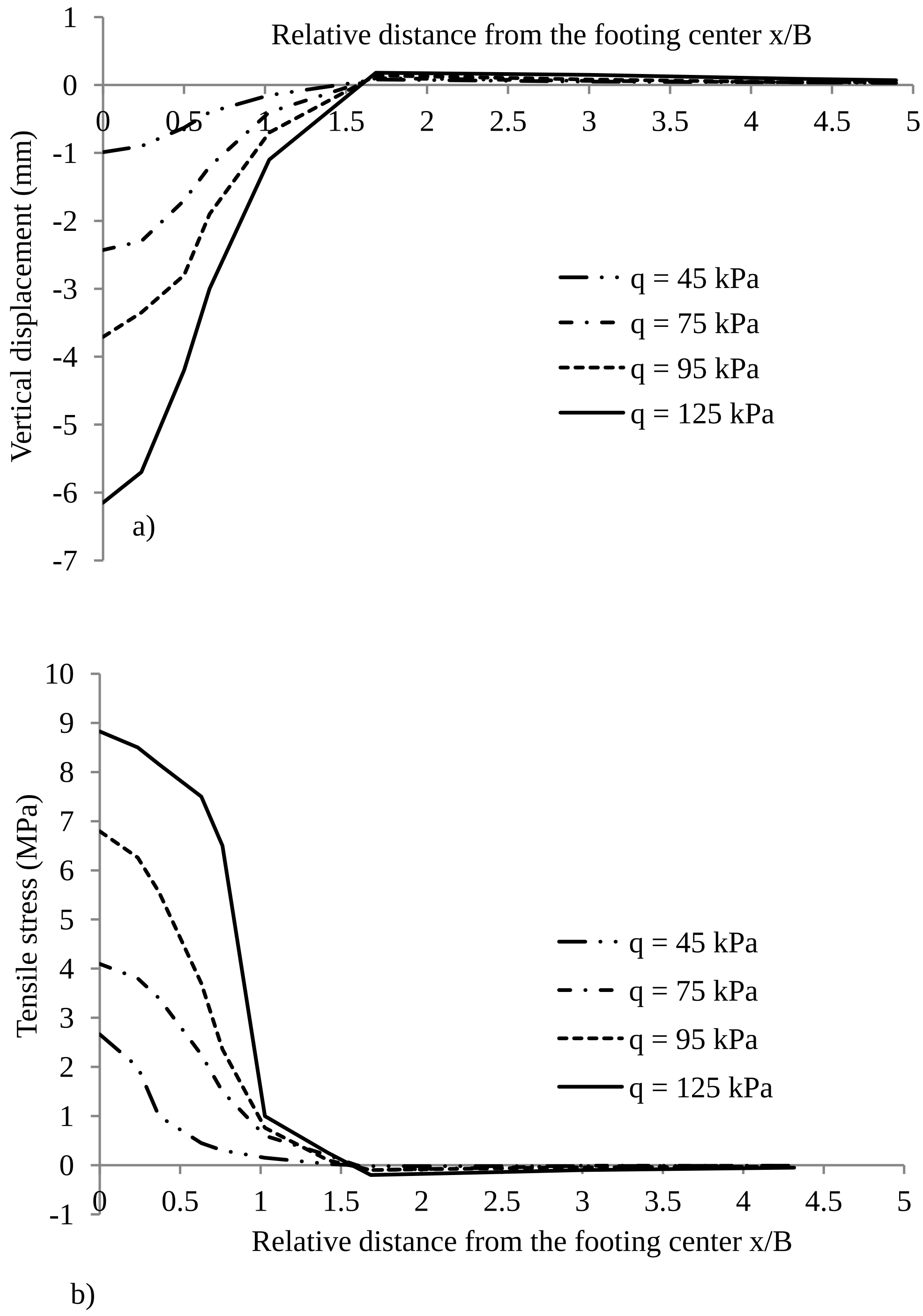

Figure 5-8 a) Vertical displacements of the geogrid (N = 1)

b) Tensile stresses of the geogrid (N = 1)

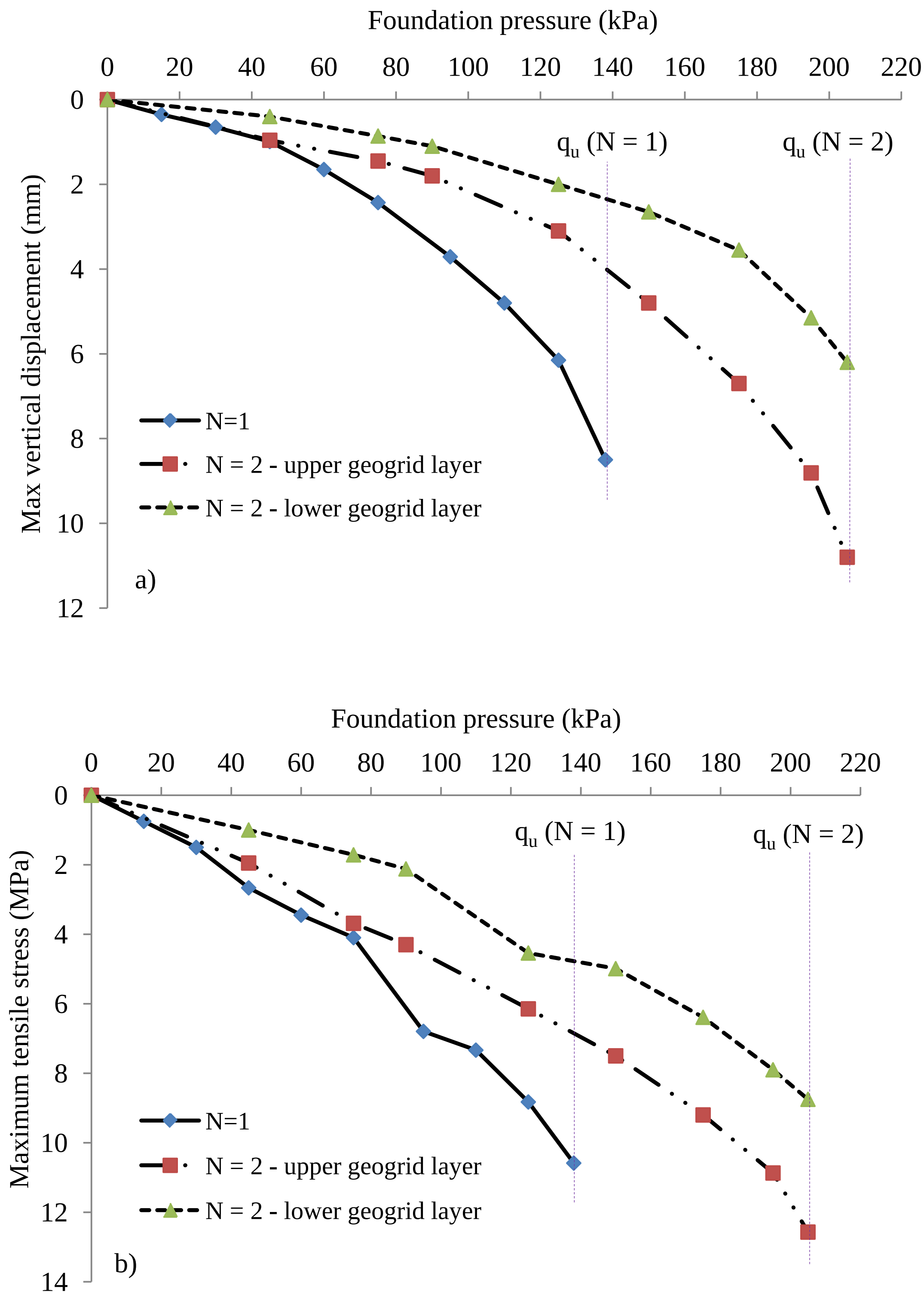

Figure 5-9 a) Maximum vertical displacements of geogrids

b) Maximum tensile stresses of geogrids

5.4.3. Response of the Reinforced Soil

The displacement field of the unreinforced soil domain at ultimate bearing capacity is shown in Figure 5-10. It can be seen that a general shear failure mode occurred and extended to a depth of D = 1.2B. Negligible soil displacements were observed outside a region that extends laterally 3.0B from the foundation center line. The displacement fields of the reinforced foundation for N = 1 prior to and at failure are shown in Figure 5-11a and 5-11b, respectively. It can be seen that prior to failure (Figure 5-11a), the horizontal displacement below the geogrid layer was small compared to the vertical displacement component. At peak loading (Figure 5-11b), a punching shear failure occurred above the geogrid followed by a general shear failure below the geogrid. With the shear band development under the footing, the displacement field at peak loading was limited to the failure zone dominated by the horizontal and upward displacements. This failure mode was reported by Meyerhof and Hanna (1978) and Wayne et al. (1998) for a strong soil layer overlaying a weaker soil. Similar observations were reported by Schlosser et al. (1983), Huang and Tatsuoka (1990) and Huang and Menq (1997) for the "deep footing" mechanism: the frictional and interlocking forces due to the interaction between the soil and geogrids result in an increase in the soil compressive strength, and thus an increase in the bearing capacity of the reinforced foundation. Similar soil deformation patterns were also reported by Michalowski and Shi (2003) using a digital motion detection technique.

The contact force network in the soil domain with and without geogrid reinforcement is shown in Figure 5-12. The contact force distributions represented the transmission of the applied load to the supporting soil. Each contact force was illustrated by a line connecting the centers of two contacting elements while the width of the line is proportional to the magnitude of the normal contact force. It can be seen that large contact forces developed immediately beneath the strip foundation as shown in Figure 5-12a, 5-12b and 5-12c for N = 0, 1 and 2, respectively. It can also be seen from Figure 5-12a that the contact force network of the unreinforced foundation developed diagonally from the foundation base.

With the presence of reinforced geogrid layers (Figure 5-12b and 5-12c), the contact forces became more vertical particularly above the geogrid layers. Below the geogrid layers, diagonal contact forces were observed which are similar to those observed beneath the unreinforced foundation. The contact force distributions in Figure 5-12 support the failure mode discussed above.

To calculate the macroscopic stress components within the soil domain, averaging windows with dimensions S_x x S_y x S_z = 0.05 m x 0.3 m x 0.025 m were used. The average stresses within a box are given by:

$$\sigma_{ij} = \frac{1}{V}\sum_{c=1}^{N_c} x^{c,i} f^{c,j} \tag{5-2}$$

where, N_c is the number of contacts within the box of volume V, $f^{c,j}$ is the contact force vector at contact *c*, $x^{c,i}$ is the branch vector connecting two contact particles A and B, and indices *i* and *j* indicate the Cartesian coordinates.

The distribution of vertical stresses with depth beneath the center of the footing is shown in Figure 5-13. In consistency with the large vertical contact forces above the geogrids (Figure 5-12), an increase in the vertical stress in the zone can be seen. The increase in the number of geogrid layers also resulted in the increase in the vertical stress. However, there was no significant change in the vertical stress beyond a depth of 1.2B below the geogrids. The vertical stress distribution is in good agreement with the displacement fields (Figure 5-11) and contact force networks (Figure 5-12).

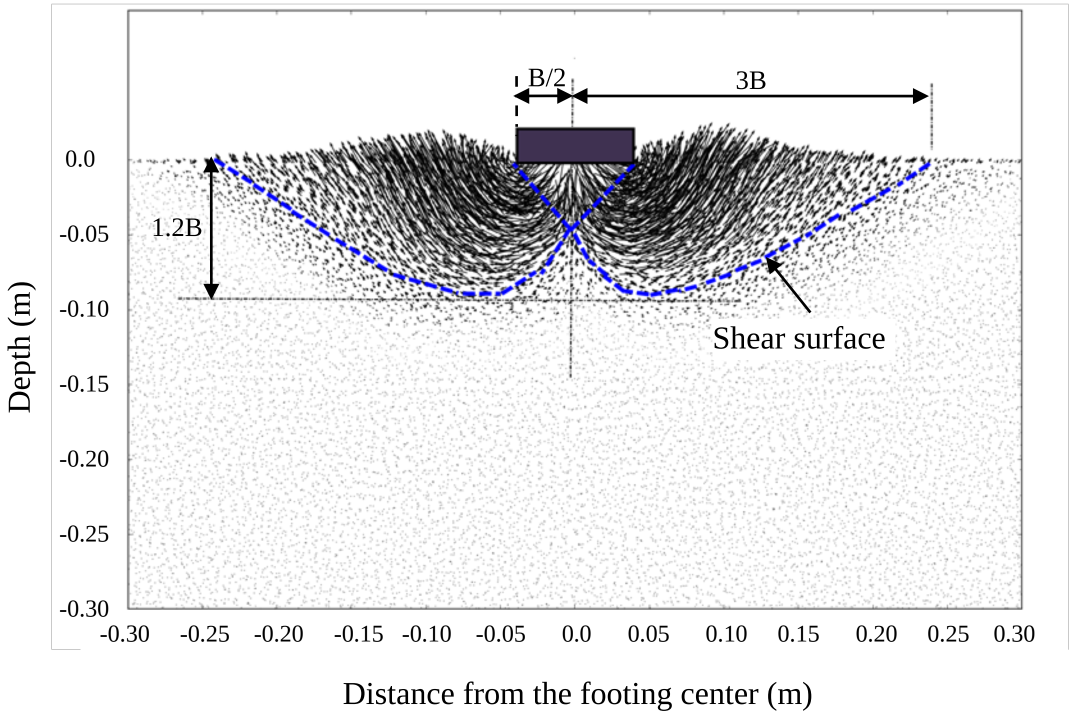

Figure 5-10 Soil displacement field of the unreinforced foundation

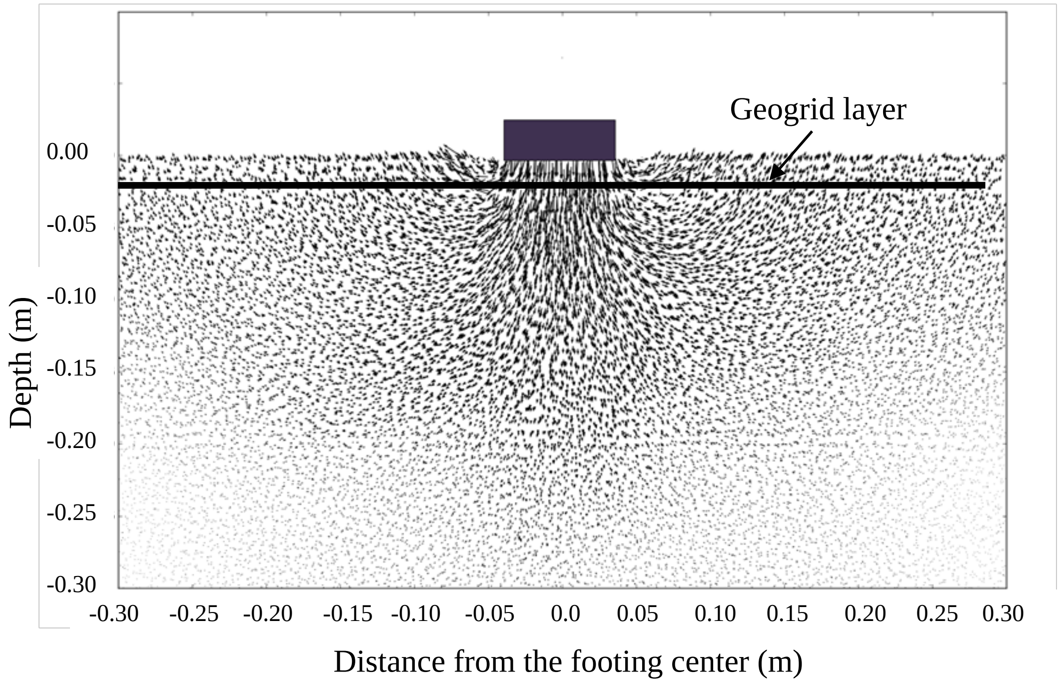

a) Before failure - N = 1

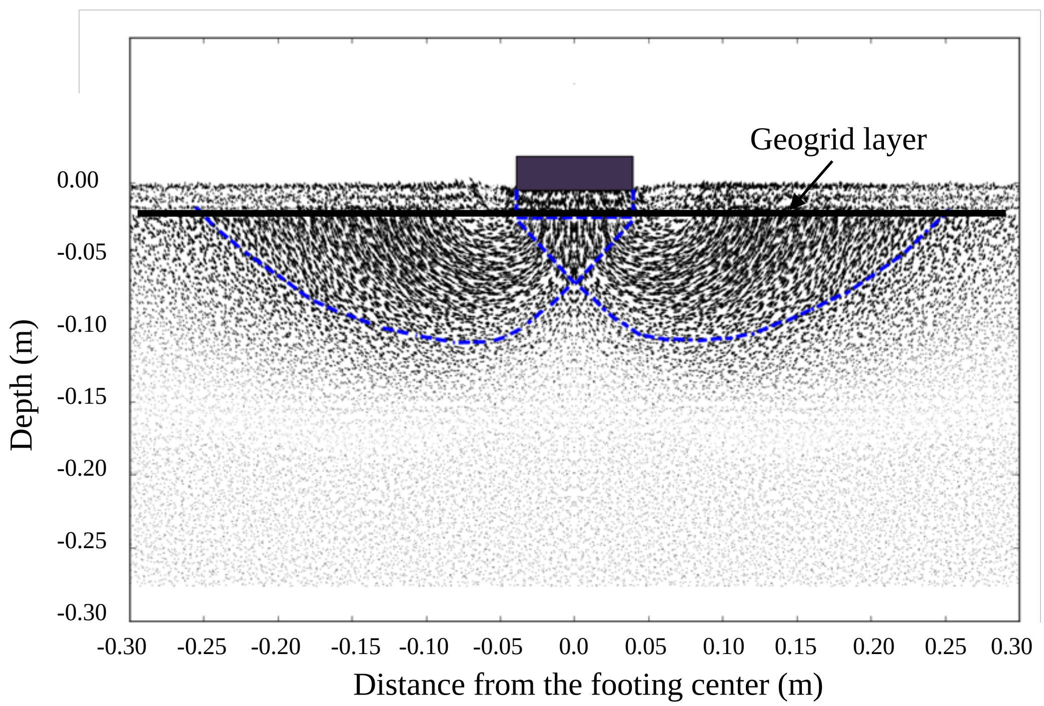

b) At failure - N = 1

Figure 5-11 Soil displacement field of the reinforced foundation (N = 1)

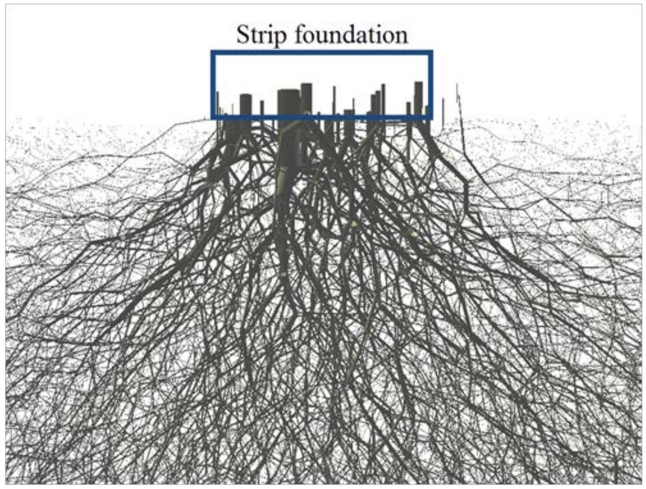

a) Unreinforced foundation

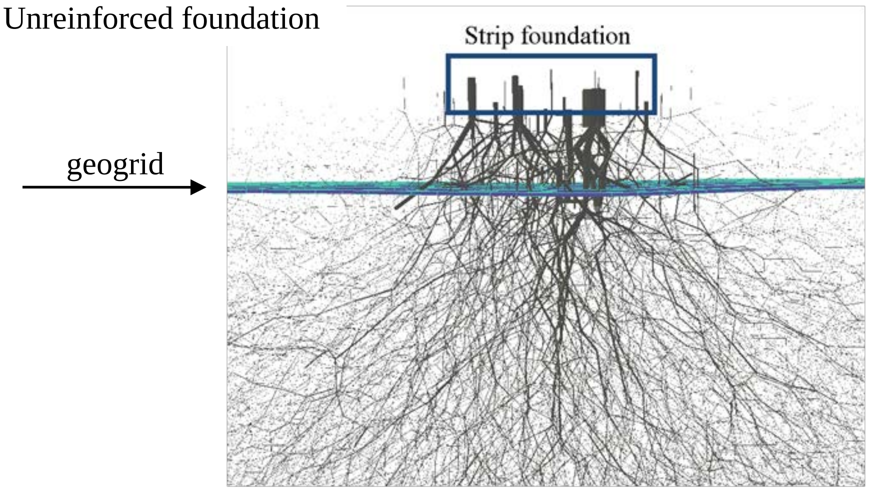

b) Reinforced foundation - N = 1

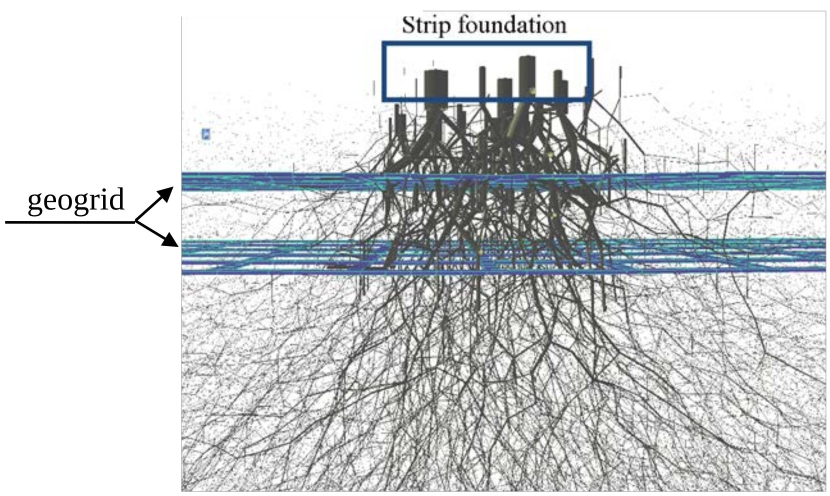

c) Reinforced foundation - N = 2

Figure 5- 12 Contact force networks within the soil

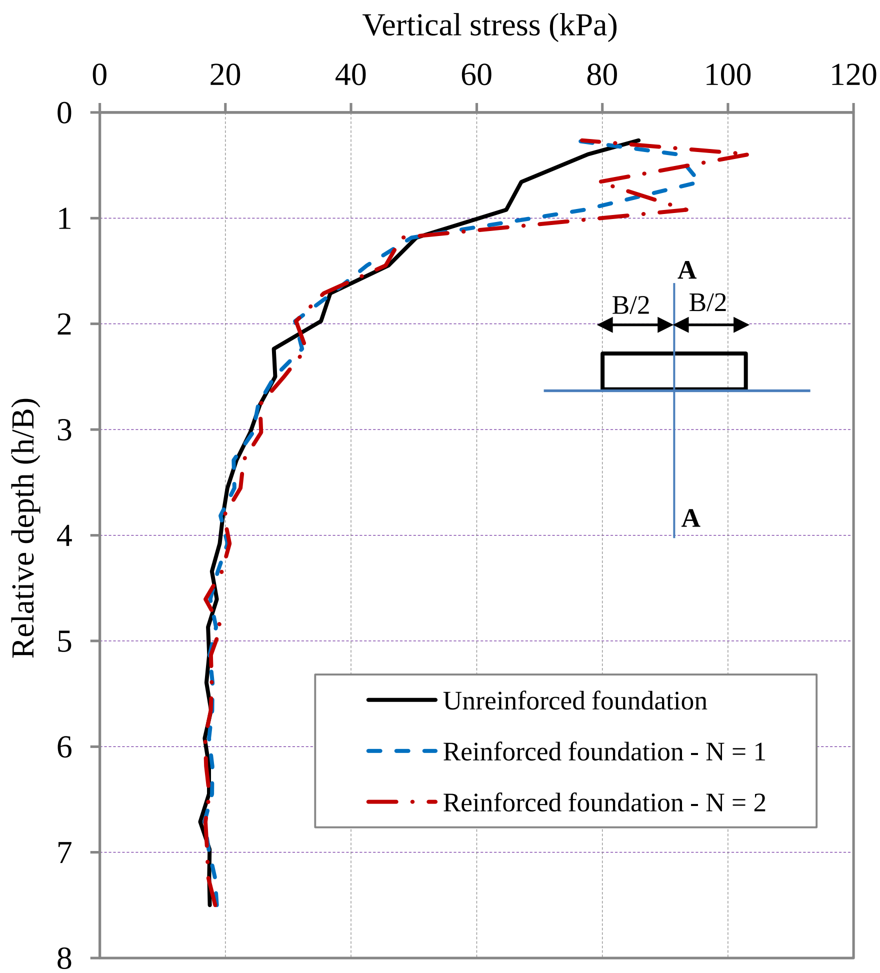

Figure 5-13 Vertical stress distributions beneath the strip foundation

(cross section A-A)

5.5. Summary and Conclusions

This study investigated soil-geogrid interaction using a coupled FE-DE framework. The soil was modeled using DE while the geogrid was modeled using FE. The interaction between the DE and FE domains was ensured by using interface elements. The developed framework was used to investigate the behavior of strip foundation over geogrid reinforced sand. The soil-geogrid interlocking effect was demonstrated. The 3D geometry of the geogrid, its deformation and stress distribution were represented. The microscopic behavior of the soil domain relative to soil displacements, contact orientations, contact forces were also analyzed.

The numerical modeling of the geogrid reinforced strip foundation provided a very good agreement with the experimental results. Increasing the number of geogrid layers resulted in an increase of the ultimate bearing capacity. Geogrid deformations and tensile stresses for N = 1 were larger than those for N = 2. When two layers of geogrid were used, the upper layer was subjected to larger deformations and tensile stresses than the lower layer. At the ultimate load, a punching shear failure occurred above the geogrid followed by a general shear failure below the geogrid. The use of geogrid reinforcement also resulted in an increase in the vertical stresses in the soil.

The proposed coupled FE-DE method has proven to be effective in capturing soil-geogrid interaction and analyzing the behavior of both geogrid and surrounding material.

Preface to Chapter 6

The efficiency of the coupled Finite-Discrete element framework in analyzing soil-structure interaction problems has been demonstrated in the previous chapters: geogrid pullout test (Chapter 4) and geogrid reinforced strip foundation (Chapter 5). A different soil reinforcement problem, which is geogrid-reinforced fill over void, is analyzed in this chapter as an example of a condition where soil below the reinforced layers experiences large vertical deformation. The microscopic behavior of the fill overlying void with and without geogrid reinforcement is investigated. The efficiency of the developed coupled program in such challenging condition is therefore demonstrated.

CHAPTER 6

Three-Dimensional Analysis of Geogrid Reinforced Fill over Void Using Finite-Discrete Element Framework *

Abstract

Three-dimensional analysis of soil-structure interaction problems considering the detailed response at the particle scale level is a challenging numerical modeling problem. An efficient numerical framework that takes advantage of both the finite and discrete element approaches to investigate soil-geogrid interaction is described in this paper. The method uses finite elements to model the structural components and discrete particles to model the surrounding soil to reflect the discontinuous nature of the granular material. The coupled framework is used to investigate the behavior of geogrid-reinforced fill over strong formation containing void. The numerical results provide a new insight into the nature of the three-dimensional interaction between the soil and the geogrid.

Keywords: geogrid reinforcement, finite-discrete element, fill system over void, numerical simulation.

---

* A version of this chapter has been submitted to *International Journal of Geomechanics ASCE*, 2013.

6.1. Introduction

Fill structures such as embankments and highways are often constructed on natural ground. Although site investigation is usually performed before the design process, it is possible that existing voids are not detected or cavities may develop during the service life of the fill. Cavities are common in coral and karstic formations or in rock with soft inclusions (Agaiby and Jones, 1995). These voids can collapse and cause severe damage to structures in their vicinity. This problem was first studied by Terzaghi (1936). A trap door at the base of a soil-filled container was lowered causing the soil to move into the generated void. The trap door problem was also modeled numerically by Koutsabeloulis and Grifiths (1989) using the FEM. One method to protect the surface structure over voids is using reinforcement beneath the foundation of the structure. Reinforcement that bridges over voids reduces settlements and protects the structures from failure. Kinney and Connor (1987) conducted field tests to investigate the performance of road embankments over voids. Results suggested that geosynthetics can be beneficial when a fill is placed over voids. The ability of geogrid reinforced pavements to provide an early warning system of a void beneath a road was reported by Bridle et al. (1994). The efficiency of reinforcement in road applications was also reported by Villard et. al (2000). Analytical solutions for reinforced systems over voids have been reported by Giroud et al. (1990), Poorooshasb (1991), Agaiby and Jones (1995), Wang et al. (1996), Villard et al. (2000) and Briançon and Villard (2008). FE modeling of the reinforced systems has been reported by Gabr et al. (1992), Gabr and Hunter (1994), Lawson et al. (1994), Agaiby and Jones (1995) and Gaetano (2010). In most cases, only 2D models were used and the 3D geometry of the geosynthetics was not represented. DE modeling of similar problems such as geogrid-reinforced embankments over piles (Han et al., 2011) did not consider the 3D geogrid geometry. However, Bridle et al. (1994) shown that interlocking mechanism generates a stiffened granular layer which prevents collapse into the void. A simplified 2D model of the geogrid geometry, may therefore, misrepresent the behavior of the reinforced earth structures. In this study, a fill on a geogrid layer overlying a void is simulated using the coupled FE-DE framework. The proposed framework is capable of representing the 3D geometry of the geogrid and the interlocking mechanism associated with the soil-geogrid interaction.

6.2. Model Generation

A granular fill layer reinforced with a geogrid layer overlying a void is analyzed in this section using the proposed coupled FE-DE framework. While cavities may not be always detected during geophysical investigation, the presence of these cavities can have a negative impact on overlying structures such as highway embankments. The numerical analysis aims at investigating the soil-geogrid interaction mechanism and the behavior of the geogrid and supported soil with the presence of small subsurface voids. In this study, a fill layer with a thickness 0.6m constructed over a natural soil formation experiencing the development of a sudden cavity (width 0.2m and height 0.3m) is simulated (Figure 6-1). It is assumed that the void develops in a rigid formation layer and is infinitely long in the out-of-plane direction. Previous studies (Giroud et al., 1990; Poorooshasb,1991; Agaiby and Jones, 1995; Wang et al., 1996, Villard et al., 2000; Briançon and Villard, 2008) generally assumed the geosynthetics layers are installed right above the rigid surface. This assumption simplifies the analysis however it does not always represent the case when a natural soil formation overlies bedrock in which voids develop. In this study, both cases have been studied using the coupled FE-DE method. The geogrid is simulated using FE while the fill (and the underlying soil) is simulated using DE whereas the rigid formation is modeled as non-deformable FE domain. The placement of the geogrid directly on the rigid formation was found to cause numerical instability in the model unless additional restraints are applied to the geogrid. These restraints affect the soil-geogrid frictional resistance and interlocking effect as they prevent the geogrid from deforming laterally. To ensure proper interaction between the geogrid and soil, the geogrid is installed over a thin soil layer of thickness 0.1m overlying the non-deformable foundation as shown in Figure 6-1. The geogrid is assumed to be installed on the natural soil surface prior to the construction of the fill. A surcharge of $5kN/m^2$ is applied on top of the fill to simulate surface loading. This surcharge is modeled using a DE layer of thickness 0.05m placed on top of the fill with high density particles. The cavity is assumed to develop after the fill has been constructed.

6.3. Numerical Simulation

The soil properties used in the previous reinforced foundation problem in Chapter 5 are used for the fill material (Table 6-1). The properties of the natural soil and the fill are assumed to be the same for the purpose of simplification. The geogrid type (Tensar SS-0) from the previous reinforced foundation experiment (Chapter 5) is also used for the reinforcement. Parametric studies show that a void width of 0.2m results in negligible deformations of the soil and geogrid outside a region 0.45 m from the void center line. Therefore, an assemblage of particles with a length 1.1m is appropriate to represent the soil domain. The numerical geogrid has a length of 1.1 m and a width of 0.3m which represents the placement of the reinforcement over the soil layer (Figure 6-2).

The assembly is generated using the multi-layer packing process mentioned previously. The rigid formation is first modeled using non-deformable FE elements without voids. The natural soil layer of thickness 0.1m is then generated followed by the generation of the geogrid layer. The fill is then generated in layers until the target thickness of 0.6 m is achieved. A surcharge of $5kN/m^2$ is applied on top of the fill by generating a 0.05 m thick layer of high density particles. The final assemblage consists of over 280,000 DE particles and 2800 FE elements. After material properties have been assigned to all FE and DE elements, the geogrid is allowed to freely deform. The initial condition of the soil assemblage is achieved when the convergence conditions are satisfied (all internal and external forces are balanced). The FE elements in the void location are then removed to numerically simulate the development of the void.

Table 6-1 Input parameters for the simulation

Type of elements	Parameter	Value
Discrete particles	Density (kg/m^3)	2650
	Material modulus E (MPa)	38
	Ratio K_T/K_N	0.25
	Coefficient of friction ($\tan\varphi$)	0.68
	β_r	0.01
	η_r	1.0
	Damping coefficient	0.2
Finite elements	Young modulus E (MPa)	1.4E+3
	Poisson's ratio ν	0.3
Interface elements	Material modulus E (MPa)	38
	Ratio K_T/K_N	0.25
	Coefficient of friction ($\tan\varphi$)	0.42

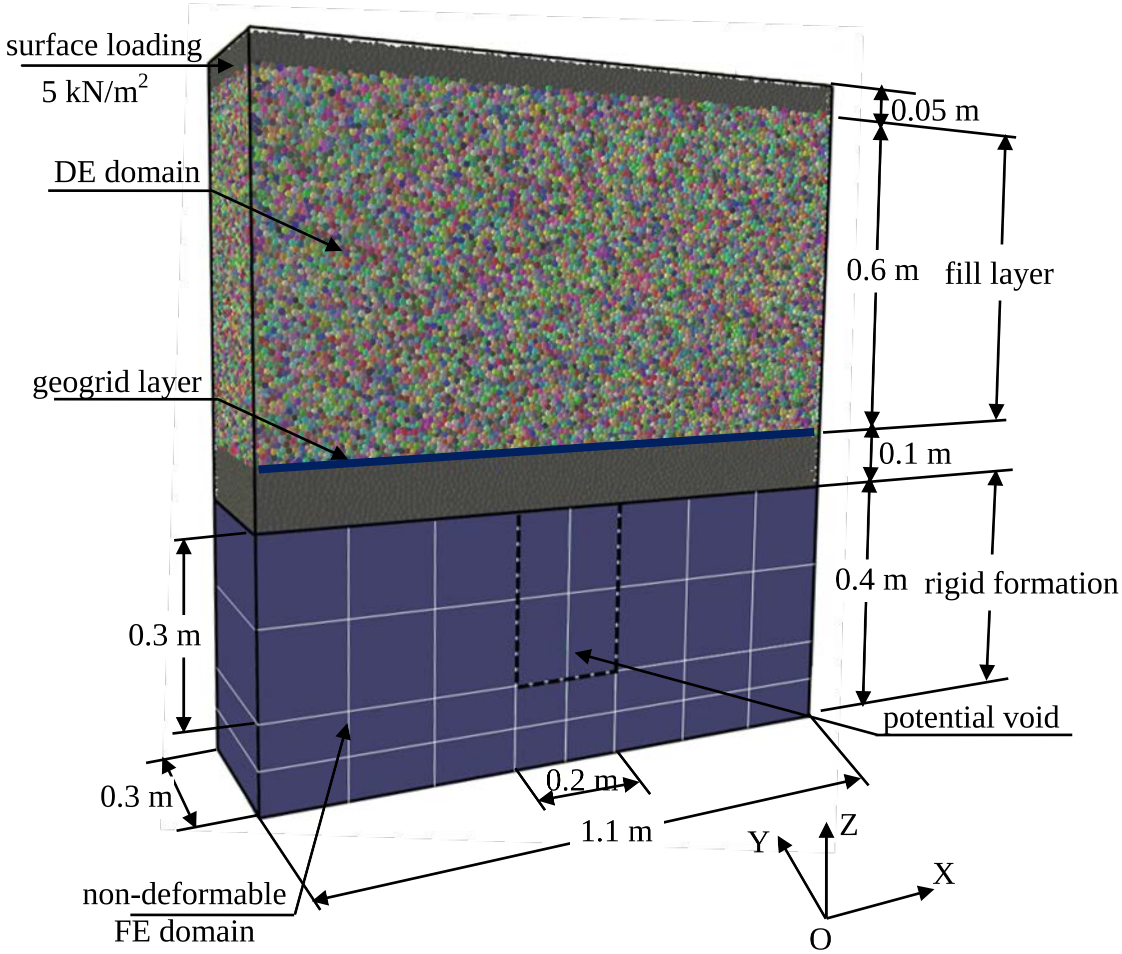

Figure 6-1 Initial geometry of the geogrid reinforced fill above void

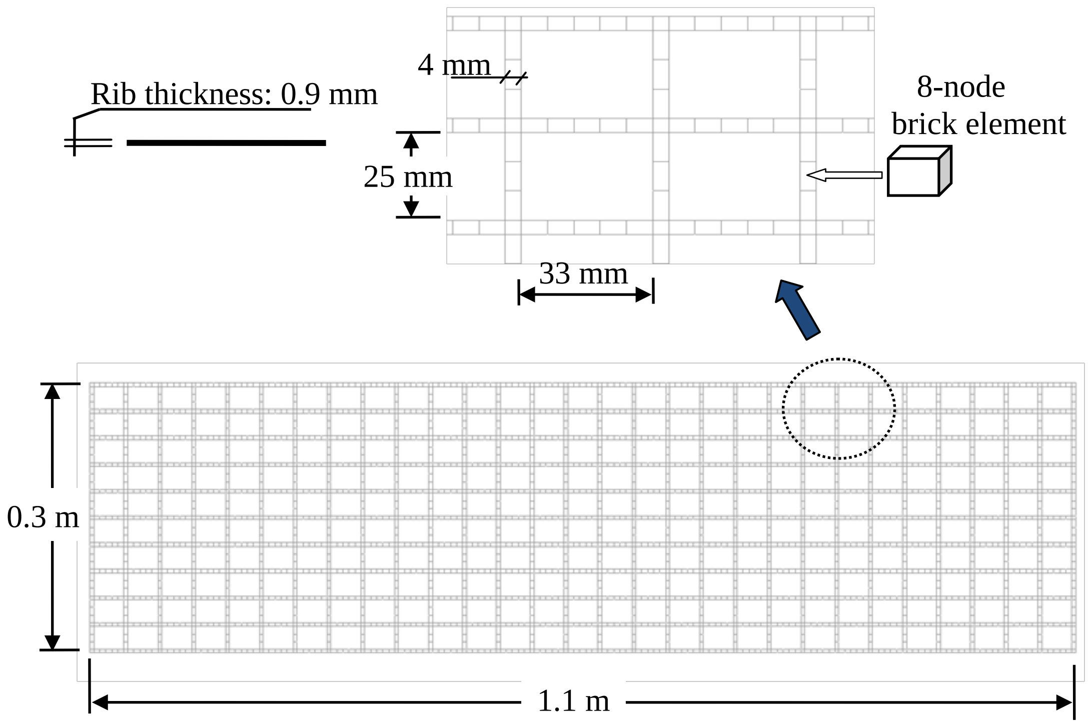

Figure 6-2 Plan view of the geogrid

6.4. Results and Discussions

6.4.1. Response of the Geogrid

The deformed shape of the geogrid is shown in Figure 6-3. The largest deformations and tensile stresses were observed in a region above the void. Due to the soil movement toward the void, the geogrid deformed and tensile stress in the geogrid developed to balance the loads acting on the geogrid sheet. Distributions of the vertical displacements and tensile stresses along the geogrid are shown in Figure 6-4. It can be seen that the vertical displacements and tensile stresses were small near the two geogrid ends and largest at the geogrid center. The interlocking and frictional contact forces contribute to the anchoring mechanism. To examine the importance of the interlocking effect, a parametric study has been performed by reducing the friction coefficient between the soil and geogrid. It was found that when the interface friction coefficient is reduced to zero, the geogrid anchoring is still ensured with a small increase in the geogrid vertical displacement. This demonstrates the dominant role of the interlocking effect in the geogrid anchoring mechanism. A similar observation on the importance of the geogrid interlocking effect was reported by Bridle et al. (1994). The feasibility of the coupled FE-DE framework to model the interlocking effect is therefore verified.

6.4.2. Response of the Reinforced Soil

The displacement fields of the fill layer without and with geogrid reinforcement are shown in Figure 6-5. In the case of unreinforced fill (Figure 6-5a), downward soil movement developed above the void location. However, soil collapse at the fill surface did not occur and the fill stability was achieved due to soil arching over the void. Figure 6-5b shows the displacement field of the geogrid reinforced fill. It can be seen that soil displacements above the geogrid layer were much smaller compared to the unreinforced fill and the geogrid efficiently prevented the soil from moving toward the void. This demonstrates the efficiency of the interlocking effect in generating a stiffened granular layer above the geogrid (Bridle et al., 1994).

The contact orientations in the unreinforced fill are shown in Figure 6-6. It can be seen that with the development of the soil arching within the fill, more contacts were seen in the x direction than in the z direction (xz plane view). This strong anisotropy induced by the soil arching which demonstrated a stronger contact orientation in the horizontal direction than in the vertical direction. The distribution of contacts in the yz plane was elliptical, with the z component being slightly larger than the y component. Meanwhile, quite uniform distribution of the contact orientation was observed in the xy plane. With the placement of a geogrid layer above the void, the distribution of contact orientations in the xz plane of the reinforced fill (Figure 6-7) showed less arching with only a slightly larger value in the horizontal direction compared to the vertical direction. Uniform contact distributions in the yz and xy planes were also observed. The geogrid reinforcement prevents the rearrangement of contact forces compared to the unreinforced fill with the creation of a void.

The soil deformation in the fill layer can also be evaluated by analyzing the change in porosity in the soil domain. Using the DE analysis, the change of porosity is obtained by comparing the change in the volume of DE particles within a given volume of dimensions S_x x S_y x S_z = 0.1 m x 0.3 m x 0.1m. The changes in porosity without and with the geogrid reinforcement are shown in Figure 6-8a and 6-8b, respectively. In both cases, there was an increase in porosity corresponding to the volumetric dilation in the fill. Maximum dilations occurred above the void location. Up to 10% of porosity changes were observed in the unreinforced fill while much smaller changes (less than 1.1%) were observed in the geogrid reinforced fill. The volumetric dilation in the fill was also reported by Costa et al. (2009) and Han et al. (2011).

Soil arching development results in the stress redistribution within the soil mass. Average stresses in the fill were calculated with boxes with dimensions S_x x S_y x

S_z = 0.05 m x 0.3 m x 0.05 m. The vertical and horizontal stress components of the unreinforced fill are shown in Figure 6-9. The corresponding stress distributions in the geogrid reinforced fill are shown in Figure 6-10. A reduction of both the vertical and horizontal stresses above the void location was observed in both cases. The vertical stresses increased in the regions adjacent to the void while the horizontal stresses were largest at the top of the soil layer due to the soil arching.

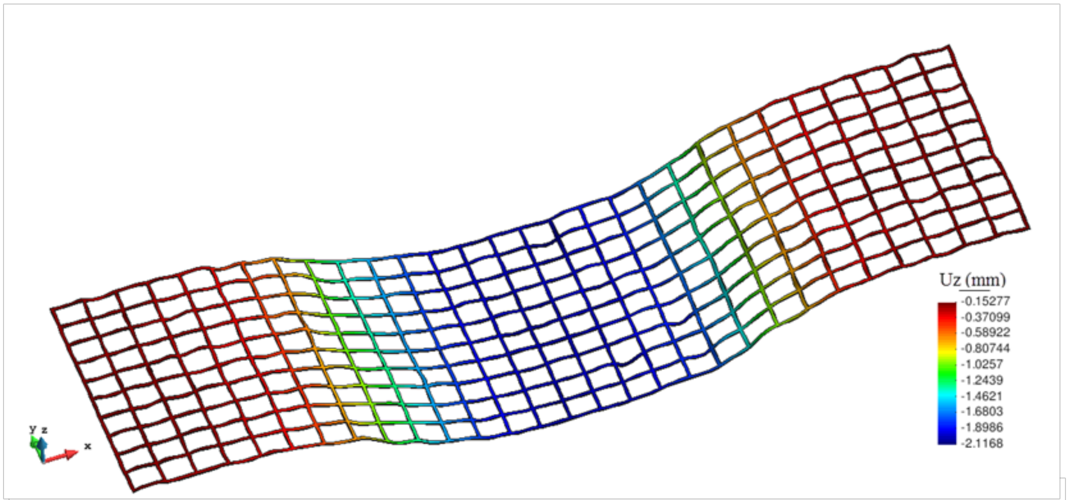

a) Vertical displacement

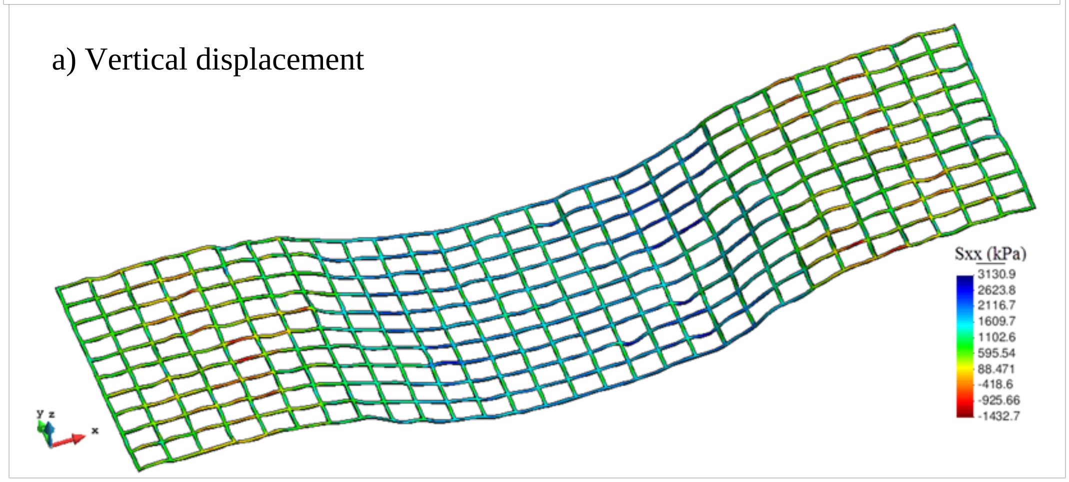

b) Tensile stress

Figure 6-3 Vertical displacement and tensile stress of the geogrid

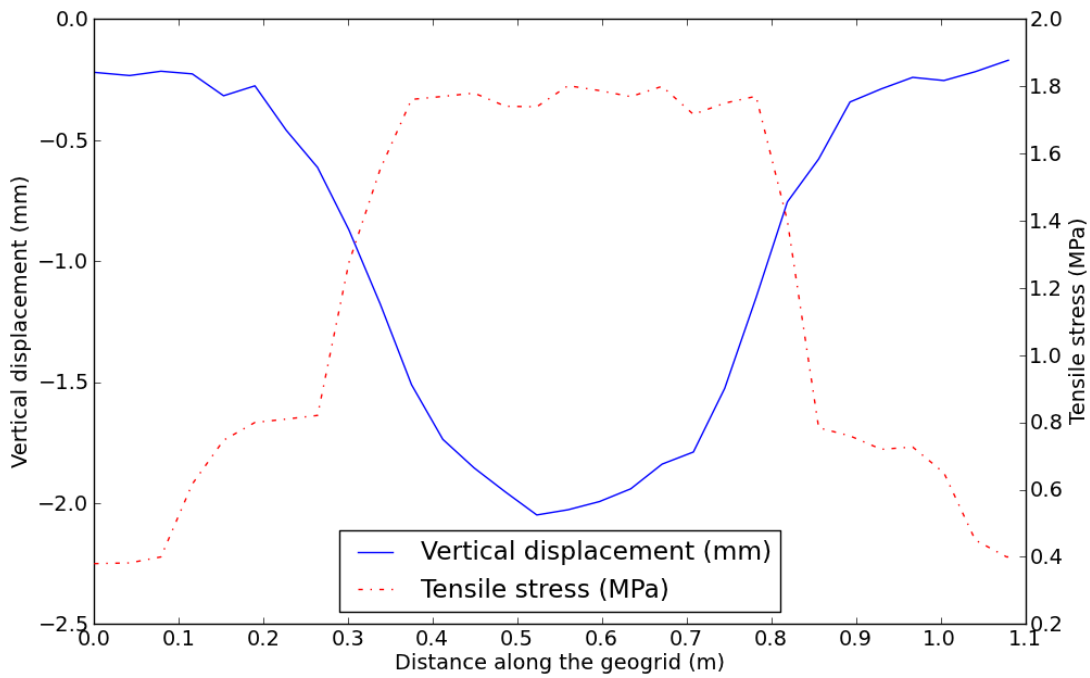

Figure 6-4 Distributions of vertical displacement and tensile stress along the geogrid

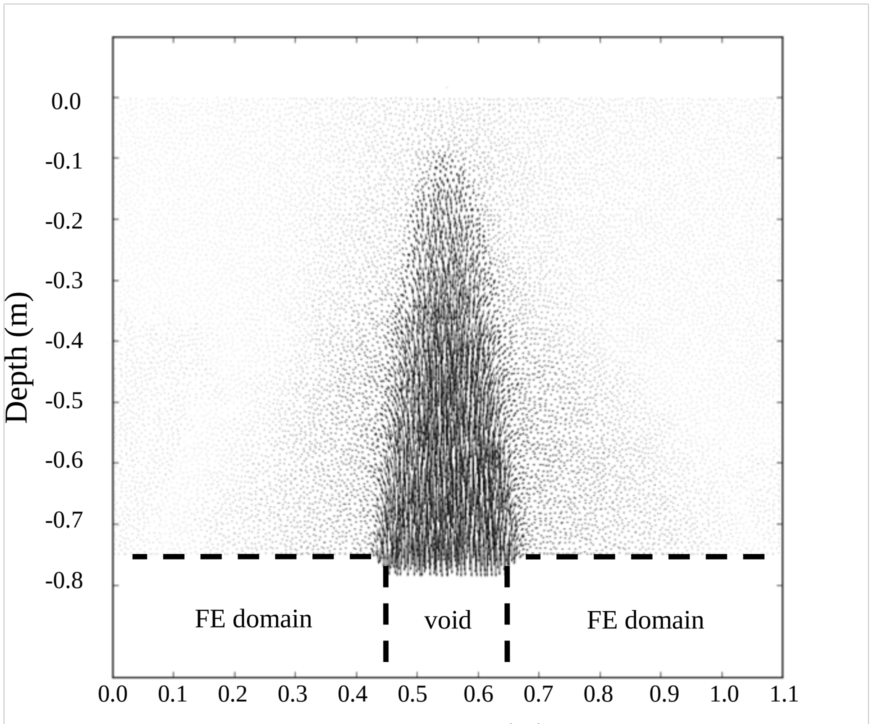

a) Unreinforced fill

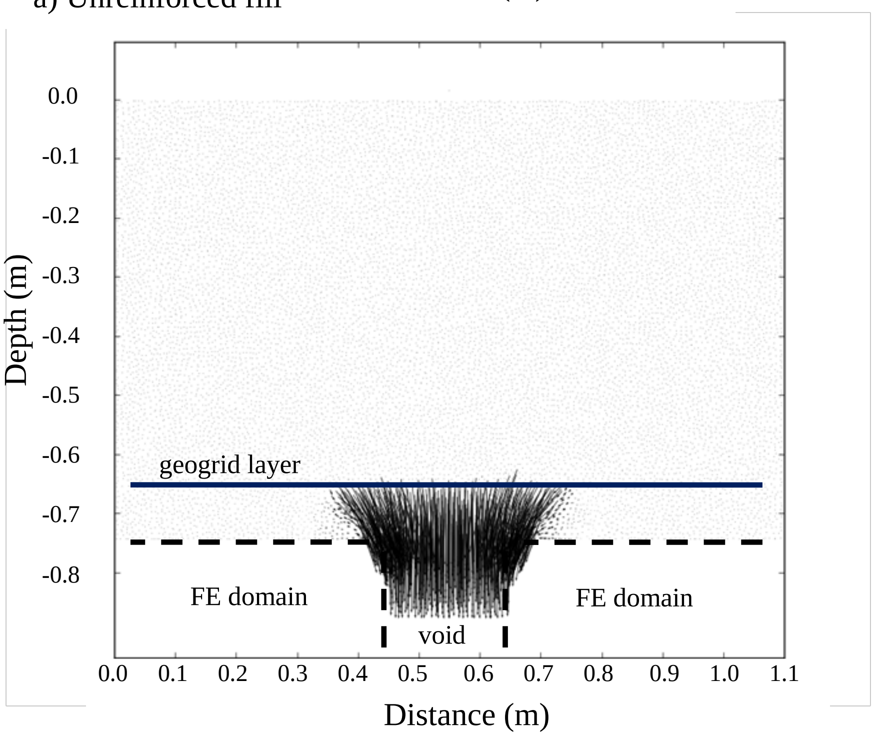

b) Reinforced fill

Figure 6-5 Soil displacement fields

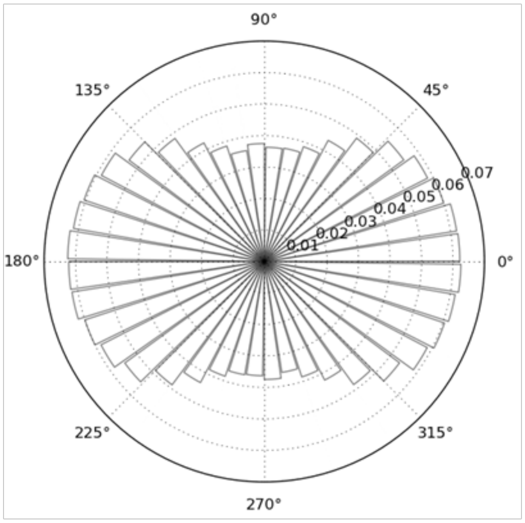

xz plane

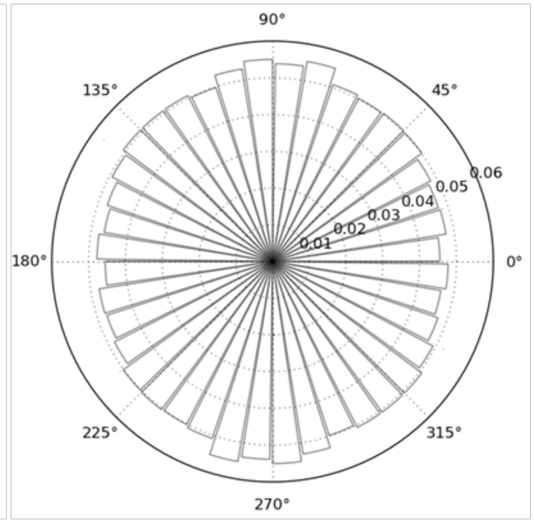

yz plane

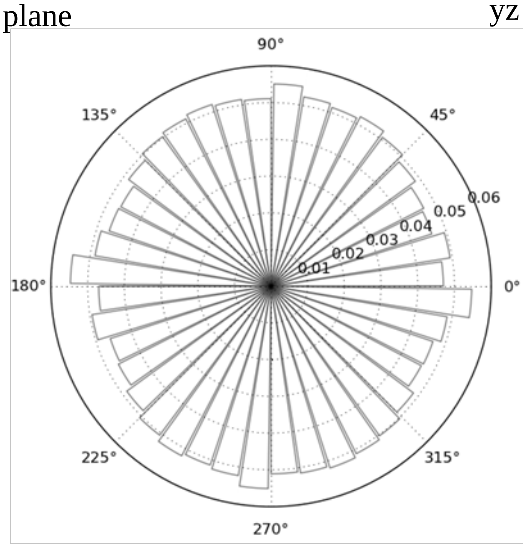

xy plane

Figure 6-6 Distributions of the contact orientation–unreinforced fill

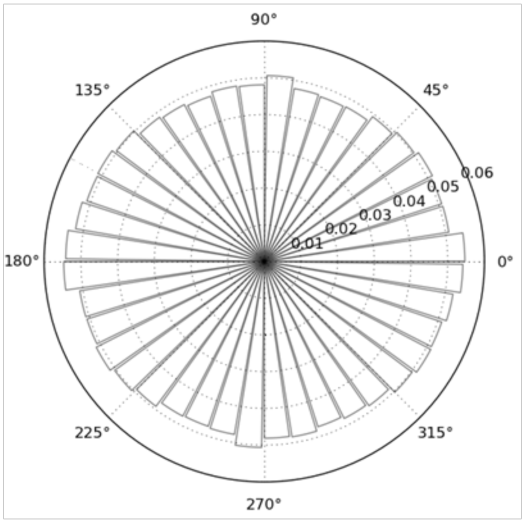

xz plane

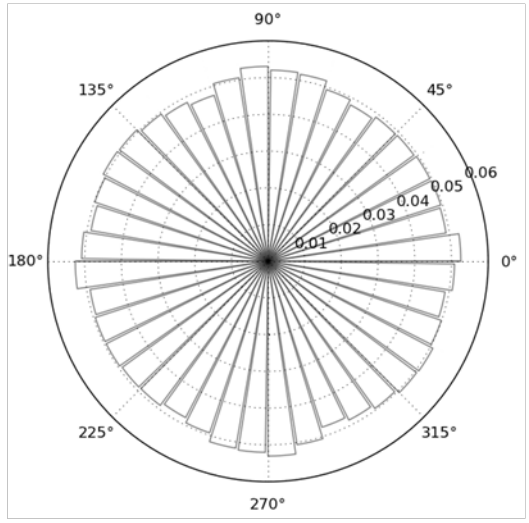

yz plane

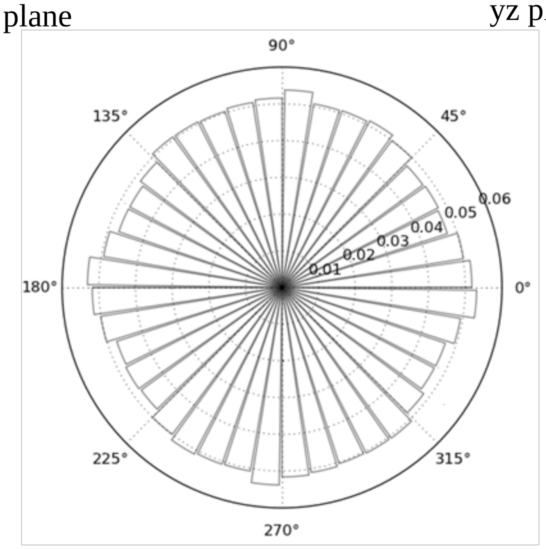

xy plane

Figure 6-7 Distributions of the contact orientation–reinforced fill

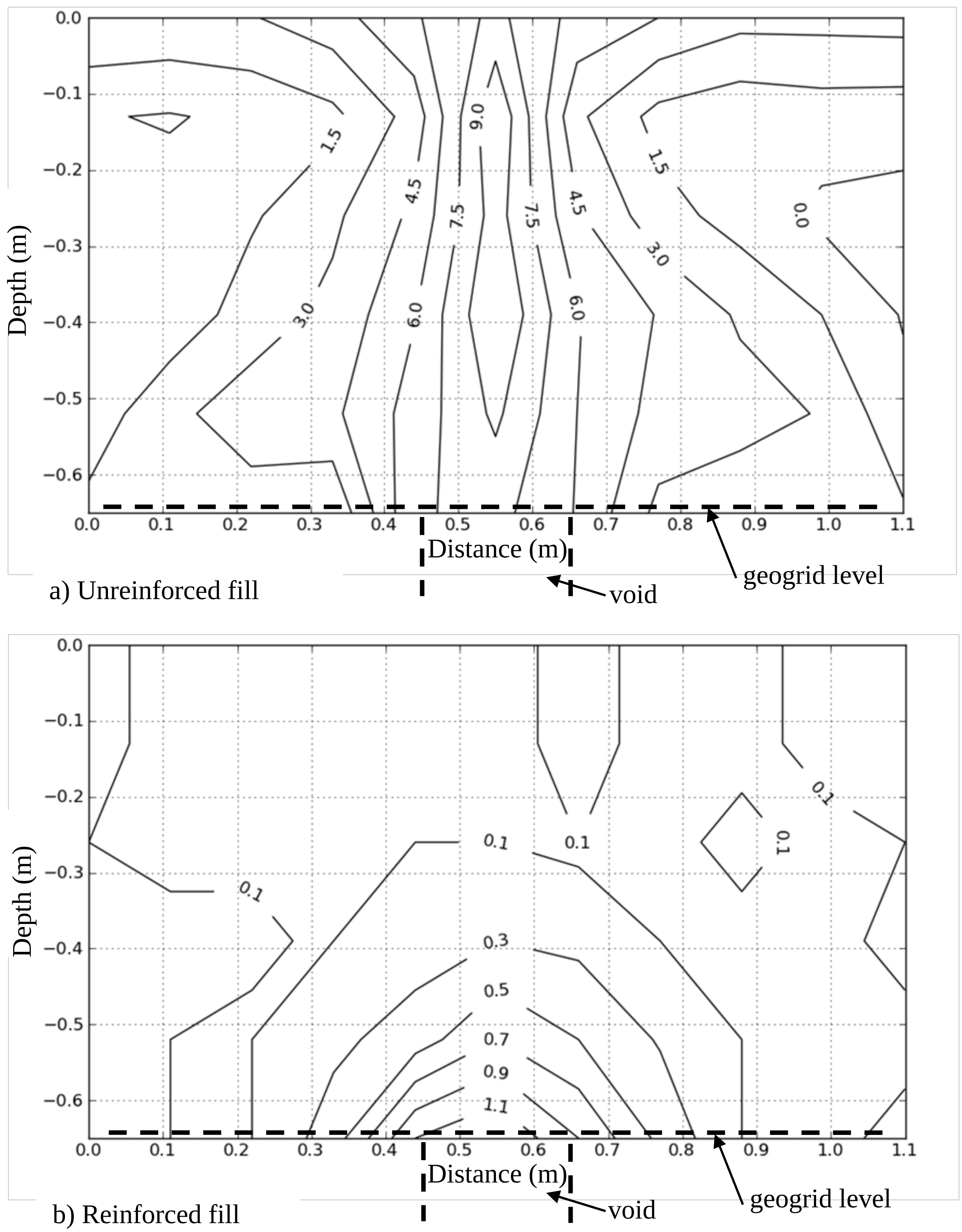

Figure 6-8 Percentage porosity changes in the unreinforced and reinforced fills

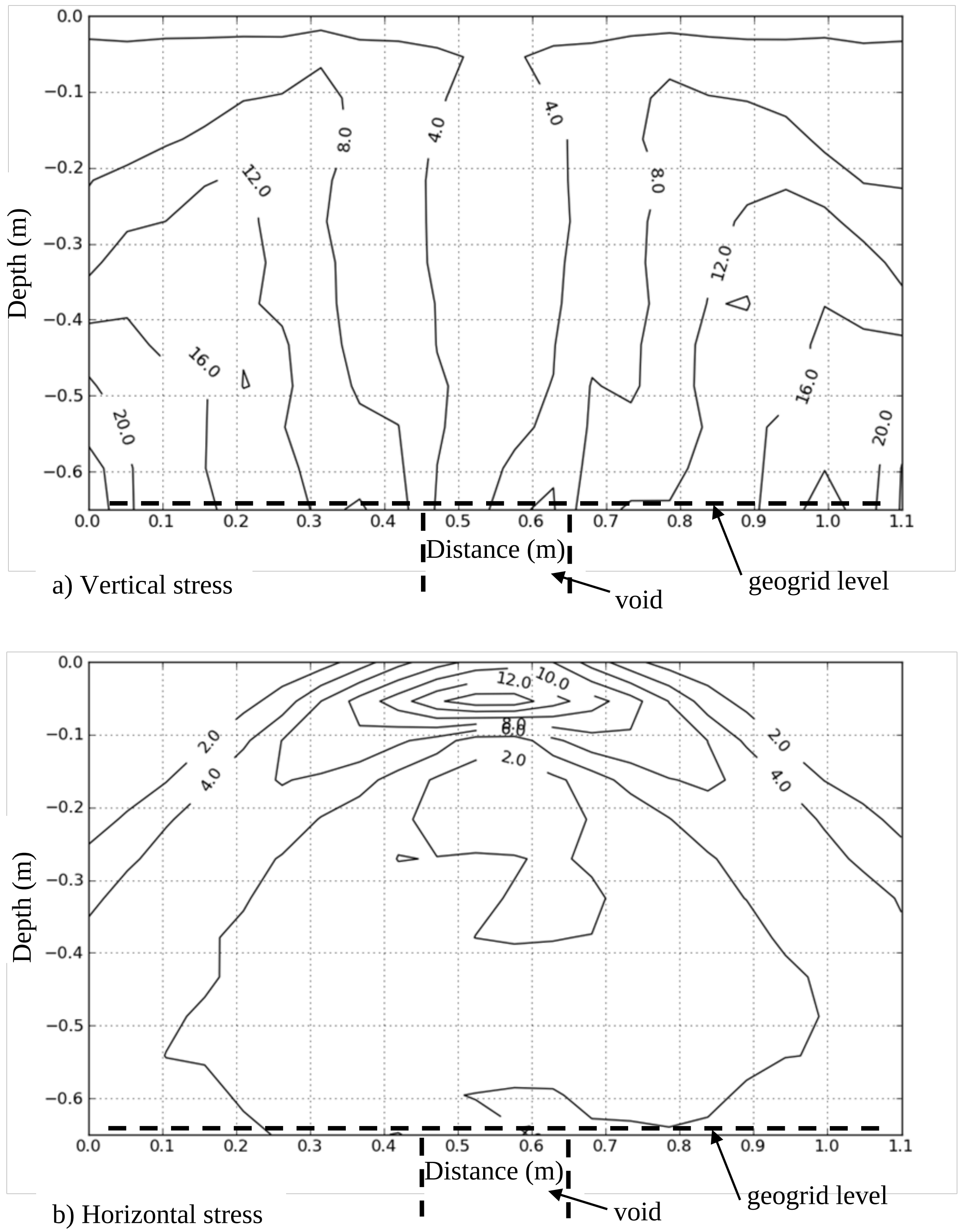

Figure 6-9 Stress distributions in the unreinforced fill

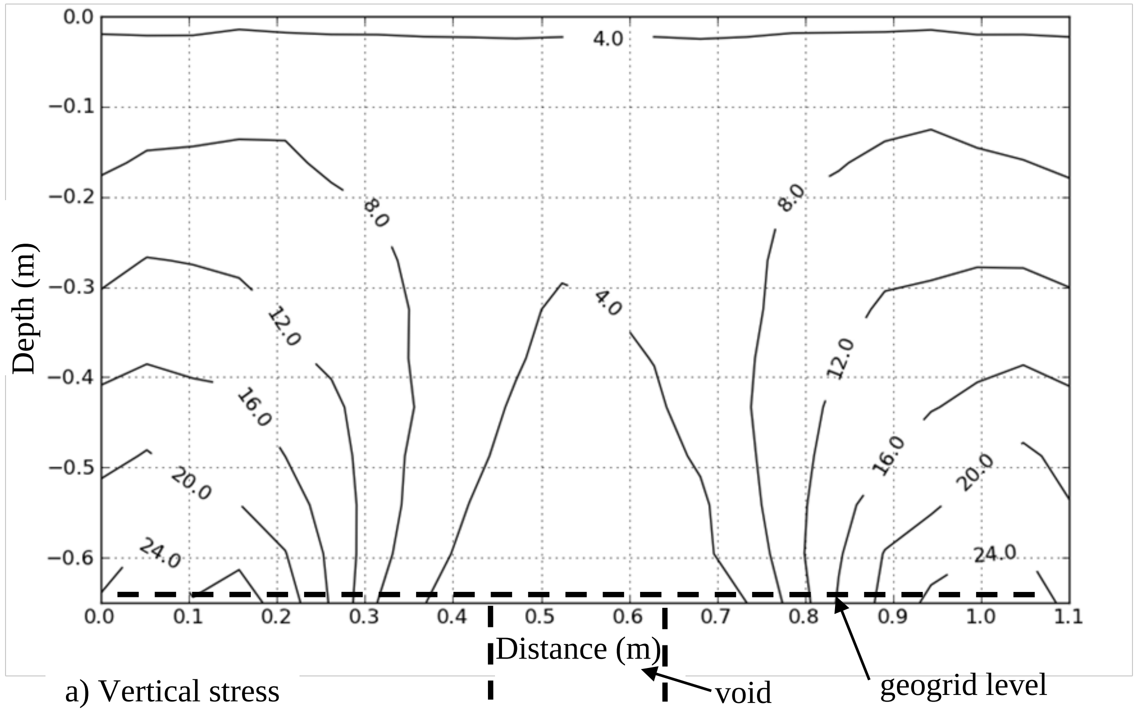

a) Vertical stress

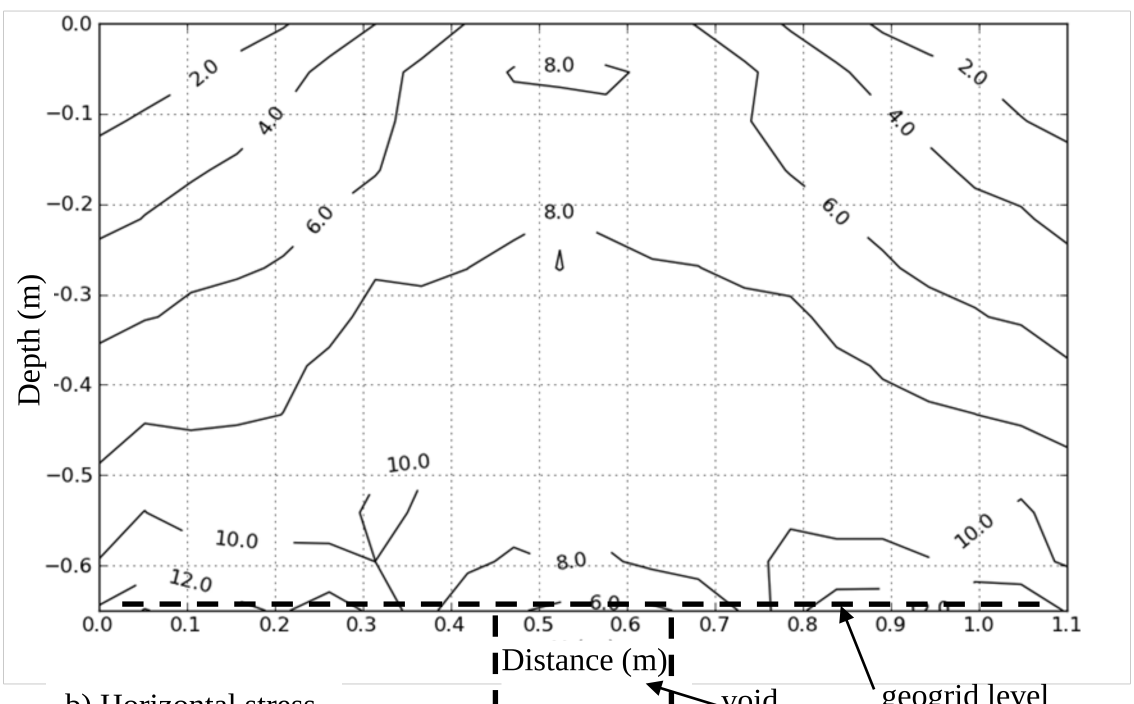

b) Horizontal stress

Figure 6-10 Stress distributions in the reinforced fill

6.5. Summary and Conclusions

This study investigated the 3D soil-geogrid interaction using the developed FE-DE framework. The soil was modeled using DE while the geogrid was modeled using FE. The interaction between the DE and FE domains was ensured by using interface elements. The developed framework was used to investigate behavior of geogrid reinforced fill over void. The 3D geometry of the geogrid, its deformation and stress distribution were represented. The microscopic behavior of the soil domain relative to soil displacements, contact orientations, stresses and porosity changes were analyzed.

The use of geogrid to reinforce a fill over a void is effective in preventing soil from moving toward the void. The stability of the fill was therefore improved. The change in porosity in the geogrid reinforced fill was much smaller than for the unreinforced case. The formation of soil arching produced a stress redistribution in the fill. A reduction of vertical and horizontal stresses above the void location was observed. Vertical stresses increased in the vicinity of the void while the largest horizontal stresses were obtained at top of the fill layer.

The proposed coupled FE-DE method has proven to be effective in capturing soil-geogrid interaction and analyzing the behavior of both geogrid and surrounding material.

CHAPTER 7

Conclusions and Recommendations

7.1. Conclusions

In this thesis, the discrete element method has been used to analyze the earth pressure distribution acting on a cylindrical shaft. Numerical results were compared with experimental and analytical solutions. The efficiency of the discrete element method in analyzing geotechnical problems involving granular material and large deformation was demonstrated. Using the validated discrete element code, a coupled finite-discrete element framework has been developed to allow soil-structure interaction analysis to be performed. The developed coupled finite-discrete element method has been implemented and used to analyze selected soil-structure interaction problems including geogrid pullout test, strip footing over geogrid-reinforced sand and geogrid-reinforced fill over potential void. The numerical results of the coupled finite-discrete element simulations were first validated using experimental data. New insight into the nature of the three-dimensional interaction between the soil and the reinforcing layer was provided. The following conclusions can be drawn from the thesis:

1) In chapter 3, a discrete element analysis was performed to investigate the lateral earth pressure acting on a cylindrical shaft. A modified multi-layer gravitational packing method was proposed to replicate the real soil packing procedure. The packing algorithm is capable of representing the actual particle size distribution. Both the physical and numerical studies demonstrated that even a limited movement of the shaft wall can lead to a rapid decrease in the lateral earth pressure acting on the shaft wall. A movement equivalent to 2.5% to 4% of the shaft radius was required to reach the full active earth pressure on the wall. Analytical solutions

proposed by Terzaghi and Berezantzev provided good agreement with the observed and calculated pressure distributions. A decrease in radial stresses and an increase in circumferential stresses in the vicinity of the shaft due to the arching effect were observed. Results obtained in this phase of the analysis provided the needed confidence in the discrete element framework that has been further used in developing the coupled Finite-Discrete element framework.

2) In chapter 4, a coupled Finite-Discrete element framework was developed to simulate the soil-structure interaction. This algorithm allows for the coupling of the finite and discrete element methods. The interaction between the finite and discrete element domains is assured using interface elements. A multiple-time-step scheme was applied to optimize the computational cost. The developed algorithm was used to investigate the behavior of a biaxial geogrid embedded in granular material and subjected to pullout loading. The geogrid was modeled using finite elements while the backfill material was modeled using discrete elements. A good agreement between numerical results and experimental data was observed. For the investigated geogrid and soil conditions, largest displacements and stresses in the geogrid occurred near the front side of the box with rapid decrease with distance away from the geogrid. The contribution of the frictional component to the total pullout resistance was found to be larger than the bearing resistance. It was also found that the contribution of the bearing resistance to the overall capacity increased as the geogrid displacement increased. The soil movement and the contact force distribution within the soil domain agreed well with experimental observations.

3) In chapter 5, the developed coupled Finite-Discrete element framework was implemented to analyze a strip footing over geogrid-reinforced sand. Both unreinforced and geogrid reinforced foundations were studied from which the efficiency of geogrid reinforcement was investigated. Validation

of the developed method was performed by simulating a laboratory experiment and comparing the calculated and measured data. An increase in the ultimate bearing capacity of the footing was found to depend on the number of reinforcing layers. Geogrid deformation and tensile stress for the case of one geogrid layer were found to be larger than those calculated for the case of two geogrid layers. The upper geogrid layer experienced larger deformation and tensile stress compared to the lower layer. At the ultimate load, a punching shear failure occurred above the geogrid followed by a general shear failure below the geogrid. An increase in the vertical stresses in the soil was also observed with the use of geogrid reinforcement.

4) In chapter 6, the behavior of a geogrid-reinforced fill over strong formation containing void was studied using the developed Finite-Discrete element method. The efficiency of the geogrid in protecting the overlying fill layer was investigated. The three-dimensional interaction between the soil and the geogrid was also analyzed. The use of geogrid to reinforce a fill layer over a locally developed void is effective in preventing soil from excessive movement and improving the stability of the fill layer. The change in porosity in the geogrid reinforced fill was found to be much smaller compared to the unreinforced case. The developed soil arching resulted in stress redistribution in the fill with a reduction of vertical and horizontal stresses above the void location. Vertical stresses increased in the vicinity of the void while the largest horizontal stresses were observed at top of the fill layer.

5) The coupled finite-discrete element analysis has proven its efficiency in analyzing soil-structure interaction problems. The framework has been implemented in an open source code with computational engines written in C++ and scripts written in Python.

7.2. Recommendations for future work

Various soil-structure interaction problems can be studied using the developed coupled finite-discrete element framework including:

- Earth pressure distribution on flexible pipes buried in granular backfill material.
- Cyclic loading of geogrid-reinforced ballast.
- Pile driving in granular material.

Computational fluid dynamics (CFD) can be coupled with the finite-discrete element framework to investigate soil-structure interaction problems involving groundwater. Computational engines for CFD can be written and incorporated into the existing framework. The coupling can also be performed using an external CFD package as an add-on such as OpenFOAM and CCFD.

The computational parts of the coupled finite-discrete element framework are written in *C++* with object oriented approach. Scripts are built using *Python*, which assures rapid and flexible simulation construction. However, capability of the graphical interface is still limited. Additional effort to improve the graphical interface is therefore encouraged. Advanced constitutive models for the finite elements can also be added to the framework to allow for a wide range of structural elements to be modeled and enhance the capability of the analysis tool.

APPENDIX A

User Manual for the Developed 3D Coupled Finite-Discrete Element Analysis Tool

A.1. INTRODUCTION

This appendix presents a user manual for the developed 3D coupled Finite-Discrete element analysis. The developed framework is implemented in *YADE*, an open source code for DE analysis. Since both FE and DE simulations are handled in a common package, the tool provides an efficient approach for solving coupled FE-DE geotechnical problems.

The computational parts of the coupled FE-DE framework are written in *C++* with object oriented approach. Scripts are built using *Python*, which assures rapid and flexible simulation construction. Users who do not wish to modify *C++* engines can develop their own analyses using *Python* scripts. Commands written in *Python* are first presented in the User Manual. *C++* framework of the analysis tool is briefly presented in latter section. Many of the commands used in the DE module are also listed in the *YADE*'s documentation (https://yade-dem.org/doc/). Knowledge of *Linux* operating system, *C++* and *Python* programming languages is strongly recommended for further development of the coupled FE-DE tool.

A.2. INSTALLATION

The developed package can be installed in many *Linux* distributions. Installations in *Kubuntu* and *Ubuntu* have been verified. It is required to install some external libraries and packages prior to compiling the package. In *Kubuntu*, required libraries and packages can be installed using the following commands:

```
sudo apt-get install scons cmake libcgal-dev git freeglut3-dev libloki-dev \
libboost-date-time-dev libboost-filesystem-dev libboost-thread-dev \
libboost-program-options-dev libboost-regex-dev fakeroot dpkg-dev \
build-essential g++ libboost-iostreams-dev liblog4cxx10-dev \
python-dev libboost-python-dev ipython python-matplotlib \
libsqlite3-dev python-numpy python-tk gnuplot doxygen \
libgts-dev python-pygraphviz libvtk5-dev python-scientific bzr \
libeigen3-dev binutils-gold python-xlib python-qt4 pyqt4-dev-tools \
gtk2-engines-pixbuf python-argparse libqglviewer-qt4-dev python-imaging \
libjs-jquery python-sphinx python-git python-bibtex libxmu-dev \
libxi-dev libgmp3-dev libcgal-dev help2man libqt3-mt-dev qt3-dev-tools \
```

After all prerequisites have been installed, the coupled FE-DE codes can be compiled inside the downloaded directory of the source code:

```
scons PREFIX=/home/username/directory
```

For example, we can install the tool inside */home/Thomas/YADE* folder:

```
scons PREFIX=/home/Thomas/YADE
```

The directory of the installed package can be defined by editing the profile file *scons.profile-default* of the source code, for example:

```
PREFIX=/home/Thomas/YADE
```

YADE can now be compiled by simply typing:

```
scons
```

A.3. PYTHON SCRIPTS

A.3.1. Getting Started

The coupled FE-DE analysis tool is mainly controlled from the terminal. In the directory of the installed folder, at least two following executable files can be seen: *yade-unknown* and *yade-unknown-batch*. In a typical simulation, *yade-unknown* is used to start the analysis (Figure A-1). If some parameters are defined in a separate table, the simulation can be run in accordance with the parameter table using batch mode *yade-unknown-batch*.

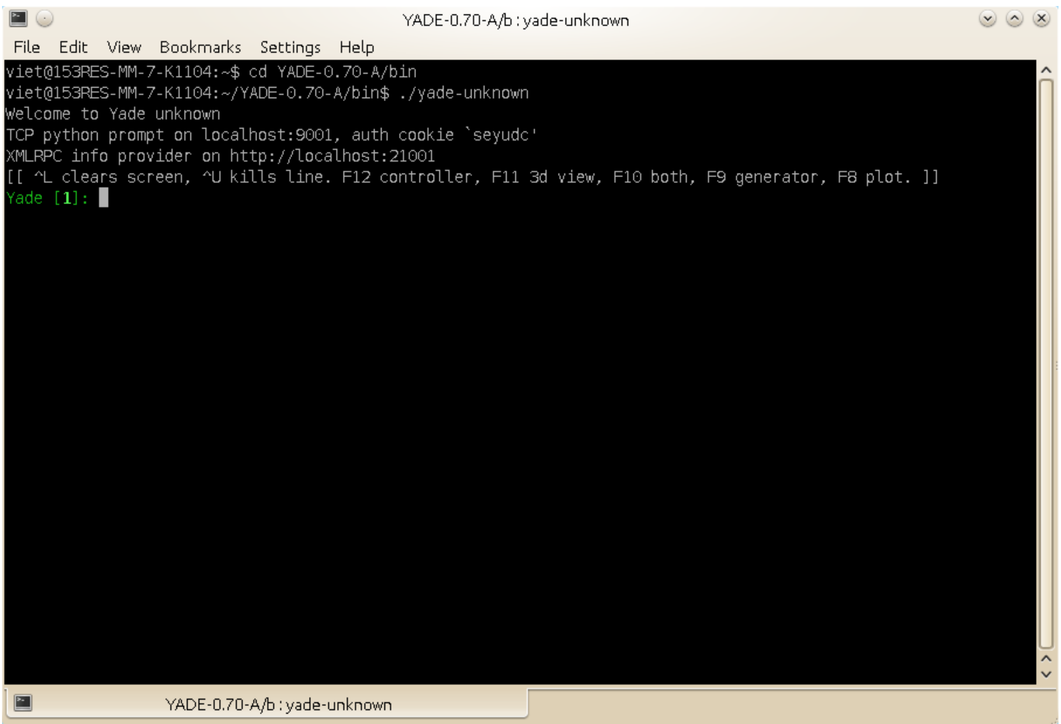

Figure A-1 Linux terminal to start YADE

To run a script *example.py* from the terminal:

./yade-unknown example.py

If users want to exit YADE immediately after running the script, *-x* is added:

./yade-unknown –x example.py

To exit a simulation:

exit()

or

Exit

To pause a running simulation:

O.pause()

To run a simulation:

O.run()

The current time-step can be achieved by:

O.dt

To obtain the current iteration:

O.iter

To turn on the *Controller*:

qt.Controller()

The *Controller* can also be activated by pressing *F12* (Figure A-2).

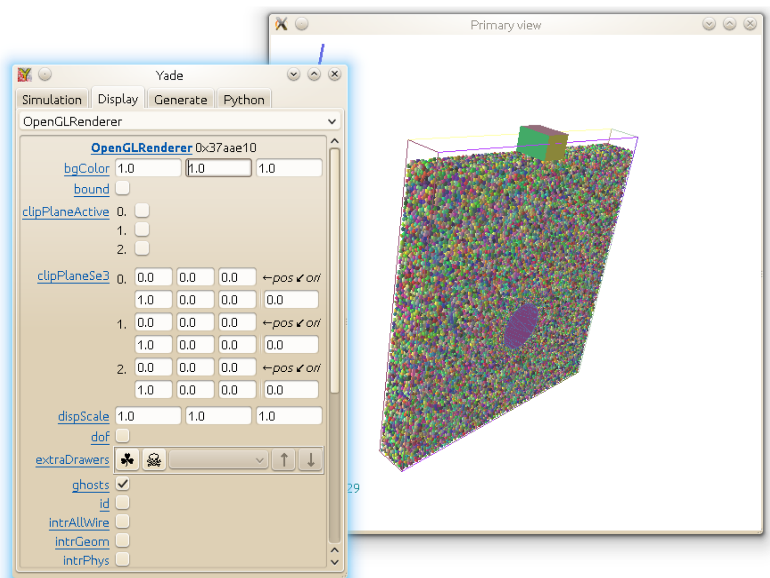

Figure A-2 Controller and graphical interface

A.3.2. Basic Commands

The number of bodies in a simulation is obtained using:

```
len(O.bodies)
```

Time-step for DE simulation can be determined using *utils.PWaveTimeStep()*:

```
O.dt = 0.5*utils.PWaveTimeStep()
```

where *0.5* is a user-determined safety coefficient.

The current position of a body can be achieved:

```
O.bodies[i].state.pos
```

where *O.bodies[i]* is i^{th} body stored in the simulation.

For example, positions of all bodies are printed to screen using the following commands:

```
# go through all bodies
for body in O.bodies:
    print body.state.pos
```

Similarly, the current velocity of a body can be determined:

```
O.bodies[i].state.vel
```

For example:

```
for body in O.bodies:
    print body.state.vel
```

To get information of the shape of a body:

```
O.bodies[i].shape
```

For example, radii of spherical particles with ids from 20 to 23 are printed:

```
for i in range (20, 24):
    print O.bodies[i].shape.radius
```

Material of a body is achieved by:

```
O.bodies[i].mat
```

For example:

```
for body in O.bodies:
    # check body's Id
    if body.id < 5:
        # print density
        print body.mat.density
```

To investigate forces acting on i^{th} element:

```
O.forces.f(i)
```

For example:

```
# go through all bodies
for i in range (0, len(O.bodies)):
    # print the first component of the force
    print O.forces.f(i)[1]
```

The interaction between two particles *i* and *j* can be checked using:

```
O.interactions[i,j]
```

For example:

```
# loop through all interactions
for I in O.interactions:
    # print ids of the two particles in contact
    print I.id1, I.id2
```

A.3.3. Sample Generation

The coupled FE-DE framework consists of several types of elements which can be categorized as:

- *DE elements*: spheres, clumps, walls, boxes and facets.

- *FE elements*: quadrilateral elements, brick elements and shell elements.
- *Interface element*: triangular and quadrilateral interface elements.

The generation of the above elements is described below:

A.3.3.1. Discrete element generation

Spherical particle generation

A spherical particle can be generated and added to a simulation:

```
# generate a sphere with center (1, 2, 4) and radius 1.5
s = utils.sphere(center = (1,2,4), radius = 1.5)
# add the generated particle to O.bodies
O.bodies.append(s)
```

A set of DE particles can be generated by loading input files:

```
load_DE_spheres (filename = "samplefile_nodes.txt")
```

- filename: text file from which centers and radii of spherical particles are imported. The format of the input file is:

  Particle ID1 center_X center_Y center_Z radius

  Particle ID2 center_X center_Y center_Z radius

  ...

A cloud of spherical particles for loose packing samples can be generated using *makeCloud()*, for example (Figure A-3):

```
# Generate a cloud of spheres within a box given by lower corner (0, 0, 0) and upper corner (1, 1, 1).
# Radii of particles follow uniform distribution between
# rMean*(1 - rRelFuzz) and rMean*(1 + rRelFuzz)
sp=yade._packSpheres.SpherePack()
sp.makeCloud(minCorner = Vector3(0, 0, 0), maxCorner = Vector3(1, 1, 1), rMean = 0.06, rRelFuzz = 0.2)
O.bodies.append([utils.sphere(s[0], s[1]) for s in sp])
```

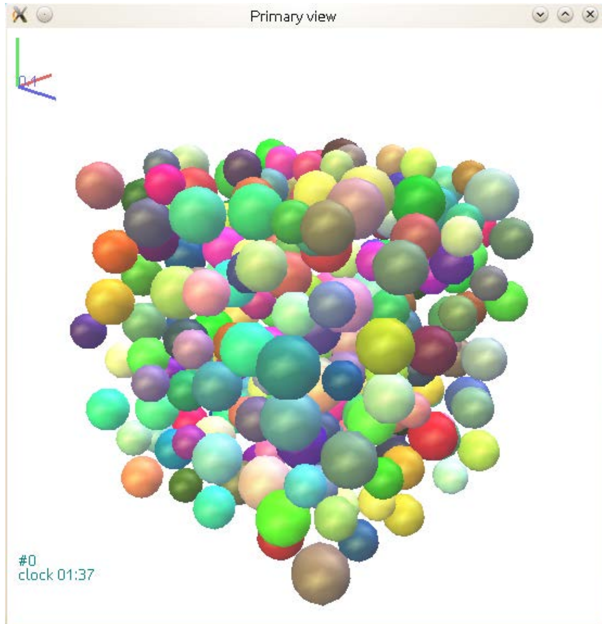

Figure A-3 A cloud of spherical particles generated using *makeCloud()*

Random dense packing can be achieved by using *pack.randomDensePack()*:

```
pred = pack.inAlignedBox((-3, -3, -3), (3, 3, 3))
O.bodies.append(pack.randomDensePack(pred,radius=0.05,rRelFuzz=.2))
```

Dense packing samples can also be generated using a radius expansion method:

```
sp.radiusExpansion(minCorner = Vector3(0, 0, 0), maxCorner = Vector3(1, 1, 1), rMean = 0.006, rRelFuzz = 0.2, maxMultiplier = 1.05)
O.bodies.append([utils.sphere(s[0],s[1]) for s in sp])
```

Medium packing samples can be generated using a multi-layer gravitational packing approach (Tran et al., 2012, 2013):

```
sp.multiLayerPacking(minCorner = Vector3(0, 0, 0), maxCorner = Vector3(1, 1, 1),rMean = 0.006, rRelFuzz = 0.2, targetPorosity = 0.39)
O.bodies.append([utils.sphere(s[0],s[1]) for s in sp])
```

A DE sample can be generated considering the particle size distribution, for example:

```
sieve = []
# add a sieve with particle size 0.0075 and % (in mass) of finer particles: 0%
sieve.append((0.0075,0))
sieve.append((0.01,85))
sieve.append((0.025,97))
sieve.append((0.03,100))
sp. makeCloud (minCorner = Vector3(0, 0, 0), maxCorner = Vector3(1, 1, 1),sieveMass = sieve, targetPorosity = 0.39)
O.bodies.append([utils.sphere(s[0],s[1]) for s in sp])
```

Clump generation

Rigid aggregate of individual particles can be generated using *appendClumped()*, for example (Figure A-4):

```
s1 = utils.sphere(center = (0, 1, 0), radius = 0.5)
s2 = utils.sphere(center = (0, 1.6, 0), radius = 0.6)
#Tie two spheres together and add the generated clump to O.bodies
O.bodies. appendClumped ([s1, s2])
```

Wall generation

A rigid wall can be generated using *utils.box()* such as:

```
O.bodies.append(utils.box(center=[-1, 0, 1],extents=[1, 1, 0]))
```

- center: center point of the box.
- extents: half lengths of the box sides.

Box generation

In order to generate a box, a function *aabbWalls()* can be used, for example:

```
mn, mx=Vector3(0,0,0),Vector3(1,1,1)
walls=utils.aabbWalls([mn,mx],thickness=0.05)
O.bodies.append(walls)
```

Facet generation

Facets are generated using *utils.facet()* such as:

 # generate a facet with three corners (.2,.2,0), (.2,0,0) and (0,.2,0)

```
O.bodies.append(utils.facet([(.2,.2,0),(.2,0,0),(0,.2,0)]))
```

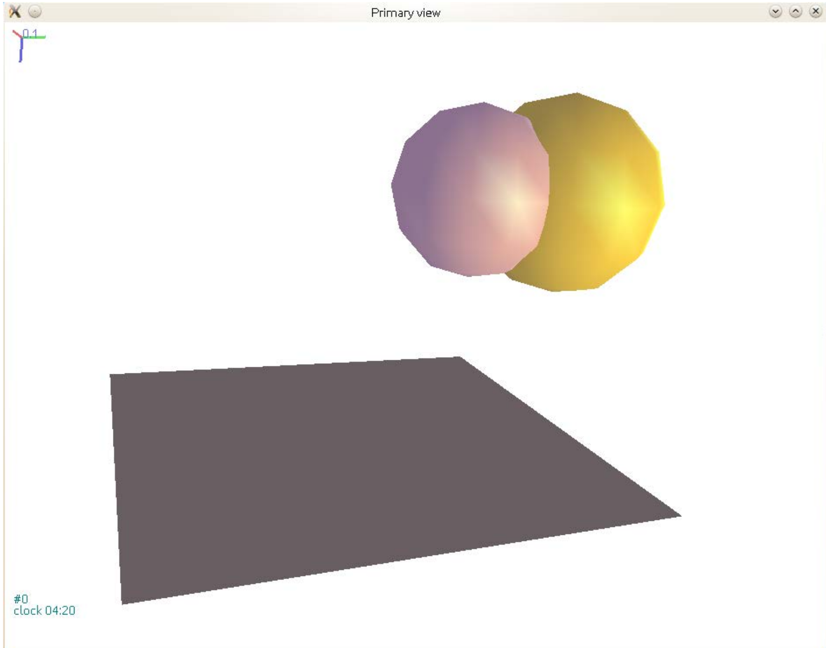

Figure A-4 Snapshot of a clump and a wall

A.3.3.2. Finite element generation

Finite elements in the coupled FE-DE framework are imported from input files. Input files consist of coordinates of FE nodes and node numbering of FE elements. These input files can be obtained from external packages. The functions built in YADE are compatible with output files exported from GID, a graphical user interface for finite element modeling.

FE nodes are imported using *load_FE_nodes()*:

```
load_FE_nodes (filename = "samplefile_nodes.txt", ndim = 3, radius = 0.0005)
```

- filename: text file from which coordinates of FE nodes are read. The format of the input file is:

  Node ID1 x1 y1 (z1)
  Node ID2 x2 y2 (z2)
  ...

- ndim: number of dimensions of the simulated problem.
- radius: radius of FE nodes, for illustration purpose only.

Solid FE elements are imported using *load_solid_elements()*:

load_solid_elements (filename = "samplefile_elements.txt", ndim = 3, elementType = "Hexahedron8N8I", matFlag = "elastic")

- filename: text file from which FE elements are imported. The format of the file is:

  Element ID1   Node ID1   Node ID2   Node ID3   ...
  Element ID2   Node ID1   Node ID2   Node ID3   ...
  ...

- ndim: number of dimensions of the simulated problem.
- elementType: type of FE elements. Different FE elements are available in the package including:

  "Quadrilateral": quadratic quadrilateral element with eight integration points.

  "Hexahedron8N1I": eight-node quadratic brick element with one integration point.

  "Hexahedron8N8I": eight-node quadratic brick element with eight integration points.

  "Hexahedron20N8I": twenty-node quadratic brick element with eight integration points.

- matFlag: flag indicating material of FE elements.
  "elastic": elastic material
  "mohrCoulomb": Mohr-Coulomb failure criterion

Shell elements are imported using *load_shell_elements()*:

load_shell_elements (filename = "samplefile_shells.txt", thickness = 0.002, matFlag = "elastic")

- filename: text file from which FE elements are imported. The format of the text file is:

  Element ID1 Node ID1 Node ID2 Node ID3 Node ID4

  Element ID2 Node ID1 Node ID2 Node ID3 Node ID4

  ...

- thickness: thickness of shell elements

A.3.3.3. Interface element generation

Interface elements are used to assure the interaction between FE and DE domains. In the coupled FE-DE framework, both triangular facets and quadrilateral facets are available. A quadrilateral facet is directly defined by the four nodes of the element (quadrilateral or hexahedron shape) located on the interface. If triangular facets are used for quadrilateral and hexahedral elements, the contact interface is divided into four triangular facets by creating a temporary center node. In the case of triangular or tetrahedron elements, a triangular facet is defined by the three nodes of the element located on the interface.

Interface elements are imported using *load_interface_elements()*:

load_interface_elements (filename = "samplefile_interfaces.txt", elementType = "Tri-interface")

- filename: text file from which interface elements are imported. The format of the file is:

  Element ID1 Node ID1 Node ID2 Node ID3 (Node ID4)

  Element ID2 Node ID1 Node ID2 Node ID3 (Node ID4)

  ...

- elementType: type of interface elements consisting of:

  "Tri-interface": triangular interface

  "Quad- interface": quadrilateral interface

Figure A-5 shows an example of FE and DE elements in a simulation. Triangular interfaces are used to assure the FE-DE interaction.

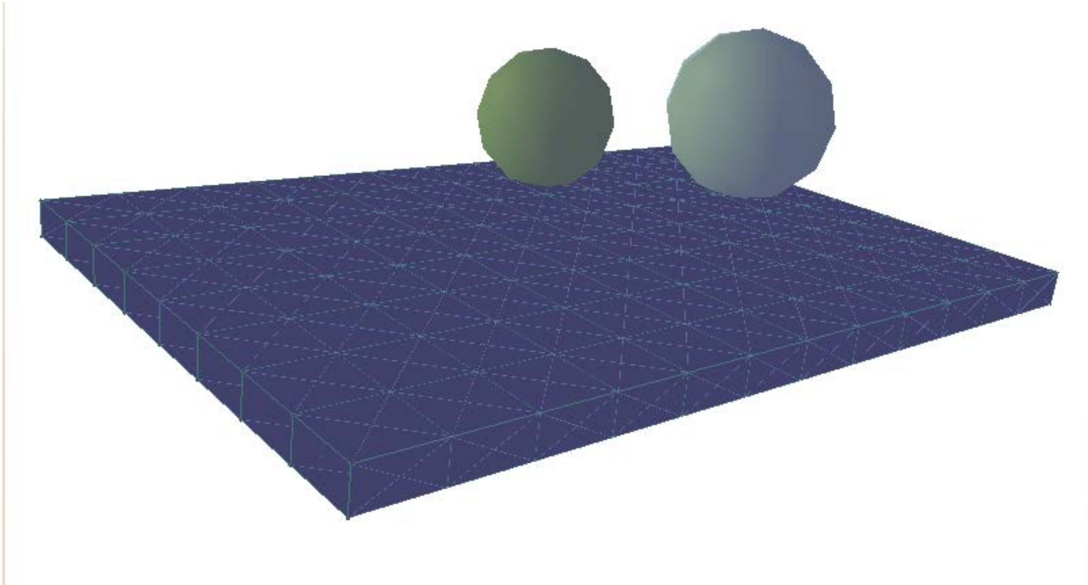

Figure A-5 Two DE particles over a FE plate. The plate is covered with triangular interface elements to assure its interaction with DE particles

A.3.3.4. Optional features for DE and FE elements

Some features can be optionally defined during the generation of DE and FE elements. If optional features are not defined, they are assigned default values.

- color = (x, y, z): determine color of elements (by default, a random color), for example:

  ```
  # add a sphere with center (1, 2, 4), radius 1.5 and color (0.2, 0.4, 0.6)
  O.bodies.append (utils.sphere(center = (1, 2, 4), radius = 1.5, color = (0.2, 0.4, 0.6)))
  ```

- wire: determine if an element is illustrated by "wired" or filled shape (by default, *wire* = *False*), for example:

  ```
  # add a sphere with center (1, 2, 4), radius 1.5 and wired shape)
  O.bodies.append(utils.sphere(center = (1,2,4), radius = 1.5, wire = True))
  ```

- dynamic: determine whether a body will be moved by Newton's law (by default, *dynamic* = *True* for DE particles and *dynamic* = *False* for FE particles). For example:

  ```
  # add to O.bodies a non-dynamic sphere
  O.bodies.append (utils.sphere(center = (1,2,4), radius = 1.5, dynamic = False))
  ```

A.3.4. Boundary Conditions

A.3.4.1. Discrete elements

The motion of DE elements can be restrained in several ways:

- dynamic: force a DE element to be non-dynamic (not moved by *NewtonIntegrator*) by setting *dynamic* = *False*:

  ```
  utils.sphere([x, y, z), radius, dynamic = False )
  ```

- fixed: positions of elements will not change in space by setting *fixed* = *True*, for example:

  ```
  O.bodies.append(utils.box(center=[0, 0, 0],extents=[.5,.5,.5],fixed=True)).
  ```

  Note: when *fixed* = *True*, DE elements can still be moved manually using commands in Python or C++.

- blockedDOFs: block any of six degrees of freedom of a particle. For example, a sphere that can only move in the *yz* plane is generated:

  ```
  O.bodies.append(utils.sphere( [1, 2, 4], 1.5))
  O.bodies[0].state.blockedDOFs = ['x', 'ry', 'rz']
  ```

Restrained conditions of DE particles during simulation can also be achieved using engines such as *UniaxialStrainer()*, *TriaxialStressController()*, *PeriTriaxController()*, *ForceEngine()*, *RotationEngine()* and *TranslationEngine()*.

A.3.4.2. Finite elements

Movement restraints of FE nodes are assigned using *load_restraints()*:

```
load_restraint(filename = "samplefile_restraints.txt")
```

The format of the input file is:

```
Node ID1    Restraint_x1   Restraint_y1   Restraint_z1
Node ID2    Restraint_x2   Restraint_y2   Restraint_z2
...
```

All restraint values of a FE node are set to zero as default. If a FE node is restrained in a direction, the restraint value corresponding to that direction is set to a value of 1.

A.3.5. Assigning Forces and Displacments

A.3.5.1. Discrete elements

Forces acting on DE particles are stored temporarily during one simulation step and reset to zero at the beginning of the next step. Forces on DE particles can be added in a simulation step:

```
# add a force (1, 5, 7) to O.bodies[25]
O.forces.addF(25, Vector3(1,5,7))
```

It is noted that modification of forces using Python is rarely used. It is usually done using C++.

Forcing the wall to move with a certain velocity can be achieved using:

```
# translational motion
O.bodies[i].state.vel = (0, 0.5, 0)
# rotational motion
O.bodies[i].state.angVel=(0.1, 0, 0)
```

A.3.5.2. Finite elements

External forces acting on a FE domain are imported from input files using *load_external_force()*:

```
load_external_force(filename = "samplefile_loads.txt", stepLoad = stepLoading)
```

- stepLoad: a user-defined vector which defines simulation load-steps, for instance:

  stepLoad = [0, 100, 200, 300]

- filename: input file which contains external forces acting on FE nodes. The format of the input file is:

  Node ID1 fx fy fz
  Node ID2 fx fy fz
  ...

It is noted that for a certain *stepLoad[i]*, real forces acting on a FE node:

(fx. stepLoad[i], fy. stepLoad[i], fz. stepLoad[i])

For displacement-controlled problems, prescribed displacements can be applied to certain FE nodes using command:

set_displacements (filename = "samplefile_displacement.txt", stepDisp=stepdisp)

- stepDisp: represents simulation displacement-steps, for instance:

  stepDisp = [0, 0.05, 0.1, 0.2]

- filename: the format of the input file is:

  Node ID1 Ux Uy Uz
  Node ID2 Ux Uy Uz
  ...

Pre-determined displacements of a FE node for a certain displacement-step are:

(fx. stepDisp[i], fy. stepDisp[i], fz. stepDisp[i]).

A.3.6. Material Models

A.3.6.1. Discrete elements

There are many material models available in YADE, some of them are:

- FrictMat
- CohFrictMat

- NormalInelasticMat
- ViscElMat
- CpmMat
- WireMat

New materials are added to the simulation using *append* command, for example:

```
O.materials.append(FrictMat(young=4E7,poisson=0.2,frictionAngle=0.5,
density=2650, label = "sand"))
```

A DE particle can be assigned its material properties during generation stage:

```
O.bodies.append (utils.sphere(center = (1,2,4), radius = 1.5, material ="sand"))
load_DE_spheres (filename = "samplefile_nodes.txt", material ="soil")
```

A.3.6.2. Finite elements

Material properties of FE elements are defined:

For elastic model:

```
FE_Elastic(young = 3E9, gamma = 15, v = 0.3, EleID = [])
```

For Mohr_Coulomb model (perfect-plasticity):

```
FE_MohrCoulomb(young = 3E9, gamma = 15, v = 0.3, c = 2, phi = 0.6, psi = 0,
EleID = [])
```

- young: Young's modulus
- gamma: specific weight
- v: Poisson's ratio
- c: cohesion
- phi: friction angle
- psi: dilatancy angle
- EleID: Only FE elements with certain *IDs* are assigned material properties. By default, EleID is an empty list and all FE elements are assigned the newest material properties.

A.3.6.3. Interface elements

Material models for DE particles can be used for interface elements. Material properties of interface elements are defined during their generation:

```
# add a FrictMat material
O.materials.append(FrictMat(young=4E7,poisson=0.2,frictionAngle=0.5,density=2650, label = "interface"))
# Generate interfaces from input file and assign materials.
load_interface_elements (filename = "samplefile_interfaces.txt", elementType = "Tri-interface", material ="interface")
```

A.3.7. Simulation Engines

Main engines of the coupled FE-DE analysis tool can be categorized as follows:

- *DE simulation engines*
- *FE simulation engines*
- *Interface – DE particle interaction engines*
- *Additional engines*

Different engines types are discussed below:

A.3.7.1. DE simulation engines

A typical DE simulation loop consists of the following tasks (as shown in Figure A-6):

- *Reset forces acting on bodies.*
- *Approximate and real interaction detections*
- *Determine physical properties of interactions.*
- *Calculate forces acting on DE elements from constitutive laws*
- *Update total forces acting on DE elements*
- *Update DE element positions*

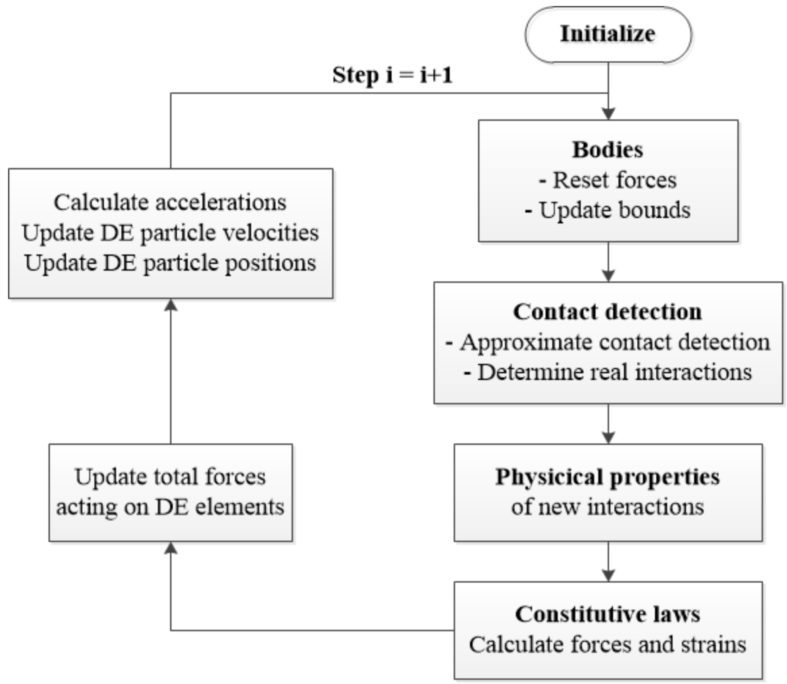

Figure A-6 Typical simulation loop of DE simulation

In a python script, essential engines are demonstrated as:

```
O.engines=[
	# reset forces and from previous step
	ForceResetter(),
	# approximate collision detection
	InsertionSortCollider(...),
	# handle interactions
	InteractionLoop([...], [...], [...]),
	# apply forces and update positions
	NewtonIntegrator(),
]
```

It is noted that functors are omitted in the above engines. The selection of functors depends on particle shapes and interaction types.

In *InsertionSortCollider()*, bounding volumes are generated for spheres, boxes and facets using corresponding functors:

- Bo1_Sphere_Aabb(): for spheres.
- Bo1_Box_Aabb(): for walls.
- Bo1_Facet_Aabb(): for facets.

In consistency with particle shapes and constitutive laws, interaction functions determined in *InteractionLoop()* consist of:

- Functors that determine potential interactions and generate geometrical information about each potential interaction. Some typical functors are listed below:

  # 6 Dofs sphere-sphere interaction
  Ig2_Sphere_Sphere_ScGeom6D()
  # 6 Dofs wall-sphere interaction
  Ig2_Box_Sphere_ScGeom6D()
  # 6 Dofs facet-sphere interaction
  Ig2_Facet_Sphere_ScGeom6D()

  and:

  # 6 Dofs sphere-sphere interaction
  Ig2_Sphere_Sphere_L6Geom()
  # 3 Dofs wall-sphere interaction
  Ig2_Wall_Sphere_L3Geom()
  # 3 Dofs facet-sphere interaction
  Ig2_ Facet _Sphere_L3Geom()

- Functors that determine non-geometrical features of interactions, some are listed below:

  Ip2_FrictMat_FrictMat_MindlinPhys()
  Ip2_FrictMat_FrictMat_FrictPhys()
  Ip2_2xNormalInelasticMat_NormalInelasticityPhys()
  Ip2_FrictMat_CpmMat_FrictPhys()
  Ip2_ViscElMat_ViscElMat_ViscElPhys()

- Functors that determine constitutive laws, for example:

  Law2_ScGeom_MindlinPhys_Mindlin()
  Law2_ScGeom_FrictPhys_CundallStrack()
  Law2_ScGeom6D_NormalInelasticityPhys_NormalInelasticity()
  Law2_ScGeom_CpmPhys_Cpm()
  Law2_ScGeom_ViscElPhys_Basic()

NewtonIntegrator() is used to apply forces and update positions of DE particles. This engine also defines gravity acting on DE particles and damping ratio, for example:

```
# Apply NewtonIntegrator() with gravity (0, 0, -9.81) and damping ratio of 0.2
NewtonIntegrator (gravity = (0,0,-9.81), damping = 0.2)
```

Problem 1: A simple script for DE simulation is presented. In the problem, a sphere and a solid box are generated. The box is fixed while the sphere can move under gravity. The simulation is set to run 20000 steps.

```
print "------------Simulation started------------"
# Omega is the super-class that controls the whole simulation
O=Omega()
# add a material FrictMat
O.materials.append(FrictMat(young=4E7,poisson=0.2,frictionAngle=0.5,density=
2650))
# add a fixed box
O.bodies.append(utils.box(center=[0,0,0],extents=[.5,.5,.5],color=[0,0,1],fixed =
True))
# add a sphere
O.bodies.append(utils.sphere([0,0,2],1,color=[0,1,0]))
# Engines which are called consecutively in a calculation step
O.engines=[
	ForceResetter(),
	InsertionSortCollider([
		Bo1_Sphere_Aabb(),
```

```
		Bo1_Box_Aabb(),
	]),
	InteractionLoop(
		[Ig2_Sphere_Sphere_ScGeom(),Ig2_Box_Sphere_ScGeom()],
		[Ip2_FrictMat_FrictMat_FrictPhys()],
		[Law2_ScGeom_FrictPhys_CundallStrack()]
	),
	NewtonIntegrator(damping=0.1, gravity=[0,0,-9.81])
]
# set time-step from p-wave speed and multiply it by safety factor of 0.2
O.dt= .2*utils.PWaveTimeStep()
# enable graphical interface
from yade import qt
qt.View()
qt.Controller()
#run the simulation for 20000 steps
O.run(20000, True)
print "------------Script ended------------"
```

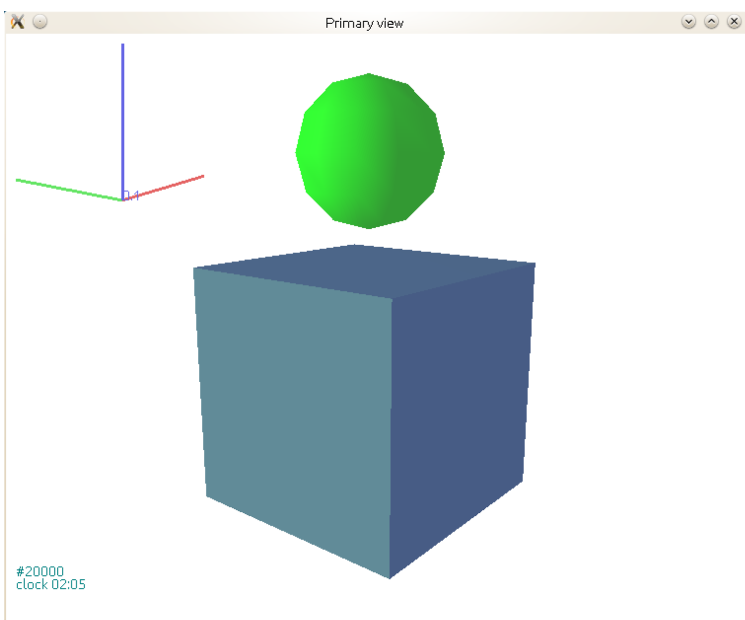

Figure A-7 The box and sphere described in problem 1

A.3.7.2. FE simulation engines

In the developed coupled FE-DE framework, a dynamic explicit approach is used for FE simulation. The flowchart of FE simulation is shown in Figure A-8.

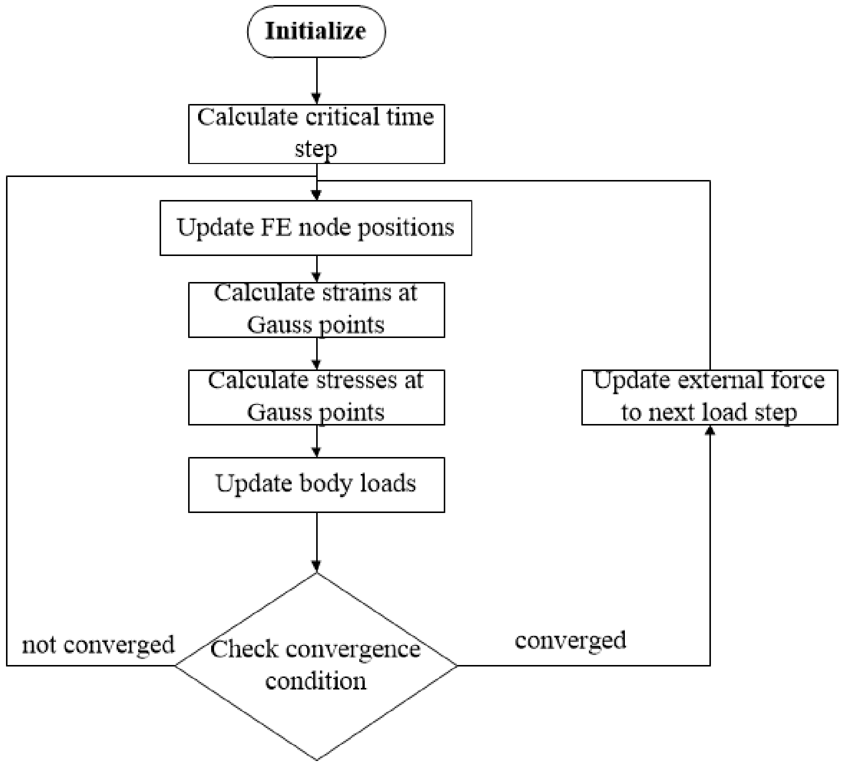

Figure A-8 Typical simulation loop of FE simulation

A typical FE simulation consists of the following engines:

- Reset forces acting on FE nodes from previous step:

  FE_ForceResetter()

- Determine physical properties of FE elements (ex: nodal masses, element stiffnesses and restraints):

  # for quadrilateral element
  SetQuadrilateralParameters()
  # for quadratic brick element Hexahedron8N1I
  SetHexahedron8N1IParameters()
  # for quadratic brick element Hexahedron8N8I

```
SetHexahedron8N8IParameters()
# for quadratic brick element Hexahedron20N8I
SetHexahedron20N8IParameters()
# for shell element
SetShellBT4()
```

- Update geometrical properties of FE elements:

```
# for quadrilateral element
SetGeoQuadrilateral2D()
# for quadratic brick element Hexahedron8N1I and Hexahedron8N8I
SetGeoHexahedron()
# for quadratic brick element Hexahedron20N8I
SetGeoHexahedron20N()
# for shell element
SetGeoShellBT4()
```

- Determine external loads acting on FE nodes:

```
SetMultiStepExternalForce()
```

- Determine FE critical time-step and multiply it by a safety factor:

```
GlobalTangentStiffnessTimeStepper(ratio = 0.5)
```

- Set FE time-step equal to n times (n >= 1) DE time-step (for coupled FE-DE problems):

```
setdtFEM(n = 100)
```

- Determine damping coefficient:

```
DampingRayleigh()
```

- Check convergence conditions:

```
CheckConvergence()
```

- Calculate strains and stresses at Gauss points and update body loads:

```
# for quadrilateral and brick elements
TangentStiffnessCPPM()
```

```
# for shell element
ElasticShellSolver()
```

- Calculate nodal velocities and update nodal positions

```
CentralDifference()
```

- Record outputs

```
OutputRecording()
```

Problem 2: This example presents a simple script for FE simulation in which a square footing over granular soil is simulated. FE elements, material properties, boundary conditions and loading information are imported from corresponding input files. Pressure acting on the footing is increased to investigate the foundation bearing capacity (Figure A-9).

```
print "------------Simulation started------------"
from yade import plot
from yade.pack import *
O=Omega()
## loading necessary files and generate FEM nodes, elements, loading
conditions,..
# Generate FE nodes
load_FE_nodes (filename = "squarefooting_nodes.txt", ndim = 3, radius = 0.001)
# Generate FE elements
load_solid_elements (filename = "squarefooting_elements.txt", ndim = 3,
elementType = "Hexahedron8N8I", matFlag = "elastic")
# Apply boundary conditions
load_restraint(filename = "squarefooting_restraints.txt")
# Apply material properties
FE_Elastic(young = 3E9, gamma = 15, v = 0.3)
# Apply loading steps
step =  [0, 100, 200, 300]
load_external_force(filename = "squarefooting_loads.txt", stepLoad = step)
## Engines that run during the simulation
```

```
O.engines= [
ForceResetter(),
SetHexahedron8N8IParameters(),
SetGeoHexahedron(),
TangentStiffnessCPPM(),
CheckConvergence(),
GlobalTangentStiffnessTimeStepper(ratio = 0.5),
DampingRayleigh(),
SetMultiStepExternalForce(),
CentralDifference(),
OutputRecording()
]
print "------------Script ended-----------"
```

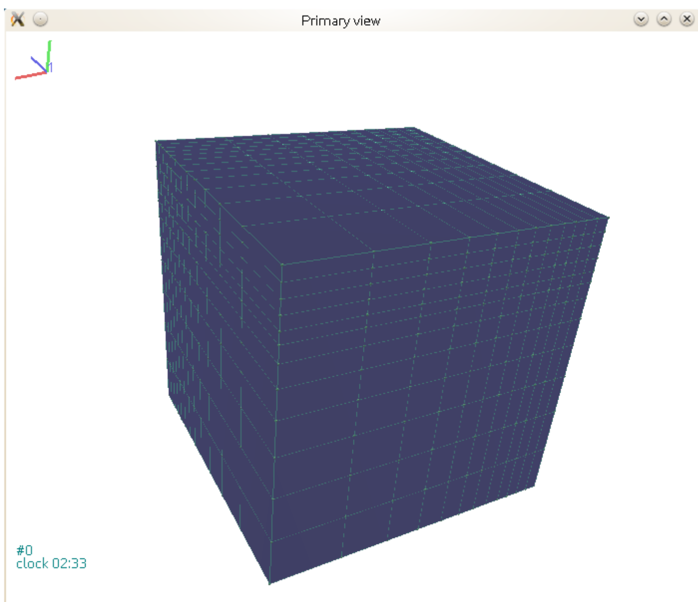

Figure A-9 FE simulation of a square footing problem in YADE

A.3.7.3. Interface-DE particle simulation engines

Contact forces resulted from particle–interface interactions are transmitted into the FE nodes. The contact algorithm used in the coupled FE-DE framework is similar to that used between DE particles. The flowchart of the coupled FE-DE framework is shown in Figure A-10.

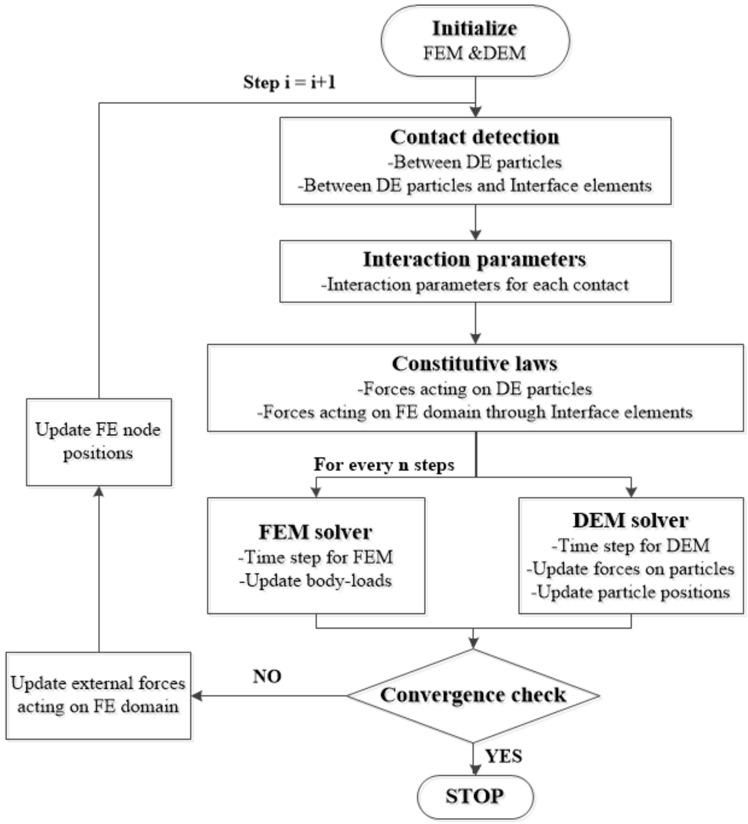

Figure A-10 Flowchart of the coupled FE-DE framework

Engines which handles the interaction between DE particles and interface elements consist of :

- Determine bounding volume of interfaces:

  Bo1_QuadInterface_Aabb()

- Determine physical properties of interfaces:

  SetInterfaceParameters()

- Update geometrical properties of interfaces:

  SetGeoQuadInterface()

- Determine potential interactions between DE particles and interfaces:

```
#  6 Dofs interface-sphere interaction
Ig2_ Interface _Sphere_ScGeom6D()
```

Problem 3: A coupled FE-DE problem which illustrates the interaction between the two domains is presented. Two spheres are generated using DEM while a plate is generated using FEM. The two spheres are then allowed to fall onto the plate. The interaction between the DE particles and the FE plate is modeled using interface elements (Figure A-11).

```
print "------------Simulation started------------"
from yade import plot
from yade.pack import *
O=Omega()
## Define materials
# for DE particles
O.materials.append(FrictMat(young = 10E7, poisson = 0.25, frictionAngle = 0.75,
density = 2650, label="sphere"))
#for interfaces
O.materials.append(FrictMat(young=10E7, poisson = 0.25, frictionAngle = 0.75,
density = 2650, label="interface"))
## Load necessary files and generate FEM nodes, elements, loading conditions,..
# Generate FE nodes
load_FE_nodes (filename = "plate_nodes.txt", radius = 0.001)
# Generate FE elements
load_solid_elements (filename = "plate_elements.txt", elementType =
"Hexahedron8N8I", matFlag = "elastic")
# Generate interface elements
load_interface_elements (filename = "plate_interfaces.txt", elementType = "Tri-
interface", material ="interface")
# Apply boundary conditions
load_restraint(filename = "plate_restraints.txt")
# Apply material properties for FE elements
FE_Elastic(young = 3E6, gamma = 16.0, v = 0.25)
```

```
# Generate 2 spherical DE particles
O.bodies.append(utils.sphere([0.3, 0.25, 0.1], 0.05, material = "sphere "))
O.bodies.append(utils.sphere([0.4, 0.15, 0.12], 0.06, material ="sphere "))
# Enable graphical interface
from yade import qt
qt.View()
qt.Controller()
## Engines that run during the simulation
O.engines= [
	ForceResetter(),
	ResetInteractingSphere(),
	# execute only at the first step
	SetHexahedron8N8IParameters(),
	# execute only at the first step
	SetInterfaceParameters(),
	SetGeoHexahedron(),
	SetGeoQuadInterface(),
	TangentStiffnessCPPM(),
	CheckConvergence(),
	DampingRayleigh(),
	SetMultiStepExternalForce(),
	# set time-step for DE calculation,  O.dt= 0.9*utils.PWaveTimeStep()
	setdtDEM(ratio = 0.9),
	InsertionSortCollider([
		Bo1_Sphere_Aabb(),
		Bo1_QuadInterface_Aabb()
		]),
	InteractionLoop([
		Ig2_Sphere_Sphere_ScGeom6D(),
		Ig2_Interface_Sphere_ScGeom6D() ],
		[Ip2_2xNormalInelasticMat_NormalInelasticityPhys()],
		[Law2_ScGeom6D_NormalInelasticityPhys_NormalInelasticity()]
```

```
        ),
        NewtonIntegrator(damping=0.1, gravity = [0,0,-9.81]),
        # set time-step for FE calculation  = 100 times DE time-sep
        setdtFEM(n = 10),
        CentralDifference(),
        OutputRecording()
        ]
print "------------Script ended------------"
```

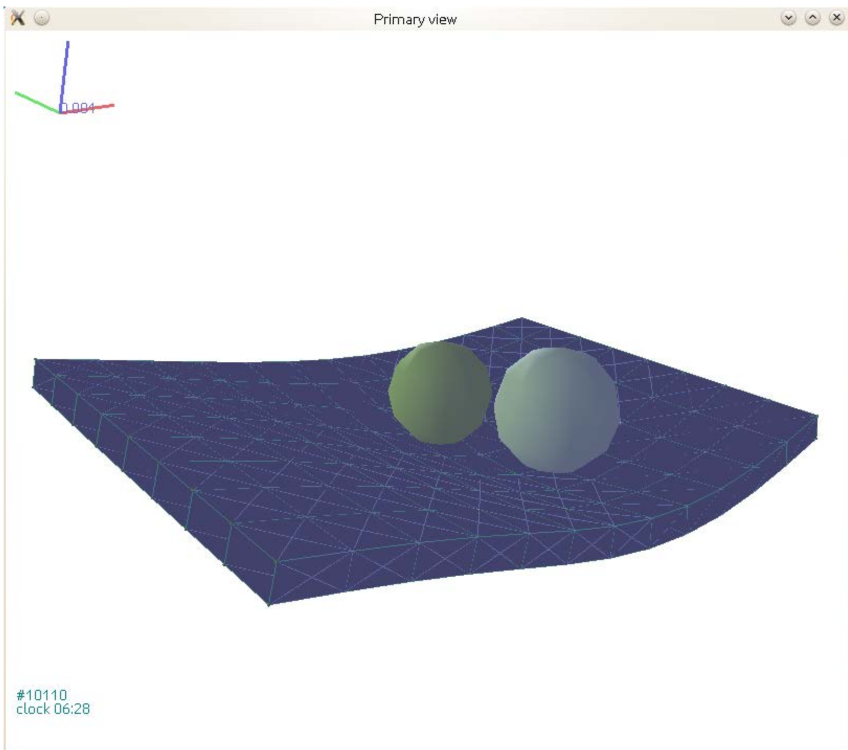

Figure A-11 Deformation of a FE plate in interaction with two DE particles using the coupled FE-DE framework

It is noted that in the above Python script, the FE time-step is 100 times the DE time-step. Since the time-step Δt_{FE} required for FE is much larger than that for DE (Δt_{DE}), it is not efficient to use a common time-step for both FE and DE models. Thus, different time-steps for each domain are implemented in the coupling framework to improve the computational efficiency. The time-step in the FE domain is selected as $\Delta t_{FE} = n\Delta t_{DE}$ where n is an integer such that $n \le \frac{[\Delta t_{FE}]}{\Delta t_{DE}}$. This algorithm is implemented by executing the FE solver for every n DE computations.

A.3.7.4. Additional engines

Additional functions can be added to the simulation to handle other required tasks. In YADE, users can develop their own functions either in Python or C++. Functions written in Python are added to the main engine using *PyRunner()*.

Problem 4: A loose sample is generated inside a container using *makeCloud()*. A function named *vertical_compress()* is written in Python to vertically compress the top wall until the wall movement reaches a target value of 0.18. Vertical position and pressure acting on the top wall are monitored during the simulation using a defined function *monitor()*. The two functions *vertical_compress()* and *monitor()* are executed for every 100 time-steps (Figure A-12).

```
print "------------Simulation started------------"
# Omega is the super-class that controls the whole simulation
O=Omega()
# add a material type FrictMat
O.materials.append(FrictMat(young = 1E7, poisson = 0.25, frictionAngle = 0.6,
density = 2650))
# Corners of the box
x_min, y_min, z_min = 0.0, 0.0, 0.0
x_max, y_max, z_max = 0.5, 0.2, 0.3
## Generate a container
# top wall
O.bodies.append(utils.box(center = [(x_min + x_max)/2, (y_min + y_max)/2,
z_max], extents = [(-x_min + x_max)/2, (-y_min + y_max)/2, 0], fixed = True,
wire=True))
# bottom wall
```

```
O.bodies.append(utils.box(center = [(x_min + x_max)/2, (y_min + y_max)/2, z_min], extents = [(-x_min + x_max)/2, (-y_min + y_max)/2, 0], fixed=True, wire=True))
# left wall
O.bodies.append(utils.box(center = [x_min, (y_min + y_max)/2, (z_min + z_max)/2], extents=[0, (-y_min + y_max)/2, (-z_min + z_max)/2], fixed=True, wire=True))
# right wall
O.bodies.append(utils.box(center = [x_max, (y_min + y_max)/2, (z_min + z_max)/2], extents=[0, (-y_min + y_max)/2, (-z_min + z_max)/2], fixed=True, wire=True))
# front wall
O.bodies.append(utils.box(center = [(x_min + x_max)/2, y_min, (z_min + z_max)/2], extents = [(-x_min + x_max)/2, 0, (-z_min + z_max)/2], fixed=True, wire=True))
# behind wall
O.bodies.append(utils.box(center = [(x_min + x_max)/2, y_max, (z_min + z_max)/2], extents = [(-x_min + x_max)/2, 0, (-z_min + z_max)/2], fixed=True, wire=True))
# Generate a cloud of spheres
sp=yade._packSpheres.SpherePack()
sp.makeCloud(Vector3(x_min, y_min, z_min), Vector3(x_max, y_max, z_max), 0.006, 0.2)
O.bodies.append([utils.sphere(s[0], s[1]) for s in sp])
# determine whether the top wall is still moved
moving_box = True
# Engines which are called consecutively in a calculation step
O.engines=[
	ForceResetter(),
	InsertionSortCollider([
		Bo1_Sphere_Aabb(),
		Bo1_Box_Aabb(),
	]),
	InteractionLoop(
```

```
            [Ig2_Sphere_Sphere_ScGeom(),Ig2_Box_Sphere_ScGeom()],
            [Ip2_FrictMat_FrictMat_FrictPhys()],
            [Law2_ScGeom_FrictPhys_CundallStrack()]
        ),
        NewtonIntegrator(damping=0.1, gravity=[0, 0, -9.81]),
        setdtDEM(ratio = 0.8),
        PyRunner(iterPeriod=100, command='vertical_compress()'),
        PyRunner(iterPeriod=100, command='monitor()'),
]
# function that compresses the soil sample by moving downward the top wall
def vertical_compress():
        global moving_box
        if moving_box:
            O.bodies[0].state.vel = (0, 0, -0.5)
            if abs(O.bodies[0].state.pos[2] -  z_max) > 0.18:
                moving_box = False
                # set velocity of the top wall to zero
                O.bodies[0].state.vel = (0,0,0.0)
# Monitor the simulation
def monitor():
        S_contact=O.bodies[0].shape.extents[0]*O.bodies[0].shape.extents[1]*4
        pressure = abs((O.forces.f(0)[2]) / S_contact/1000)
        vertical_pos = O.bodies[0].state.pos[2]
        print "pressure and vertical pos of top wall: ",pressure,"\t\t", vertical_pos
print "------------Script ended------------"
```

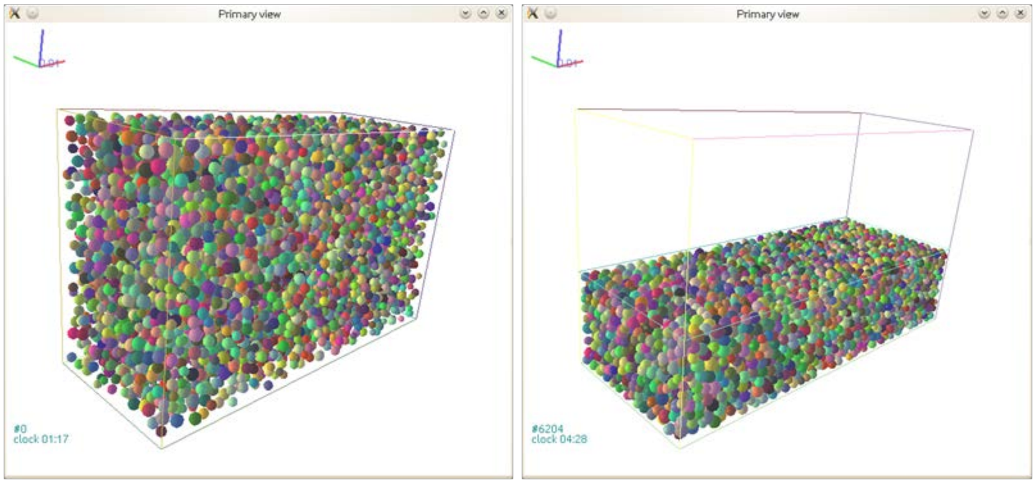

a) before compression b) after compression

Figure A-12 Soil sample in problem 4 before and after compression

Problem 5: A python script is presented here to simulate a direct shear test. DE particles are imported from an input file. The sample is first vertically compressed to reach a target vertical stress. The lower part of the sample is then horizontally moved while the upper part is kept stationary. Vertical stress acting on top of the sample is maintained during the simuation. Two addtional engines are used: *KinemDirectShearCompEngine*() and *KinemDirectShearMovingEngine*() (Figure A-13).

```
print "------------Simulation started------------"
O=Omega()
# add material for DE particles
O.materials.append(FrictMat(young = 1E7, poisson = 0.25, frictionAngle = 0.6,
density = 2650))
# add material for side walls
O.materials.append(FrictMat(young = 1E7, poisson = 0.25, frictionAngle = 0.0,
density = 2650))
# add material for top and bottom walls
O.materials.append(FrictMat(young = 1E7, poisson = 0.25, frictionAngle = 0.8,
density = 2650))
# size of the shear box
```

```
L_x, L_y, L_z  = 0.06, 0.0125, 0.06
# names of input and output files
sphere_input_file_name = "Direct_shear_test_sphere_input.txt"
out_put_file_name = "Direct-shear-test-ouput.txt"
## now define boxes
# lower part, left wall
left_low_center, left_low_extents  = (0, L_y/2, L_z/2), (0, L_y/2, L_z/2)
# lower part, right wall
right_low_center, right_low_extents = (L_x, L_y/2, L_z/2), (0, L_y/2, L_z/2)
# bottom wall
bot_center, bot_extents = (L_x/2, 0, L_z/2), (L_x/2, 0, L_z/2)
# lower part, behind wall
behind_low_center, behind_low_extents = (L_x/2, L_y/2, 0), (L_x/2,  L_y/2, 0)
# lower part, front wall
front_low_center, front_low_extents = (L_x/2, L_y/2, L_z), (L_x/2,  L_y/2, 0)
# upper part, left wall
left_upper_center, left_upper_extents = (0, 3*L_y/2 , L_z/2), (0, L_y/2, L_z/2)
# upper part, right wall
right_upper_center, right_upper_extents = (L_x, 3*L_y/2, L_z/2), (0,L_y/2,
L_z/2)
# top wall
top_center, top_extents = (L_x/2, 2*L_y, L_z/2), (L_x/2, 0, L_z/2)
# upper part, behind wall
behind_upper_center, behind_upper_extents=(L_x/2,3*L_y/2,0),(L_x/2,L_y/2, 0)
# upper part, front wall
front_upper_center, front_upper_extents = (L_x/2, 3*L_y/2,L_z), (L_x/2,L_y/2,
0)
## generate two additional panels at the middle height of the sample to avoid
particles from falling out during shearing, the two panels will be expanded
following shearing process.
# left panel
left_panel_center, left_panel_extents = (0, L_y, L_z/2), (0, 0, L_z/2)
```

```
# right panel
right_panel_center, right_panel_extents = (L_x, L_y , L_z/2), (0, 0, L_z/2)
# now add walls to simulation
leftBox_low = utils.box(center = left_low_center, extents = left_low_extents, fixed = True, wire = True, material = O.materials[1])
rightBox_low = utils.box(center = right_low_center, extents = right_low_extents, fixed = True, wire = True, material=O.materials[1])
botBox = utils.box(center = bot_center, extents=bot_extents, fixed = True, wire = True, material=O.materials[2])
behindBox_low = utils.box(center = behind_low_center, extents = behind_low_extents, fixed = True, wire = True, material=O.materials[1])
frontBox_low = utils.box(center = front_low_center, extents = front_low_extents , fixed = True, wire = True, material=O.materials[1])
leftBox_upper = utils.box(center = left_upper_center, extents = left_upper_extents, fixed = True, wire = True, material=O.materials[1])
rightBox_upper = utils.box(center = right_upper_center, extents = right_upper_extents , fixed=True, wire = True, material=O.materials[1])
topBox = utils.box(center=top_center, extents = top_extents, fixed = True, wire = True, material=O.materials[2])
behindBox_upper = utils.box( center = behind_upper_center, extents = behind_upper_extents , fixed=True,wire=True,material=O.materials[1])
frontBox_upper = utils.box( center = front_upper_center, extents = front_upper_extents, fixed=True,wire=True,material=O.materials[1])
leftPanel = utils.box( center = left_panel_center, extents = left_panel_extents, fixed=True,wire=True)
rightPanel = utils.box( center = right_panel_center, extents = right_panel_extents, fixed=True,wire=True)
# add to O.bodies
O.bodies.append([leftBox_low, rightBox_low, botBox, behindBox_low, frontBox_low, leftBox_upper, rightBox_upper, topBox, behindBox_upper, frontBox_upper,leftPanel, rightPanel])
# add spheres
infile = open(sphere_input_file_name,"r")
lines = infile.readlines()
```

```
for line in lines:
    data = line.split()
    center = Vector3(float(data[0]),float(data[1]),float(data[2]))
    radius = float(data[3])
    O.bodies.append([utils.sphere(center,radius,material=O.materials[0])])
# engines of the simulation
O.engines=[
        ForceResetter(),
        InsertionSortCollider([
                Bo1_Sphere_Aabb(),
                Bo1_Box_Aabb(),
                ]),
        InteractionLoop(
                [Ig2_Sphere_Sphere_ScGeom(),Ig2_Box_Sphere_ScGeom()],
                [Ip2_FrictMat_FrictMat_FrictPhys()],
                [Law2_ScGeom_FrictPhys_CundallStrack()]
        ),
        NewtonIntegrator(damping = 0.2, gravity = (0, -9.81, 0)),
        ]
# set DE time-step
O.dt=.5*utils.PWaveTimeStep()
# add a compression engine to generate vertical stress = 50 kPa
O.engines = O.engines+[KinemDirectShearCompEngine(compSpeed =0.004,
targetSigma = 50)]
# run 2000 steps to reach the target vertical stress
O.run(2000,True)
# add shearing engine, shearing speed = 0.001, max shearing distance = 0.03
O.engines=O.engines[:4] + [KinemDirectShearMovingEngine(shearSpeed =
0.001 ,targetSigma = 50, gammalim=0.03)]
# now run
O.run()
print "------------Script ended------------"
```

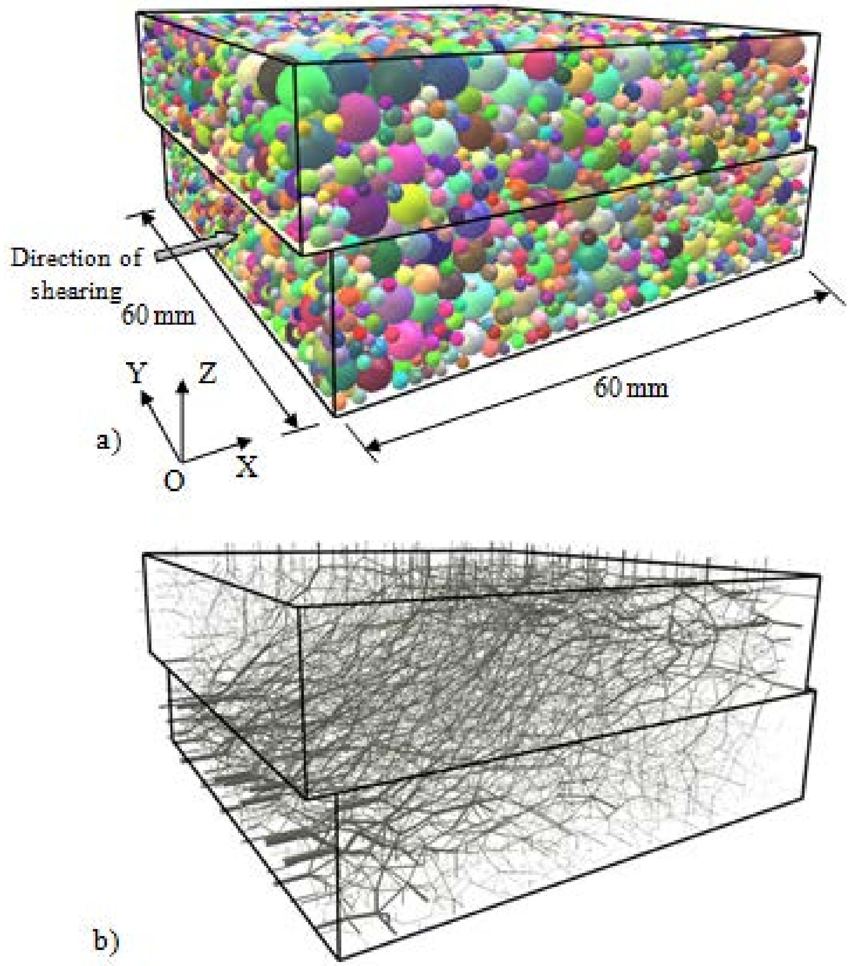

Figure A-13 DE used in the three-dimensional direct shear test and b) Three-dimensional contact force network

Problem 6: A trip foundation over geogrid reinforced soil is simulated using the coupled FE-DE framework. The geogrid is modeled using FEM while the soil is modeled using DEM. Interaction between the two domains are assured using triangular interface elements. Pressure at the foundation base is applied in small increments using a C++ written function *FoundationLoadingEngine()* (Figure A-14).

```
print "------------Simulation started------------"
O=Omega()
## Define materials
```

```
# for DE particles
O.materials.append (NormalInelasticMat(young=4E7,poisson=0.2,
frictionAngle=0.5, density=2650, label="sphere"))
# for interfaces
O.materials.append(NormalInelasticMat(young=4E7,poisson=0.2,frictionAngle
=0.5, density=2650, label="interface"))
## Load necessary files and generate FEM nodes, elements, loading conditions,..
# Generate FE nodes
load_FE_nodes (filename = "foundation_nodes.txt", ndim = 3, radius = 0.001)
# Generate FE elements
load_solid_elements (filename = " foundation _elements.txt", ndim = 3,
elementType = "Hexahedron8N8I", matFlag = "elastic")
load_interface_elements (filename = " foundation _interfaces.txt", elementType =
"Tri-interface", material ="interface")
# Apply boundary conditions
load_restraint(filename = " foundation _restraints.txt")
# Apply material properties for FE elements
FE_Elastic(young = 3E9, gamma = 15, v = 0.3)
# Generate spheres from input file
load_DE_spheres(filename = "sphere_nodes.txt", material ="sphere")
# generate the container
x_min, y_min, z_min = 0.0, 0.0, 0.0
x_max, y_max, z_max = 1.1, 0.3, 0.6
# add bottom wall
O.bodies.append(utils.box(center=[(x_min + x_max)/2, (y_min + y_max)/2,
z_min], extents=[(-x_min + x_max)/2, (-y_min + y_max)/2, 0], fixed=True,
wire=True))
# add left wall
O.bodies.append(utils.box(center=[x_min,(y_min + y_max)/2,(z_min +
z_max)/2], extents=[0, (-y_min + y_max)/2,(-z_min + z_max)/2], fixed=True,
wire=True))
# add right wall
```

```
O.bodies.append(utils.box(center=[x_max,(y_min + y_max)/2,(z_min +
z_max)/2], extents=[0, (-y_min + y_max)/2,(-z_min + z_max)/2],fixed=True,
wire=True))
 # add front wall
O.bodies.append(utils.box(center=[(x_min + x_max)/2,y_min,(z_min +
z_max)/2], extents=[(-x_min + x_max)/2 , 0, (-z_min + z_max)/2 ],fixed=True,
wire=True))
# add behind wall
O.bodies.append(utils.box(center=[(x_min + x_max)/2,y_max,(z_min +
z_max)/2], extents=[(-x_min + x_max)/2 , 0, (-z_min + z_max)/2
],fixed=True,wire=True))
## generate the strip footing
footing_width = 0.1
f_x_min = (x_min + x_max)/2 - footing_width/2
f_x_max = (x_min + x_max)/2 + footing_width/2
f_y_min = y_min
f_y_max = y_max
f_z_min = z_max
# determine id of the strip footing
ID = len(O.bodies)
# add the footing to O.bodies()
O.bodies.append(utils.box(center=[(f_x_min + f_x_max)/2,(f_y_min +
f_y_max)/2, f_z_min ],extents=[(footing_width)/2, (-f_y_min + f_y_max)/2,
0],fixed=True, wire=False))
# Loading steps: footing pressure increases from 0 to 200 kPa
pressure = []
for i in range (0,11):
   pressure.append(i*20)
# Enable graphical interface
from yade import qt
qt.View()
qt.Controller()
## Engines that run during the simulation
```

```
O.engines= [
	ForceResetter(),
	FE_ForceResetter(),
	SetHexahedron8N8IParameters(),
	SetInterfaceParameters() ,
	SetGeoHexahedron(),
	SetGeoQuadInterface(),
	TangentStiffnessCPPM(),
	CheckConvergence(),
	DampingRayleigh(),
	SetMultiStepExternalForce(),
	# time-step for DE simulation
	setdtDEM(ratio = 0.9),
	InsertionSortCollider([
		Bo1_Sphere_Aabb(),
		Bo1_Box_Aabb(),
		Bo1_QuadInterface_Aabb()
		]),
	InteractionLoop([
		Ig2_Sphere_Sphere_ScGeom6D(),
		Ig2_Box_Sphere_ScGeom6D(),
		Ig2_Interface_Sphere_ScGeom6D()
		],
		[Ip2_2xNormalInelasticMat_NormalInelasticityPhys()],
		[Law2_ScGeom6D_NormalInelasticityPhys_NormalInelasticity()]

	),
	NewtonIntegrator(damping=0.1, gravity=[0, 0, -9.81]),
	## Moving the strip foundation downward following defined pressure
steps
	# compression speed = 0.005
```

```
        FoundationLoadingEngine(id_top = ID, val = pressure, compSpeed =
0.005),
        setdtFEM (n = 100),
        CentralDifference(),
        OutputRecording()
        ]
print "------------Script ended------------"
```

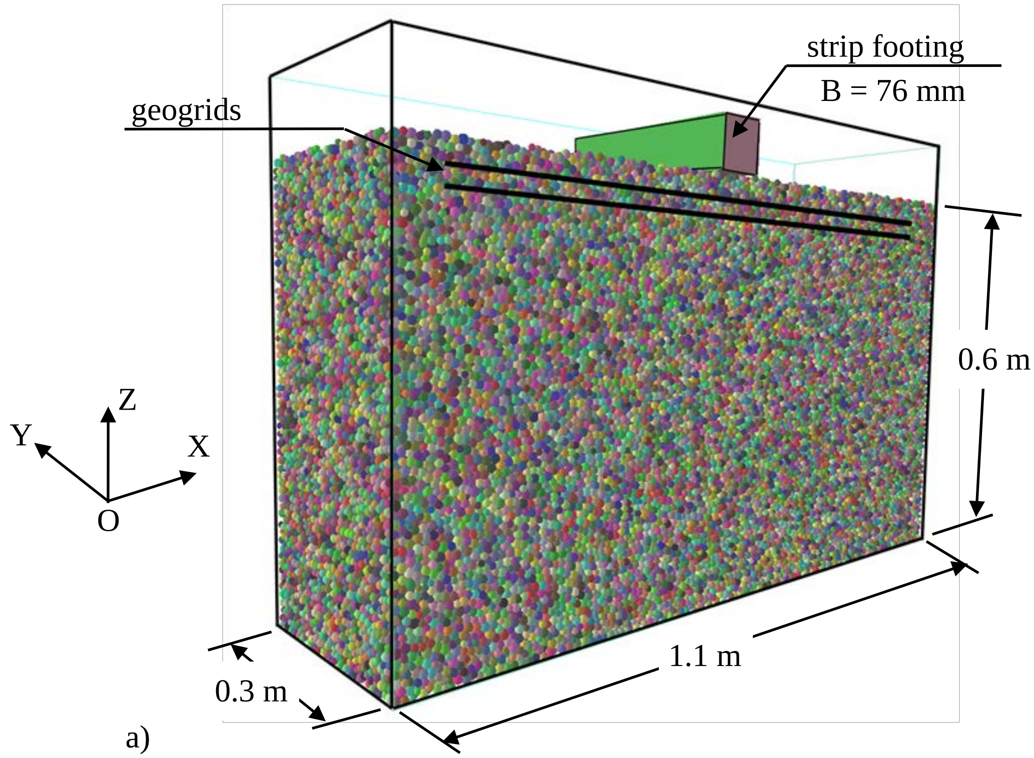

a)

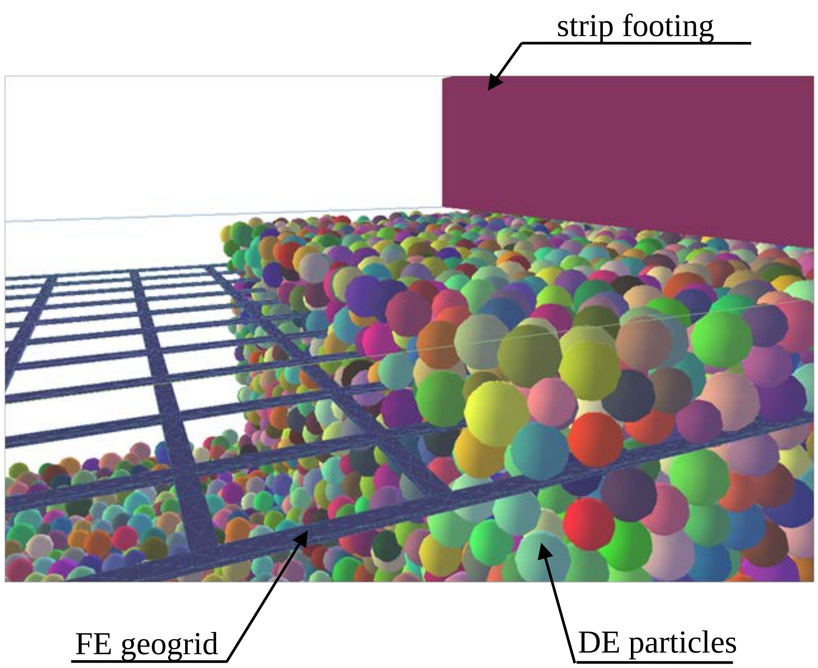

b)

Figure A-14 a) Initial geometry of the geogrid reinforced foundation b) Partial view of the DE particle-geogrid interaction

Problem 7: A geogrid pullout test is simulated using the coupled FE-DE framework. The geogrid is modeled using FEM while the soil is modeled using DEM. Vertical stress acting on top of the sample is kept constant during the test using a stress control mechanism. The pullout procedure is numerically performed using a displacement control approach in which lateral displacements were applied in different increments. Two new C++ built engines are used in the simulation: *PressureControlEngine()* to control the vertical stress and *GeogridPulloutEngine()* to numerically simulate the pullout of the geogrid (Figure A-15).

```
print "------------Simulation started------------"
O=Omega()
## Define materials
# for DE particles
O.materials.append(NormalInelasticMat(young=4E7,poisson=0.2,frictionAngle=0
.5, density=2650, label="sphere"))
# for interfaces
O.materials.append(NormalInelasticMat(young=4E7,poisson=0.2,frictionAngle=0
.5, density=2650, label="interface"))
## load necessary files and generate FEM nodes, elements, loading conditions,..
# generate FE nodes
load_FE_nodes (filename = "geogrid_nodes.txt", ndim = 3, radius = 0.001)
# generate FE elements
load_solid_elements (filename = "geogrid_elements.txt", elementType =
"Hexahedron8N8I", matFlag = "elastic")
# generate interfaces
load_interface_elements (filename = "geogrid_interfaces.txt", elementType =
"Tri-interface", material ="interface")
# apply boundary conditions
load_restraint(filename = "geogrid_restraints.txt")
# apply material properties for FE elements
FE_Elastic(young = 3E9, gamma = 15, v = 0.3)
# load spheres from input file
```

```
load_DE_spheres(filename = "sphere_nodes.txt", material ="sphere")
# generate the box
x_min, y_min, z_min = 0.0, 0.0, 0.0
x_max, y_max, z_max = 0.68, 0.3, 0.62
# determine id of the top wall
ID = len(O.bodies)
## add walls of the container
# top wall
O.bodies.append(utils.box(center=[(x_min + x_max)/2,(y_min + y_max)/2,
z_max], extents=[(-x_min + x_max)/2, (-y_min + y_max)/2, 0],fixed=True,
wire=True))
# bottom wall
O.bodies.append(utils.box(center=[(x_min + x_max)/2,(y_min + y_max)/2,
z_min], extents=[(-x_min + x_max)/2, (-y_min + y_max)/2, 0],fixed=True,
wire=True))
# left wall
O.bodies.append(utils.box(center=[x_min,(y_min + y_max)/2,(z_min +
z_max)/2], extents=[0, (-y_min + y_max)/2,(-z_min + z_max)/2],fixed=True,
wire=True))
# right wall
O.bodies.append(utils.box(center=[x_max,(y_min + y_max)/2,(z_min +
z_max)/2], extents=[0, (-y_min + y_max)/2,(-z_min + z_max)/2],fixed=True,
wire=True))
# front wall
O.bodies.append(utils.box(center=[(x_min + x_max)/2,y_min,(z_min +
z_max)/2], extents=[(-x_min + x_max)/2 , 0, (-z_min + z_max)/2 ],fixed=True,
wire=True))
# behind wall
O.bodies.append(utils.box(center=[(x_min + x_max)/2,y_max,(z_min +
z_max)/2], extents=[(-x_min + x_max)/2 , 0, (-z_min + z_max)/2 ],fixed=True,
wire=True))
# pullout displacement: from 0 to 40 mm
geogrid_disp = []
for i in range (0,11):
```

```
    geogrid_disp.append(i*0.004)
# target vertical stress acting on top of the sample (kPa)
vertical_stress = 50
# enable graphical interface
from yade import qt
qt.View()
qt.Controller()
## Engines that run during simulation
O.engines= [
	ForceResetter(),
	ResetInteractingSphere(),
	SetHexahedron8N8IParameters(),
	SetInterfaceParameters() ,
	SetGeoHexahedron(),
	SetGeoQuadInterface(),
	TangentStiffnessCPPM(),
	CheckConvergence(),
	DampingRayleigh(),
	SetMultiStepExternalForce(),
	setdtDEM(ratio = 0.9), #set time-step for DE calculation
	InsertionSortCollider([
		Bo1_Sphere_Aabb(),
		Bo1_Box_Aabb(),
		Bo1_QuadInterface_Aabb() ]),
	InteractionLoop([
		Ig2_Sphere_Sphere_ScGeom6D(),
		Ig2_Box_Sphere_ScGeom6D(),
		Ig2_Interface_Sphere_ScGeom6D() ],
		[Ip2_2xNormalInelasticMat_NormalInelasticityPhys()],
		[Law2_ScGeom6D_NormalInelasticityPhys_NormalInelasticity()]
	),
	NewtonIntegrator(damping=0.1,gravity=[0,0,-9.81]),
```

```
# Maintaining the vertical stress acting on top of the sample
PressureControlEngine(id_top = ID, stress = vertical_stress),
# Moving the geogrid following different lateral displacement increments
# pullout speed = 0.005
GeogridPulloutEngine(val = geogrid_disp, pullSpeed = 0.005),
setdtFEM(n = 100),
CentralDifference(),
OutputRecording()
]
print "------------Script ended------------"
```

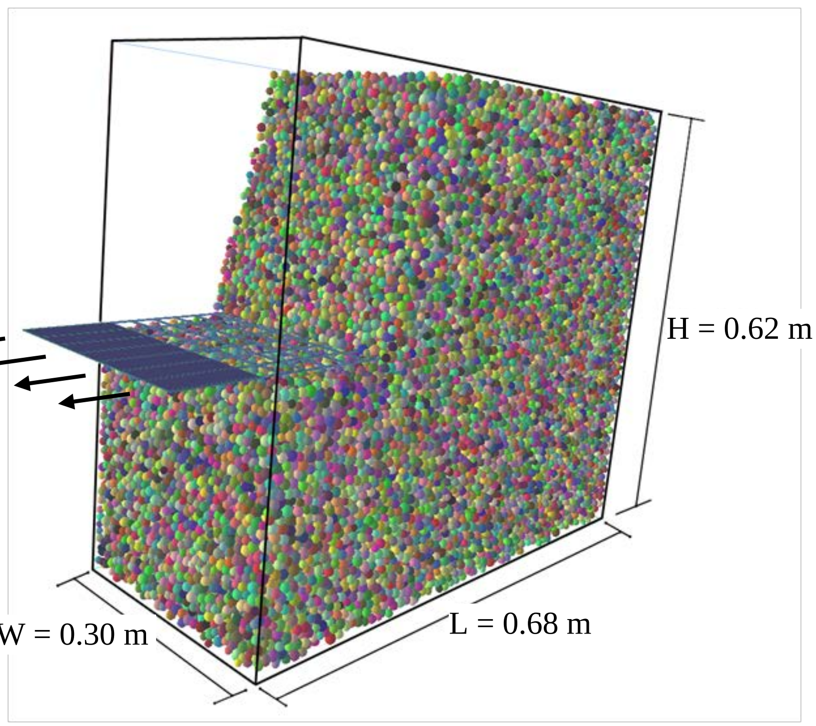

Figure A-15 Initial DE specimen for the geogrid pulout test (partial view for illustration purpose)

Problem 8: The problem examines the behavior of a buried pipe in granular fill. The pipe with a diameter of 0.15 m is modeled using FE *shell* elements. Soil above the springline is modeled using DE particles while soil below the springline is modeled using FE *Hexahedron20N8I* elements. *Mohr-Coulomb* material model is used for the FE soil domain while *elastic* behavior is assumed for the pipe. A material *NormalInelasticMat()* is used for the DE particles. Vertical stresses are uniformly applied to top of the fill using *PressureControlEngine()*. Deformations and earth pressures acting on the pipe at different vertical stresses are illustrated in Figure A-16.

```
print "------------Simulation started------------"
O=Omega()
## Define materials
# for DE particles
O.materials.append(NormalInelasticMat(young=10E7,poisson=0.3,frictionAngle=0.65, density=2650, label="sphere"))
# for interfaces
O.materials.append(NormalInelasticMat(young=10E7,poisson=0.3,frictionAngle=0.4, density=2650, label="interface"))
## load necessary files and generate FEM nodes, elements, loading conditions,..
# generate FE nodes
load_FE_nodes (filename = "fill_nodes.txt", ndim = 3, radius = 0.001)
# generate FE elements for soil domain
load_solid_elements (filename = "fill_FE_soil.txt", elementType = "Hexahedron20N8I", matFlag = "mohrCoulomb")
# generate FE shell element for pipe
load_shell_elements (filename = "fill_FE_shells.txt", thickness = 0.004, matFlag = "elastic")
# generate interfaces
load_interface_elements (filename = "fill_interfaces.txt", elementType = "Tri-interface", material ="interface")
# apply boundary conditions
load_restraint(filename = "fill_restraints.txt")
# apply material properties for FE soil elements
FE_MohrCoulomb(young = 20E6, gamma = 19, v = 0.3, c = 2, phi = 0.6, psi = 0, forShell = False)
# apply material properties for FE shell elements
```

```
FE_Elastic (young = 450E6, gamma = 15, v = 0.46, forShell = True)
# load spheres from input file
load_DE_spheres(filename = "sphere_nodes.txt", material ="sphere")
# generate the box
x_min, y_min, z_min = 0.0, 0.0, -0.1
x_max, y_max, z_max = 0.8, 0.15, 0.4
# determine id of the top wall
ID = len(O.bodies)
## add walls of the container, the bottom wall is not generated letting soil be in
contact with the FE domain.
# top wall
O.bodies.append(utils.box(center=[(x_min + x_max)/2,(y_min + y_max)/2,
z_max], extents=[(-x_min + x_max)/2, (-y_min + y_max)/2, 0],fixed=True,
wire=True))
# left wall
O.bodies.append(utils.box(center=[x_min,(y_min + y_max)/2,(z_min +
z_max)/2], extents=[0, (-y_min + y_max)/2,(-z_min + z_max)/2],fixed=True,
wire=True))
# right wall
O.bodies.append(utils.box(center=[x_max,(y_min + y_max)/2,(z_min +
z_max)/2], extents=[0, (-y_min + y_max)/2,(-z_min + z_max)/2],fixed=True,
wire=True))
# front wall
O.bodies.append(utils.box(center=[(x_min + x_max)/2,y_min,(z_min +
z_max)/2], extents=[(-x_min + x_max)/2 , 0, (-z_min + z_max)/2 ],fixed=True,
wire=True))
# behind wall
O.bodies.append(utils.box(center=[(x_min + x_max)/2,y_max,(z_min +
z_max)/2], extents=[(-x_min + x_max)/2 , 0, (-z_min + z_max)/2 ],fixed=True,
wire=True))
# loading steps:  vertical stress increases from 0 to 500 kPa
pressure = []
for i in range (0,11):
   pressure.append(i*50)
```

```
# enable graphical interface
from yade import qt
qt.View()
qt.Controller()
## Engines that run during simulation
O.engines= [
	ForceResetter(),
	ResetInteractingSphere(),
	SetHexahedron8N8IParameters(),
	# physical parameters of shell elements
	SetShellBT4(),
	SetInterfaceParameters(),
	SetGeoHexahedron(),
	# geometrical parameters of shell elements
       SetGeoShellBT4(),
	SetGeoQuadInterface(),
	# stresses, strains, body loads for brick elements
	TangentStiffnessCPPM(),
	# stresses, strains, body loads for shell elements
	ElasticShellSolver(),
	CheckConvergence(),
	DampingRayleigh(),
	SetMultiStepExternalForce(),
	setdtDEM(ratio = 0.9),
	InsertionSortCollider([
		Bo1_Sphere_Aabb(),
		Bo1_Box_Aabb(),
		Bo1_QuadInterface_Aabb()
		]),
	InteractionLoop([
		Ig2_Sphere_Sphere_ScGeom6D(),
		Ig2_Box_Sphere_ScGeom6D(),
```

```
                Ig2_Interface_Sphere_ScGeom6D()
                ],
                [Ip2_2xNormalInelasticMat_NormalInelasticityPhys()],
                [Law2_ScGeom6D_NormalInelasticityPhys_NormalInelasticity()]

        ),
        NewtonIntegrator(damping=0.1,gravity=[0, 0, -9.81]),
        # maintaining the vertical stress acting on top of the sample
        PressureControlEngine(id_top = ID, stress = pressure),
        setdtFEM(n = 100),
        CentralDifference(),
        OutputRecording()
        ]
print "------------Script ended------------"
```

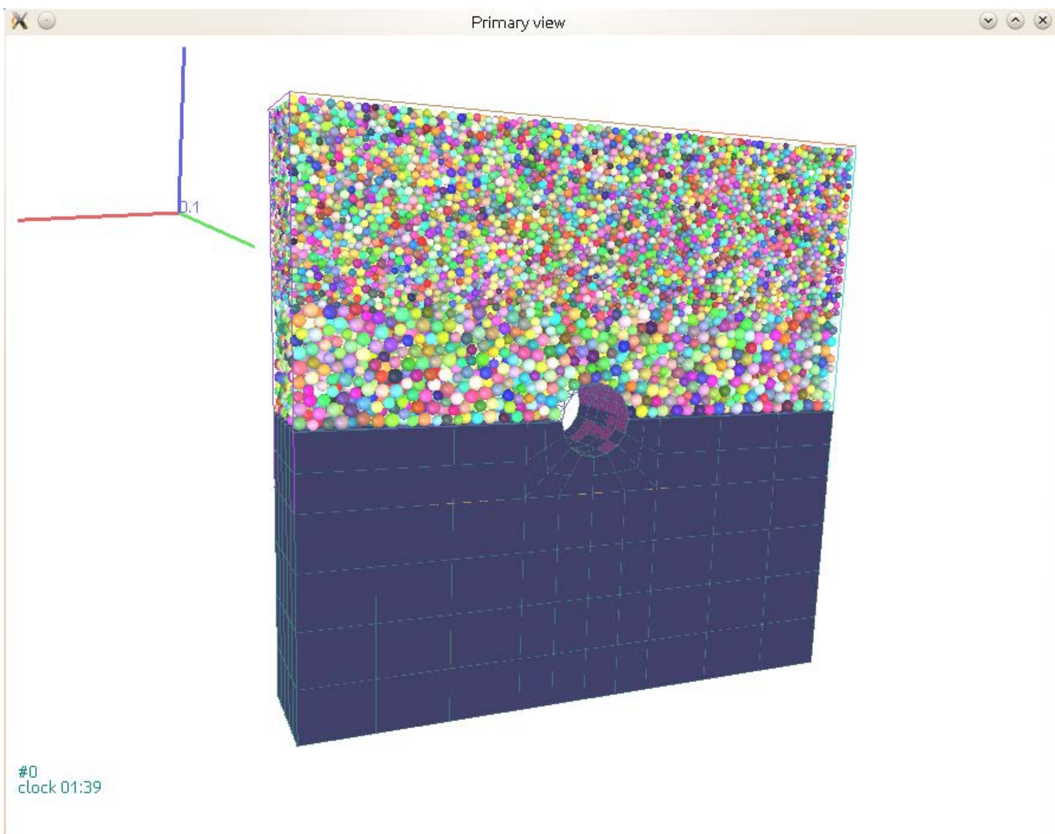

Figure A-16 Initial sample geometry for problem 8

In the coupled FE-DE analyis tool, some engines written in C++ have been developed and used to model certain geotechnical engineering problems including:

- ThreeDTriaxialEngine(): triaxial test
- KinemSimpleShearBox(): simple shear test
- KinemDirectShearBox(): direct shear test
- PressureControlEngine(): control pressure acting on a wall
- GeogridPulloutEngine(): geogrid pullout test
- FoundationLoadingEngine(): foundation bearing capacity
- TunnellingEngine(): tunnelling simulation.

A.3.8. Post-processing

It is necessary to interpret calculated data from export files. Users can use many tools to extract required data. In this section, python scripts and external packages are discussed.

A.3.8.1. Displacement field

Soil displacement fields can be generated by tracking movements of DE particles. Displacements of DE particles are calculated using *OutputRecording()* and saved in *DEdisplacementField.txt.* A displacement field can be plotted using Python, for example:

```
from pylab import *
# initial x-coordinates of DE particles
ini_X = []
# initial y-coordinates of DE particles
ini_Y = []
# initial z-coordinates of DE particles
ini_Z = []
```

```
# x-displacements of DE particles
Disp_X = []
# y-displacements of DE particles
Disp_Y = []
# z-displacements of DE particles
Disp_z = []
# get data from file
infile = open("DEdisplacementField.txt","r")
lines = infile.readlines()
for line in lines:
    data = line.split()
    ini_X.append(float(data[0]))
    ini_Y.append(float(data[1]))
    ini_Z.append(float(data[2]))
    Disp_X.append(float(data[3]))
    Disp_Y.append(float(data[4]))
    Disp_Z.append(float(data[5]))
figure()
Q = quiver( ini_X, ini_Z, Disp_X, Disp_Z,width = 0.01)
qk = quiverkey(Q, 0.5, 0.92, 0.000,"", labelpos='W', fontproperties={'weight': 'bold', 'size':52})
axis([min(ini_X), max(ini_X), min(ini_Z),max(ini_Z)])
xlabel("X (m)",size = 14)
ylabel("Z (m)",size = 14)
plt.show()
```

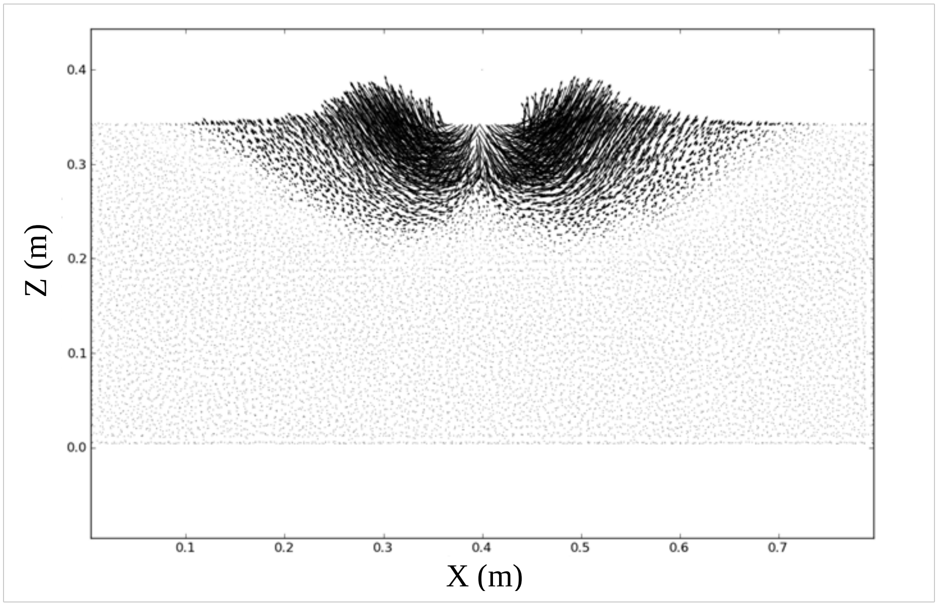

Figure A-17 Displacement field in the soil domain (problem 6)

A.3.8.2. Contact orientation

Contact orientations are obtained using *OutputRecording()* and saved in *contactOrientation.txt* The contact orientations of a DE sample in space are plotted using Python:

```
import pylab,math
import numpy as npy
import matplotlib.cm as cm
from matplotlib.pyplot import figure, show, rc
axis = 0
name = ""
# determine contacts in which plane will be plotted
if axis==0:
   name = "yz"
elif  axis==1:
   name = "xz"
else:
   name = "xy"
```

```
# open input file
Angle = []
NumIntr = []
infile = "contactOrientation.txt "
infile = open(infile,"r")
lines = infile.readlines()
for line in lines:
   data = line.split()
   Angle.append(float(data[0]))
   NumIntr.append(float(data[1]))
bins = len(Angle)
fc=[0,0,0]; fc[axis]=1.
# now plot
fig = figure(figsize=(6,6))
rect = fig.patch
rect.set_facecolor('white')
ax = fig.add_axes([0.1, 0.1, 0.8, 0.8], polar=True)
bars = ax.bar(Angle, NumIntr, width=2*math.pi/(1.1*bins),fc=fc)
for bar in bars:
   bar.set_facecolor( [1,1,1])
   bar.set_alpha(0.5)
show()
```

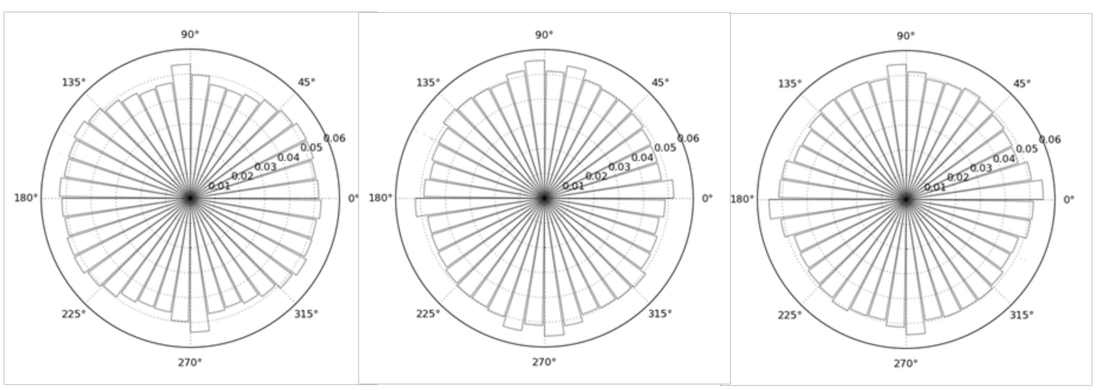

xz plane yz plane xy plane

Figure A-18 Distributions of contact orientation (problem 6)

A.3.8.3. Stresses in soil

Stresses in soil can be calculated based on contact forces between DE particles. In the framework, soil stresses are calculated using *OutputRecording() and* saved in *soilStress.txt. S*oil stresses can be plotted using Python:

```
import matplotlib
import numpy as np
import matplotlib.cm as cm
import matplotlib.mlab as mlab
import matplotlib.pyplot as plt
# devide the soil domain into grids num_row x num_col
num_row, num_col = 0, 0
min_X, max_X  = 0.0, 0.0
min_Z, max_Z = 0.0, 0.0
# x-stresses from file
sX = []
# z-stresses from file
sZ = []
infile = open("soilStress.txt","r")
lines = infile.readlines()
count = 0
for line in lines:
    count += 1
    data = line.split()
    # first line
    if count == 1:
            num_row = float(data[0])
            num_col = float(data[1])
            min_X = float(data[2])
            max_X = float(data[3])
            min_Z = float(data[4])
```

```
            max_Z = float(data[5])
    else:
            sX.append(float(data[0]))
            sZ.append(float(data[1]))
# stresses arranged in arrays
stress_X = []
stress_Z = []
count = 0
for i in range (0,  num_row):
    stress_X.append([])
    stress_Z.append([])
    for j in range (0, num_col):
            count = i*num_col + j
            stress_X[i].append(sX[count])
            stress_Z[i].append(sZ[count])
x = np.linspace(min_X, max_X, num_col)
z = np.linspace(min_Z, max_Z, num_row)
X, Z = np.meshgrid(x, z)
plt.figure()
CS = plt.contour(X, Z, stress_Z)
plt.axis([min_X, max_X, min_Z,max_Z])
plt.clabel(CS, inline=1, fontsize=8)
plt.title('Vertical stress')
plt.xlabel('X (m)',size = 8)
plt.ylabel('Y (m)',size = 8)
plt.show()
```

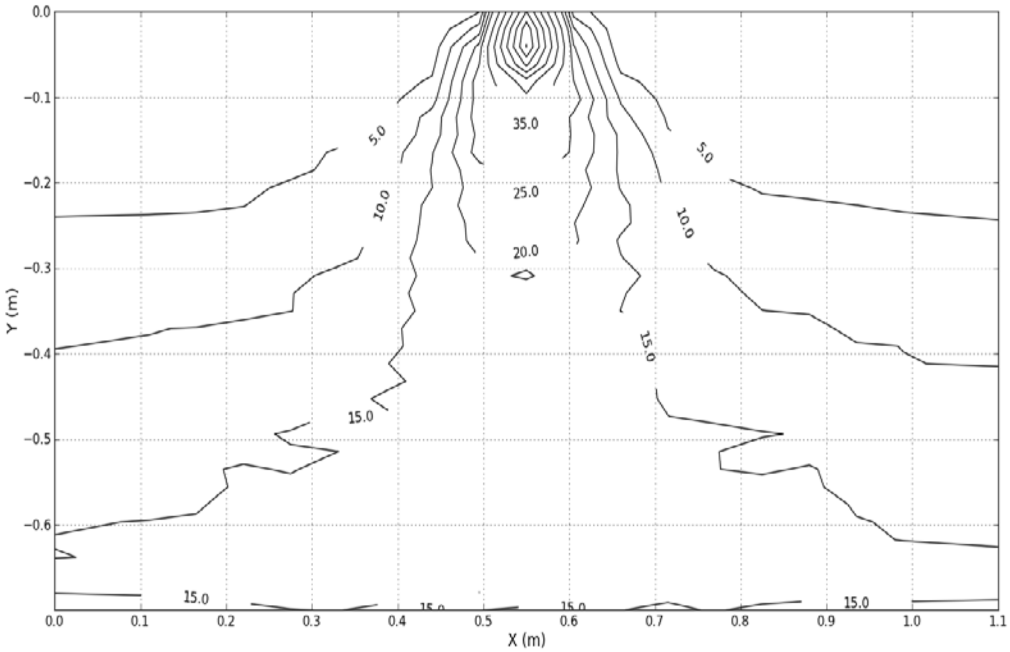

Figure A-19 Vertical stress distribution (problem 6)

A.3.8.4. Data analysis using GID

The FE analysis component can be performed by integrating the external package GID. During simulation, *FEanalysis_output.post.res* is generated using *OutputRecording(),* which can be read directly by GID. Deformed shapes, stresses and strains of DE domains can then be analyzed. Figure A-20 shows the deformed shape and tensile stress distribution of a FE geogrid during pullout test (problem 7) generated using GID. The deformations of the buried pipe and FE soil domain (problem 8) are presented in Figure A-21.

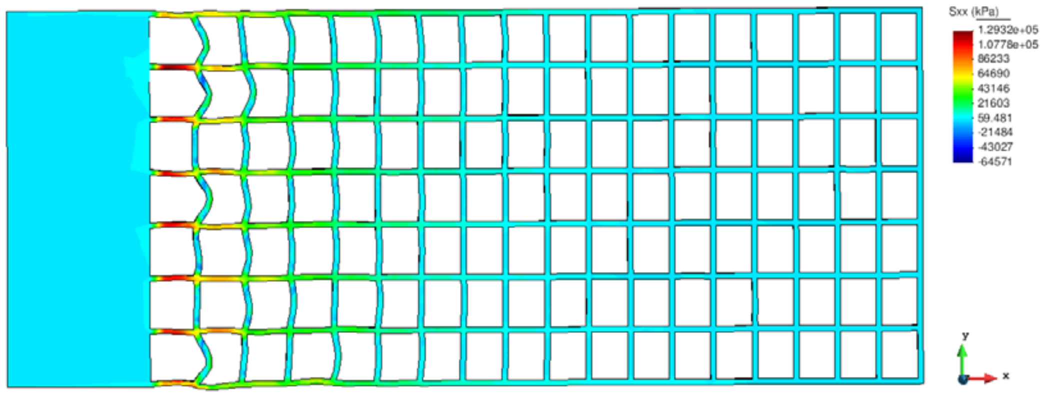

Figure A-20 Tensile stress of a geogrid during pullout test (problem 7)

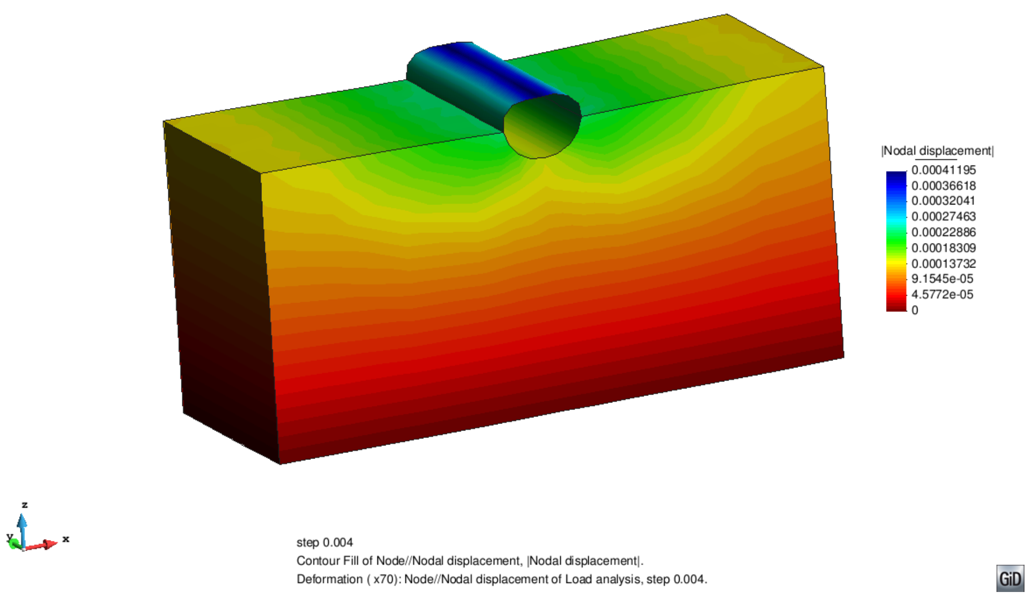

Figure A-21 Deformation of the buried pipe and the FE soil domain (problem 8)

A.3.8.5. Post-processing using PARAVIEW

The simulation can be visualized using PARAVIEW, which is an open-source, multi-platform data analysis and visualization application. The engine *VTKRecorder()* in YADE generates output files with the *.vtu* extension, which can be read by PARAVIEW. *VTKRecorder()* is added to the simulation loop:

```
O.engines= [
        #.....
        VTKRecorder(iterPeriod = 100, recorders = ["spheres", "colors"], filename = "paraview-" )
        ]
```

- iterPeriod: determine how often to save simulation data
- recorders: determine what data to be saved
- filename: prefix of saved files

An example that illustrates the strain field of a soil sample during geogrid pullout test (problem 7) is shown in Figure A-22:

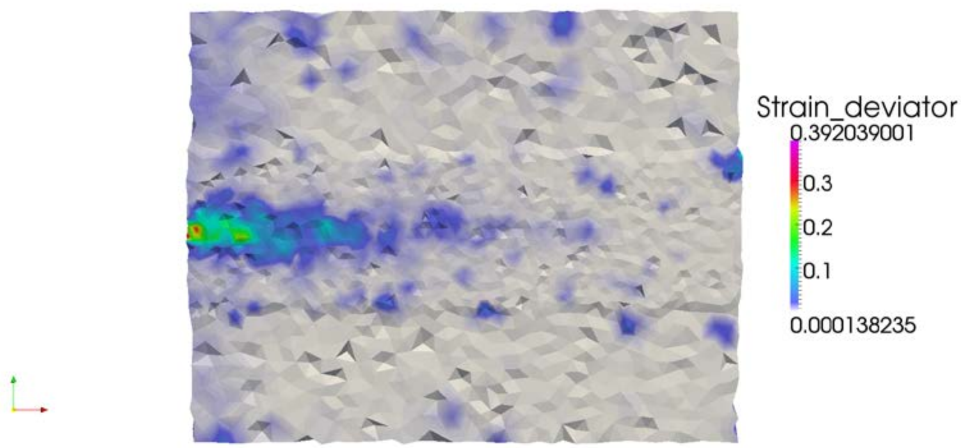

Figure A-22 Strain field in the soil domain (problem 7)

A.3.8.6. 3D rendering and videos

There are several ways to produce a video of simulation:

- Use VTKRecorder() and generate videos in PARAVIEW.
- Capture screen output using the available tools in LINUX such as recordMyDesktop and Istanbul.
- Use SnapshotEngine():

```
O.engines= [
        #.....
```

SnapshotEngine (iterPeriod = 100, fileBase = "video-")

]

The exported image files can be merged externally to generate videos.

A.4. C++ ENGINES

A.4.1. C++ Codes

Engines of the coupled FE-DE framework are written in C++. Most C++ classes are wrapped in Python which allows them to be called from Python scripts. C++ codes written in YADE have the following features:

- **Essentials**:

  compiler: YADE uses *g++* as C++ compiler.

  boost: YADE uses extensively *boost* library.

  python: python is the scripting language of the coupled FE-DE framework.

- **Optional libraries**:

  log4cxx

  opengl

  vtk

  openmp

  gts

  cgal

  ...

- **Extensions**: C++ source files have *.hpp* extension for headers and *.cpp* for implementation.

- **Pointers**: Extensive use of shared pointers *shared_ptr*.

- **Typecasting**: shared pointers can have dynamic (*dynamic_pointer_cast*) or static casting (*static_pointer_cast.* YADE provides two macros:

  YADE_CAST: expands to *static_cast* in optimized builds and *dynamic_cast* in debug builds.

YADE_PTR_CAST: expands to *static_ptr_cast* in optimized builds and *dynamic_ptr_cast* in debug builds.

A.4.2. C++ Framework

- Scene**:** is the object containing the whole simulation. All engines and functors have a *Scene* scene* pointer which assures the current scene can be accessed from codes.
- BodyContainer: contains all bodies of a simulation. *BodyContainer* stores bodies using their *shared_ptr*.

  A new body can be inserted in C++:

  ```
  scene = shared_ptr<Scene>(new Scene);
  shared_ptr<Body> femElement;
  createElement(femElement);  //define element
  scene ->bodies->insert(femElement);
  ```

  BodyContainer can be iterated using FOREACH macro:

  ```
  FOREACH(const shared_ptr<Body> & body, *scene->bodies) {
          if (body->groupMask==1)  {
                  //do something
                  }
  }
  ```
- InteractionContainer: stores interactions during simulation. Interactions between particles are identified by a pair of ids of the two particles. s*hared_ptr* storage is used by I*nteractionContainer*. Iteration over interactions can be handled using *FOREACH* or:

  ```
  InteractionContainer::iterator ii    = scene->interactions->begin();
  InteractionContainer::iterator iiEnd = scene->interactions->end();
  for(  ; ii!=iiEnd ; ++ii ) {
          if ((*ii)->isReal()) {
                  //do something
          }
  ```

}

- ForceContainer: stores forces and torques of each body.

  Adding a force to a body in C++ :

  scene->forces.addForce(id, force);

  Getting force acting on a body:

  scene->forces.sync(); //sync before reading
  Vector3r f = scene->forces.getForce(id);

- Handling interactions: the following actions are performed to handle interactions:
  Potential interactions are identified using *Collider*.
  InteractionLoop calls appropriate *IGeomFunctor* based on *Shape* of both bodies.
  InteractionLoop calls appropriate *IPhysFunctor* based on *Material* of both bodies.
  InteractionLoop calls appropriate *LawFunctor* based on *IGeom* and *IPhys* of the interaction.

A.4.3. Omega Class

All simulation-related functionality is handled by *Omega* class. In the current scene, *Omega.materials* corresponds to *Scene::materials*, which is the same for *bodies*, *interactions*, *engines*, *iter*, *dt*, *time*, *realtime* and *stopAtIter*.

A.4.4. Wrapping C++ Classes

All C++ classes deriving from *Serializable* can be called from Python. This is achieved via *YADE_CLASS_BASE_DOC_* macro family*.

REFERENCES

Abu-Farsakh, Murad, CHEN QIMING, Radhey Sharma, and Xiong Zhang (2008) "Large-Scale Model Footing Tests on Geogrid-Reinforced Foundation and Marginal Embankment Soils," ASTM geotechnical testing journal, Vol. 31, No. 5, pp 413-423.

Adams, M.T., and Collin, J.G. (1997) "Large model spread footing load tests on geosynthetic reinforced soil foundations," Journal of Geotechnical and Geoenvironmental Engineering, Vol. 123, No. 1, pp 66-72.

Agaiby, Sherif W, and Colin JFP Jones (1995) "Design of reinforced fill systems over voids," Canadian Geotechnical Journal, Vol. 32, No. 6, pp 939-945.

Alagiyawanna, AMN, M Sugimoto, S Sato, and H Toyota (2001) "Influence of longitudinal and transverse members on geogrid pullout behavior during deformation," Geotextiles and Geomembranes, Vol. 19, No. 8, pp 483-507.

Andresen, Lars, Hans Petter Jostad, and Knut H Andersen (2011) "Finite Element Analyses Applied in Design of Foundations and Anchors for Offshore Structures," International Journal of Geomechanics, Vol. 11, No. 6, pp 417-430.

Bagi, Katalin (2006) "Analysis of microstructural strain tensors for granular assemblies," International Journal of Solids and Structures, Vol. 43, No. 10, pp 3166-3184.

Basudhar, PK, Santanu Saha, and Kousik Deb (2007) "Circular footings resting on geotextile-reinforced sand bed," Geotextiles and Geomembranes, Vol. 25, No. 6, pp 377-384.

Belheine, N, J-P Plassiard, F-V Donzé, F Darve, and A Seridi (2009) "Numerical simulation of drained triaxial test using 3D discrete element modeling," Computers and Geotechnics, Vol. 36, No. 1, pp 320-331.

Berezantzev, V. G. (1958) "Earth pressure on the cylindrical retaining walls," Conference on earth pressure problems, Brussels, pp 21-27.

Bergado, Dennes T, and Jin-Chun Chai (1994) "Pullout force/displacement relationship of extensible grid reinforcements," Geotextiles and Geomembranes, Vol. 13, No. 5, pp 295-316.

Bfer, G (1985) "An isoparametric joint/interface element for finite element analysis," International journal for numerical methods in engineering, Vol. 21, No. 4, pp 585-600.

Bhuvaraghan, Baskaran, Sivakumar M Srinivasan, Bob Maffeo, Robert D McCLain, Yogesh Potdar, and Om Prakash (2010) "Shot peening simulation using discrete and finite element methods," Advances in Engineering Software, Vol. 41, No. 12, pp 1266-1276.

Binquet, Jean, and Kenneth L Lee (1975) "Bearing capacity analysis of reinforced earth slabs," Journal of the geotechnical Engineering Division, Vol. 101, No. 12, pp 1257-1276.

Binquet, Jean, and Kenneth L Lee (1975) "Bearing capacity tests on reinforced earth slabs," Journal of the geotechnical Engineering Division, Vol. 101, No. 12, pp 1241-1255.

Briancon, LAURENT, and Pascal Villard (2008) "Design of geosynthetic-reinforced platforms spanning localized sinkholes," Geotextiles and Geomembranes, Vol. 26, No. 5, pp 416-428.

Bridle, R.J., Jenner, C.G., and Barr, B. (1994) "Novel applications of geogrids in areas of shallow mineworkings," 5th Int Conf on Geotextiles, Geomembranes and Related Products, Singapore, Vol. 1, pp 297-300.

Calvetti, Francesco (2008) "Discrete modelling of granular materials and geotechnical problems," European Journal of Environmental and Civil Engineering, Vol. 12, No. 7-8, pp 951-965.

Chen, Cheng, GR McDowell, and NH Thom (2012) "Discrete element modelling of cyclic loads of geogrid-reinforced ballast under confined and unconfined conditions," Geotextiles and Geomembranes, Vol. 35, pp 76-86.

Chen, Q., Abu-Farsakh, M., Sharma, R., and Zhang, X. (2007) "Laboratory investigation of behavior of foundations on geosynthetic-reinforced clayey soil," Transportation Research Record: Journal of the Transportation Research Board, Vol. 2004, pp 28–38.

Chen, Qiming, Murad Abu-Farsakh, and Radhey Sharma (2009) "Experimental and Analytical studies of reinforced crushed limestone," Geotextiles and Geomembranes, Vol. 27, No. 5, pp 357-367.

Cheng, YM, YY Hu, and WB Wei (2007) "General axisymmetric active earth pressure by method of characteristics—theory and numerical formulation," International Journal of Geomechanics, Vol. 7, No. 1, pp 1-15.

Cheng, Y. M., and Hu, Y. Y. (2005) "Active earth pressure on circular shaft lining obtained by simplified slip line solution with general tangential stress coefficient," Chinese Journal of Geotechnical Engineering, Vol. 27, No. 1, pp 110-115.

Cheung, G. (2010) "Micromechanics of sand production in oil wells," Ph.D thesis, Imperial College London.

Choudhary, AK, JN Jha, and KS Gill (2010) "Laboratory investigation of bearing capacity behaviour of strip footing on reinforced flyash slope," Geotextiles and Geomembranes, Vol. 28, No. 4, pp 393-402.

Chun, B., and Shin, Y. (2006) "Active earth pressure acting on the cylindrical retaining wall of a shaft," South Korea Ground and Environmental Engineering Journal, Vol. 7, No. 4, pp 15-24.

Chung, Wilson, and Giovanni Cascante (2007) "Experimental and numerical study of soil-reinforcement effects on the low-strain stiffness and bearing capacity of shallow foundations," Geotechnical and Geological Engineering, Vol. 25, No. 3, pp 265-281.

Costa, Yuri D, Jorge G Zornberg, Benedito S Bueno, and Carina L Costa (2009) "Failure mechanisms in sand over a deep active trapdoor," Journal of Geotechnical and Geoenvironmental Engineering, Vol. 135, No. 11, pp 1741-1753.

Costalonga, M.A.R. (1988) "Geogrid pull-out tests in clay," MSc. Dissertation, The University of Alberta, Alberta, Canada.

Costalonga, M.A.R. (1990) "Geogrid pull-out tests in clay," 4th International Conference on Geotextiles, Geomembranes and Related Products, The Hague, The Netherlands, Vol. 2.

Cui, L, and C O'Sullivan (2006) "Exploring the macro-and micro-scale response of an idealised granular material in the direct shear apparatus," Geotechnique, Vol. 56, No. 7, pp 455-468.

Cui, L, C O'sullivan, and S O'neill (2007) "An analysis of the triaxial apparatus using a mixed boundary three-dimensional discrete element model," Geotechnique, Vol. 57, No. 10, pp 831-844.

Cundall, Peter A, and Otto DL Strack (1979) "A discrete numerical model for granular assemblies," Geotechnique, Vol. 29, No. 1, pp 47-65.

Dang, HK, and MA Meguid (2009) "Algorithm to generate a discrete element specimen with predefined properties," International Journal of Geomechanics, Vol. 10, No. 2, pp 85-91.

Dang, HK, and MA Meguid (2010) "Evaluating the performance of an explicit dynamic relaxation technique in analyzing non-linear geotechnical engineering problems," Computers and Geotechnics, Vol. 37, No. 1, pp 125-131.

Dang, HK, and MA Meguid (2013) "An efficient finite–discrete element method for quasi-static nonlinear soil–structure interaction problems," International journal for numerical and analytical methods in geomechanics, Vol. 37, No. 2, pp 130-149.

Das, BM, EC Shin, and MT Omar (1994) "The bearing capacity of surface strip foundations on geogrid-reinforced sand and clay—a comparative study," Geotechnical & Geological Engineering, Vol. 12, No. 1, pp 1-14.

Dash, Sujit Kumar, NR Krishnaswamy, and K Rajagopal (2001) "Bearing capacity of strip footings supported on geocell-reinforced sand," Geotextiles and Geomembranes, Vol. 19, No. 4, pp 235-256.

Deluzarche, R, and B Cambou (2006) "Discrete numerical modelling of rockfill dams," International journal for numerical and analytical methods in geomechanics, Vol. 30, No. 11, pp 1075-1096.

Dhia, Hachmi Ben (1998) "Problèmes mécaniques multi-échelles: la méthode Arlequin," Comptes Rendus de l'Académie des Sciences-Series IIB-Mechanics-Physics-Astronomy, Vol. 326, No. 12, pp 899-904.

Dhia, Hashmi Ben, and Guillaume Rateau (2005) "The Arlequin method as a flexible engineering design tool," International journal for numerical methods in engineering, Vol. 62, No. 11, pp 1442-1462.

Duriez, J, F Darve, and F-V Donze (2011) "A discrete modeling-based constitutive relation for infilled rock joints," International journal of rock mechanics and mining sciences, Vol. 48, No. 3, pp 458-468.

Dyer, M.R. (1985) "Observations of the stress distribution in crushed glass with applications to soil reinforcement," D.Phil. Thesis, University of Oxford, Oxford, UK.

Elmekati, Ahmed, and Usama El Shamy (2010) "A practical co-simulation approach for multiscale analysis of geotechnical systems," Computers and Geotechnics, Vol. 37, No. 4, pp 494-503.

Faheem, Hamdy, Fei Cai, and Keizo Ugai (2004) "Three-dimensional base stability of rectangular excavations in soft soils using FEM," Computers and Geotechnics, Vol. 31, No. 2, pp 67-74.

Fakhimi, Ali (2009) "A hybrid discrete–finite element model for numerical simulation of geomaterials," Computers and Geotechnics, Vol. 36, No. 3, pp 386-395.

Farrag, Khalid, Yalcin B Acar, and Ilan Juran (1993) "Pull-out resistance of geogrid reinforcements," Geotextiles and Geomembranes, Vol. 12, No. 2, pp 133-159.

Finno, Richard J, J Tanner Blackburn, and Jill F Roboski (2007) "Three-dimensional effects for supported excavations in clay," Journal of Geotechnical and Geoenvironmental Engineering, Vol. 133, No. 1, pp 30-36.

Gabr, MA, and TJ Hunter (1994) "Stress-strain analysis of geogrid-supported liners over subsurface cavities," Geotechnical & Geological Engineering, Vol. 12, No. 2, pp 65-86.

Gabr, M.A., Hunter, T.J., and Collin, J.G. (1992) "Stability of geogrid-reinforced landfill liners over sinkholes," Proceedings, Earth Reinforcement practice. Edited by H . Ochiai, S. Hayashi and J. Otani. A.A. Balkema, pp 595-600.

Gabrieli, Fabio, Simonetta Cola, and Francesco Calvetti (2009) "Use of an up-scaled DEM model for analysing the behaviour of a shallow foundation on a model slope," Geomechanics and Geoengineering: An International Journal, Vol. 4, No. 2, pp 109-122.

Gaetano, E.A. (2010) "The response of flexible pavement systems to local deterioration of the base layer," Master thesis, McGill University.

Galli, G, ANTONIO Grimaldi, and A Leonardi (2004) "Three-dimensional modelling of tunnel excavation and lining," Computers and Geotechnics, Vol. 31, No. 3, pp 171-183.

Garikipati, K.R. and Hughes, T.J.R. (1998) "A study of strain localization in a multiple scale framework—the one dimensional problem," Comput. Methods Appl. Mech. Eng., Vol. 159, pp 193–222.

Ghazavi, Mahmoud, and Arash Alimardani Lavasan (2008) "Interference effect of shallow foundations constructed on sand reinforced with geosynthetics," Geotextiles and Geomembranes, Vol. 26, No. 5, pp 404-415.

Ghosh, Ambarish, and Utpal Dey (2009) "Bearing ratio of reinforced fly ash overlying soft soil and deformation modulus of fly ash," Geotextiles and Geomembranes, Vol. 27, No. 4, pp 313-320.

Giroud, JP, R Bonaparte, JF Beech, and BA Gross (1990) "Design of soil layer-geosynthetic systems overlying voids," Geotextiles and Geomembranes, Vol. 9, No. 1, pp 11-50.

Guido, Vito A, Dong K Chang, and Michael A Sweeney (1986) "Comparison of geogrid and geotextile reinforced earth slabs," Canadian Geotechnical Journal, Vol. 23, No. 4, pp 435-440.

Han, Jie, Anil Bhandari, and Fei Wang (2011) "DEM analysis of stresses and deformations of geogrid-reinforced embankments over piles," International Journal of Geomechanics, Vol. 12, No. 4, pp 340-350.

Han, K, DRJ Owen, and D Peric (2002) "Combined finite/discrete element and explicit/implicit simulations of peen forming process," Engineering Computations, Vol. 19, No. 1, pp 92-118.

Herten, Markus, and Matthias Pulsfort (1999) "Determination of spatial earth pressure on circular shaft constructions," Granular matter, Vol. 2, No. 1, pp 1-7.

Huang, CC, and FY Menq (1997) "Deep-footing and wide-slab effects in reinforced sandy ground," Journal of Geotechnical and Geoenvironmental Engineering, Vol. 123, No. 1, pp 30-36.

Huang, Ching-Chuan, and Fumio Tatsuoka (1990) "Bearing capacity of reinforced horizontal sandy ground," Geotextiles and Geomembranes, Vol. 9, No. 1, pp 51-82.

Hughes, Thomas JR (1995) "Multiscale phenomena: Green's functions, the Dirichlet-to-Neumann formulation, subgrid scale models, bubbles and the origins of stabilized methods," Computer methods in applied mechanics and engineering, Vol. 127, No. 1, pp 387-401.

Imamura, S., Nomoto, T., Fujii, T., and Hagiwara, T. (1999) "Earth pressures acting on a deep shaft and the movements of adjacent ground in sand," Proceedings of the international symposium on geotechnical aspects of underground construction in soft ground. Tokyo, Japan: Balkema, Rotterdam, pp 647-652.

Itasca (2004) "PFC 2D 3.10 Particle Flow Code in two dimensions, theory and background volume (third ed.)," Minneapolis, Minnesota.

Jenck, Orianne, Daniel Dias, and Richard Kastner (2009) "Discrete element modelling of a granular platform supported by piles in soft soil–Validation on a small scale model test and comparison to a numerical analysis in a continuum," Computers and Geotechnics, Vol. 36, No. 6, pp 917-927.

Jewell, R. (1980) "Some effects of reinforcement on soils," PhD. Thesis, University of Cambridge, UK.

Jiang, MJ, JM Konrad, and S Leroueil (2003) "An efficient technique for generating homogeneous specimens for DEM studies," Computers and Geotechnics, Vol. 30, No. 7, pp 579-597.

Karabatakis, DA, and TN Hatzigogos (2002) "Analysis of creep behaviour using interface elements," Computers and Geotechnics, Vol. 29, No. 4, pp 257-277.

Karthigeyan, S, VVGST Ramakrishna, and K Rajagopal (2007) "Numerical investigation of the effect of vertical load on the lateral response of piles," Journal of Geotechnical and Geoenvironmental Engineering, Vol. 133, No. 5, pp 512-521.

Kasper, Thomas, and Günther Meschke (2004) "A 3D finite element simulation model for TBM tunnelling in soft ground," International journal for numerical and analytical methods in geomechanics, Vol. 28, No. 14, pp 1441-1460.

Khedkar, MS, and JN Mandal (2009) "Pullout behaviour of cellular reinforcements," Geotextiles and Geomembranes, Vol. 27, No. 4, pp 262-271.

Khing, KH, BM Das, VK Puri, EE Cook, and SC Yen (1993) "The bearing-capacity of a strip foundation on geogrid-reinforced sand," Geotextiles and Geomembranes, Vol. 12, No. 4, pp 351-361.

Khodair, Yasser A., and Sophia Hassiotis (2005) "Analysis of soil–pile interaction in integral abutment," Computers and Geotechnics, Vol. 32, No. 3, pp 201-209.

Kinney, Thomas C, and Billy Connor (1987) "Geosynthetics supporting embankments over voids," Journal of cold regions engineering, Vol. 1, No. 4, pp 158-170.

Konig, D., Guettler, U., and Jessberger, H. L. (1991) "Stress redistribution during tunnel and shaft construction," Proceedings of the International Conference Centrifuge 1991, Boulder, Colorado, pp 129-135.

Koutsabeloulis, NC, and DV Griffiths (1989) "Numerical modelling of the trap door problem," Geotechnique, Vol. 39, No. 1, pp 77-89.

Kozicki, J, and FV Donzé (2009) "Yade-open dem: an open-source software using a discrete element method to simulate granular material," Engineering Computations, Vol. 26, No. 7, pp 786-805.

Kumar, Arvind, and Swami Saran (2003) "Bearing capacity of rectangular footing on reinforced soil," Geotechnical & Geological Engineering, Vol. 21, No. 3, pp 201-224.

Kurian, Nainan P, KS Beena, and R Krishna Kumar (1997) "Settlement of reinforced sand in foundations," Journal of Geotechnical and Geoenvironmental Engineering, Vol. 123, No. 9, pp 818-827.

Labra, Carlos, and Eugenio Onate (2009) "High-density sphere packing for discrete element method simulations," Communications in Numerical Methods in Engineering, Vol. 25, No. 7, pp 837-849.

Ladd, R. S. (1978) "Preparing test specimens using undercompaction," Geotechnical Testing Journal, GTJODJ 1978, Vol. 1, No. 1, pp 16-23.

Lade, P. V., Jessberger, H. L., Makowski, E., and Jordan, P. (1981) "Modeling of deep shafts in centrifuge test," Proceedings of the International Conference on Soil Mechanics and Foundation Engineering, Stockholm, Sweden, Vol. 1, pp 683-691.

Latha, G Madhavi, and Amit Somwanshi (2009) "Bearing capacity of square footings on geosynthetic reinforced sand," Geotextiles and Geomembranes, Vol. 27, No. 4, pp 281-294.

Lawson, C.R., Jones, C.J.F.P., Kempton, G.T., and Passaris, E.K.S. (1994) "Advanced analysis of reinforced fills over areas prone to subsidence," Proceedings, 5th International Conference on Geotextiles, Geomembranes and Related Products. A.A. Balkema, Singapore, Vol. 1, pp 311-317.

Li, Fu-Lin, Fang-Le Peng, Yong Tan, W Kongkitkul, and MSA Siddiquee (2012) "FE simulation of viscous behavior of geogrid-reinforced sand under laboratory-scale plane-strain-compression testing," Geotextiles and Geomembranes, Vol. 31, pp 72-80.

Liu, SH, De’an Sun, and Hajime Matsuoka (2005) "On the interface friction in direct shear test," Computers and Geotechnics, Vol. 32, No. 5, pp 317-325.

Lobo-Guerrero, S, and LE Vallejo (2005) "DEM analysis of crushing around driven piles in granular materials," Geotechnique, Vol. 55, No. 8.

Lobo-Guerrero, Sebastian, and Luis E Vallejo (2006) "Discrete element method analysis of railtrack ballast degradation during cyclic loading," Granular matter, Vol. 8, No. 3-4, pp 195-204.

Madhavi Latha, G, and Amit Somwanshi (2009) "Effect of reinforcement form on the bearing capacity of square footings on sand," Geotextiles and Geomembranes, Vol. 27, No. 6, pp 409-422.

Maheshwari, BK, KZ Truman, PL Gould, and MH El Naggar (2005) "Three-dimensional nonlinear seismic analysis of single piles using finite element model: effects of plasticity of soil," International Journal of Geomechanics, Vol. 5, No. 1, pp 35-44.

Maynar, Manuel J, and Luis E Rodríguez (2005) "Discrete numerical model for analysis of earth pressure balance tunnel excavation," Journal of Geotechnical and Geoenvironmental Engineering, Vol. 131, No. 10, pp 1234-1242.

McDowell, G.R., Harireche, O., Konietzky, H., Brown, S.F., Thom, N.H. (2006) "Discrete element modelling of geogrid-reinforced aggregates," Proceedings of the ICE - Geotechnical Engineering, Vol. 159, No. 1, pp 35-48.

Meguid, MA, and HK Dang (2009) "The effect of erosion voids on existing tunnel linings," Tunnelling and Underground Space Technology, Vol. 24, No. 3, pp 278-286.

Meguid, MA, and RK Rowe (2006) "Stability of D-shaped tunnels in a Mohr Coulomb material under anisotropic stress conditions," Canadian Geotechnical Journal, Vol. 43, No. 3, pp 273-281.

Meyerhof, GG, and AM Hanna (1978) "Ultimate bearing capacity of foundations on layered soils under inclined load," Canadian Geotechnical Journal, Vol. 15, No. 4, pp 565-572.

Michalowski, Radoslaw L (2004) "Limit loads on reinforced foundation soils," Journal of Geotechnical and Geoenvironmental Engineering, Vol. 130, No. 4, pp 381-390.

Michalowski, Radoslaw L, and Lei Shi (2003) "Deformation patterns of reinforced foundation sand at failure," Journal of Geotechnical and Geoenvironmental Engineering, Vol. 129, No. 5, pp 439-449.

Milligan, G.W.E., Earl, R.F., Bush, D.I. (1990) "Observations of photo-elastic pullout tests on geotextiles and geogrids," 4th International Conference on Geotextiles, Geomembranes and Related Products, The Hague, The Netherlands, Vol. 2, pp 747-751.

Mohamed, MHA (2010) "Two dimensional experimental study for the behaviour of surface footings on unreinforced and reinforced sand beds overlying soft pockets," Geotextiles and Geomembranes, Vol. 28, No. 6, pp 589-596.

Moraci, Nicola, and Piergiorgio Recalcati (2006) "Factors affecting the pullout behaviour of extruded geogrids embedded in a compacted granular soil," Geotextiles and Geomembranes, Vol. 24, No. 4, pp 220-242.

Mroueh, Hussein, and Isam Shahrour (2002) "Three-dimensional finite element analysis of the interaction between tunneling and pile foundations," International journal for numerical and analytical methods in geomechanics, Vol. 26, No. 3, pp 217-230.

Ng, Tang-Tat (2004) "Triaxial test simulations with discrete element method and hydrostatic boundaries," Journal of engineering mechanics, Vol. 130, No. 10, pp 1188-1194.

O’Sullivan, C. (2011) "Particulate discrete element modeling, a geomechanics perspective," Spon Press.

Ochiai, Hidetoshi, Jun Otani, Shigenori Hayashic, and Takao Hirai (1996) "The pull-out resistance of geogrids in reinforced soil," Geotextiles and Geomembranes, Vol. 14, No. 1, pp 19-42.

Onate, E, and J Rojek (2004) "Combination of discrete element and finite element methods for dynamic analysis of geomechanics problems," Computer methods in applied mechanics and engineering, Vol. 193, No. 27, pp 3087-3128.

Osman, Ashraf S, and Mark F Randolph (2011) "Analytical Solution for the Consolidation around a Laterally Loaded Pile," International Journal of Geomechanics, Vol. 12, No. 3, pp 199-208.

O'Sullivan, Catherine, and Liang Cui (2009) "Micromechanics of granular material response during load reversals: Combined DEM and experimental study," Powder Technology, Vol. 193, No. 3, pp 289-302.

Palmeira, E.M. (1987) "The study of soil-reinforcement interaction by means of large scale laboratory tests," DPhil. Thesis, University of Oxford, Oxford, UK.

Palmeira, Ennio Marques (2004) "Bearing force mobilisation in pull-out tests on geogrids," Geotextiles and Geomembranes, Vol. 22, No. 6, pp 481-509.

Palmeira, Ennio Marques (2009) "Soil–geosynthetic interaction: Modelling and analysis," Geotextiles and Geomembranes, Vol. 27, No. 5, pp 368-390.

Pan, JL, ATC Goh, KS Wong, and AR Selby (2002) "Three-dimensional analysis of single pile response to lateral soil movements," International journal for numerical and analytical methods in geomechanics, Vol. 26, No. 8, pp 747-758.

Park, Jung-Wook, and Jae-Joon Song (2009) "Numerical simulation of a direct shear test on a rock joint using a bonded-particle model," International journal of rock mechanics and mining sciences, Vol. 46, No. 8, pp 1315-1328.

Patra, CR, BM Das, M Bhoi, and EC Shin (2006) "Eccentrically loaded strip foundation on geogrid-reinforced sand," Geotextiles and Geomembranes, Vol. 24, No. 4, pp 254-259.

Poorooshasb, Hormoz B (1991) "Load settlement response of a compacted fill layer supported by a geosynthetic overlying a void," Geotextiles and Geomembranes, Vol. 10, No. 3, pp 179-201.

Potyondy, DO, and PA Cundall (2004) "A bonded-particle model for rock," International journal of rock mechanics and mining sciences, Vol. 41, No. 8, pp 1329-1364.

Prater, EG (1977) "An examination of some theories of earth pressure on shaft linings," Canadian Geotechnical Journal, Vol. 14, No. 1, pp 91-106.

Sadoglu, Erol, Evrim Cure, Berkan Moroglu, and Bayram Ali Uzuner (2009) "Ultimate loads for eccentrically loaded model shallow strip footings on geotextile-reinforced sand," Geotextiles and Geomembranes, Vol. 27, No. 3, pp 176-182.

Salgado, R, and M Prezzi (2007) "Computation of cavity expansion pressure and penetration resistance in sands," International Journal of Geomechanics, Vol. 7, No. 4, pp 251-265.

Schlosser, F., Jacobsen, H.M., and Juran, I. (1983) "Soil reinforcement," Genereal Report, Eighth European Conference on Soil Mechanics and Foundation Engineering, Balkema, Helsinki, pp 83–103.

Sharma, Radhey, Qiming Chen, Murad Abu-Farsakh, and Sungmin Yoon (2009) "Analytical modeling of geogrid reinforced soil foundation," Geotextiles and Geomembranes, Vol. 27, No. 1, pp 63-72.

Shin, E.C., Das, B.M., Puri, V.K., Yen, S.C., and Cook, E.E. (1993) "Bearing capacity of strip foundation on geogrid-reinforced clay," Geotechnical Testing Journal, ASTM, Vol. 16, No. 4, pp 534–541.

Siddiquee, MSA, and CC Huang (2001) "FEM simulation of the bearing capacity of level reinforced sand ground subjected to footing load," Geosynthetics International, Vol. 8, No. 6, p 501.

Sieira, Ana Cristina CF, Denise Gerscovich, and Alberto SFJ Sayão (2009) "Displacement and load transfer mechanisms of geogrids under pullout condition," Geotextiles and Geomembranes, Vol. 27, No. 4, pp 241-253.

Šmilauer, V., Catalano, E., Chareyre, B., Dorofeenko, S., Duriez, J., Gladky, A., Kozicki, J., Modenese, C., Scholtès, L., Sibille, L., Stránský, J., and Thoeni, K. (2010) "Yade Documentation," The Yade Project 2010. (http://yade-dem.org/doc/).

Sugimoto, M, and AMN Alagiyawanna (2003) "Pullout behavior of geogrid by test and numerical analysis," Journal of Geotechnical and Geoenvironmental Engineering, Vol. 129, No. 4, pp 361-371.

Sugimoto, M, AMN Alagiyawanna, and K Kadoguchi (2001) "Influence of rigid and flexible face on geogrid pullout tests," Geotextiles and Geomembranes, Vol. 19, No. 5, pp 257-277.

Tafreshi, SN, and AR Dawson (2010) "Behaviour of footings on reinforced sand subjected to repeated loading–Comparing use of 3D and planar geotextile," Geotextiles and Geomembranes, Vol. 28, No. 5, pp 434-447.

Terzaghi, K. (1936) "Stress distribution in dry and saturated sand above a yielding trap door," Proceedings, International Conference of Soil Mechanics, Harvard University, Cambridge, Mass., Vol. 1, pp 307-311.

Terzaghi, K. (1943) "Theoretical soil mechanics," New York: John Wiley & sons Inc.

Thornton, Colin, and Ling Zhang (2003) "Numerical simulations of the direct shear test," Chemical engineering & technology, Vol. 26, No. 2, pp 153-156.

Tobar, T. (2009) "An experimental study of the earth pressure distribution on cylindrical shafts," Master’s thesis, McGill University.

Tobar, Tatiana, and Mohamed A Meguid (2011) "Experimental study of the earth pressure distribution on cylindrical shafts," Journal of Geotechnical and Geoenvironmental Engineering, Vol. 137, No. 11, pp 1121-1125.

Tran, VDH, MA Meguid, and LE Chouinard (2013) "A finite–discrete element framework for the 3D modeling of geogrid–soil interaction under pullout loading conditions," Geotextiles and Geomembranes, Vol. 37, pp 1-9.

Tran, VDH, MA Meguid, and LE Chouinard (2013) "Three-Dimensional Analysis of Geogrid Reinforced Soil Using Finite-Discrete Element Framework," International Journal of Geomechanics (submitted).

Tran, VDH, MA Meguid, and LE Chouinard (2012) "Discrete Element and Experimental Investigations of the Earth Pressure Distribution on Cylindrical Shafts," International Journal of Geomechanics (in press).

Van Langen, H, and PA Vermeer (1991) "Interface elements for singular plasticity points," International journal for numerical and analytical methods in geomechanics, Vol. 15, No. 5, pp 301-315.

Villard, Pascal, and Bruno Chareyre (2004) "Design methods for geosynthetic anchor trenches on the basis of true scale experiments and discrete element modelling," Canadian Geotechnical Journal, Vol. 41, No. 6, pp 1193-1205.

Villard, P, B Chevalier, B Le Hello, and G Combe (2009) "Coupling between finite and discrete element methods for the modelling of earth structures reinforced by geosynthetic," Computers and Geotechnics, Vol. 36, No. 5, pp 709-717.

Villard, P, JP Gourc, and H Giraud (2000) "A geosynthetic reinforcement solution to prevent the formation of localized sinkholes," Canadian Geotechnical Journal, Vol. 37, No. 5, pp 987-999.

Walz, B. (1973) "Left bracket apparatus for measuring the three-dimensional active soil pressure on a round model caisson right bracket," Baumaschine und Bautechnik, Vol. 20, No. 9, pp 339-344

Wang, MC, YX Feng, and M Jao (1996) "Stability of geosynthetic-reinforced soil above a cavity," Geotextiles and Geomembranes, Vol. 14, No. 2, pp 95-109.

Wayne, M.H., Han, J., and Akins, K. (1998) "The design of geosynthetic reinforced foundations," Proceedings of ASCE's 1998 Annual Convention & Exposition. ASCE Geotechnical Special Publication, Vol. 76, pp 1–18.

Weatherley, D., Boros, V., and Hancock, W. (2011) "ESyS - Particle Tutorial and User's Guide Version 2.1," The University of Queensland.

Xiao, SP, and Ted Belytschko (2004) "A bridging domain method for coupling continua with molecular dynamics," Computer methods in applied mechanics and engineering, Vol. 193, No. 17, pp 1645-1669.

Yamamoto, Kentaro, and Jun Otani (2002) "Bearing capacity and failure mechanism of reinforced foundations based on rigid-plastic finite element formulation," Geotextiles and Geomembranes, Vol. 20, No. 6, pp 367-393.

Yan, Ying, and Shunying Ji (2010) "Discrete element modeling of direct shear tests for a granular material," International journal for numerical and analytical methods in geomechanics, Vol. 34, No. 9, pp 978-990.

Yetimoglu, Temel, Jonathan TH Wu, and Ahmet Saglamer (1994) "Bearing capacity of rectangular footings on geogrid-reinforced sand," Journal of Geotechnical Engineering, Vol. 120, No. 12, pp 2083-2099.

Yoo, Chungsik (2013) "Interaction between tunneling and bridge foundation–A 3D numerical investigation," Computers and Geotechnics, Vol. 49, pp 70-78.

Zdravkovic, L, DM Potts, and HD St John (2005) "Modelling of a 3D excavation in finite element analysis," Geotechnique, Vol. 55, No. 7, pp 497-513.

Zienkiewicz, OC, and GC Huang (1990) "A note on localization phenomena and adaptive finite-element analysis in forming processes," Communications in applied numerical methods, Vol. 6, No. 2, pp 71-76.

Zienkiewicz, O. C., M. Pastor, and Mao-song Huang (1995) "Softening, localisation and adaptive remeshing. Capture of discontinuous solutions," Computational mechanics, Vol. 17, No. 1-2, pp 98-106.

Zienkiewicz, O. C. and Huang, G. C. (1990) "A note on localization phenomena and adaptive finite-element analysis in forming processes," Commun. appl. numer. methods, Vol. 6, pp 71–76.